Technische Universität München
Physik Department
Institut für Theoretische Physik T39
Univ.-Prof. Dr. W. Weise

QCD Matter under extreme Conditions

—

Heavy Ion Collisions

Dipl.-Phys. (Univ.) Thorsten Renk

CONTENTS

Summary

The main goal of this work is a comprehensive description of the fireball created in current ultrarelativistic heavy-ion collisions. This has to be a three-step process: In the first step, properties of hot and dense hadronic matter are investigated, culminating in the introduction of a phenomenological quasiparticle model for the description of the quark-gluon plasma (QGP) phase. In a second step, this information is used as input into the construction of a thermodynamically self-consistent model of the fireball. Hadronic observables are shown to yield tight constraints on the formulation of such a model. In the last step, the model is shown to describe several different other sets of observables, such as the emission of dileptons and photons and the suppression of charmonium production. Summarizing all information from different observables, there is strong evidence for a partonic phase being created already at the CERN SPS accelerator.

Zusammenfassung

Das Hauptziel dieser Arbeit liegt in einer umfassenden Beschreibung des Feuerballs, der in ultrarelativistischen Schwerionenstössen erzeugt wird. Dies wird in drei Schritten erreicht: Als erstes werden allgemein Eigenschaften heisser und dichter hadronischer Materie untersucht. Phänomenologisch lässt sich die Thermodynamik des Quark-Gluon Plasmas (QGP) gut im Rahmen eines hier beschriebenen Quasiteilchenmodells beschreiben. In einem zweiten Schritt wird diese Quasiteilchenbeschreibung als Ausgangspunkt für ein dynamisches Modell der Feuerballentwicklung verwendet und gezeigt, dass die Messung hadronischer Observablen einem solchen Modell enge Einschränkungen setzt. Dieses Modell wird nun weiter dazu verwendet, auch andere experimentall zugängliche Grössen zu beschreiben, unter anderem die Emission von Dileptonen und Photonen oder die Unterdrückung der Produktion von Charmonia. In der zusammenfassenden Betrachtung aller gewonnen Informationen werden deutliche Hinweise erkennbar, die für die Erzeugung einer partonischen Phase schon am SPS Beschleuniger (CERN) sprechen.

Φυσις δε καθ′ Ηρακλειτον κρυπθεσται φιλει.
'Nature loves to hide.' (Heraklit)

Εαν μη ελπηται, ανελπιστον ουκ εξευρησει, ανεξερευνητον εον και απορον.
'If you do not expect the unexpected, you will not find it; for it is hard to be sought out and difficult.' (Heraklit)

Chapter 1

INTRODUCTION

$\kappa\alpha\iota\ \epsilon\kappa\ \pi\alpha\nu\tau\omega\nu\ \epsilon\nu\ \kappa\alpha\iota\ \epsilon\xi\ \epsilon\nu o\varsigma\ \pi\alpha\nu\tau\alpha.$
'Out of all things there comes a unity, and out of a unity all things.' (Heraklit)

It sometimes happens in nature that seemingly complex phenomena can be explained by a very simple general principle, whereas seemingly simple ideas lead to very complex consequences. The Lagrangian of Quantum Chromodynamics (QCD), $\mathcal{L}_{QCD}$, is a good illustration of this idea: It can be written down in a single line (see appendix A for a summary), but in this line, a rich variety of apparently unrelated phenomena is contained: The binding force of nuclear matter, the mass spectrum of all hadronic excitations, the high-energy behaviour of hadronic scattering cross sections, the momentum and spin distribution of partons contained inside the nucleon — all of these follow from the dynamics encoded in $\mathcal{L}_{QCD}$.

However, a first principles calculation of the mentioned phenomena directly from $\mathcal{L}_{QCD}$ is still out of reach. Therefore, in order to see the beauty that lies in the simplicity of $\mathcal{L}_{QCD}$, one has to probe the theory in situations where its effects become manifest in a simple way. Two problems prohibit this in most situations: The coupling constant is strong (which makes a perturbative expansion impossible) and the theory is non-Abelian, leading to interactions of the gauge bosons among each other which eventually are responsible for *confinement*, the impossibility to observe the fundamental degrees of freedom in the Lagrangian as asymptotic states.

However, as shown in appendix A, QCD exhibits the property of *asymptotic freedom*, i.e at large momentum transfers, the coupling becomes weak and therefore the fundamental degrees of freedom, quarks and gluons, are quasifree. This can be pictured as follows: Any colour charge in the vacuum is surrounded by a cloud of quantum fluctuations. In QCD, these quantum fields act in such a way as to enhance the original charge ('antiscreening'). At large momentum transfers however, a small spatial region is resolved and as a consequence the antiscreening cloud is penetrated, the charge 'seen' by the interaction appears weaker.

1

Deep inelastic electron scattering off nucleons probes QCD in a regime where the coupling actually becomes small and the theory gets simple. Conversely, it was soon realized that if one would heat up hadronic matters to such temperatures that typical momentum transfers in collisions in the heat bath would be very large, asymptotic freedom would lead to a system of quasifree quarks and gluons — the most simple manifestation of $\mathcal{L}_{QCD}$ one could think of. This partonic state of matter should be characterized by properties vastly different from those of ordinary hadronic matter. In analogy to the ordinary gas – plasma transition, this state of matter has been baptized quark-gluon plasma (QGP).

The prediction of the existence of the QGP has triggered enormous activity from both theory and experiment with the aim to verify its existence and study its properties, notably the equation of state (EoS). The experimental search for the QGP was started with heavy-ion collisions, where an enormous amount of energy can be concentrated in a small volume and the production of several hundreds of secondary particles makes equilibration of the produced matter possible.

But as the greek philosopher Heraklit put it: 'Nature loves to hide.' In spite of the tremendous research activity, the QGP has remained elusive so far. Several observables have been proposed as signals for the creation of the QGP, among them the suppression of charmonium states in nucleus-nucleus (A-A) collisions with respect to scaled nucleon-nucleon (p-p) or nucleon-nucleus (p-A) collisions due to the screening properties of a deconfined partonic medium, changes in the shape of the invariant mass spectrum of emitted dileptons due to the different production mechanism ($q\bar{q}$ annihilation vs. $\pi\pi \rightarrow \rho, \omega, \phi \rightarrow e^+e^-$) where the characteristic peaks caused by the intermediate vector meson states should disappear and the enhancement of strange particles in the finally measured particle yield due to the relatively abundant creation of strange quarks in a QGP.

None of these signals has given the unambiguous proof researchers had hoped for. The reason is that different models could be built that explain the measured data with and without the creation of a QGP. But there is a deeper reason for this: Heavy-ion collisions are very dynamical events with several evolution phases following each other and involve physical processes which are not well known and cannot easily be inferred from p-p or p-A collisions. Therefore, a model which describes e.g. the dissociation of charmonia inside the medium must also contain a part in which the evolution of the medium is described. Models involving different mechanisms of charmonium dissociation: screening of the binding potential and dissociation by collisions with hadrons can still describe the same data well if the medium evolutions in both models has been chosen differently. In many models, the medium evolution was *tuned* to describe the data, naturally resulting in different medium evolutions for different processes under consideration.

Obviously, this does not lead to progress in the search for the creation of the QGP. Rather, research should be organized in three distinct steps:

- First, the properties of the QGP and hot hadronic matter have to be assessed in an ideal situation, i.e. for an infinite, static system. In this way, a foundation can be established regarding signals to be expected from this phase of matter and an input for dynamical models, e.g. in terms of the EoS, can be provided. Naturally, progress along this front can only be made in theory, notably in lattice simulations of QCD.

- Once the properties of the QGP and ordinary hadronic matter are known in an idealized situation, this information must be incorporated into a model of the conditions realized in experiment. As this cannot be done from first principles, a subset of all available data has to be used as a guideline for modelling the medium evolution. For that purpose, preferably data most closely connected to the bulk of the produced matter, i.e. hadronic observables should be chosen.

- Only after the evolution of the medium has been fixed, processes like dilepton emis-

sion or charmonium suppression can be calculated in the framework given by the medium evolution specified before. This ensures that the resulting model is consistent with all available data and eliminates ambiguities as much as possible.

The aim of the present work is to contribute to the quest for the QGP by following the program outlined above. We will not do this by trying to construct a model based entirely on hadronic degrees of freedom and infer the existence of the QGP from the failure of such a model — if we do not expect the unexpected, we will not find it; instead, we rather make use of the information about the QGP coming from lattice calculations and incorporate it from the beginning into a model of fireball evolution to show that the existence of the QGP follows naturally from the creation of a thermalized system at present accelerator energies and is consistent with the data obtained so far. This is, of course, not to be considered as a proof, but certainly as circumstantial evidence at the present level of empirical information.

Chapters 2 and 3 discuss properties of a static QGP. The first of these two chapters introduces finite temperature field theory, the appropriate framework in which to calculate the thermodynamics of hot QCD. Perturbative and non-perturbative calculation schemes are shown and their abilities assessed carefully. Chapter 3 then turns to the discussion of the results obtained with these techniques — this will mainly involve a discussion of the phase transition from ordinary hadronic matter to the QGP, which is manifest in a pronounced change of thermodynamical properties, the (de)confinement transition and chiral restoration.

We then turn towards a discussion of the conditions realized in current heavy-ion collision experiments. In chapter 4, we introduce the relevant terminology, estimate orders of magnitude and then go qualitatively through the physics of all evolution phases of the system created in such a collision. Chapter 5 takes up the thread as we try to quantify the statements made in chapter 4 by presenting experimental results on hadronic observables along with their interpretation in terms of the space-time geometry of the fireball. In the second part of the chapter, we combine this information with the thermodynamic properties of the QGP discussed in chapter 3 to construct a simple but self-consistent model of the fireball evolution.

This model then serves as the baseline for the next chapters: Using the medium evolution, we discuss the relative abundance of hadron species formed after the collision in chapter 6, the emission of dileptons from the fireball in chapter 7, the emission of real photons in chapter 8 and the dissociation of charmonia in chapter 9. All four calculations are compared to data and the potential of the observables to serve as a signal for the creation of the QGP is discussed in some detail.

In the last chapter, we review the main results and draw conclusions. Finally, a brief outlook to possible extensions of the model framework will be given. Several short appendices serve to complement the material presented in the main body of the text.

Chapter 2

BASICS OF THERMAL FIELD THEORY

In order to describe the physics of heavy-ion collisions, we will generally start from the assumption that we are dealing with a system in local thermal equilibrium unless stated otherwise. This assumption can not be strictly proven, but there are hints from both theory and experiment that early thermalization of the produced matter is possible and most likely realized in collisions at current beam energies.

The appropriate tool to calculate the properties of a thermalized system of strongly interacting particles is thermal field theory (TFT). In the following, we introduce the main concepts and techniques of TFT which will be of importance for the discussion of the physics of heavy ion collisions in later chapters. The presentation here mostly follows [1] and [2].

2.1 BASIC RELATIONS

A large ensemble of interacting particles in equilibrium can be characterized by macroscopic variables such as the temperature T, its volume V or its chemical potential μ (we define also the inverse temperature $\beta = 1/T$) which emerge from a statistical averaging procedure over microscopic dynamics. Key quantity for the properties of such an ensemble is the partition function

$$\mathcal{Z}(T,V) = \mathrm{Tr}\exp[-\beta H] = \sum_n \langle n|e^{-\beta H}|n\rangle. \qquad (2.1)$$

Here, H is the Hamiltonian of the ensemble and the sum extends over a complete set of physical eigenstates. The statistical average of any operator O in this ensemble is then

obtained using

$$\langle O \rangle_\beta = \frac{1}{\mathcal{Z}} \text{Tr} O \exp[-\beta H] = \sum_n \langle n | O e^{-\beta H} | n \rangle. \tag{2.2}$$

(In the presence of conserved quantum numbers Q which can be treated within the grand canonical ensemble, that is, which need to be conserved on average, $\exp[-\beta H]$ has to be replaced by $\exp[-(\beta H - \mu_Q Q)]$ with the appropriate chemical potential μ_Q.)

The propagation of particles in the heat bath is obtained by evaluating the thermal average of the Green's function

$$\langle G(x, x') \rangle_\beta = \langle \mathcal{T} \phi(x) \phi(x') \rangle_\beta = \sum_n \langle n | G(x, x') e^{-\beta H} | n \rangle, \tag{2.3}$$

where $\mathcal{T}$ denotes the time-ordered product. (For simplicity, we consider first the case of a non-interacting scalar field ϕ). Using the operator identity

$$\mathcal{T} \phi(x) \phi(x') = \langle 0 | \mathcal{T} \phi(x) \phi(x') | 0 \rangle + \mathcal{N} \phi(x) \phi(x'), \tag{2.4}$$

one immediately observes that in addition to the first term, the usual $T = 0$ propagator, the normal-ordered product $\mathcal{N}$ does not vanish in the heat bath due to the presence of the term $\sum_n \langle n | \ldots | n \rangle$. Decomposing the field ϕ into the usual set of creation operators $a_k^\dagger$ and annihilation operators a_k, the new contribution is

$$2 \int \frac{d^3 k}{(2\pi)^3} \frac{1}{2E_k} e^{ik(x-x')} \langle a_k^\dagger a_k \rangle_\beta = 2 \int \frac{d^3 k}{(2\pi)^3} \frac{1}{2E_k} e^{ik(x-x')} f_B(E_k), \tag{2.5}$$

where we have introduced the Bose-Einstein distribution $f_B(E_k) = \frac{1}{e^{\beta E_k} - 1}$, as this is the average number of particles in a state with energy E_k in a thermalized ensemble. The propagator in momentum space can then be found as

$$D_F(k) = \frac{i}{k^2 - m^2 + i\epsilon} + 2\pi \delta(k^2 - m^2) n_B(k_0). \tag{2.6}$$

Here, $n_B(k_0) = f_B(|k_0|)$. There is a new contribution to the propagator which describes the on-shell propagation of particles from the thermal ensemble with the statistical probability of having the appropriate momentum. Thus, for the propagation of particles in a thermal environment, one has to deal not only with virtual fluctuations (first term) but also with thermal fluctuations (second term). Note that the second contribution breaks Lorentz invariance due to the presence of k_0 in the expression. The reason for this is the presence of the heat bath which constitutes a preferred frame of reference. Introducing u_μ, the four-velocity of the heat bath, Lorentz invariance can be formally recovered by the substitution $k_0 \to k_\mu u^\mu$.

The calculation for free fermion fields is similar and results in the thermal propagator

$$S_F(k) = (k_\mu \gamma^\mu + m) \cdot \left(\frac{i}{k^2 - m^2 + i\epsilon} - 2\pi \delta(k^2 - m^2) n_D(k_0) \right) \tag{2.7}$$

Here, $n_D(k_0) = f_D(|k_0|)$ with the Fermi-Dirac distribution $f_D(k_0) = \frac{1}{e^{\beta k_0} + 1}$. Again, we find the presence of virtual and thermal fluctuations in the propagation of particles in the heat bath as in the case of the scalar field.

2.2   Perturbative techniques

Consider now the case of an interacting field theory. If the interaction is a small correction to the free Hamiltonian, then a perturbative expansion in powers of the coupling constant

can be performed. The framework is developed in close analogy with the $T = 0$ case as follows:

First, we observe that there is a striking similarity between the statistical density operator $\rho = \exp[-\beta H]$ and the time evolution operator $\exp[iHt]$. In fact, the statistical operator can be interpreted as the evolution from 0 to β in imaginary time $\tau = it$. Therefore, the partition function can be expressed in terms of an Euclidean path integral. In the case of a scalar field, this reads

$$\mathcal{Z}(T, V) = \oint \mathcal{D}\phi \exp\left(-\int_0^\beta d\tau \int_V d^3x \mathcal{L}_E[\phi(\tau, \mathbf{x})]\right) \tag{2.8}$$

with a restriction to periodic field configurations, $\phi(0, \mathbf{x}) = \phi(\beta, \mathbf{x})$. The corresponding expression for full QCD reads

$$\mathcal{Z}(T, V, m_0, \mu) = \oint \mathcal{D}A_\mu \mathcal{D}\overline{\Psi} \mathcal{D}\Psi \exp\left(-\int_0^\beta d\tau \int_V d^3x \left\{\mathcal{L}_G^E + \mathcal{L}_q^E(m_0) - \mu\Psi^\dagger\Psi\right\}\right) \tag{2.9}$$

with $\mathcal{L}_G^E$ and $\mathcal{L}_q^E$ being the Euclidean versions of the Lagrange density for gluons and quarks respectively (explicit expressions for $\mathcal{L}_G$ and $\mathcal{L}_q$ are given in appendix A). For fermionic fields Ψ, antiperiodic boundary conditions are required, $\Psi(0, x) = -\Psi(\beta, x)$.

In close analogy to the derivation of Feynman rules in the $T = 0$ case, we can interpret these expressions as generating functionals from which we can obtain the thermal 2-point functions, if we add a source term $j(x)$ to Eqs. (2.8) and (2.9) and differentiate with respect to this source,

$$G(x, x') = \frac{1}{\mathcal{Z}_\beta} \left.\frac{\delta^2 Z[J]_\beta}{i\delta j(x) i\delta j(x')}\right|_{j=0}, \tag{2.10}$$

where $Z[J]_\beta$ emerges from e.g. Eq. (2.8) as

$$Z[J] = \oint \mathcal{D}\phi \exp\left(-\int_0^\beta d\tau \int_V d^3x \mathcal{L}_E[\phi(\tau, \mathbf{x})] + j(x)\phi(x)\right), \tag{2.11}$$

with appropriate adaptions as in Eq. (2.9) for the QCD case. From this expression, different choices of the path going from an arbitrary time t_i to $t_i - i\beta$ now lead to different calculational frameworks.

2.2.1 The imaginary time formalism

The simple choice of the direct path leads to the so-called *imaginary time formalism*. The (anti)periodic boundary conditions of the fields then imply a discretization of imaginary (Matsubara) frequencies in momentum space. The Feynman rules which can be derived within this framework coincide with the ones at $T = 0$ if the following changes are implemented:

Loop integrals have to be replaced as

$$\int \frac{d^4k}{i(2\pi)^4} \rightarrow \frac{1}{\beta} \sum_{n=-\infty}^{+\infty} \int \frac{d^3k}{(2\pi)^3}, \tag{2.12}$$

where the sum extends over the discrete frequencies in imaginary time. For the same reason, the momentum conserving delta functions become

$$i(2\pi)^4\delta^4(k) \rightarrow \beta(2\pi)^3\delta_{n,0}\delta^3(\mathbf{k}) \tag{2.13}$$

The discrete Matsubara frequencies appear as

$$k_0 \rightarrow \frac{2\pi i}{\beta}(n + \zeta) \tag{2.14}$$

with n running from $-\infty$ to $+\infty$ and $\zeta = 0$ for bosons and $1/2$ for fermions. In this representation, the distinction between virtual (quantum) fluctuations and thermal fluctuations is not evident from the form of the propagators but is implicit in the theory and becomes apparent only after calculations have been performed.

2.2.2 The real-time formalism

The lack of the explicit separation of thermal and quantum fluctuations and the fact that the imaginary time formalism has difficulties in dealing with dynamical quantities, such as emission rates from a hot region, has given rise to the choice of a different path C in the imaginary time plane connecting t_i and $t_i - i\beta$. This path first goes along the real axis, thus probing the evolution in real time, then into imaginary direction towards $-t_i - i\sigma$, returns parallel to the real axis until it finally reaches the final point $t_i - i\beta$ (see Fig. 2.1). In doing so, an unphysical parameter σ is introduced, which should not affect observables in the end.
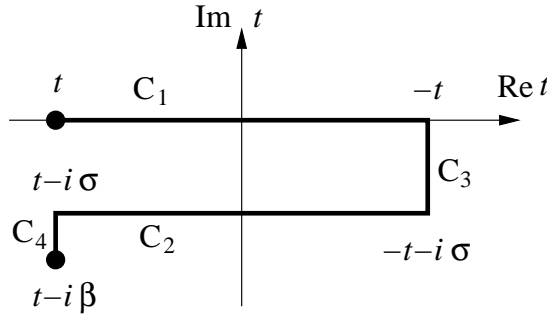
FIGURE 2.1: The path in the imaginary time plane leading to the real time formalism of thermal field theory.

Eq. (2.11) can now be computed as in $T = 0$ field theory by a Gaussian integration. One finds

$$\begin{aligned} Z[J]_\beta = &const. \cdot \exp\left(-\frac{1}{2}\int_C d^4x \int_C d^4x' j(x) D_F(x - x') j(x')\right) \\ &\times \exp\left(-i\int_C d^4x \left[V\left(\frac{\delta}{i\delta j(x)}\right)\right]\right) \end{aligned} \tag{2.15}$$

where we have written the full Hamiltonian H as a sum of the free Hamiltonian H_0 and an interaction potential $V(\phi)$, $H = H_0 + V(\phi)$. It can be proven that in the limit $t \rightarrow \infty$, the free generating functional factorizes in a part corresponding to the sections C_1 and C_2 of the path C and a second part corresponding to the vertical pieces C_3 and C_4. The last part can be neglected as long as one calculates graphs with at least one external line and the propagator $D_F(x - x')$ is given by the free thermal propagator. In this way, the discretization of frequencies along the imaginary time direction is avoided.

Labelling the source terms as $j_1(t)$ and $j_2(t - i\sigma)$ according to the section of C they live

on, we can rewrite $Z[J]_\beta$ as

$$Z[J]_\beta = const. \cdot \exp\left(-\frac{1}{2}\int_{-\infty}^{\infty} d^4x \int_{-\infty}^{\infty} d^4x' j(x)_a D_F(x-x')^{ab} j(x')_b\right)$$
$$\times \exp\left(\int_{-\infty}^{\infty} d^4x \left[V\left(\frac{\delta}{i\delta j_1(x)}\right) - V\left(\frac{\delta}{i\delta j_2(x)}\right)\right]\right) \tag{2.16}$$

with a summation over $a, b = 1, 2$. The propagator has now acquired a 2×2 matrix structure, corresponding to propagation along C_1, C_2 and off-diagonal elements for the transition between C_1 and C_2. We find a doubling of degrees of freedom, there is a ghost field living on C_2 with an unphysical imaginary time component. This, however, is essential for the calculation of loop diagrams, as the contributions of this ghost field exactly cancel out unphysical products of delta functions. Of course, only the field ϕ_1 corresponds to a physical quantity and can appear on the external lines of a diagram.

The explicit form of the propagator in momentum space for the scalar theory can be found as

$$D_F^{11}(k) = \frac{i}{k^2 - m^2 + i\epsilon} + 2\pi\delta(k^2 - m^2)n_B(k_0), \tag{2.17}$$

$$D_F^{22}(k) = \frac{-i}{k^2 - m^2 - i\epsilon} + 2\pi\delta(k^2 - m^2)n_B(k_0), \tag{2.18}$$

$$D_F^{12}(k) = e^{\sigma k_0}[n_B(k_0) + \theta(-k_0)]2\pi\delta(k^2 - m^2), \tag{2.19}$$

$$D_F^{21}(k) = e^{-\sigma k_0}[n_B(k_0) + \theta(k_0)]2\pi\delta(k^2 - m^2). \tag{2.20}$$

Here, the clean separation of quantum and thermal fluctuations is again manifest from the beginning, different from the imaginary time formalism. For practical calculation, usually $\sigma = 0$ (Keldysh-Schwinger prescription) or $\sigma = \beta/2$ (symmetrical choice) are used.

The matrix structure of the propagator leads to the following modification of the Feynman rules:

- There are two types of vertices, (1) and (2). (1) Vertices correspond to the normal $T = 0$ vertices, whereas (2) vertices are characterized by opposite sign and can only be internal. These vertices couple the ghost fields ϕ_2.

- D^{11} propagators connect (1) vertices, D^{22} propagators (2) vertices and the transitions are given by D^{12} propagators connecting physical and ghost field.

- One has to sum over all possible combinations of internal vertices of type (1) and (2).

- All propagators with at least one external leg have to be physical, that is, they have to connect to a ϕ_1 field.

The derivation of the propagators in the case of QCD can be done along the similarly; it is in principle straightforward, though technically more involved. It turns out that the 2×2 matrix structure of the propagators is also realized in QCD, therefore the above rules regarding vertices of type (1) and (2) also apply.

The resulting propagator for quarks reads

$$S_F^{11}(k) = (\not{k} + m)\left(\frac{i}{k^2 - m^2 + i\epsilon} - 2\pi\delta(k^2 - m^2)n_D(k_0)\right), \tag{2.21}$$

$$S_F^{22}(k) = (\not{k} + m)\left(\frac{-i}{k^2 - m^2 - i\epsilon} - 2\pi\delta(k^2 - m^2)n_D(k_0)\right), \tag{2.22}$$

$$S_F^{12}(k) = (\not{k} + m)\left(e^{\sigma k_0}[-n_D(k_0) + \theta(-k_0)]2\pi\delta(k^2 - m^2)\right), \tag{2.23}$$

$$S_F^{21}(k) = (\not{k} + m)\left(e^{-\sigma k_0}[-n_D(k_0) + \theta(k_0)]2\pi\delta(k^2 - m^2)\right). \qquad (2.24)$$

The fact that gluons are gauge bosons causes some additional difficulties. First of all, a gauge has to be chosen in order to do calculations. Here, the choice of a non-covariant gauge poses no additional difficulties, as Lorentz invariance is broken already due to the presence of the heat bath.

We already know from $T = 0$ field theory that a 'ghost' field (the Fadeev-Popov ghosts) has to be introduced into the theory to cancel unphysical degrees of freedom appearing in the perturbative expansion of $\mathcal{L}_{QCD}$ (see e.g. [3]). This is a general feature of non-Abelian gauge theories. In finite temperature field theory, we encounter exactly the same problem. Both $T = 0$ and thermal part of the propagators develop unphysical degrees of freedom (longitudinal and time-like gluons) which need to be cancelled out by the $T = 0$ and thermal part of the ghost propagator.

However, recall that thermal expectation values of an operator O are calculated by taking the trace over *physical* states $|n\rangle$,

$$\langle O \rangle = \mathcal{Z}^{-1}\sum_n \langle n|e^{\beta H}O|n\rangle \qquad (2.25)$$

with the partition function $\mathcal{Z} = \sum_n \langle n|e^{\beta H}|n\rangle$, therefore the thermal part of the propagator is directly associated with particles in the physical states only. Consequently, only physical degrees of freedom can acquire a thermal part of the propagator while unphysical degrees of freedom never come to equilibrium. Therefore, thermal contributions from ghosts and unphysical degrees of freedom can be set zero from the beginning [2]. In doing so, the gauge propagator can be separated into a $T = 0$ part (using $\sigma = 0$ and Feynman gauge)

$$D_F^{\mu\nu}|_{T=0} = \delta_{ab}(-g^{\mu\nu})\begin{pmatrix} \frac{i}{q^2 + i\epsilon} & 2\pi\theta(-q_0)\delta(q^2) \\ 2\pi\theta(q_0)\delta(q^2) & \frac{-i}{q^2 - i\epsilon} \end{pmatrix} \qquad (2.26)$$

and a thermal part

$$D_F^{\mu\nu}|_{T\neq0} = \delta_{ab}P_T^{\mu\nu}2\pi\delta(q^2)n_B(q_0)\begin{pmatrix} 1 & 1 \\ 1 & 1 \end{pmatrix} \qquad (2.27)$$

with the the transverse projection tensor $P_T^{\mu\nu}$ as defined in Eq. (C.11). In this scheme, no contributions of thermal ghosts need to be taken into account. The structure of vertices, apart from the rules regarding (1) and (2) vertices is identical to the one of $T = 0$ QCD.

2.3 THERMAL SELF-ENERGIES

Self-energies of particles in the medium are important quantities, as they reflect the modification of particle properties caused by the interaction with the heat bath. Specifically, one would like to know the 'physical' self-energy $\overline{\Pi}$, i.e. the one that modifies the $T = 0$ part of the propagator and corresponds to a modification of particle mass and decay width:

$$\frac{i}{k^2 - m^2 + i\epsilon} \rightarrow \frac{i}{k^2 - (m^2 + \overline{\Pi}) + i\epsilon} \qquad (2.28)$$

The matrix structure of the propagator introduces some complication into the calculation of $\overline{\Pi}$, as there as there is now not only a self energy corresponding to the $T = 0$ part of the physical D^{11} propagator but also self-energies corresponding to the thermal parts of this propagator and additional ones for the D^{12}, D^{21} and D^{22} propagators. This makes the extraction of a physical self energy $\overline{\Pi}$ seem difficult. However, one can proceed as follows:

The free propagator matrix $\mathbf{D}_F$ can be diagonalized by a matrix $\mathcal{U}(k_0)$ such that

$$\mathbf{D}_F = \mathcal{U}(k_0)\begin{pmatrix} D_F^0 & 0 \\ 0 & D_F^{0*} \end{pmatrix}\mathcal{U}(k_0) \qquad (2.29)$$

with the $T = 0$ propagator D_F^0 and e.g.

$$\mathcal{U}(k_0) = \begin{pmatrix} \sqrt{1 + n_B(k_0)} & \sqrt{n_B(k_0)} \\ \sqrt{n_B(k_0)} & \sqrt{1 + n_B(k_0)} \end{pmatrix} \qquad (2.30)$$

for the symmetric choice $\sigma = \beta/2$.

The Dyson equation for the full propagator becomes a matrix equation in the real time formalism

$$\mathbf{D} = \mathbf{D}_F + \mathbf{D}_F(-i)\mathbf{\Pi}\mathbf{D} \qquad (2.31)$$

with a thermal self-energy matrix $\mathbf{\Pi}$. Hence the full propagator is also diagonalized by $\mathcal{U}$, implying

$$-i\mathbf{\Pi}(k) = \mathcal{U}^{-1}\begin{pmatrix} -i\overline{\overline{\Pi}}(k) & 0 \\ 0 & (-i\overline{\overline{\Pi}}(k))^* \end{pmatrix}\mathcal{U}^{-1} \qquad (2.32)$$

where a single scalar function appears, the physical self-energy $\overline{\overline{\Pi}}$.

Solving the matrix equation, one can derive relations between matrix elements of the full self-energy matrix $\mathbf{\Pi}$ and the physical self-energy $\overline{\overline{\Pi}}$:

$$\mathrm{Re}\overline{\overline{\Pi}}(k) = \mathrm{Re}\Pi^{11}(k), \qquad (2.33)$$

$$\mathrm{Im}\overline{\overline{\Pi}}(k) = \frac{\mathrm{Im}\Pi^{11}(k)}{1 + 2n_B(k_0)}, \qquad (2.34)$$

$$\mathrm{Im}\overline{\overline{\Pi}}(k) = \frac{i\epsilon(k_0)}{2}\frac{1}{f_B(k_0)}\Pi^{12}(k) \qquad (2.35)$$

for the Keldysh-Schwinger choice $\sigma = 0$, or

$$\mathrm{Im}\overline{\overline{\Pi}}(k) = \frac{\sinh(\beta|k_0|/2)}{-i}\Pi^{12}(k) \qquad (2.36)$$

for the symmetric choice $\sigma = \beta/2$. Thus, in order to find the physical self energy $\overline{\overline{\Pi}}$, it is sufficient to know real and imaginary parts of certain matrix elements of $\mathbf{\Pi}$ only. The expression for fermion self energies follow from the replacement $n_B \rightarrow -n_D$ in Eqs. (2.33) - (2.35).

As a simple example, the decay width Γ of a scalar particle ϕ immersed in a heat bath can be found from the self energy of the D^{12} propagator as

$$-m_\phi\Gamma = \mathrm{Im}\overline{\overline{\Pi}}(m_\phi) = \frac{\sinh(\beta|m_\phi|/2)}{-i}\Pi^{12}(m_\phi). \qquad (2.37)$$

2.4 Hard Thermal Loop Resummation

From the form of the propagators in the real time formalism, Eqs. (2.17) – (2.20) it is immediately clear that there are no new ultraviolet divergencies introduced by the thermal part of the propagators, since large momenta in loop integrals are exponentially suppressed by the distribution functions f_B or f_D. The only place where these divergencies can appear

is the normal $T = 0$ part of the propagators, and these divergencies can be treated within the usual framework of renormalization.

The infrared behaviour of naive perturbation theory however can be more dangerous. At $T = 0$, the only scale that enters a massless, renormalizable theory is the renormalization scale Λ. If one considers the calculation of e.g. a self-energy correction to a propagator, dimensional counting and Lorentz invariance dictate $\Pi(p) = g^2 p^2 f(p^2/\lambda^2)$, where f is a dimensionless function. Thus, for small g, the correction is small compared to the scale set by the external momentum p even if p is soft and the self-energy can be resummed in the propagator.

This is not so at finite T: Here a new scale is introduced by the temperature and loop integrals for soft external momenta with $p < T$ are now dominated by momenta $k \sim T$ due to the on-shell character of thermal fluctuations propagating in the loop. In this case, dimensional counting leads to a correction $\Pi \sim g^2 T^2$, so for soft external momenta $\sim gT$, the correction becomes as large as the inverse bare propagator and naive perturbation theory breaks down. A resummation of the dominant collective effects becomes crucial.

The Hard Thermal Loop (HTL) resummation scheme improves the infrared behaviour of the theory by a consistent resummation of all loops dominated by hard thermal fluctuations [4]. For hard external momenta, $p \sim T$, no modification of the propagators need to be taken into account, but for soft momenta $p \sim gT$, resummed propagators and vertices have to be used from the start.

The effects of hard thermal loops also appear in gauge theories where the gauge bosons acquire a thermally generated mass. It can be proven that in this case the HTL resummation scheme is still manifestly gauge invariant, thus a consistent treatment of QCD within this scheme is possible, though very involved.

2.5 LATTICE TECHNIQUES

If the coupling of the theory is not small (which is most likely the case for QCD in the energy regime of current heavy-ion experiments), a perturbative treatment of Eq. (2.9) is impossible. Instead, the partition function can be calculated numerically using Monte-Carlo techniques by evaluating it on a discrete lattice of space-time points. This is possible since one is dealing with an Euclidean path integral, where the dominant region can easily be identified since strong fluctuations are exponentially damped, unlike in Minkowski space, where the dominant contribution to the path integral emerges from the interference pattern of oscillating amplitudes.

The introduction of a lattice spacing a then automatically introduces an ultraviolet cutoff, thus regularizing any divergences appearing in the continuum. At the same time, Lorentz invariance is broken. The total extension of the lattice is given by the number of spatial N_σ^3 and temporal N_τ sites. The volume and temperature of the simulation can then be identified as

$$V = (N_\sigma a)^3 \qquad \text{and} \qquad \beta = N_\tau a. \tag{2.38}$$

The total size of the lattice hence defines an infrared cutoff.

Fermion fields are defined on the grid of space-time points given by the lattice and the gauge fields live on the links connecting adjacent lattice sites x and $x + a\hat{\epsilon}$, where $\hat{\epsilon}$ is a unit vector along one of the three spatial or the temporal axis.

2.5.1 Gauge fields

The link variables corresponding to the gauge fields are defined as

$$U_\mu(x) = \mathcal{P}\exp\left(ig\int_x^{x+a\hat{\epsilon}} dx'_\mu A^\mu(x')\right) \tag{2.39}$$

with $\mathcal{P}$ denoting path ordering along the integration contour. As these links transform homogeneously under a gauge transformation, $U_\mu(x) \to G(x)U_\mu(x)G^\dagger(x+a\hat{\epsilon})$, the simplest gauge invariant object that can be constructed is a closed set of four links around a lattice plaquette

$$\mathcal{U}_{\mu\nu} = \text{Tr}[U_\mu(na)U_\nu(na+\hat{\epsilon}_1 a)U_\mu^\dagger(na-\hat{\epsilon}_2 a)U_\nu^\dagger(na)]. \tag{2.40}$$

This is already a discretized approximation to the gauge field action (up to errors in powers of the lattice spacing a which vanish in the continuum limit), since

$$\text{Re}\,\mathcal{U}_{\mu\nu} = N_c - \frac{N_c g^2 a^4}{2}\mathcal{G}_{\mu\nu}\mathcal{G}^{\mu\nu} + O(a^6). \tag{2.41}$$

Summing over all lattice sites, the so-called Wilson action for the gauge fields is obtained as

$$S_\mathcal{G}^W = \frac{2N_c}{g^2}\sum_{n,0\le\mu<\nu\le 3} 1 - \frac{1}{N_c}\text{Re}\,\mathcal{U}_{\mu\nu}. \tag{2.42}$$

Since this expression has no dimensionful parameter, the lattice spacing a enters via renormalization group arguments demanding that physical quantities remain unchanged under a change of a. The emerging renormalization scale parameter Λ can then be determined by a lattice computation of an experimentally known quantity, typically the mass of the ρ meson or the string tension σ of the colour field connecting two static sources.

2.5.2 Fermion fields

The implementation of chirally symmetric fermions in lattice calculations is difficult. The naive implementation of the discretized version of the kinetic term in $\mathcal{L}_q$, $\partial_\mu\Psi(x) \to (\Psi(x+\hat{\epsilon}) - \Psi(x-\hat{\epsilon}))/(2a)$ leads to a doubling of the particle content for each dimension as compared to the continuum theory. The reason is that the propagator for a massless fermion has not only a pole at $p = 0$ but also at the end of the first Brillouin zone $pa = \pi$, leading to $2^4 = 16$ fermions for a typical lattice simulation.

One possible solution is the addition of a mass term for the 'doubler' fermions that diverges as $1/a$, effectively eliminating them in the continuum limit. This prescription, leading to so-called Wilson fermions, however, violates chiral symmetry to $O(a)$, rendering lattice simulations of quantities such as the chiral condensate $\langle\overline{\Psi}\Psi\rangle$ difficult.

An alternative way of dealing with the doublers while retaining a continuous subgroup of chiral symmetry at finite a is to distribute the Dirac spinors over several lattice sites, thus reducing the number of doubling fermions to $N_f/4$. This leads to the so-called Kogut-Susskind or staggered fermions.

In general, the simulation of dynamical fermions on the lattice is computationally about a factor 100 more involved than the simulation of gauge fields. Therefore, many lattice results have been calculated for static fermion sources and dynamical gluons only, which in perturbation theory corresponds to neglecting any virtual $q\overline{q}$ pairs in internal loops ('quenched approximation'). This may not be too bad in cases where the dynamics is dominated by gluons.

Chapter 3

PROPERTIES OF THE QUARK GLUON PLASMA

Based on the observation that the coupling constant of QCD becomes weak at large energy scales ('asymptotic freedom') and that the average momentum of a particle in a thermalized system with temperature T is given by $\langle p \rangle \approx 3T$, it was predicted that at large enough temperature T a perturbative treatment of thermalized QCD in terms of a quasifree quark and gluon gas should be appropriate. Specifically, the coupling should behave as

$$\alpha_s(T) = \frac{12\pi}{\beta_0 \log(T^2/\Lambda_T^2)} \quad \text{with} \quad \Lambda_T \simeq \Lambda_{QCD}/3 \simeq 100\,\text{MeV} \tag{3.1}$$

(see appendix A for the scale dependence of the QCD coupling, also e.g. [5]). This state of quasifree quark and gluon matter has been named Quark Gluon Plasma (QGP), as it shares some properties with ordinary plasmas. The transition from normal hadronic hot matter to the QGP is supposedly accompanied by three characteristic phenomena:

- As the relevant degrees of freedom in a hadronic gas and the QGP are fundamentally different, distinct *changes in thermodynamic properties* should occur at a transition temperature T_C. In simple model calculations, one finds a first order phase transition with a corresponding discontinuity in the T-dependence of the energy density associated with a latent heat. This result, however, changes once one treats the interacting system more carefully. For full QCD, the order of the transition depends crucially on the masses of the active quark flavours. Present knowledge favours a crossover, but a weak first order transition cannot be excluded. These issues are covered more in depth in section 3.1.

- A phase transition is frequently associated with the restoration of a spontaneously broken symmetry. In the strict sense, an order parameter can be chosen for the QCD Lagrangian only in the limit $m_q = \infty$ (purely gluonic theory) or $m_q = 0$ (chiral

limit). For a purely gluonic theory, one expects a *confinement/deconfinement* transition with the Polyakov loop L (see Eq. (3.11) as an order parameter. The deconfined phase is characterized by colour charges which can move freely over large distances, as the confining colour forces are screened in the hot partonic medium. This can be observed in the temperature dependent changes of the potential between two static coloured sources. The (de)confinement transition will be covered in greater detail in section 3.2.

- In the case $m_q = 0$, the relevant order parameter is given by the chiral condensate $\langle \overline{\Psi}\Psi \rangle$. The chiral symmetry of the QCD Lagrangian in the absence of quark masses is spontaneously broken in the ground state, resulting in the large mass of constituent quarks, $M_q \sim 300$ MeV [6]. The chiral transition corresponds to a 'melting' of the vacuum structure resulting in a vanishing chiral condensate and, physically, a restoration of the constituent quark masses to current quark masses of order $m_q \sim 10$ MeV. The chiral symmetry restoration is the main topic of section 3.3.

In spite of the fact that neither the Polyakov loop nor the chiral condensate can be regarded as order parameters in the strict sense, both transitions are relevant for the physics at finite but small quark masses and are observed in lattice QCD simulations. The goal of this chapter is to elaborate on these properties and especially introduce the thermodynamics of the QGP in order to prepare the ground for the description of heavy-ion collisions in terms of equilibrated hot matter. This will be done with the help of the tools of thermal field theory which have been introduced in the last chapter. A more detailed treatment of several of the topics of this chapter can be found in [7].

3.1 THERMODYNAMICS OF THE QGP

3.1.1 *The ideal quark-gluon gas*

The simplest ansatz for the QGP thermodynamics is to assume that the temperature is sufficiently high so that the interaction can be neglected. In this case, one finds a free gas of quarks and gluons. Pressure p, energy density ϵ and entropy density s of such a free gas can be calculated from the thermal distribution functions $f_B(E_k^g)$ for gluons with energy E_k and $f_D(E_k^i)$ for massless quarks of flavour i and energy E_k^i as [8]

$$p(T) = \frac{d_g}{6\pi^2} \int_0^\infty dk f_B(E_k^g) \frac{k^4}{E_k^g} + \sum_{i=1}^{N_f} \frac{2N_c}{3\pi^2} \int_0^\infty dk f_D(E_k^i) \frac{k^4}{E_k^i} - B(T), \qquad (3.2)$$

$$\epsilon(T) = \frac{d_g}{2\pi^2} \int_0^\infty dk k^2 f_B(E_k^g) E_k^g + \sum_{i=1}^{N_f} \frac{2N_c}{\pi^2} \int_0^\infty dk k^2 f_D(E_k^i) E_k^i + B(T) \qquad (3.3)$$

and

$$s(T) = \frac{d_g}{2\pi^2 T} \int_0^\infty dk k^2 f_B(E_k^g) \frac{\frac{4}{3}k^2}{E_k^g} + \sum_{i=1}^{N_f} \frac{2N_c}{\pi^3 T} \int_0^\infty dk k^2 f_D(E_k^i) \frac{\frac{4}{3}k^2}{E_k^i}. \qquad (3.4)$$

Here, we have introduced the 'bag pressure' term $B(T)$ which corresponds to the amount of energy necessary to 'melt' the QCD vacuum structure and allow free quarks and gluons to exist. For massless particles, these expressions can be solved approximately and one finds e.g. for the energy density

$$\epsilon(T) \approx \frac{\pi^2}{30}(d_g + \frac{7}{8}d_q)T^4 + B(T). \qquad (3.5)$$

The degeneracy factors d_g and d_q evaluate as $d_g = 2(N_c^2 - 1) = 16$ for gluons and $d_q = 2 \cdot 2 \cdot N_c N_f = 24$ for two light flavours. Thus, the system shows completely distinct properties from those of a massless free pion gas, which should be an approximate description of the QCD thermodynamics at low temperatures. There one finds

$$\epsilon T = \frac{\pi^2}{30} d_\pi T^4 \tag{3.6}$$

with a degeneracy factor $d_\pi = 3$. There is a huge difference between Eq. (3.5) and Eq. (3.6) due to the drastically different number of active degrees of freedom. Using $p = \frac{1}{3}\epsilon(-\frac{4}{3}B)$, one can use the $T = 0$ bag pressure $B(T = 0) = 100\,\text{MeV/fm}^3$ as obtained in bag model descriptions of hadrons and equate $p_\pi(T)$ and $p_{QGP}(T)$ to get an estimate for the favoured phase as a function of temperature. One finds that at a temperature of $T_C \approx 180$ MeV the transition from the pionic phase to the QGP phase should occurs. Evaluating the energy density at this temperature, one finds a first order transition with a huge latent heat of 2 GeV/fm^3 (see e.g. [9]).

Naturally, this is an oversimplified treatment of both the hadronic and the QGP phase. The scale of 180 MeV is large enough for other hadronic states besides pions to be thermally excited. Even the contribution of heavy resonances, such as the Δ, can not be neglected, as the huge degeneracy factor $d_\Delta = 32$ partially compensates the exponential suppression introduced by its large mass in the distribution function $f_D^\Delta(T_C)$.

Considering the QGP phase above T_C, one finds that the average momentum scale $\langle p \rangle = 3T_C \approx 600$ MeV is by no means a perturbative scale where one could expect the coupling constant to be small, therefore interactions cannot be neglected and the description in terms of free particles is bound to fail. In order to deal with this, a more careful treatment of the QCD thermodynamics is mandatory.

3.1.2 Perturbative QCD thermodynamics

Assuming a sufficiently large temperature so that α_s can be considered small, the perturbative techniques of thermal field theory described in chapter 2 can be used to calculate the properties of weakly interacting partonic matter in an expansion in powers of the coupling g. The naive expansion scheme, however, is bound to fail.

Scales in the plasma

In order to see this failure of perturbation theory, consider for the time being a purely gluonic theory. For massless gluons, there is no infrared cutoff, and this is at the origin of the problem once one considers degrees of freedom of the gluon field. The average fluctuations of the gluon field A can be obtained from

$$\langle A^2 \rangle \approx \int^\Lambda \frac{d^3k}{(2\pi)^3} \frac{f_B(T)}{E_k}. \tag{3.7}$$

Here, we consider the fluctuations entering the theory at a scale Λ. This scale can be set e.g. by the momentum of a particle propagating through the medium with momentum $k \sim \Lambda$. The fluctuations then enter as a correction to the propagator at a scale $g\overline{A}$ ($\overline{A} = \sqrt{\langle A^2 \rangle}$), which has to be small compared to k in order for perturbation theory to give meaningful results. We can now evaluate Eq. (3.7) for three different momentum regimes [10]:

- For 'hard' degrees of freedom, $k \sim \Lambda \sim T$. The momentum integration in Eq. (3.7) is cut off by the Bose-Einstein distribution $f_B(T)$ at a scale T where the dominant

contributions to the integral come from. Thus, $\langle A^2 \rangle_{\Lambda=T} \sim \frac{T^3}{T} \sim T^2$. The correction entering the propagator is then $g\overline{A} \sim gT$, which is indeed a small scale if g is sufficiently small. Therefore, for the hard degrees of freedom in an interacting gluonic system, perturbation theory can indeed be applied and gives small corrections to particle properties.

- For 'soft' degrees of freedom, we assume that the (small) scale is set by $k \sim \Lambda \sim gT$. In this case, we can expand the Bose-Einstein distribution $f_B(T) = \frac{1}{\exp[E_k/T]-1} \approx \frac{T}{E_k}$. The integral is cut off by the scale $\Lambda \sim gT$, so we find $\langle A^2 \rangle_{\Lambda=gT} \sim gT^2$. In this case, the correction entering a propagator evaluates to $g\overline{A} \sim g^{3/2}T < gT$, which is still a small scale for sufficiently small g. Thus, in this case, the fluctuations are of a scale comparable to the propagating field excitation, but their correction can still be treated perturbatively — we are not dealing with plasma particles any more as in the case of hard degrees of freedom but rather with soft, collective excitations.

- For 'ultrasoft' degrees of freedom, we consider a scale $k \sim \Lambda \sim g^2T$. In analogy to the previous case, we may expand $f_B(T)$ and cut the integral at a scale $\Lambda = g^2T$. In this case we obtain for the scale of the field fluctuations $\langle A^2 \rangle_{\Lambda=g^2T} = g^2T^2$. The fluctuation $\overline{A} \sim gT$ is of a larger scale than the one of the field excitation g^2T. Furthermore, the correction to the propagator is $g\overline{A} \sim g^2T$; it enters at the same scale, a perturbative expansion is impossible even if g is small, as all possible diagrams enter at the same order in g. These ultrasoft degrees of freedom can be identified with essentially unscreened chromomagnetic fluctuations.

Unlike in a scattering process, where the scales are set by the incoming momenta, all scales enter in a quantity like the partition function. Therefore, a perturbative expansion can be started, but higher orders in g do not only give corrections to the leading order but also pick up qualitatively new phenomena — in the first place the corrections due to collective excitations, which must be consistently resummed. As soon as the expansion resolves the magnetic fluctuations, the perturbative series breaks down eventually, regardless of the size of g. Magnetic fluctuations start entering at $O(g^4)$, but the divergencies can be regularized in this order by introducing a magnetic mass $m_g \sim g^2T$. This does not cure the problem — at $O(g^6)$, infinitely many diagrams contribute even with the introduction of this mass term.

Standard perturbation theory

This is manifest in a calculation of the free energy $F(T)$ in pure SU(3) gauge theory [11]. The expansion in powers of g reads:

$$F(T) = F_0(1 - 0.095g^2 + 0.12g^3 + [0.212 - 0.086\log(1/g)]g^4 - 0.082g^5). \quad (3.8)$$

Even for a small coupling, the series shows bad convergence. For temperatures of interest, $T \sim T_C$, g is of $O(1)$ and the series oscillates and even overshoots the ideal gas limit at order g^3. In order to reach convergence, asymptotically high temperatures $T \sim 10^{10}T_C$ have to be considered, which are clearly without any practical relevance. At $O(g^4)$, ultrasoft magnetic fluctuations are picked up by the expansion, resulting in infrared divergencies which can be regularized by the introduction of a magnetic screening mass $\sim g^2T$. This mass, however, gives contributions to $O(g^6)$ from diagrams with an arbitrary number of loops. The presence of terms absent in any naive expansion scheme ($\sim g^3, \sim \log(1/g)g^4$) is an additional indication that the loop expansion gets sensitive to qualitatively new physics from order to order and careful procedures have to be carried out to consistently treat those contribution.

The obvious importance of collective plasma effects indicates that the degrees of freedom, around which a perturbative expansion is carried out, should not be bare particles, but rather 'dressed' quasiparticles which take into account the interaction with the medium from the beginning. The resulting series in g has then to be treated consistently.

Approximately self-consistent HTL perturbation theory

Such a perturbative expansion employing the full HTL spectral representation has been carried out in [12]. The result can be seen in Fig. 3.1, where the pressure of an interacting gas of gluons is shown. The resulting EoS is comparable with data obtained in lattice simulations (see next section), this agreement however is in a temperature region where g is not small and the perturbative approach is questionable from the beginning. The temperature dependence of the pressure in this approach is, apart from the trivial T^4 dependence, entirely governed by the running $\alpha_s(T)$, since there is no scale in the problem besides Λ_{QCD}. The resummation procedure only affects the normalization. The results of the calculation are shown as a band, as there is an uncertainty in the approach regarding the precise value of the renormalization point, which is of order $O(T)$, but has been chosen between πT and $4\pi T$ in order to estimate the uncertainty attached to this choice. This may partially explain the description of the data in spite of the fact that the coupling is not small — there is no strong dependence on T visible in the data for $T > 3T_C$,
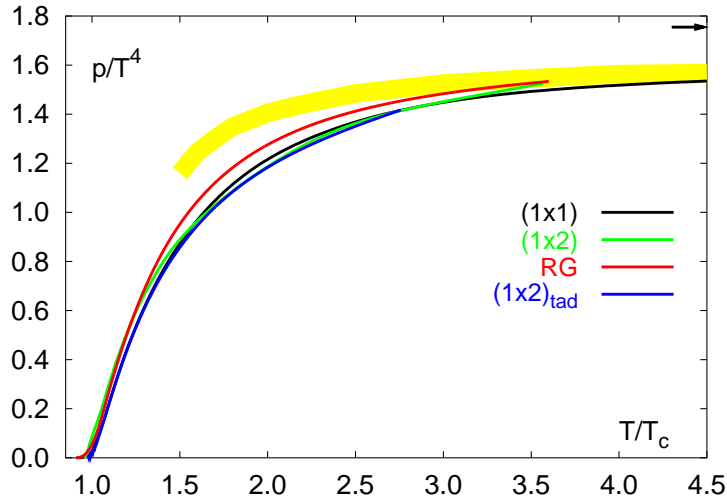
FIGURE 3.1: Approximately self-consistent HTL perturbation theory result for the pressure of hot gluonic matter [12] (shaded band) vs. lattice results, calculated with different actions [13–16]. The small arrow in the upper right indicates the ideal gas value.

3.1.3 *Lattice simulations*

In lattice simulations, information on the QCD thermodynamics can be obtained independent of assumptions about the smallness of the coupling g. Therefore, these simulations are up to now the only reliable source of information about the properties of hot partonic matter in the temperature region of interest for current heavy-ion experiments.

For pure SU(3) gauge theory, lattice simulations have been carried out and reached a high level of accuracy, allowing a reliable continuum extrapolation. The resulting EoS is shown in Fig. 3.2. A first order phase transition is observed at a temperature $T_C = 271 \pm 2$ MeV.

FIGURE 3.2: The EoS of pure SU(3) gauge theory as obtained in lattice simulations [14] as a function of T/T_C. The dashed band indicates the presence of a latent heat. The dashed line corresponds to the ideal gas limit. The error bars at $2\,T_C$ are a measure for statistical and systematic uncertainties.

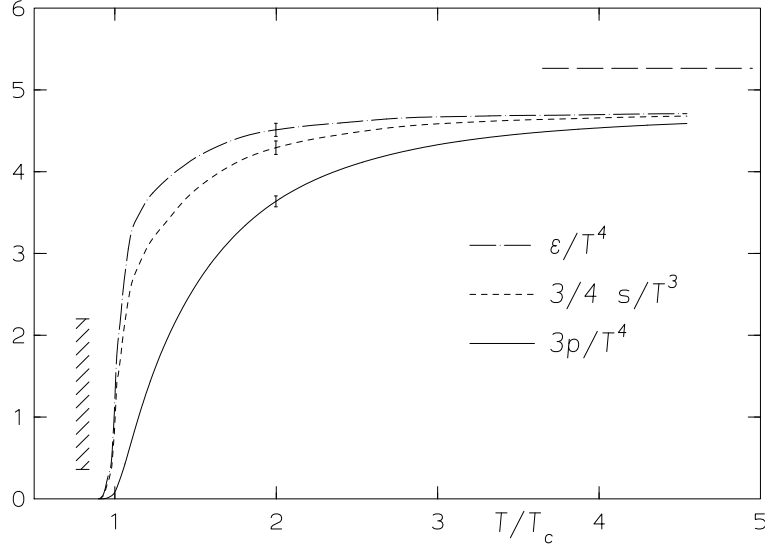Lattice calculations with dynamical quarks are computationally more involved and the effort increases even more for small quark masses. For that reason, the thermodynamics of full QCD is not known with the same level of accuracy as the one for SU(3) gauge theory. At present, the mass of the pseudoscalar Goldstone boson on the lattice is still of order 500 MeV or larger, a scale well above the pion mass. This fact makes the lattice calculations unable to contribute to the knowledge of the thermodynamics in the hadronic phase and makes an extrapolation towards realistic quark masses mandatory if the results of these calculations is to be used to describe the physics of heavy-ion collisions.

The result of calculations with dynamical quarks depends on the number of quark flavours involved. In general, the transition temperature T_C is lowered if more flavours are included. This is immediately obvious from the simple considerations for the ideal quark-gluon gas — the more degrees of freedom enter the thermodynamics, the sooner the pressure gets equal in both the hadronic phase and partonic phase and the transition occurs.

Simulations have been carried out for both two and three flavour QCD and the physical case of two light and one heavy flavour. As an example, we present the dependence of the energy density on T and N_f in Fig. 3.3. Note that the critical temperature T_C is different in each case: For the critical temperature in the chiral limit [18],

$$T_C = (173 \pm 8)\,\text{MeV} \quad \text{for} \quad N_f = 2 \tag{3.9}$$

and

$$T_C = (154 \pm 8)\,\text{MeV} \quad \text{for} \quad N_f = 3. \tag{3.10}$$

For the physical case of two light quarks and one heavy flavour, the transition temperature remains close to the two-flavour value, indicating that the quark mass dependence of T_C is small. From Fig. 3.3, we can also infer that qualitative features of the thermodynamics appear to be rather insensitive to the number of flavours involved. Instead, the normalization is changed, and these changes are essentially given by the change in the number of active degrees of freedom as evident from the ideal gas case.

Two remarkable features are present in the equation of state (EoS) of SU(3) gauge theory and also persist in the presence of dynamical quarks. First, even in the high temperature
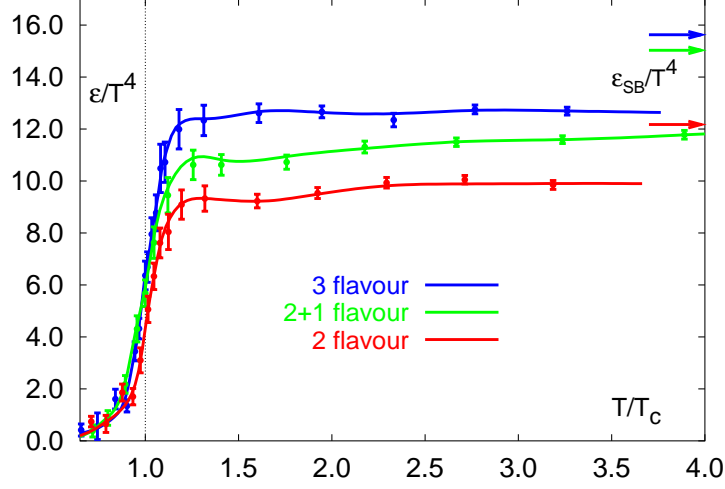
FIGURE 3.3: The energy density of thermal QCD for different numbers of active quark flavours as found in lattice calculations [17]. The arrows on the upper right denote the ideal gas limit.

limit $T \gg T_C$, there is no indication that the ideal gas limit is reached. In perturbative calculations, this is caused by the appearance of a thermal mass term for quarks and gluons and motivates the interpretation of the lattice results in terms of quasiparticles even an $T \approx T_C$. Secondly, in all cases there is a strong variation in the thermodynamical parameters in a narrow temperature region, suggesting the transition from hadronic matter (with a comparatively small number of active degrees of freedom) to partonic matter (with a large number of active degrees of freedom). In order for this interpretation to be valid, we must proceed by examining the deconfinement transition in somewhat greater detail.

3.2 DECONFINEMENT

In the absence of thermodynamically active quarks ($m = \infty$), the QCD Lagrangian exhibits a global $Z(N_c) \epsilon$ SU(N_c) center symmetry which is broken at high temperatures. The associated order parameter is given by the gauge-invariant Polyakov loop (Wilson line) winding around the imaginary time direction

$$\langle L(x) \rangle = \frac{1}{N_c} \text{Tr} \left[\mathcal{P} \exp \left(ig \int_0^\beta d\tau A_0(\tau, x) \right) \right]. \tag{3.11}$$

Here, A_0 is the time component of the gauge field A_μ.

The relation of this order parameter to the usual picture of deconfinement associated with the breaking of the colour string between two coloured sources can be established as follows: The excess free energy $F_q(T) - F_0$ of a single static quark source (located at $x = 0$ for simplicity) can be related to L via

$$\langle L \rangle = e^{-\beta(F_q(T) - F_0)} \tag{3.12}$$

with

$$\langle L \rangle = \frac{1}{V} \int d^3x \langle L(x) \rangle. \tag{3.13}$$

In the confined phase, colour sources are connected by a binding potential (a 'colour string') which increases linearly with the source separation, $V(r) \sim \sigma r$ for large distances. A colour source cannot be screened in this phase due to the absence of dynamical quarks, as it is impossible to break the confining string by quark pair creation. Hence the free energy of such a source is infinite and $\langle L \rangle = 0$. In the deconfined phase, the free energy of a static quark antiquark source remains finite as the distance increases, indicating the presence of a (perturbative accessible) short range potential but the absence of long-range confining forces. Thus, $\langle L \rangle$ can acquire a nonzero value. In this case it is possible to relate the Polyakov loop to the potential $V(r, T)$ acting between a static quark-antiquark pair via

$$e^{\beta V_{\bar{q}q}(r,T)} = \langle L(r)L^\dagger(0) \rangle. \tag{3.14}$$

In the case of finite but small quark masses realized in QCD, the Polyakov loop ceases to be an order parameter in the strict sense. Nevertheless, lattice simulations reveal a strong change in the behaviour of $\langle L \rangle$ and the associated susceptibility $\chi_L = V(\langle L^2 \rangle - \langle L \rangle^2)$ within a small interval in T, indicating that there is indeed a phase transition happening at a temperature T_C (see Fig. 3.4).

FIGURE 3.4: The temperature dependence of the Polyakov loop and the associated susceptibility χ_L in two-flavour QCD as obtained in lattice simulations [19].

3.3 CHIRAL SYMMETRY RESTORATION

In the limit of vanishing quark masses, $m_q = 0$ (chiral limit), the QCD Lagrangian with N_f quark flavours exhibits a $\mathrm{SU}(N_f)_V \otimes \mathrm{SU}(N_f)_A$ symmetry. It is spontaneously broken in the QCD ground state. The chiral condensate $\langle \overline{\Psi}\Psi \rangle$ is a natural order parameter associated with this symmetry breaking pattern.

The restoration of chiral symmetry is an entirely non-perturbative phenomenon. From the $T < T_C$ region, the condensate can be calculated in chiral effective field theories and the result of these calculations indicate indeed the correct qualitative behaviour [20], but any perturbative expansion breaks down near the phase transition. Perturbative expansions around quarks and gluons as degrees of freedom are unable to calculate the chiral condensate. Only lattice simulations can contribute here, but the way quarks are treated on the

lattice has to be chosen carefully, as chiral symmetry is explicitly broken by the implementation of Wilson fermions.

The behaviour of the chiral condensate rapidly changes in a narrow temperature region even at finite quark masses as indicated by lattice results [19](see Fig. 3.5). The chiral susceptibility

$$\chi_m = \frac{\partial}{\partial m_0} \langle \overline{\Psi}\Psi \rangle \tag{3.15}$$

exhibits a pronounced peak structure, indicating a transition from a chirally broken phase to a restored one.
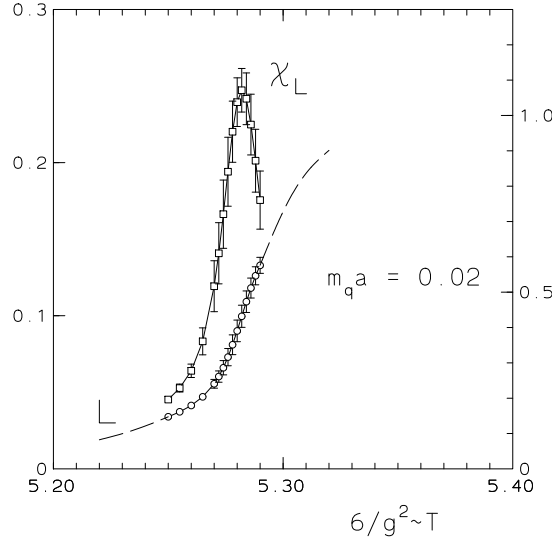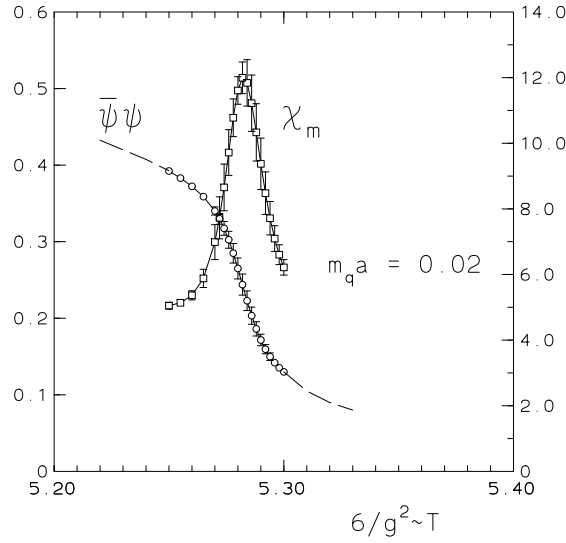

FIGURE 3.5: The temperature dependence of the chiral condensate and the associated susceptibility χ_m in two-flavour QCD as obtained in lattice simulations [19].

A priori, there is no reason why T_C^L, the temperature characterized by the peak position of χ_L and T_C^χ, the temperature extracted from the peak position of χ_m, should be the same. However, it turns out in the lattice calculations that $T_C^L = T_C^\chi = T_C$, where T_C is the point characterized by strong changes in thermodynamic properties of the system. This is puzzling, as the deconfinement transition occurs even in the absence of quarks, though at a different temperature T_C^L, so why should the presence of quarks force the two temperatures to become the same?

In [21], a conceptual answer to the problem has been suggested. In the presence of light quarks, the confining string between two static sources can break as soon as $V(r) = \sigma r = 2m_q$ due to pair creation from the vacuum. This leads to

$$L(T) \sim e^{-2m_q T} \tag{3.16}$$

for the Polyakov loop. So, for sufficiently small m_q, the deconfinement transition should disappear. On the other hand, in a chirally broken phase, the breaking of the string proceeds via the formation of a meson, which in turn requires a mass of the order of twice the constituent quark mass, $2M_q$, for its creation. Therefore, the relevant scale should rather be given by

$$L(T) \sim e^{-2M_q T} \tag{3.17}$$

which allows for a confining potential over a much larger distance. For sufficiently large M_q, the deconfinement transition is recovered even in the presence of quarks.

The chiral transition would therefore trigger the onset of the deconfinement transition via the string breaking mechanism in the transition from Eq. (3.17) to Eq. (3.16). The change in the active degrees of freedom which is implied by the deconfinement transition would then in turn result in an appropriate change in the thermodynamics of the system. This scenario would provide a natural explanation for the coinciding transition temperatures.

3.4 A QUASIPARTICLE PICTURE OF THE QGP

3.4.1 Introduction

In order to apply the results of the previous section to the physics of heavy-ion collisions, a suitable interpretation of all the lattice data gathered so far has to be found.

Recall that perturbative results obtained at very high temperatures indicate that the relevant degrees of freedom are not given by bare quarks and gluons, but rather by dressed quasiparticles. Simple phenomenological quasiparticle models inspired by the perturbative results are very successful in parametrizing the thermodynamics observed on the lattice even at $T \approx T_C$. Therefore we will use quasiparticles as degrees of freedom inside the QGP phase in the following.

Several of such models have been suggested so far [34, 112]. We will use the one described in [7, 8].

3.4.2 The quasiparticle picture

Two key elements enter in the description of the quasiparticles. The first one is motivated the appearance of a mass term for quarks and gluons in perturbative calculations. We assume that quasiparticles are massive due to the interaction with the heat bath also at $T \approx T_C$ with a mass term that should approach the perturbative result for $T \gg T_C$ and become small near T_C. The latter assumption is motivated by the observation that at the phase transition all correlation lengths should diverge, hence the screening masses should become small.

This behaviour, however, introduces a mismatch as compared to the lattice data, where a reduction of the entropy density near the phase boundary is observed, whereas a dropping mass would lead to an increase of active degrees of freedom and in turn to an increase of the entropy density. We attribute the observed reduction to confinement, assuming that quasiparticles become bound into heavier states which vanish from the observed excitation spectrum due to their large mass. This statistical reduction of degrees of freedom due to confinement is parametrized in a phenomenological way.

We assume that the thermal excitations in the QGP can then be described by a dispersion equation

$$E^2(k, T) = k^2 + m_i^2(T). \tag{3.18}$$

Here, $k = |\mathbf{k}|$, and the subscript i labels the particle species: $i = g$ for gluons and $i = q$ for quarks. $m_i(T)$ stands for a thermal mass which is derived from the self-energy of the corresponding particle, evaluated at thermal momenta $E, k \sim T$. This is expected to be meaningful as long as the self-energy is only weakly momentum dependent in that kinematic region. Additionally, for a quasiparticle to be a meaningful concept at all, we require the imaginary part of the self-energy, and hence its thermal width, to be small.

The gluon mass, following ref. [8], becomes

$$\frac{m_g(T)}{T} = \sqrt{\frac{N_C}{6} + \frac{N_f}{12}} \; \tilde{g}(T, N_C, N_f) \tag{3.19}$$

with the effective coupling specified as

$$\tilde{g}(T, N_C, N_f) = \frac{g_0}{\sqrt{11N_C - 2N_f}} \left([1 + \delta] - \frac{T_C}{T}\right)^\gamma. \tag{3.20}$$

N_C and N_f stand for the number of colours and flavours, respectively. The functional dependence of $m_g(T)$ on T is based on the conjecture that the phase transition is weakly first order or second order which suggests an almost powerlike behaviour $m \sim (T - T_C)^\gamma$ with some pseudo-critical exponent $\gamma > 0$. Setting $g_0 = 9.4$, $\delta = 10^{-6}$ and $\gamma = 0.1$, the effective mass (3.19) approaches the HTL result at high temperatures.

The thermal quark mass reads

$$\frac{m_q(T)}{T} = \sqrt{\left(\frac{m_{q,0}}{T} + \frac{1}{4}\sqrt{\frac{N_C^2 - 1}{N_C}}\tilde{g}(T)\right)^2 + \frac{N_C^2 - 1}{16N_C}\tilde{g}(T)^2} \tag{3.21}$$

with the zero-temperature bare quark mass $m_{q,0}$. Note that in contrast to previous quasiparticle models extrapolated from HTL calculations [34, 112], the thermal masses used here *drop* as T_C is approached from above. Of course, for $T \gg T_C$, the near-critical behaviour inferred in (3.20) ceases to be valid and the perturbative limit of $m_g(T)$ and $m_q(T)$ will be recovered.
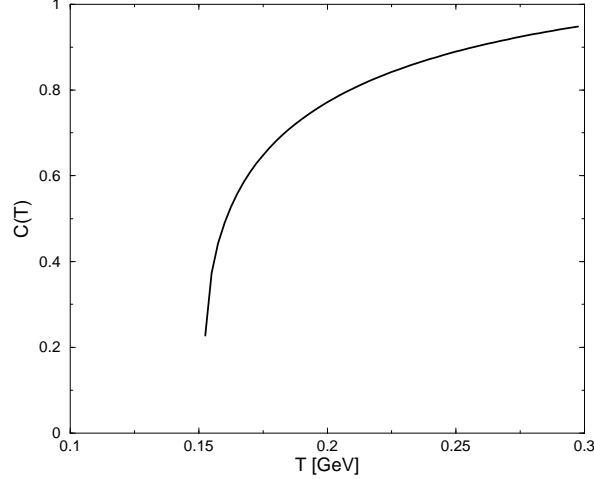
FIGURE 3.6: The confinement factor $C(T)$ as a function of temperature for two light flavours ($m_{u,d} = 0$) and one heavier flavour ($m_s \simeq 170$ MeV).

We parametrize the statistical reduction of active degrees of freedom due to confinement in a function $C(T)$ which multiplies the particle distribution functions. The pressure of the QGP system takes then the following form:

$$p(T) = \frac{\nu_g}{6\pi^2} \int_0^\infty dk \, [C(T)f_B(E_k^g)] \frac{k^4}{E_k^g} + \sum_{i=1}^{N_f} \frac{2N_C}{3\pi^2} \int_0^\infty dk \, [C(T)f_D(E_k^i)] \frac{k^4}{E_k^i} - B(T). \tag{3.22}$$

Energy density $\epsilon(T)$ and entropy density $s(T)$ follow accordingly (see [8] for details):

$$\epsilon(T) = \frac{\nu_g}{2\pi^2} \int_0^\infty dk k^2 [C(T) f_B(E_k^g)] E_k^g + \sum_{i=1}^{N_f} \frac{2N_C}{\pi^2} \int_0^\infty dk k^2 [C(T) f_D(E_k^i)] E_k^i + B(T),$$

(3.23)

$$s(T) = \frac{\nu_g}{2\pi^2 T} \int_0^\infty dk k^2 [C(T) f_B(E_k^g)] \frac{\frac{4}{3} k^2 + m_g^2(T)}{E_k^g}$$

$$+ \sum_{i=1}^{N_f} \frac{2N_C}{\pi^2 T} \int_0^\infty dk k^2 [C(T) f_D(E_k^i)] \frac{\frac{4}{3} k^2 + m_i^2(T)}{E_k^i}.$$

(3.24)

Here, $E_k^g = \sqrt{k^2 + m_g^2(T)}$ and $E_k^i = \sqrt{k^2 + m_i^2(T)}$ for each quark flavour $q = i$. The multiplicity $\nu_g = 16$ counts the transverse gluonic degrees of freedom.

The explicit form of $C(T)$ is obtained by calculating the entropy density of the QGP with the gluon mass (3.19) and the quark mass (3.21). Dividing the lattice entropy density by this result yields $C(T)$. It can be parametrized as

$$C(T) = C_0 \left([1 + \delta_c] - \frac{T_C}{T} \right)^{\gamma_c}.$$

(3.25)

For two light quarks and one heavy quark, the parameters take the values $C_0 = 1.16$, $\delta_c = 0.02$ and $\gamma_c = 0.29$ (see figure 3.6)[1]. The function $B(T)$ is now uniquely determined from $m_i(T)$ and $C(T)$ up to an integration constant that is fixed by Gibbs' condition $p_{QGP} = p_{hadr}$ at T_C.

Figure 3.7 shows the pressure, energy and entropy density for two light quark flavours ($m_{u,d} = 0$) and a heavier strange quark ($m_s \simeq 170$ MeV) in our confinement model. We will use this result to discuss the thermodynamics of the QGP phase in heavy-ion collisions in the following.

3.5 THE EQUATION OF STATE

As we have already argued, the fact that the mass of the pseudoscalar Goldstone boson on the lattice is still far from the physical pion mass renders the lattice results meaningless for a description of the EoS in the hadronic phase below T_C. Essentially all degrees of freedom are suppressed due to their enhanced mass in such calculations.

On the other hand, a description in terms of a free hadronic resonance gas is hardly appropriate in the vicinity of a phase transition. Furthermore, there is good evidence that in the environment of a heavy-ion collision the pion phase space is overpopulated as compared to the equilibrium case due to the decay of heavy resonances (for a detailed discussion see chapter 6). Thus, the required calculation of an interacting hadronic resonance gas (involving about 50 different states) and incorporating the dynamical overpopulation of pion phase space is extremely involved.

---

[1] We mention that the proposed method relies on input from the lattice. Whereas high precision data exist in the pure gauge sector, calculations with dynamical quarks are not yet in a satisfactory position to yield proper continuum-extrapolated results with physical quark masses. We estimate that the results obtained within our confinement model may still change by 5-15% in the vicinity of T_C once high statistics data are available. However, this small correction does not influence the results of the following discussion.
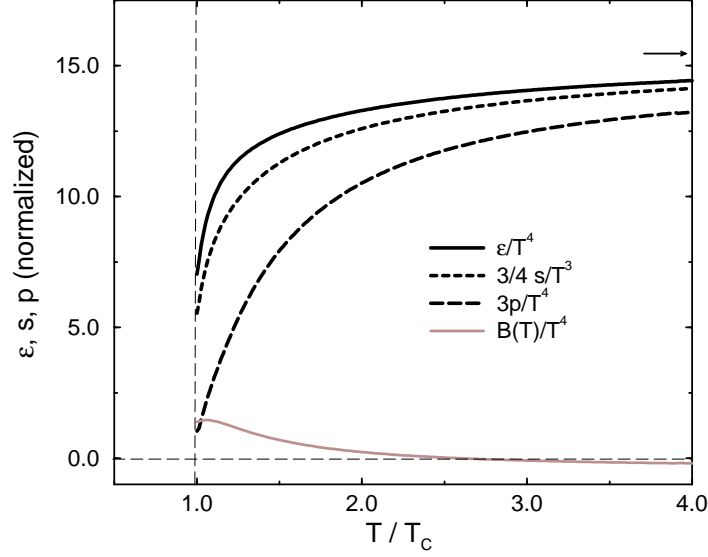
FIGURE 3.7: Pressure, energy density and entropy density for two light quark flavours ($m_{u,d} = 0$) and a heavier strange quark ($m_s \simeq 170$ MeV) in the quasiparticle model [8]. The arrow indicates the ideal gas limit of massless three-flavour QCD. The function $B(T)$ is also shown.
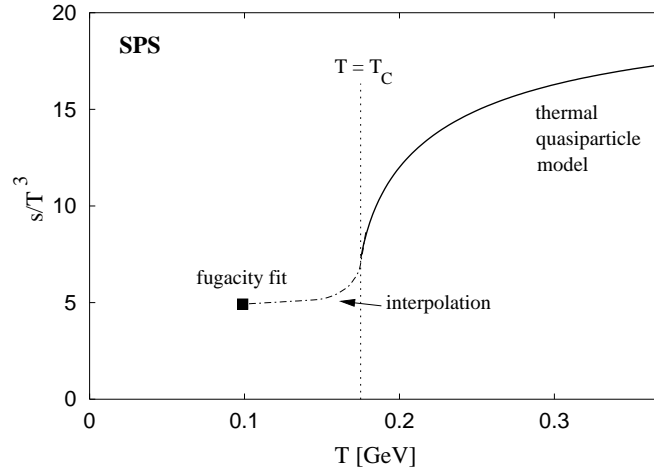
FIGURE 3.8: The interpolation between the EoS given by the quasiparticle model and the point extracted by a fit to experimental multiplicity assuming an ideal hadronic resonance gas, shown for conditions realized at SPS.

Therefore, we will proceed as follows: We adopt the picture of a free resonance gas at the end of the evolution where the matter ceases to interact (the thermal freeze-out point). At this point, a free gas should be appropriate. We use the experimentally measured enhancement of pions to determine a fugacity factor z_π which multiplies the Bose-Einstein distribution for pions. We then interpolate smoothly between the EoS given above T_C by the quasiparticle model and the extracted ideal resonance gas point to find the EoS relevant for the fireball evolution at all temperatures (it is unnecessary to know the EoS at temperatures below 100 MeV, as this temperature region is not probed in current heavy-ion

experiments). In Fig. 3.8, this procedure is indicated for collisions at the CERN SPS for the entropy density s.

Chapter 4

HEAVY ION COLLISION DYNAMICS

4.1 INTRODUCTION

Up to now, the only possibility to actually study QCD matter under extreme conditions experimentally are (ultra)relativistic heavy-ion collisions. Here, heavy nuclei currently accelerated up to energies of 200 GeV per nucleon collide and deposit an enormous amount of energy inside a relatively small volume, thus creating the desired extreme conditions regarding temperature and density for a short time of order $10^{-23} - 10^{-22}$ sec.

The hot fireball created in such a collision is not a static object but undergoes an accelerated expansion, leading to a rapid cooling of the produced state and eventually a decoupling of the strongly interacting matter, after which the produced particles cease to interact with each other and move freely to the detector.

Any observable measured to probe the partonic phase is therefore likely to be mixed with signals from the later hadronic phase. This is the main reason that the extraction of un-ambiguous signals for the QGP is so difficult. It is therefore mandatory to understand the dynamics of such a collision and the evolution of the resulting fireball in order to extract any information about the early phases and the QGP.

Many obstacles have hindered a complete theoretical understanding of fireball evolution so far. The properties of the presumably created partonic phase, which determine the first part of the evolution, are not well known. The same is true even in the hadronic phase: Near the phase boundary, properties of hadrons such as masses and decay widths are unknown and, in fact, the very existence of the phase boundary makes perturbative calculations of those properties impossible. A good part of the resonances which give a large contribution to the dynamics of the early hadronic phase are poorly known even in the vacuum. The initial

conditions cannot be assessed reliably: Shadowing and energy loss phenomena make an extrapolation from p-p collisions difficult. Despite these problems, ongoing efforts both from the experimental and theoretical side have resulted in a common picture of fireball evolution, which is, at least qualitatively, accepted by most researchers in the field. It is the goal of this chapter to introduce this standard scenario along with all of the relevant timescales and to familiarize the reader with the terminology used to describe heavy-ion collisions.

4.2   KINEMATICS AND GEOMETRY

Let us take a brief look onto the space-time geometry of fireball expansion and define some useful quantities.

In the following, the beam axis will always be the z-direction of the coordinate system, any momentum along this axis will be denoted by a subscript z (p_z, k_z ...). The z-direction will also be called longitudinal direction, as it is the main expansion axis of a cylindrical fireball.

Usually, rotational symmetry around the z-axis will be assumed, any distance in transverse direction from the z-axis will then typically be called s or b, otherwise, the distinction between the x and y axis will be made explicitly. Momenta perpendicular to the beam axis will have a subscript t (p_t...).

4.2.1 Kinematic variables

As the energies of the incoming nuclei in a heavy-ion collision are typically much larger than their rest masses, all velocities in the center-of-mass (c.m.) frame are close to c, the speed of light. It is therefore convenient to introduce the rapidity of a particle with energy p_0 and longitudinal momentum p_z as

$$y = \frac{1}{2} \ln \left(\frac{p_0 + p_z}{p_0 - p_z} \right), \tag{4.1}$$

a quantity which is additive under Lorentz boosts, and, for $v \ll c$, is equal to the particle velocity. Experimentally, two quantities have to be measured in order to identify a particle's rapidity, such as p_0 and p_z. Unfortunately, sometimes all that can be measured is the angle of the particle relative to the beam axis. In this case, the pseudorapidity variable

$$\eta = -\ln[\tan(\theta/2)] = \frac{1}{2} \ln \left(\frac{p + p_z}{p - p_z} \right) \tag{4.2}$$

is used, where $p = |\mathbf{p}|$. Obviously, $\eta \simeq y$ if the momentum is large.

Transverse momenta are often described in terms of the transverse mass of a particle,

$$m_t = \sqrt{m^2 + p_t^2}, \tag{4.3}$$

leading to the useful relations

$$p_0 = m_t \cosh y, \qquad p_z = m_t \sinh y \qquad \text{and} \qquad p_z = p_t \sinh \eta \tag{4.4}$$

The spacetime rapidity η_s is also commonly defined as

$$\eta_s = \frac{1}{2} \ln \left(\frac{t + z}{t - z} \right) \tag{4.5}$$

Under certain conditions (see below), it coincides with the rapidity.

For processes involving particles moving very near the speed of light, it is often convenient introduce light cone coordinates. One defines positions r as

$$r_+ = r_0 + r_z \quad \text{and} \quad r_- = r_0 - r_z \tag{4.6}$$

and momenta p

$$p_+ = p_0 + p_z \quad \text{and} \quad p_- = p_0 - p_z \tag{4.7}$$

The transverse coordinates remain unchanged. Note that the metric tensor in light cone coordinates is not diagonal any more: The invariant mass reads $p^2 = 2p_+p_- - p_\perp^2$ and $p_{+(-)}$ and $r_{-(+)}$ are conjugate variables.

4.2.2 Spacetime picture

What is the relevant region in spacetime for the expanding system created after the initial collision? In order to answer the question, let us take a look at p-p collisions first. In the c.m. frame, the rapidity of the incoming particles constitutes a kinematic limit for the rapidity positioning of secondary particles. As the particle production in such a collision uses a certain amount of energy, the actual distribution of the produced particles will generally be narrower than allowed by the limit, in p-p collision typically one unit of rapidity lies between the limit and the bulk of secondary particles ('rapidity loss'). This behaviour may be even more pronounced in heavy-ion collisions where the number of binary collisions per participant is larger than one.

It turns out that the distribution of particles across rapidity is, for large enough energies ($\sqrt{s} > 10$GeV), approximately independent of y, giving rise to a 'plateau' around midrapidity. Inside this rapidity window, the conditions are independent on the value of y. This is called 'boost-invariance'.
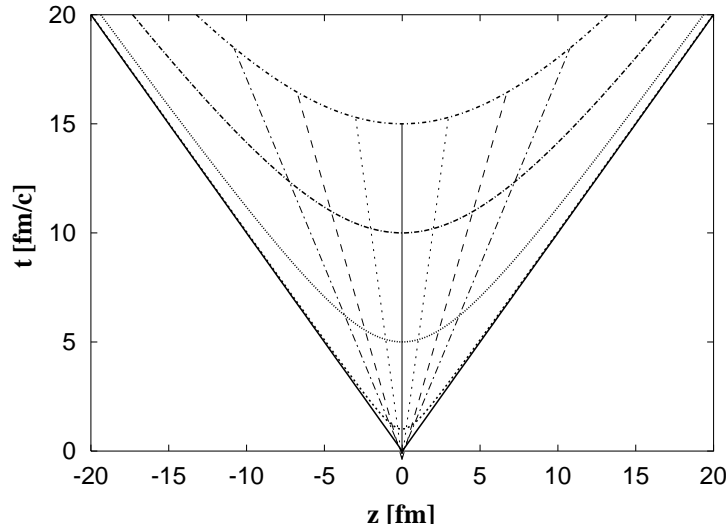

FIGURE 4.1: Particle trajectories emerging from the collision point and lines of constant proper time.

Figure 4.1 depicts a situation where produced particles emerge from a small collision region distributed evenly across some rapidity window (the region indicated inside the forward lightcone). In this situation, particle rapidity and spacial position are connected and y

and η_s coincide. In such a boost invariant scenario, the physical conditions depend only on the time a particle has spent on its trajectory, not on choice of the specific trajectory. Therefore, conditions along lines of constant proper time $\tau = \sqrt{t^2 - z^2}$ are equivalent. If one considers some time-dependent process such as decay of produced resonances, one observes that due to time dilatation the process starts on the inside of the relevant volume in space and moves outward.

When one goes from p-p collisions to heavy-ion experiments, the whole picture changes somewhat. First of all, the collision need not be a central one, which leaves a subset of nucleons not participating in the collisions. These so called spectator nucleons are of course observed at the kinematic limit, as they do not participate in any energy consuming scattering process. Only participant nucleons give rise to particle production. Secondly, there is now a probability that a nucleon undergoes multiple scattering, a process absent in p-p collisions. Therefore, one would expect an enhanced energy loss due to scattering and a different rapidity loss as compared to p-p of the bulk of the produced matter. There are two extreme cases describing this behaviour — the Landau scenario and the Bjorken scenario.

For low-energetic collisions, a complete stopping of the incoming nuclei due to multiple collisions is expected, which leads to a very dense (baryon-rich), though not necessarily hot system. The system thermalizes rather quickly and the resulting pressure leads to a spherical expansion around the collision point. This is the Landau scenario.

For very high beam energies, multiple collisions cannot account for significant energy loss as compared to the incident energy. Therefore the nuclei pass through each other without noticeable deceleration. The energy loss due to the collisions is deposited as a 'vapour trail' of produced particles, filling the rapidity region between the target and projectile fragmentation region. In contrast to the Landau scenario, in this so-called Bjorken scenario the distribution of baryon number (linked to the target and projectile) and the main bulk of particles forming the fireball (produced secondaries) is very different, leading to interesting consequences. The expansion geometry here is more reminiscent of a cylinder, though time-dilatation makes it impossible to observe this shape in any Lorentz frame. As in p-p collisions, particles remain essentially on their initial trajectories given by their rapidity, thus equating rapidity and spacetime rapidity.
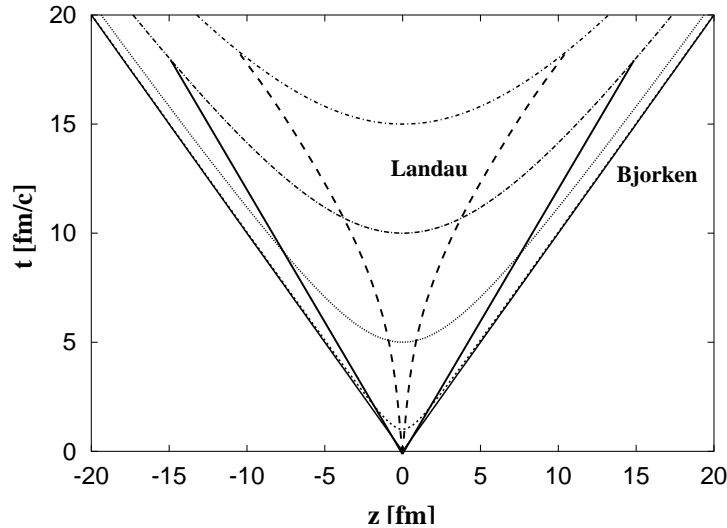

FIGURE 4.2: The schematic longitudinal dynamics of the Bjorken (solid) and the Landau (dashed) expansion scenario in spacetime; indicated is the fireball front.

Figure 4.2 indicates the different longitudinal dynamics of the two scenarios (for obvious

reasons, the transverse coordinate has been suppressed). Clearly, one expects at some intermediate beam energy a transition from complete stopping (Landau) to longitudinal free streaming (Bjorken). At what $\sqrt{s}$ this transition should occur shall be left open at this point of the discussion.

4.3 INITIAL CONDITIONS

In the very first moments of a heavy-ion collision, as the two nuclei just pass through each other, the relevant physics resembles a superposition of many nucleon-nucleon collisions. Only later on, when secondary particle production has set in and collisions among the secondaries start to dominate the dynamics, a fireball characteristic for heavy-ion collisions begins to emerge. Therefore, some gross properties regarding collision geometry can be calculated.

As the colliding nuclei are very close to the speed of light and are essentially flat discs when seen in the center of mass (c.m.) frame, the situation is almost ideally suited for an eikonal-type approach as far as the transverse geometry is concerned. On the other hand, information on the longitudinal geometry is not obtained readily and many issues are still open.

4.3.1 Overlap geometry

Starting out with the nuclear density, e.g. in the Woods-Saxon parametrization

$$n_A(r) = \frac{n_0}{1 + \exp(\frac{r-R_0}{d})}, \tag{4.8}$$

where n_0 is normal nuclear matter density ($0.17 \, \text{fm}^{-3}$), R_0 the nuclear radius and $d = 0.54$ fm, one defines the thickness function for a nucleus $T_A(b)$ corresponding to the density integrated along the beam axis

$$T_A(b) = \int_{-\infty}^{\infty} dz \, n_A(\sqrt{b^2 + z^2}). \tag{4.9}$$

Taking σ_{NN} as the total nucleon-nucleon cross section, one finds $T_A(b)\sigma_{NN}$ as the total number of binary collisions encountered by a nucleon passing through a nucleus at impact parameter b. Hard processes (like J/Ψ production) scale typically with the number of binary collisions.

Defining the nuclear overlap function

$$T_{AB}(b) = \int d^2 s \, T_A(\mathbf{s}) T_B(\mathbf{s} - \mathbf{b}) \tag{4.10}$$

for a given impact parameter b, one finds $T_{AB}(b)\sigma_{NN}$ as the number of binary collisions in an A-A collision.

Nucleons which have encountered at least one collision are called participants. Their number is relevant for soft particle production processes, where it is assumed that once a participant is 'ripped open' (a valence quark has been displaced), fragmentation sets in and a subsequent hit does not change this picture. The number of participants can be calculated

as

$$N_{part}(b) = \int d^2s\, T_A(\mathbf{s}) \left\{ 1 - \left[1 - \frac{\sigma_{NN} T_B(\mathbf{s} - \mathbf{b})}{B} \right]^B \right\}$$
$$+ \int d^2s\, T_B(\mathbf{s}) \left\{ 1 - \left[1 - \frac{\sigma_{NN} T_A(\mathbf{s} - \mathbf{b})}{A} \right]^A \right\}. \tag{4.11}$$

Here, the factors in square brackets correspond to the probability for one nucleon to pass through the whole nucleus without any collision.

4.3.2 Longitudinal dynamics

The question of initial conditions regarding longitudinal dynamics is not so readily answered. Basically, it boils down to the initial rapidity distribution of the produced secondary particles, where the Landau and the Bjorken expansion scenario can be considered as two limiting cases. Obviously, this distribution across rapidity space depends on the incident beam energy, but exactly what this dependence is is a matter still under debate.

Unfortunately, the experimentally observed rapidity distributions are unable to resolve the issue. Conventional multiparticle fragmentation models, like the Lund string model [49], are able to explain the measured spectra in terms of a Bjorken-type scenario, whereas classes of models which assume thermalization necessarily have to incorporate a certain amount of longitudinal acceleration during the expansion. These issues will be discussed in length later on.

4.4   THERMALIZATION

There is evidence from both theory and experiment pointing toward the fact that the system formed during the collision moves fast toward equilibrium. Experimentally, this is manifest in flow phenomena, especially elliptic flow, which is discussed in greater detail in sections 4.4.2 and 5.2.4.

From the theoretical side, a mechanism capable of achieving thermalization has been suggested in [22], the so-called 'Bottom-up' thermalization. As estimates of the thermalization stage rely on perturbative QCD, the scenario is only able to deal with very high energy collisions, such as they may be realized at LHC and possibly at RHIC. Nevertheless, it allows interesting insights into the physics in the very early phases of a heavy-ion collision.

In the 'Bottom-up' scenario, which is described more in detail in appendix B, several evolution phases characterize the system before complete thermal equilibrium is reached. The presentation both here and in the appendix closely follows [22].

4.4.1   The 'Bottom Up' scenario

Parton saturation

Initially, parton saturation determines the behaviour of the system. In p-p collisions, the gluon distribution in the proton grows as one probes smaller and smaller fractions of the light cone momentum, but this growth cannot persist to arbitrary gluon densities due to unitarity constraints, so at some momentum fraction x the density of gluons will saturate. In heavy-ion collisions at ultrahigh energies, parton distribution of many nucleons overlap,

thus the critical saturation density can be reached at larger values of x. The initial state is characterized by a saturation momentum Q_S, below which the occupation number of states is high ($O(1/\alpha)$) but does not grow any further [23–28]. For RHIC, Q_S can be estimated as 1 GeV, for LHC $Q_S \sim 2-3$ GeV, so RHIC might just be at the borderline of the kinematic region where perturbative QCD estimates can be expected to work.

As the nuclei collide, dominantly gluons with momenta near Q_S are released from the nuclear wave function. These are called 'hard gluons'. This process takes place at times $\tau \sim 1/Q_S$ (0.2 fm/c for RHIC, 0.08 fm/c for LHC).

Emission of soft gluons

As the system expands, the density of hard gluons decreases like $1/\tau$. The hard gluons undergo elastic scattering (which broadens the momentum distribution) as well as inelastic scattering (which produces soft gluons). The production of soft gluons is the dominant process, leading to a quickly growing number of gluons with momenta in the nonperturbative region. Hard gluons and soft gluons contribute equally to Debye screening of color charges as long as the occupation number of hard gluons stays large, this ceases to be the case at $Q_S\tau \sim \alpha^{-3/2}$ ($\tau \sim 0.95$ fm/c at RHIC, $\tau \sim 0.64$ fm/c at LHC).

Pre-Thermalization

For $Q_S\tau \gg \alpha^{-3/2}$, the characteristics of the system changes somewhat. The occupation number of hard gluons drops below one, and although the number of hard gluons is still larger than the number of soft ones, soft gluon contributions dominate the debye screening. As the coupling constant of the soft gluons is in a nonperturbative region, they interact frequently and form a thermalized system, but it is not sensible to attribute a thermal description to the system yet as the majority of the gluons is still hard. This changes only for times $Q_S\tau \sim \alpha^{-5/2}$, when the number of soft gluons exceeds the number of hard gluons ($\tau \sim 2.75$ fm/c for RHIC, $\tau \sim 2.55$ fm/c for LHC).

Thermalization

After $Q_S\tau \sim \alpha^{-3/2}$, the majority of gluons constitutes a soft heat bath, whereas most of the energy of the system still resides in the hard gluons. As these move through the heat bath, interactions take place and energy flows from the hard to the soft modes, heating the system. This leads to a temperature which grows linearly in time, unless the energy of the hard modes is depleted. This happens approximately at $Q_S\tau \sim \alpha^{-13/5}$ ($\tau \sim 3$ fm/c for RHIC, $\tau \sim 2.95$ fm/c for LHC). After that, the system is completely thermalized and the temperature decreases again as the volume expands.

As the above estimates are based on perturbative reasoning, they probably constitute only an upper bound of the relevant timescales. Especially for the RHIC scenario, the validity of perturbative results is far from being obvious. The most interesting feature of the scenario is, however, that thermalization can be obtained within times considerably smaller than typical fireball lifetimes, therefore the system is likely to be in thermal equilibrium during most of its evolution. Unfortunately, it is impossible to apply the above reasoning to heavy-ion collisions at SPS energies. There are, however, indications from the experimental side that early thermalization is also achieved at these beam energies.

4.4.2 Elliptic flow — an experimental signal of thermalization

The experimental evidence for early thermalization rests on the fact that a system which undergoes many scattering processes and is thus (nearly) thermalized develops pressure and its expansion is governed by the equations of hydrodynamics, whereas this is not true for a system with very few interactions where particles emerge on free flow trajectories.

Therefore, the mapping of initial spatial anisotropies of the fireball created in noncentral collisions to finally observed anisotropies in momentum space is different for systems in and out of equilibrium. This was first suggested in [29] as a signature for early thermalization.
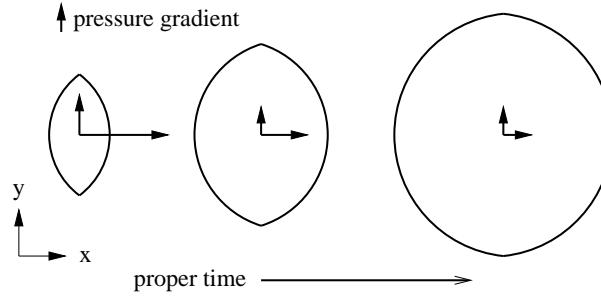

FIGURE 4.3: Schematic evolution of the transverse spatial geometry of a fireball created in a non-central collision. The initial anisotropy in space is soon washed out as the system undergoes initially free flow expansion driven by intrinsic transverse momentum of the collision partners. As soon as thermalization sets in, the spatial anisotropy is translated into a pressure gradient, as the system is hottest inside.

The main idea is sketched in Fig. 4.3. If the fireball expands initially in a free streaming phase, the anisotropy in the geometry is soon washed out by the expansion. As soon as the system is thermalized, a pressure can be defined. The acceleration acting on a volume element is then given by the ratio of pressure gradient over energy density, $a = \frac{\nabla p}{\epsilon}$. The pressure is highest in the center of the fireball (as temperature and density are highest there) and drops toward the edge. Thus, the pressure gradient must be dependent on the geometry, and the difference Δ_p in $\nabla_x p$ and $\nabla_y p$ then creates an anisotropy in the momentum distribution. If thermalization sets in late, Δ_p is very small.

These momentum anisotropies can be measured and indicate a medium which is thermalized after only 2–3 fm/c evolution time. A more detailed discussion of the data will be given in section 5.2.4.

4.5 THE PARTONIC PHASE

Once the medium has reached thermal equilibrium, what will be its properties? As we have seen in chapter 3, lattice simulations indicate that at temperatures above $T_C \approx 170$ MeV there is indeed a deconfined phase, characterized by degrees of freedom different from those of an hadronic gas. This medium, however, is still far from being an ideal quark-gluon gas, especially close to the phase transition where current experiments probe.

The task in understanding the partonic phase is twofold: From the theoretical side, properties of the medium must be understood and the relevant degrees of freedom identified; from experiment, signals from this early phase must be found, measured and compared to the theoretical predictions.

4.5.1 Theoretical considerations

Strings versus QGP

Before we actually discuss a thermalized partonic QGP, let us briefly comment on the possibility of an out-of equilibrium partonic phase. The most prominent candidate for such a phase are colour strings.

The notion of strings is based on the observation that the potential between two quarks can at large distances be described as $V \sim \sigma r$ with a 'string tension' sigma. This potential describes a field configuration in which a strong gluonic flux tube connects the two quarks, forming a 'string'.

As discussed in section 3.3, the string can be broken due to the creation of a $q\overline{q}$ pair from the vacuum. Both the q and the $\overline{q}$ are then connected with the original colour sources by strings again. If the string breaks more than one time, quarks combine with antiquarks from adjacent breaking points to form multiple strings.

Consider the situation after a high energy p-p collision. The remnants of projectile and target travel into $\pm$ z direction approximately on the light cone, a colour string inbetween. The breaking of this string will now lead to the creation of bound quarks and antiquarks in the rapidity region between target and projectile. As the secondary $q\overline{q}$ pairs will be closer in rapidity, the energy of the bound system will decrease and eventually these states will hadronize. Thus, the distribution of produced hadrons can be linked to the position of the $q\overline{q}$ production vertices.

In a longitudinal free streaming scenario as sketched here, there is a unique correspondence between position space and momentum space, thus we may label the $q\overline{q}$ vertex position by proper momentum $\Gamma = p_+ p_-$ and rapidity y. Theoretically, one expects to fall the vertices on curves of constant proper time, which in turn leads to a boost invariant production of hadrons. This implies that the distribution of the primary breaking vertex (denoted '0') is given by

$$dP_0 = \rho(\Gamma_0)d\Gamma_0 dy_0 \tag{4.12}$$

Given this vertex, a second breaking can occur and form a state of quark-antiquark connected by a string with invariant mass M inbetween. The second vertex (denoted '1') can be labelled by its forward light cone fraction z_+ given the primary vertex ($z_+ = (p_{0+} - p_{1+})/p_{0+}$) and the invariant mass of the created state. Thus, secondary vertices are distributed as

$$dP_1 = f_{01}(z_+, M_{01}^2)g(M_{01}^2)dz_+ dM_{01}^2 \tag{4.13}$$

Here, $g(M^2)$ stands for the distribution of invariant mass formed in the string breaking process. For example, it can be a given by a discrete set of hadron masses with appropriate weight factors adjusted to experimental yields. The joint probability for the occurrence of both breaking vertices is then $dP_0 \dot{d}P_1$, but this has to be the same as the probability if vertex 1 occurs first, followed by vertex 0. From this, in [49] the fragmentation function f has been derived as

$$f(z_+, M^2) = N z_+^{-1}(1 - z_+)^a e^{-bM^2/z_+} \tag{4.14}$$

with normalization constant N and parameters a and b which reflect the typical proper time at which the breaking vertices occur and the standard deviation of that time.

The parameters of the string model can be adjusted to give good agreement to data in the case of p-p collisions. In the case of A-A collisions, multiple strings must be considered between target and projectile where the basic translation from the known nucleon nucleon process to a many nucleon system is done in a Glauber approach.

Thus, the string breaking picture describes the longitudinal dynamics of a system of colliding nucleons from the initial collision to hadronization without reference to a thermalized partonic system. This corresponds to the absence of partonic collisions (no strong 'string-string' interaction leading to additional breaking). In such a scenario, thermalization can only occur after hadrons have been formed.

The main differences between a string fragmentation picture and a thermalized partonic phase are the following:

- String matter does not have nontrivial transverse dynamics. There is the possibility of intrinsic transverse momentum of the partons connected by the string which leads to a free flow expansion, but accelerated expansion requires pressure which in turn needs equilibrated matter with high interaction rates. Thus, transverse expansion and elliptic flow can, in the pure string fragmentation picture, only be built up after hadronization which gives tight constraints on the timescales of the expansion.

- The longitudinal dynamics of thermalized and string matter is also quite different. This is due to energy conservation. In the case of thermalization, the initial rapidity distribution of particles has to shrink considerably as compared to the kinematic limit in order to transfer the excess kinetic energy in random motion corresponding to the temperature. This energy stored in the random particle motion is then transferred into collective longitudinal and transverse expansion driven by the pressure (i.e. the rapidity distribution grows again). This is not the case for string dynamics — here, energy conservation demands that as soon as transverse motion is built up (in the hadronic phase or by string-string interactions), the rapidity distribution has to shrink continuously.

- The string model is well constrained in the case of nucleon nucleon collisions. In principle, a non-trivial interplay between strings can take place in A-A collisions, i.e. overlap of strings, string-string fusion and string-string scattering. These phenomena help explaining the transverse dynamics observed in flow, however, there are no constraints on the magnitude of such effects from any experiment besides heavy-ion collisions. The more important these effects are, however, the more likely is the system to approach equilibrium conditions, where the relevant degrees of freedom are not given by the string matter any more.

- Quark antiquark pairs connected by a string are not free to interact with other quarks and antiquarks, therefore electromagnetic processes like the emission of photons or dilepton pairs, which are in a QGP dominated by annihilation and bremsstrahlung processes, are very different in string matter.

Experimentally, there appears to be the need for early accelerated expansion, which is naturally explained in the context of a thermalized system but does not take place in a pure string fragmentation picture (see chapter 5 for a survey of experimental data). If a string fragmentation scenario is to explain the data, non-trivial interactions of strings have to be included which lead the system closer to equilibration.

Chemical (under)saturation

In the following, we will return to the assumption that a thermalized partonic phase is created in the early moments of a heavy ion collision.

As we have seen in section 4.4, the early dynamics leading to thermal equilibrium is mainly driven by gluons, especially for high impact energies, as gluons are the most abundant particle species in the nuclear wave function when small momentum fractions are probed. This

naturally raises the question if quarks do reach not only equilibrium momentum distributions ('thermal equilibrium') but also their equilibrium density ('chemical equilibration'), and, if so, at what times. The dynamics resulting from late chemical equilibrium can be quite different from a scenario which is chemically equilibrated all the time, leading to a 'hot glue' scenario as suggested in e.g. [31]. Here, the total entropy content of the system is carried by gluons only in the early stages, leading almost do a doubled initial temperature of the fireball. As the quark distribution moves towards equilibrium, the system eventually cools rapidly.

The subject has been investigated in some detail in [32] using rate equations for the processes $gg \leftrightarrow ggg$ and $gg \leftrightarrow q\bar{q}$ at RHIC conditions, employing perturbative (massless) quarks and gluons as degrees of freedom. The result of this analysis can be summarized in Fig. 4.4, where the density of quarks and antiquarks at hadronization is shown divided by the equilibrium density, along with variations of the thermalization time τ_0 and the strong coupling α_S.
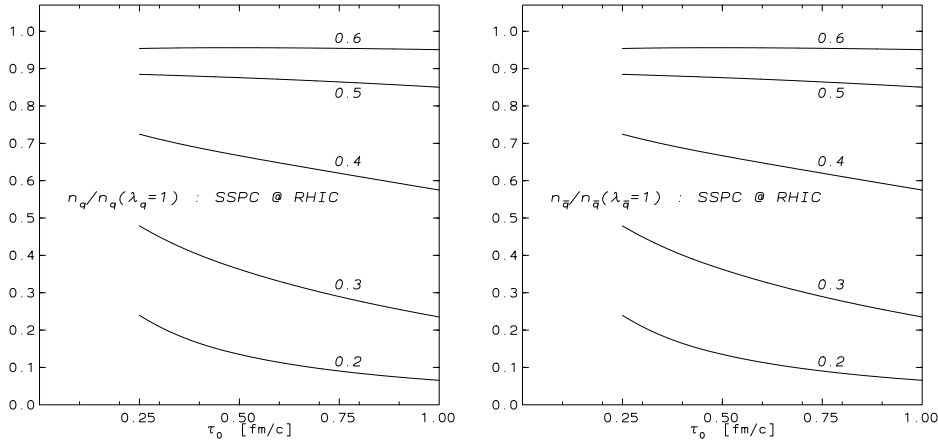

FIGURE 4.4: Densities of quarks and antiquarks normalized to their chemical equilibrium density as calculated in [32] for different thermalization times and coupling constants.

Two trends are clearly visible in Fig. 4.4. First of all, the relative undersaturation increases with the thermalization time. This is reasonable — a system which thermalizes earlier is characterized by higher particle densities which allow for more collisions and faster equilibration. Secondly, the undersaturation decreases strongly for increasing coupling, and at $\alpha_S \sim 0.6$, hardly any trace of chemical undersaturation is left.

What can be learned from these results? If we estimate typical momenta to be of the order $p = 3\langle T \rangle$, we find initial temperatures at RHIC (which follow from thermodynamical considerations to be discussed later) leading to scales of order 1 GeV, which might indeed lend credibility to a perturbative approach with α_S between 0.4 and 0.3. As the temperature drops toward the phase transition temperature $T_C \approx 170$ MeV however, the argument completely breaks down. A likely scenario therefore may involve a chemical undersaturation in the very early partonic phase, but as the fireball expands, quark densities will develop rapidly towards their equilibrium value.

Degrees of freedom

In chapter 3, we have seen that it is evident from lattice results that the assumption of an ideal gas of quarks and gluons does not provide an adequate description of the thermodynamics of the partonic phase. The possibly better description employs non-interacting

quark and gluon quasiparticles which acquire a temperature dependent mass $m_{q(g)}(T)$ due to their interaction with the heat bath. This is outlined e.g. in [33, 34].

Let us briefly review the basic properties of a quasiparticle approach: The quasiparticle mass is e.g. assumed to be of the functional form of the perturbative limit,

$$m_g(T) = \frac{g(T)^2 T^2}{2}\left(\frac{N_C}{3} + \frac{N_f}{6}\right) \quad \text{and} \quad m_q(T) = \frac{g(T)^2 T^2}{8}\frac{N_C^2 - 1}{2N_C}. \qquad (4.15)$$

This form is now fitted to the thermodynamics of the QGP as obtained by lattice calculations, assuming that the dynamics near the phase transition can be absorbed into the behaviour of the coupling $g(T)$. The reduction of active degrees of freedom as it is observed on the lattice translates in this approach into a strongly increased coupling constant, leading to large quasiparticle masses near T_C. The fit leads to a good description of the QGP thermodynamics on the lattice. Despite the thermal masses,it does not support the appearance longitudinally polarized gluonic degrees of freedom. The temperature dependent mass $m(T)$ leads, by thermodynamic consistency, necessarily to a background field $B(T)$ which adds to the energy density and subtracts from the pressure. This field is occasionally identified with the confining bag pressure.

There are more refined versions of the quasiparticle picture, some based on the more complex dispersion relations [10, 35] obtained within HTL resummed expressions (see section 2.4), or the one used in the present approach (see chapter 3) where the onset of confinement is parametrized in a statistical way. It turns out that all these descriptions are able to describe the thermodynamic properties of the system as they are found in lattice calculations, but the question which of them, if any, describes best the actual nature of the systems degrees of freedom.

In order to elaborate on this question, consider the emission of a (virtual) photon out of the QGP phase. The fundamental QCD Lagrangian tells us that the dominant emission process is the annihilation of a $q\bar{q}$ pair. But what are the properties of these quarks? Are they bare quarks, as in the vacuum, or does one need to consider the thermally acquired mass (as necessary for the description of the thermodynamics)? If so, which prescription is the correct one? Thermal quasiparticle masses imply a rise in the invariant mass threshold for the emission process, thus the predictions of the individual quasiparticle models differ vastly near the phase transition, where $m(T)$ rises steeply in one model whereas it drops in the other.

Obviously, also the description of the QGP in terms of massive quasiparticles cannot be applied to all processes — it fails completely for the emission of real photons, which is kinematically impossible for non-interacting massive particles (apart from the purely electromagnetic process which is $O(\alpha^2)$). In order to discuss such a process, one needs to consider the substructure of the quasiparticles. Then, if the momentum scales involved are large enough to penetrate the thermally screened region, interactions can also happen between quasiparticles and the photon emission process becomes possible.

In principle, a set of parton distribution functions describing the structure of the quasiparticles could be formulated, in close analogy to the description of the nucleon substructure in deep inelastic scattering experiments, which describe the scale dependent response to an external perturbation. How this should be done quantitatively remains however unclear.

We will discuss the effects of the quasiparticle properties on the emission of dileptons in greater detail later in chapter 7.

4.5.2 Experimental signals

Experimentally, obtaining information on this early phase is very challenging. Hadrons, the most prominent particle species inside the fireball, do not escape until thermal freeze-out, hence all information on the QGP phase carried in hadrons is lost by then. Direct signals of the QGP become only apparent when one considers electromagnetic probes (photons and dileptons). Their mean free path exceeds the dimensions of the fireball by far due to the smallness of α_{em} and so they directly reflect the conditions inside the fireball during the whole evolutions. However, electromagnetic radiation is also emitted during the later stages of the evolution and therefore signals from the QGP phase and from the hadronic phase have to be disentangled in order to study the early evolution. This subject will be treated in detail in chapter 3.

There is also indirect evidence for the creation of a QGP. As the charges of the degrees of freedom in a hadronic and a partonic system are quite different, event by event fluctuations of the charge observed within a given rapidity bin have been proposed as a signal for the QGP, as these fluctuations probe the squared charge of the degrees of freedom [36]. The main idea is to consider the observable

$$\langle N_{ch}\rangle\langle\delta R^2\rangle = 4\frac{\langle\delta Q^2\rangle}{\langle N_{ch}\rangle},\tag{4.16}$$

where R denotes the ratio of positive charge over negative charge $\frac{N_+}{N_-}$, Q the charge and N_{ch} the number of charged particles in a given rapidity bin. $\langle\ldots\rangle$ stands for an averaging procedure over a number of measured events. Hence, $\langle\delta Q^2\rangle$ is the squared deviation of the mean value of the charge measured in the relevant rapidity bin, averaged over the number of measured events. Comparing pion and quark-gluon gas, one finds that the net charge is naturally the same, but $\langle Q^2\rangle$ is sensitive to the fractional quark charges. Hence, one expects $\langle N_{ch}\rangle\langle\delta R^2\rangle \approx 4$ for a pion gas, but $\langle N_{ch}\rangle\langle\delta R^2\rangle \approx 0.75$ for a QGP. As the system expands, the volume over which initial fluctuations are large becomes magnified so that one can probe the early history of the system by considering larger and larger bins in the analysis.

Other evidence can be gained by considering the effect of the QGP on a heavy, bound state (like J/Ψ). As the probe is heavy, its production can be estimated more or less reliably in perturbative calculations. After the state has been formed, the binding potential is then subject to the medium. Specifically, a QGP screens the potential and so any heavy bound state immersed into a QGP dissolves. As this view characterizes a rather static situation, the complementary point of view would involve the dissociation of the bound state by the interaction with thermally excited gluons. This issue will be discussed specifically in chapter 9. As well as the ones discussed so far, the dissociation process is also mixed up with later dissociation in the hadronic medium and early suppression due to nuclear absorption effects.

4.6 THE PHASE TRANSITION

As the system approaches the critical temperature T_C, both chiral restoration and confinement become important. As we have seen in chapter 3, lattice simulations indicate that the transition appears to be a crossover rather than a first order transition, but unless the physical quark masses can be used in lattice simulations, this issue is open. The fact that the fireball is a only finite system enforces a crossover anyway.

From the thermodynamics obtained from lattice calculations, the following information can be inferred: The ratio of pressure over energy density $p(T)/\epsilon(T)$ drops as T_C is ap-

proached. As this ratio characterizes the accelerated expansion of the system, it implies that the acceleration due to the pressure almost stops near T_C and the system enters a brief phase of free flow, until the fireball is completely hadronized and the collisions in the hadronic phase build up pressure again. This 'soft point' in the EoS can be interpreted in some models as the confining 'bag pressure' counteracting the thermal pressure.

Furthermore, the entropy density $s(T)$ on the lattice displays a strong reduction of degrees of freedom near the phase transition. In the quasiparticle picture of the QGP, this can be interpreted as a growing quasiparticle mass near the phase transition or as the separation of the system into a fraction $C(T)$ of quasiparticles with dropping mass and another fraction $(1 - C(T))$ of heavy states which contribute negligible to thermodynamics. If the second view is taken (as in the present work), the heavy confined states are naturally identified with hadrons once T_C has been reached. This implies that there is a smooth transition from free quasiparticle states co-existing with pre-hadronic confined clusters of particles.

The physics of hadronization and the phase transition is the part of the fireball evolution which is least understood, as perturbative methods break down. Luckily, if there is no large latent heat (and there is no indication for it in either experiment or lattice calculations), the system spends only a small fraction of its total evolution time at T_C and then continues cooling towards the hadronic phase, so unless some observable is specifically sensitive to the phase transition, the contribution of the transition period to any process is small.

4.7 THE HADRONIC PHASE

As the temperature drops below T_C, the degrees of freedom of the system cease to be quarks and gluons. Instead, mesons, nucleons and resonance states constitute the new degrees of freedom. A priori, there is no reason why the number densities of different hadronic particle species should be determined by thermal distributions, but experimentally one observes that the finally measured abundancies of particles can be described by a thermally distributed ensemble with temperature $T \approx T_C$. In a scenario with a sudden phase transition, this is surprising, as hadronization itself is required to produce the thermal abundancies of particles, there is no time for dynamical equilibration. In the quasiparticle picture presented here, one might think of the thermalization of pre-hadronic clusters, which then again lead to thermal distributions of hadrons after the phase transition.

The fact that the measured abundancies correspond to a (grand canonical) ensemble with $T \approx T_C$, but the momentum spectra rather indicate $T \ll T_C$, has given rise to the idea of subsequent chemical and thermal (kinetic) freeze-out. This can be understood as follows: If inelastic hadronic cross sections are much smaller than elastic ones (which is true up to few exceptions to be discussed later), then there are not enough reactions within the lifetime of the hadronic phase which can change the number of long-lived particles, e.g. true pion annihilation can be neglected. Therefore the abundancies of particles seem to originate from a system with $T = T_C$, provided that resonance decays are taken into account properly, whereas elastic reactions still determine the momentum spectra of all particles, thus the system remains thermalized until final freeze-out.

From a theorist's point of view, the hadronic phase is complicated, as many different hadronic species contribute to its properties. Mainly, one is interested in the properties of hadrons in a hot and dense medium, and this is also subject of experimental investigation.

4.7.1 Theoretical considerations

Relevant degrees of freedom

It is tempting to assume that the pions, due to their small mass, have the largest probability to be thermally excited and dominate the other heavier mesons and baryons. Accepting the picture of subsequent chemical and thermal freeze-out, this can be clearly ruled out. At $T_C \approx 170$ MeV, the thermally excited pions are only about 20% of the finally observed number, the rest comes from the decay of heavy resonances. At first sight this is surprising, as the heavy states are exponentially suppressed due to their large mass, but usually they have large degeneracy factors (spin and isospin) and the number of resonance states increases exponentially with their mass, so they actually dominate the dynamics near T_C.

As the temperature drops, heavy resonances decay and fill up the pion phase space, which becomes therefore overpopulated as compared to the thermal expectation. One has to distinguish between a baryon-rich scenario and a baryon-free scenario here. In a baryon-rich scenario, participant nucleons have been stopped and placed inside the thermalized region. The finite net baryon number leads to the creation of additional resonances as compared to the thermally expected number without the presence of participant baryons. These additional resonances in turn decay mostly into pions. Therefore the pion density is always larger in baryon-rich than in baryon-poor fireballs, therefore also the freeze-out conditions and the EoS become different.

The question of chemical freeze-out and resonance decay is discussed more in detail in chapter 6.

Thermodynamic properties

Concerning the thermodynamics of hadronic systems, what has been calculated so far are the properties of an interacting pion gas up to three loops [37] and the behaviour of an ideal resonance gas including the changes introduced by resonance decays as the system cools down [71].

As we have seen, the properties of a pion gas are clearly insufficient to describe the dynamics of the system until the very late stage. The ideal hadron gas however may miss an essential property of the evolution: On the lattice, there is a soft region in the EoS in the vicinity of T_C. In spite of the fact that the lattice calculations become increasingly unreliable below T_C due to the large quark masses entering the simulations, there is no indication that this soft region ends with a sudden jump to ideal gas properties, $p/\epsilon \approx 1/3$. Instead, it rather continues even below T_C and this gives a qualitative estimate for the behaviour of a hot hadronic resonance gas. Therefore one might expect that the soft region continues somewhat further down in T also in nature.

Clearly, once T_f is reached, interactions between different particles cease to be important and that is exactly the definition of the ideal gas, so in the vicinity of the thermal freeze-out point, the thermodynamics of the system should be well described by a non-interacting hadronic resonance gas, where the abundancies of particles follow from resonance decays of a thermalized ensemble at T_C.

In-medium modifications of particle properties

The properties of hadrons embedded into a hot and/or dense medium are expected to differ considerably from those in the vacuum. A dense medium implies frequent interactions

with baryons whereas in a hot medium at low baryon density mostly interactions with the mesonic heat bath are responsible for changes of particle properties.

In [38], it was shown for the lowest lying $J^P = 1^-$ excitations of the vacuum, the vector mesons ρ, ω and ϕ that considerable modifications of their properties occur due to their interaction with a dense baryonic medium. Specifically, the ρ dissolves almost completely and both the ω and ϕ undergo strong broadening. Additionally, the mass of the ω shifts down. Although these results where obtained in linear density approximation, they cast some light onto the changes likely to occur inside a medium.

In [39] and [40], changes of the vector meson properties at finite temperature were discussed using techniques of thermal field theory. Only small modifications of the ρ and ϕ were found, but the ω completely dissolves due to the scattering process $\omega\pi \rightarrow \pi\pi$.

Self-consistent mean field calculations of hot nuclear matter find a dropping of the nucleon mass with increased temperature [41]. It might be reasonable to argue that nuclear resonances behave in a similar way. Pions, due to their nature as Goldstone bosons, are to some degree protected from such modifications.

In summary, a wealth of calculations indicates that particle properties in the medium are considerably different from those in the vacuum. Such investigations have primarily focused on the vector mesons, as they directly couple to the photon and are therefore reflected in the invariant mass spectrum of dileptons emitted from the medium. Not much is known, however, about the changes of hadronic spectral functions in the vicinity of the phase transition.

4.7.2 Experimental signals

The most interesting physics question of the hadronic phase probably concerns the in-medium properties of particles mentioned before, most prominently the vector mesons. Furthermore, adopting the picture of sequential chemical and thermal freeze-out, the abundancies of particles can be measured. They reflect the temperature of the system at the chemical freeze-out point. One can also compare the amount of produced strangeness in a thermalized system with predictions of conventional multiparticle inelastic scattering in order to learn about the degree of thermalization. Most information about the hadronic phase, however, is only available after the bulk of particles has left the strongly interacting thermalized region and moves towards the detector. This subject is covered in chapter 6.

4.8 FREEZE-OUT

As the system expands, interactions between the particles become less and less frequent. Therefore, their mean free path inside the thermalized medium grows until it exceeds the dimensions of the system. Pions are by far the most abundant species in the system, especially in the late stages of the expansion when most of the resonances have decayed, so it is reasonable to assume that it is the pion density that determines the freeze-out point. Specifically, freeze-out occurs as soon as the condition

$$\sigma \rho_\pi \lambda = 1 \qquad\qquad (4.17)$$

is met. Here, σ is a typical hadronic cross section and λ is a length scale of the order of the fireball. In a thermalized system, the critical value of the pion density ρ_π can be uniquely related to a given temperature once the EoS is known.

In reality, freeze-out occurs over an extended period of time, as the outer layers of the fireball will be less hot and dense than the core, so that particles will more or less continuously be emitted via the so-called freeze-out hypersurface. But the main bulk of particles is expected to freeze-out for a relatively short proper time (less than 4 fm/c). This period can extend considerably when seen in the c.m. frame as large parts of the fireball are moving with relativistic velocities causing substantial time dilatation.

Looking again at Eq. 4.17, there is a subtlety regarding σ. Hadrons can have quite different cross sections with pions, and there is no reason why this should not influence the freeze-out conditions. Specifically, one would expect particles with small pion scattering cross sections to freeze-out earlier. Experimentally, this would be manifest in differences to the general trend of the observed momentum spectra. Extended freeze-out of different particle species has been studied theoretically e.g. in [43]. Recently, a universal freeze-out criterion based on the escape probability of a particle, which is in turn a function of the number of collisions it encounters on its way to the fireball surface has been proposed [42]. This corresponds to an even more refined treatment where the freeze-out depends on the particles species, position and momentum.

After the medium has become dilute, interactions rapidly cease to be important. Instead, particles stream freely towards the detector. In this very last stage of fireball evolution, in-medium effects are irrelevant. Long-lived particles and resonances (like the ω and the ϕ) undergo strong decays in the vicinity of the collision point. Much later, weak and electromagnetic decays occur far outside of the interaction region and change the abundancies of particles on their way outward.

Chapter 5

HADRONIC OBSERVABLES —
A BASIS FOR MODELS

5.1 INTRODUCTION

The models used for the description of heavy-ion collisions generally fall in one of three different groups — event generators, hydrodynamic simulations and models based on bulk thermodynamics.

5.1.1 Event generators

Event generators aim at a description of heavy-ion collisions by making use of physics known from p-p scattering. The dynamics of A-A collisions then emerges as particles produced in initial binary nucleon-nucleon collisions subsequently re-scatter off further nucleons or off other secondary particles. In order to include these re-scatterings, particles are used as explicit degrees of freedom and individual particle trajectories and reactions are followed through the evolution. This can only be done if particles are not treated in a fully quantum field theoretical fashion but are approximated as localized wave packets. Additionally, reaction cross sections are typically implemented by purely geometrical considerations. Observables are then calculated by a Monte Carlo simulation of a large sample of collisions.

A variety of event generator models has been proposed, dependent on the degrees of freedom employed, the way hadronization is implemented and the implementation of additional physics not present in p-p collisions. Among the most prominent ones are RQMD [44] and UrQMD [45] tracking hadronic degrees of freedom, HIJING [46] tracking hard partonic evolution and hadronization and LUCIFER [47] as a two stage model.

The main difficulty of event generators lies in the initial multiparticle production. Here, soft and hard processes contribute, and the choice of the correct degrees of freedom is therefore not obvious. Usually, soft particle production is calculated in the framework of the Dual Parton Model [48] or the Lund string model [49] which describe the particle production as the breaking of color strings stretching between scattering partners. For the hard particle production, partonic degrees of freedom have to be employed along with the fragmentation functions known from e.g. deep inelastic scattering experiments. If there is any QGP phase, its properties are encoded in nontrivial physics of particle production within event generator type models. Suggested concepts involve interactions or fusion among color strings ('color ropes' , implemented in RQMD and UrQMD), percolation of strings and modifications of the string tension (HIJING). In general, the implementation of these additional mechanisms allows no straightforward connection to equilibrium properties of the QGP extracted from the lattice, which makes it difficult to make use of this information.

Once the transition to hadronic degrees of freedom from either strings or partons has been made, measured hadron-hadron cross sections enter the simulation and the model dependence is greatly reduced. However, many masses, cross sections and decay channels of high-lying resonances are experimentally poorly known and thus introduce uncertainties into the model. Event generators reach their optimal performance near the kinetic freeze-out. Here, the system is dominated by well-known long-lived particles and no assumption regarding freeze-out conditions has to be made as particles just cease to interact as the system becomes less and less dense.

5.1.2 Hydrodynamics

If the particle density is large enough and interactions occur frequently enough to maintain equilibrium, the transition from individual particles as degrees of freedom to a fluid description can be made. This step relies entirely on the validity of local thermal equilibrium. The fluid is characterized by a given temperature T, energy density ϵ, entropy density s and particle density n at each point in spacetime. These quantities are not independent but are connected by the EoS. Imposing energy and momentum conservation

$$\partial_\mu T_{\mu\nu} = 0 \tag{5.1}$$

(here, $T_{\mu\nu} = (\epsilon + p)u_\mu u_\nu + pg_{\mu\nu}$ denotes the energy momentum tensor of the fluid, u^μ its four-velocity, ϵ the energy density and p its pressure in the local restframe) and particle number conservation

$$\partial_\mu n_q u_\mu = 0 \tag{5.2}$$

(n_q stands for the density of particles carrying a conserved quantum number q), one finds the basic equation of relativistic hydrodynamics. In order to close the system of equations (5.1) and (5.2), the EoS has to be specified as $p(T)/\epsilon(T) = f(T))$ or an equivalent expression. The remaining parameters can then be fixed by thermodynamical relations. The resulting fluid dynamics is much easier to solve than the microscopic description employing particles as degrees of freedom. The ability to incorporate the known information on the QGP, specifically the EoS, in a straightforward way is one of the main strengths of such hydrodynamic simulations.

For the description of heavy-ion collisions, this has been carried out e.g. in [43, 50, 51]. Individual models differ in the type of EoS which is used, the degree of symmetry assumed (boost invariance, radial symmetry) which allows the reduction of a 3 dimensional system to a 2 or even 1 dimensional description and the freeze-out conditions imposed. The performance of hydrodynamic models is expected to decrease near the kinetic freeze-out as the system becomes less dense and thus the assumption of local thermal equilibrium becomes questionable. For this reason, some hydrodynamic simulations switch to an event generator

description once the hadronic phase is reached ('hybrid models', see e.g. [43]). If this is not done, a suitable freeze-out condition must be defined at which the hydrodynamic evolution is stopped. Usually, the hypersurface characterized by $T = T_f$ is taken for this purpose.

Contact between microscopic description and hydrodynamic evolution can be made by a suitable averaging procedure. In this way, an 'effective EoS' can be extracted from an event generator description if the system is close to equilibrium. This has been carried out e.g. for RQMD in [52]. It was found that the system is very close to equilibrium for some 2 fm/c in the hadronic phase (a direct comparison in the partonic phase is impossible in the case of RQMD) and that the effective EoS is very simple, $p/\epsilon \approx const.$ — in close resemblance to the EoS of a non-interacting resonance gas.

5.1.3 Thermodynamics

If one is interested in bulk properties of the expanding system only, the dynamics can be simplified even further. Assuming local thermal equilibrium, a spatial averaging procedure across the whole fireball volume contained inside the freeze-out hypersurface can be carried out, resulting in a homogeneous distribution of matter inside an 'effective' volume. This is best done for the collection of volume elements characterized by a given proper time τ in order not to artificially average out effects of time dilatation. Assuming entropy conservation, the EoS then governs the response in the thermodynamical parameters ϵ, s and T to a change of the effective volume $V(\tau)$. This volume expansion can be given by a suitable parametrization, which must be chosen such as to resemble hydrodynamic evolution (obviously, arguments based on thermodynamics alone do not constrain evolution timescales) and to reproduce the experimentally observed freeze-out state which manifests itself in the measured momentum distributions of hadrons. Examples for these kinds of models are e.g. [31, 53].

The assumptions made in thermodynamic models appear rather drastic, as any possibility for internal dynamics such as shock waves or pressure anisotropies is gone. Furthermore, a continuous flow of particle across the freeze-out hypersurface as it appears in hydrodynamic simulations becomes a single freeze-out moment in proper time in thermodynamical models. Any distinction between the cool fireball edge and the hot core has been erased by the averaging procedure. However, no detector is capable of resolving the spatial and temporal scales of the fireball (10-20 fm/c), unless there is a strong correlation between position and momentum of particles emerging from a specific region such as between longitudinal position and rapidity (see section 4.2.2). But for most observables, only integrated particle emission rates can be measured, and for such processes, the description in terms of a model which is a priori averaged in space might be valid. We expect a serious breakdown of such a model only if some process is specifically sensitive to inhomogeneities in the distribution of matter inside the fireball or if thermalization ceases to be a useful concept (such as in very peripheral collisions).

The main advantage of thermodynamic models lies in their simplicity. Systematic variations of certain parameters can rapidly be tested and in doing so a general understanding of the behaviour of the model can be gained. Therefore, we will use a model of this type as the starting point of our investigations.

5.2 HADRONIC OBSERVABLES

As the matter contained inside the fireball is composed of the remnants of the colliding nuclei and produced secondaries which eventually hadronize again, hadronic observables

are the most revealing ones if one wants to learn about the fireball itself. Momentum distributions of different hadron species have the potential to provide information on the conditions at freeze-out, two particle correlation measurements, so-called Hanbury-Brown-Twiss (HBT) interferometry [54] (see [55] for a review of the application to URHIC), can tell about the geometric shape of the emission source and the distribution of particles across rapidity space directly reflects the longitudinal geometry of the fireball.

If thermalization of the fireball matter is a useful concept, hadrons cannot carry any information on the evolution history. A thermalized system is in equilibrium, regardless of its history, and therefore hadronic spectra only reflect the status of the system at freeze-out. The evolution history is probed in a more subtle may — the early stages may leave indirect traces in phenomena like collective and elliptic flow [29] and event-by-event fluctuations of observables [36].

But information on the freeze-out state is valuable: It provides the last snapshot of the fireball dynamics and defines an important constraint which every model for this evolution has to meet. Understanding the measured distributions of hadrons and reconstructing the freeze-out conditions based on this information is therefore crucial.

5.2.1 dN/dy Spectra

A measurement of rapidity distributions reflects the longitudinal dynamics of the fireball at freeze-out. In p-p collisions, no final state scattering takes place, and so the measured rapidity distribution corresponds directly to the rapidity distribution of produced particles, but in heavy-ion collision, one way of describing the data is the assumption of thermalization. As a thermalized system builds up pressure, it may accelerate also in longitudinal direction, thus allowing for different initial and final rapidity distributions.

Rapidity distributions have been measured at SPS by the NA49 collaboration [56]. The result is shown in Fig. 5.1 for protons and net baryons, and in Fig. 5.2 for negatively charged hadrons (h^-).
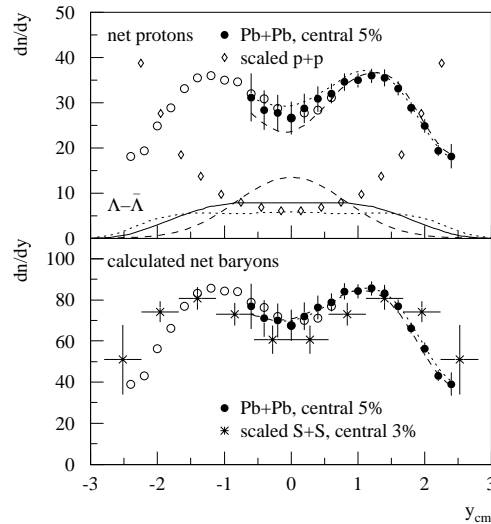

FIGURE 5.1: dN/dy distribution of protons and net baryons for p-p and Pb-Pb collisions as obtained at SPS by NA49 [56]

The distribution of protons reveals a striking difference between heavy-ion and p-p collisions. Predominant source for protons in both cases are target and projectile fragmentation

processes. In p-p collisions, the distribution is strongly peaked towards the kinematic limits, reflecting a high probability of the collision partners to undergo only small deceleration and emerge as leading particles. This is clearly not the case in heavy-ion collisions. Here, the protons emerge in a broad plateau around midrapidity, cleanly separated from the kinematic limit set by the initial rapidities of the collision partners. This indicates a high degree of energy loss of valence quarks during the collision process. The fact that the net baryon distribution shows a similar plateau shape in rapidity as the proton distribution is important since it indicates that the region is indeed populated by the baryon number of the collision partners and not by secondary proton-antiproton pairs.
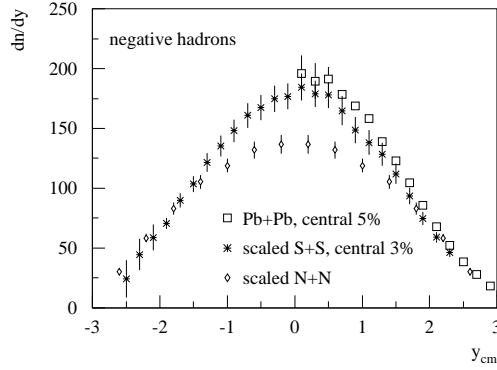

FIGURE 5.2: dN/dy distribution of negatively charged hadrons (h^-) for p-p, S-S and Pb-Pb collisions as obtained at SPS by NA49 [56]

On the other hand, the distribution of h^- consists of secondary particles only. The shapes of these distributions in rapidity are very similar for p-p and Pb-Pb collisions, hinting that the underlying dynamics of secondary particle production might be common in both cases. The rapidity density of h^- is significantly higher than that of net protons, indicating that the dominant contribution to the fireball matter comes from secondary particle production. The rapidity region in which both the distribution of net baryons and h^- are large is similar; this supports the assumption of models based on thermodynamics that we can indeed define a volume in which the fireball matter is distributed approximately evenly.

5.2.2 m_t Spectra

Measuring transverse mass m_t (see section 4.2) spectra of hadrons can tell about the system's dynamics perpendicular to the beam axis. Fig. 5.3 shows typical experimental results obtained by the NA44 collaboration [57].

The resulting spectra for particle species i are well described by a fit of the form

$$\frac{1}{m_t}\frac{dN_i}{dm_t} = C(T_i) \cdot e^{-m_t/T_i}. \tag{5.3}$$

Here, the distribution of particles i is characterized by a parameter T_i measuring the slope and $C(T_i)$ describes the normalization. This ansatz reminds of the decay of a thermalized ensemble of particles, where the exponential simply reflects a Boltzmann distribution with a temperature T_i dependent on the particle species. This temperature appears to increase with particle mass, $T_i \approx 120$ MeV for π^+ and $T_i \approx 220$ MeV for p.

If T_i indeed describes a temperature, this is surprising at first sight, as elastic scattering reactions between e.g. π^+ and p should equilibrate the whole ensemble of particles. There-
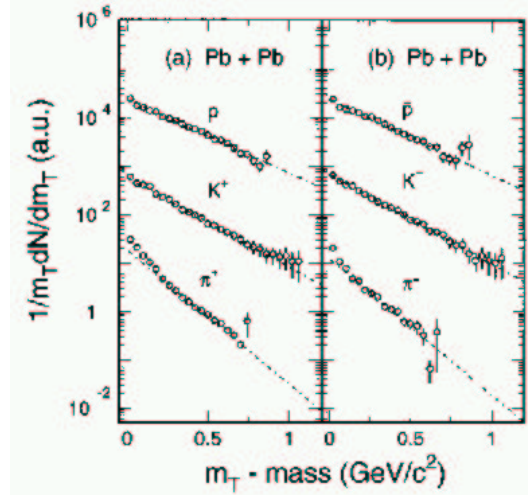
FIGURE 5.3: Transverse mass spectra for different particle species as obtained at SPS by the NA44 collaboration [57].

fore, the system should be described by a common temperature T_f characteristic for the kinetic freeze-out.

There are two main options left to explain the data: Either the assumption of thermalization is dropped at this point, or, retaining thermalization, some other contribution to the transverse momentum spectra is present which distorts the spectra in a characteristic way.

If a thermalized particle emission source is expanding radially at freeze-out, the particles will not only receive a contribution to their momentum from the random, thermal motion but also from the directed motion of the volume element containing the particle. The Boltzmann distribution describes the probability of a particle having energy E in an ensemble with a typical energy scale given by T. In the presence of flow, however, the typical energy of the ensemble contains also the collective flow, one should therefore replace (for non-relativistic transverse velocities)

$$T \to T_i^* = T + m_i \langle v_T \rangle^2, \tag{5.4}$$

where T stands for the temperature in the local rest frame of the heat bath, $\langle v_T \rangle$ denotes the average collective radial velocity and m_i is the mass of particle species i. This simple expression offers a natural explanation for the apparent dependence of the freeze-out temperature on the particle species.

In a more refined treatment of this problem, the general expression for the slope has been derived in [58] as

$$1/T^* = \frac{I_1(\frac{p_T \sinh \rho}{T})}{I_0(\frac{p_T \sinh \rho}{T})} \frac{m_T}{p_T} \frac{\sinh \rho}{T} - \frac{K_0(\frac{m_T \cosh \rho}{T})}{K_1(\frac{m_T \cosh \rho}{T})} \frac{\cosh \rho}{T} \tag{5.5}$$

This expression involves the modified Bessel functions $I_n(x)$ and $K_n(x)$. ρ denotes the transverse rapidity, $\rho = \text{arctanh } v_T$. In the limit of large transverse momenta, this expression simplifies to

$$T^* = T \sqrt{\frac{1 + v_T}{1 - v_T}}, \tag{5.6}$$

i.e. the slope ceases to be dependent on the particle masses.

Alternative descriptions of the transverse mass spectra are possible without assuming thermalization, see e.g. [59]. In this event-generator based approach, particle production is

assumed to follow the string fragmentation scenario extracted from p-p collisions [48]. Under the additional assumption that the colored strings connecting the initial scattering quarks may interact and also fuse before they fragment into hadrons and introducing an intrinsic transverse momentum k_t distribution of the scattering quarks (which is transferred to the strings), the momentum spectra are also approximately reproduced, provided that the re-scattering of hadrons after string fragmentation is treated appropriately.

A striking difference between the two pictures is given by the transverse size of the emitting source: In the thermalized picture, the source has been expanding for some time before freeze-out occurs, whereas in the string fragmentation picture the particles emerge from a region corresponding to the initial transverse overlap, slightly washed out by re-scattering in the hadronic phase, with approximately the final momentum distributions. Can one distinguish these two pictures? As we will see, HBT correlation measurements allow to observe the source size at emission time [55] and therefore favour a scenario with an expanding emission source.

5.2.3 HBT correlation measurements

Hanbury-Brown-Twiss (HBT) interferometry [54] is a technique to extract the phase space density $S_i(x, p)$ of a given particle species i from a combination of one particle spectra

$$E\frac{dN_i}{d^3p} = \int d^4x S_i(x, p)$$
(5.7)

and two particle correlations

$$C(k, q) = 1 + \frac{|\int d^4x e^{iqx} S_i(x, k)|^2}{\int d^4x S_i(x, p_1) \int d^4y S_i(y, p_2)}.$$
(5.8)

Here, k denotes the c.m. momentum of the pair with individual momenta p_1, p_2 and q is the relative momentum. Two particle correlations can occur for several reasons, the most important ones being quantum statistics (stimulated emission for bosons) and a common origin of both particles from a decaying resonance. Experimentally, $C(k, q)$ is defined as

$$C(k, q) = \frac{\text{number of actual pairs in } (\Delta q \Delta k)}{\text{number of actual pairs in sample}} \bigg/ \frac{\text{number of reference pairs in } (\Delta q \Delta k)}{\text{number of reference pairs in sample}}.$$
(5.9)

The reference pairs are generated by randomly picking particles from different events within the set of events yielding the actual pairs. In this way, pair correlations are removed. In order to extract the phase space density $S(x, p)$, a trial ansatz can be made and its parameters fitted to the existing data. A commonly used parametrization for the phase space density at freeze-out is given by [60]

$$S(x, k)d^4x = \frac{m_t \cosh(y - \eta)}{(2\pi)^3} \exp\left(-\frac{ku(x)}{T} + \frac{\mu}{T}\right) G(r) \exp\left(-\frac{(\eta - \eta_0)^2}{2\Delta\eta^2}\right)$$
$$\times \frac{1}{\sqrt{2\pi\Delta\tau_f^2}} \exp\left(-\frac{(\tau_f - \tau_f^0)^2}{2\Delta\tau_f^2}\right) d\eta r dr d\phi d\tau_f.$$
(5.10)

This expression utilizes a thermal momentum spectrum, where the energy is evaluated in the rest frame of the heat bath moving with velocity $u(x)$. Gaussian distributions for the rapidity η of emitting volume elements around η_0 and with a width $\Delta\eta$ (see section 5.2.1) and for the freeze-out proper time τ_f around τ_f^0 with width $\Delta\tau_f$ have been assumed. Assuming radial symmetry, the density in transverse direction r is described by a yet to
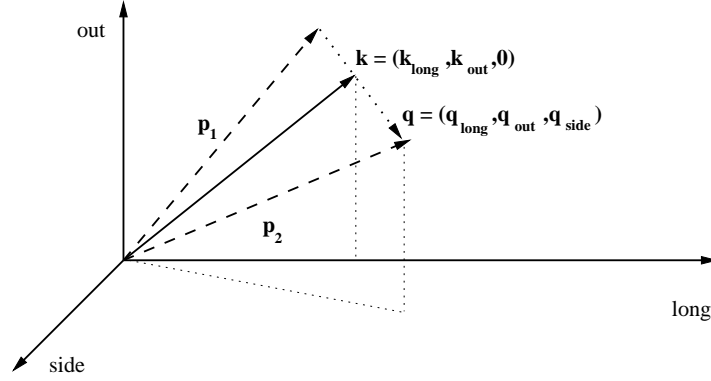
FIGURE 5.4: The 'out-side-long' coordinate system. The 'long' axis is given by the beam direction. For a pair of particles with momenta p_1 and p_2, the component of the c.m. momentum k perpendicular to the beam axis defines the 'out' direction and the direction perpendicular to both 'out' and 'long' is then called 'side'. The relative pair momentum q can have components along all directions.

be specified distribution $G(r)$. The trial functions $G(r)$ employ for example Gaussian $G(r) = \exp\left(-\frac{r^2}{2R_G^2}\right)$ and box density profiles $G(r) = \theta(R_B - r)$.

Usually, experimental data on HBT correlation radii in the context of heavy ion collisions is given in the out-side-long (osl) coordinate system [61] (see Fig. 5.4). In this system, the 'long' axis is defined by the beam direction. For a particle pair to be correlated in the analysis, the component of the c.m. momentum of the pair k transverse to the beam axis then defines the 'out' direction. Finally, the 'side' direction lies perpendicular to both 'out' and 'long'.

Extracted correlation radii do in general not coincide with the geometrical dimensions of the emitting source. If the system expands, volume elements move with different velocities. The larger the relative velocity of two volume elements becomes, the smaller is the probability of finding a correlated pair from both regions. A rapidly expanding source will therefore lead to smaller correlation radii in HBT measurements than a source at rest.

In a Gaussian ansatz for the expanding emission function, the following combinations of coordinates and velocities contribute to the correlation radii (assuming azimuthal symmetry and z to coincide with 'long', x with 'out' and y with 'side'):

$$R_{side}^2(k) = \langle y^2 \rangle(k) \,,\; R_{out}^2(k) = \langle (x - v_\perp \cdot \Delta\tau)^2 \rangle(k) \,,\; R_{long}^2(k) = \langle (z - v_z \cdot \Delta\tau)^2 \rangle(k)$$
$$\text{and}\quad R_{out-long}^2(k) = \langle (x - v_\perp \Delta\tau)(z - v_z \Delta\tau) \rangle(k)$$

$$(5.11)$$

Here $\langle \ldots \rangle$ denotes an averaging procedure over the phase space density $S(x.k)$ of the emission source,

$$\langle f(x) \rangle = \frac{\int d^4 x f(x) S(x, k)}{\int d^4 x S(x, k)}, \quad\quad (5.12)$$

$\beta_\perp$ and β_l are the transverse and longitudinal velocities of the relative pair motion characterized by the momentum q and $\Delta\tau$ characterizes the duration of the emission.

As apparent from these equations, the radii do not characterize the spatial extent of the source directly but rather through a 'filter' of wavelength $1/k$; they measure a region of

homogeneity from which particles with pair momentum k are most likely to be emitted. Only if there is no correlation between position and momentum in the source, the extracted radii are independent of k.

R_{side} is sensitive to the geometrical extension of the source only, whereas R_{out} is also sensitive to a term $\beta_\perp \langle \Delta\tau \rangle$ which measures the duration of the emission. The difference between R_{out} and R_{side} therefore allows to partially disentangle the spatial and temporal information contained in the radius parameters, provided that $\Delta\tau$ is sufficiently large to dominate R_{out}. Similarly, R_{long} measures a combination of longitudinal extent of the source, longitudinal pair motion and emission duration.
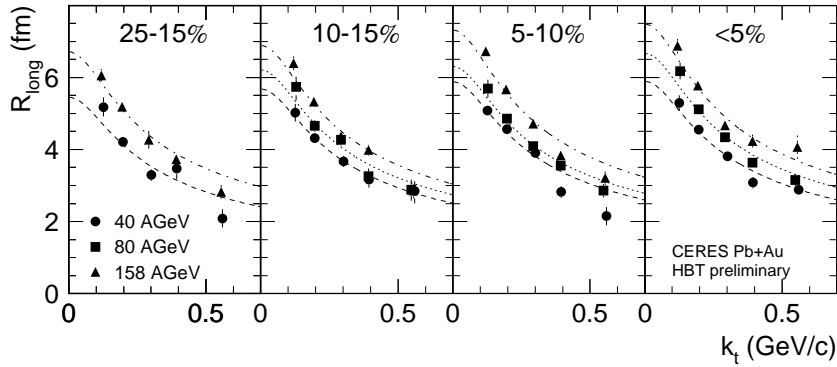
FIGURE 5.5: R_{long} as obtained by CERES/NA49 [62] in Pb-Au collisions for different centralities and beam energies (k_t denotes the transverse momentum of the correlated pair).
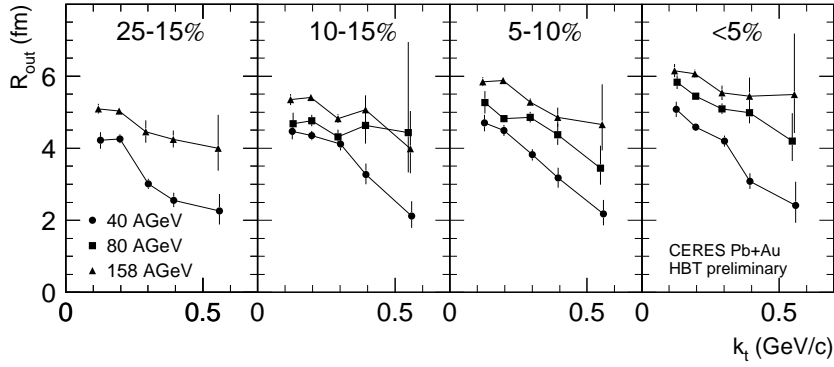

FIGURE 5.6: R_{out} as obtained by CERES/NA49 [62] in Pb-Au collisions for different centralities and beam energies (k_t denotes the transverse momentum of the correlated pair).

Figs. 5.5, 5.6 and 5.7 show experimental data on correlation radii as obtained by the CERES collaboration for different centrality and beam energy, separated into transverse pair momentum k_t bins using pion correlations [62].

In the thermalized expansion scenario presented here, the relative pair momentum q is affected by two different effects: Random thermal motion and collective motion. If the two particles of the pair under consideration come from different regions of the source which are moving with different collective velocities, the probability to find a correlated pair out of these regions will decrease due to the 'intrinsic' momentum difference of the particles caused by this collective motion. The thermal motion of the particles can partially counteract this effect by washing out the strict position/momentum correlation of collective flow.
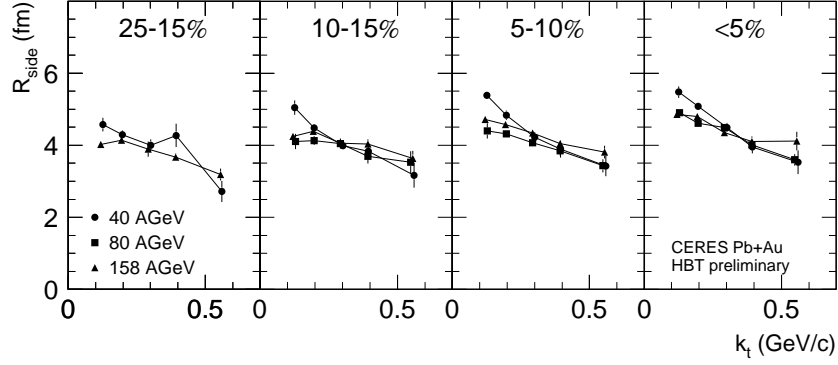
FIGURE 5.7: R_{side} as obtained by CERES/NA49 [62] in Pb-Au collisions for different centralities and beam energies (k_t denotes the transverse momentum of the correlated pair).

For a strong source expansion in longitudinal direction, the size of the region of homogeneity is almost entirely determined by the thermal length scale $\sim (T_f/m_t)^{1/2}$. This quantity decreases as m_t increases along with k_t and that causes the decrease of the measured R_{long} with k_t (see Fig. 5.5). If the expansion follows the Bjorken scenario, $R_{long} = \tau_f (T_f/m_t)$ can be used to estimate the time τ_f from the collision to kinetic freeze-out. In this way, lifetimes of order 6-8 fm/c can be estimated. Note that this estimate breaks down once the system is allowed to accelerate in the course of its evolution. The HBT measurement is only able to tell about the time-instance of the kinetic freeze-out, all backward extrapolation is necessarily model dependent.

The fact that there is no striking difference between R_{out} and R_{side} indicates that R_{out} is not dominated by the $\beta_\perp \langle \Delta\tau \rangle$ term. Instead, this term appears to be a correction responsible for the stronger $k_\perp$ dependence of R_{out} with respect to R_{side}. This in turn implies that the emission duration $\Delta\tau$ is short and the kinetic freeze-out occurs rather suddenly (see Figs. 5.6 and 5.7).

There appears to be a moderate increase of both R_{long} and R_{out} with both beam energy and centrality, consistent with the picture of a prolonged lifetime and therefore a larger geometrical source radius due to increased entropy production. Transverse (Gaussian) radii are of order 5 fm (see R_side), corresponding to a r.m.s. radius of ~ 7 fm, clearly exceeding the initial nuclear overlap radius.

5.2.4 Elliptic Flow and early thermalization

As already discussed in section 4.4.2, anisotropies in the finally observed momentum distribution of produced particles in decental collisions can provide an indication for early thermalization.

Experimental measurements of elliptic flow are not straightforward, as the reaction plane, the plane defined by the momentum vectors of the colliding nuclei and the collision remnants, is not known a priori. Instead, one studies a Fourier decomposition of the azimuthal distribution of transverse energy. This quantity is defined as a sum over the energy of all particles weighted with their angular deviation θ from the beam axis:

$$\mathbf{E}_t(\eta, \phi) = \sum_i E_i \sin\theta_i \cdot \mathbf{r}_i(\eta, \phi_i) \tag{5.13}$$

In this equation, $\mathbf{r}_i$ denotes the vector from the collision point to the impact point in the detector. At a given (pseudo)rapidity η, the transverse energy can be decomposed in a

Fourier series

$$\frac{dE_t}{d\phi}(\eta) = \frac{\langle E_t \rangle}{2\pi} \left(1 + \sum_{n=1}^{\infty} 2v_n \cos\left(n(\phi - \Phi_R)\right) \right) \tag{5.14}$$

Here, the azimuthal orientation of the reaction plane is given by Φ_R. It can be determined by considering two particle correlations assuming that both of them are correlated with the reaction plane.

v_1, the first Fourier coefficient corresponds to the so called *directed flow*, v_2 is the measure for *elliptic flow*.

Directed flow results essentially from the bouncing of the colliding systems off each other in the course of baryon stopping: It is peaked in the reaction plane and has, on general grounds, a very characteristic 'wiggle' shape in rapidity [63]. For larger beam energies, the nuclei become more and more transparent, baryon stopping ceases to be important and the directed flow vanishes. Therefore, we will not focus on directed flow in the following.

At large beam energies, elliptic flow is predominantly caused by the pressure gradient of a thermalized, spatially inhomogeneous system. This is demonstrated in Fig. 5.8 for SPS and Fig. 5.9 for RHIC, where a hydrodynamical predictions for v_2 are compared to data.
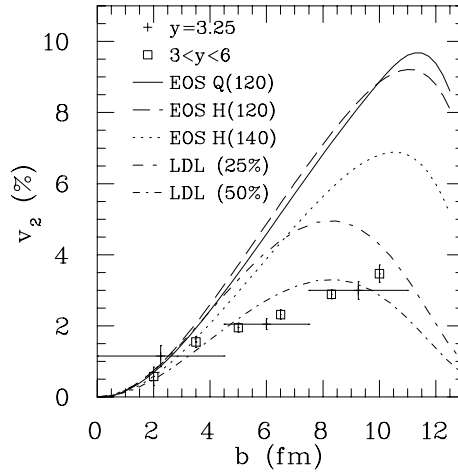

FIGURE 5.8: Impact parameter dependence of v_2 in hydrodynamical calculations [64] as compared to experimental data [65].

For small centralities and low transverse momenta, hydrodynamic calculations give the correct order of magnitude for the effect, indicating that it is indeed driven by the pressure in a thermalized evolution scenario. This is sensible: Equilibration is more likely to be realized in central collisions and for low momentum particles, as particles with large transverse momentum have a high probability to escape from the dense region of the fireball.

In a recent paper [68], it has been shown that this agreement to the data can not be achieved by a partially thermalized system: Free streaming of particles in longitudinal direction and transverse equilibration do not give the correct order of magnitude for v_2. Furthermore, thermalization times τ_0 larger than 2 fm/c can be excluded by the observed elliptic flow. Therefore, we may indeed conclude that there is substantial evidence from experiment that early thermalization is indeed achieved, at least for central and near central collisions and for particles with transverse momenta below 1 GeV (which covers more than 90% of all particles in the fireball).
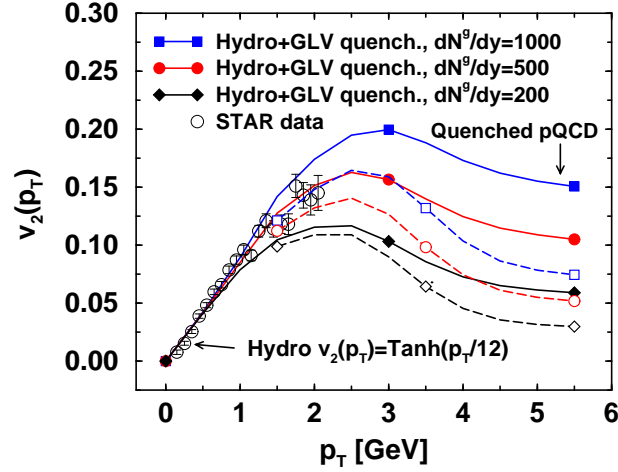
FIGURE 5.9: Transverse momentum dependence of v_2 in hydrodynamical calculations [66] as compared to experimental data [67].

5.2.5 An intermediate summary

What information can be obtained by looking at the observables discussed in the previous sections? First of all, there are clear differences between A-A and p-p collisions, evident from the different distributions of baryon number across rapidity space (see Fig. 5.1), which indicate the importance of subsequent collisions, leading to an increased stopping of the incident nuclear matter.

The evidence for multiple collisions, indicates some degree of equilibration, which indeed finds support by examining the transverse mass spectra. These can be explained by (approximately) thermal distributions, provided that the emission source expands radially in order to account for the changes in the slope with particle mass.

The expansion picture in turn is reinforced by the HBT data which clearly indicate a source radius exceeding the nuclear overlap radius. This can only be explained if the system had some time for transverse expansion before kinetic freeze-out, which in turn contradicts any scenario involving early free-flow conditions.

Qualitatively, the picture of fireball evolution indicated in Chapter 4 indeed emerges again — after the collision, a strongly interacting system is formed which is likely to be in or near equilibrium, this system expands and after some extended period of time (which appears to grow with particle production, see Fig. 5.5 and 5.6), kinetic freeze-out occurs over a short period of time, after which the momentum spectra of all particles remain unchanged.

Can one also obtain quantitative information from the data? This poses a somewhat more difficult task. Recall that the shapes of the m_t spectra for different particle species, for example, are caused by a combination of freeze-out temperature T_f and collective radial motion $v_\perp(r)$, which in general is different for different positions r. Schematically, $p_t \sim T + mv_\perp(r)$. From the spectra, however, only a spatially averaged flow velocity $\overline{v}$ can be extracted, which in turn can be caused by a variety of flow profiles $v(r)$. Attempts to fit the m_t spectra find an anticorrelation between flow and temperature but are unable to resolve the ambiguity, leaving the freeze-out temperature virtually unconstrained between ~ 170 and 90 MeV(see e.g. Fig. 5.10). Similar difficulties appear if one tries to extract the geometrical radius from the HBT correlation radius without knowing details of the position/momentum correlation inside the emission source.

Luckily, the dependence of the HBT radii on flow is of a different type than that of the

m_t-spectra. This opens up the possibility to resolve the ambiguities by a global fit to all existing observables.

5.2.6 A global analysis of the freeze-out state

Using the emission function Eq. 5.10, a global fit to hadronic observables has been performed in [60]. The fit assumes the fireball to be in local thermal equilibrium with temperature T_f. Transverse rapidity is assumed to grow linearly with the radius, $\eta_\perp(r) = \frac{r}{R_{rms}}\eta_f$, thus specifying the flow profile and for the transverse density distribution of the system, a Gaussian $G(r) = \exp\left(-\frac{r^2}{2R_G^2}\right)$ and a box profile $G(r) = \theta(R_B - r)$ have been tested. Resonance decays, which are known to influence the m_t distributions, have been included up to masses of 1020 MeV for mesons and up to 1400 MeV for baryons.
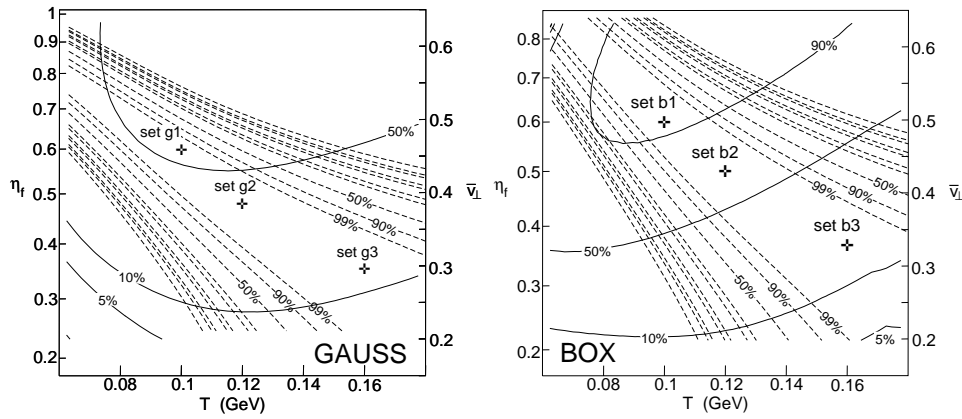

FIGURE 5.10: χ^2 contours for Gaussian (left panel) and box density profile (right panel) fits [60] to m_t spectra of negatively charged hadrons [69] (dashed) and HBT correlation measurements [70] (solid), all for SPS, 158 AGeV central Pb-Pb collisions.

The fit results can be seen in Fig. 5.10. Evidently, the χ^2 contours for the fit to m_t spectra only are ill suited to disentangle contribution of freeze-out temperature and flow, as already mentioned. The χ^2 contours of the fit to HBT spectroscopy however display a quite different pattern, and the combined fit therefore yields an unambiguous result for both the Gaussian and the box density profile. The box shaped density profile is more favoured by the fit, mainly because of the HBT results. The indicated data set b1 appears to be the most likely candidate for a description of the freeze-out state.

This freeze-out state (set b1 in Fig. 5.10) is characterized by a low temperature ($T_f \sim 100$ MeV), a rather large radial expansion velocity ($\overline{v}_\perp \sim 0.5 \cdot c$) and a geometrical radius $R_B \approx 12.1$ fm, corresponding to a r.m.s radius of $R_{rms} \approx 8.55$ fm. Assuming longitudinal free streaming of particles, the system lifetime is found to be 6.3 fm/c. This would imply an expansion of the r.m.s. radius from ~ 4.5 fm (initial overlap) to 8.55 fm within only 6.3 fm/c, with the additional constraint that the initial transverse expansion velocity is close to zero. This does not appear to be a realistic scenario and indeed can be taken as the first hint that longitudinal free streaming is not a good assumption for SPS conditions.

5.3 A MODEL BASED ON THERMODYNAMICS

In the following, we want to set up a model which incorporates the information on the freeze-out state in an essential way. The knowledge of initial and final geometry and expan-

sion velocity enables us do interpolate the evolution of the volume inbetween. Assuming spatial homogeneity and local thermal equilibrium, we can calculate the thermodynamics of the system once the volume growth is specified, assuming an isentropic expansion scenario. This is justified by the observation that most of the particle production must have happened early in order to reach equilibrium conditions, after that, the collision rate goes down as the volume increases and the creation of new particles ceases to be an important process. On the other hand, the particle number cannot decrease as the entropy cannot decrease.

5.3.1 The spacetime picture of a homogeneous fireball

As we have seen in section 4.2.2, global thermodynamics can only defined sensibly for a volume at the same proper time τ. In a variety of models (see e.g. [31,71], this volume has been parametrized using the simplifying assumption $V \sim v_z\tau$ or $V \sim v_z^0\tau + \frac{a_z}{2}\tau^2$, where v_z ($v_z^0 + a \cdot \tau$) directly reflects the longitudinal expansion velocity at given τ.

This is a good approximation, as long as velocities are much smaller than the speed of light. In heavy-ion collisions however, the longitudinal expansion velocity v_z is about $0.9\,c$, and for RHIC it is even larger, so one has to take into account time dilatation, which (in the c.m. system) causes the expanding front of the fireball to be characterized by the proper time $\tau = 1/\sqrt{1-v_z}t$ (where t is the time elapsed in the c.m. frame since the collision), whereas the midrapidity region at rest displays the conditions at a (much later) proper time $\tau = t$. Thus, a mismatch between the naive volume expansion and the exact expression in τ is introduced.
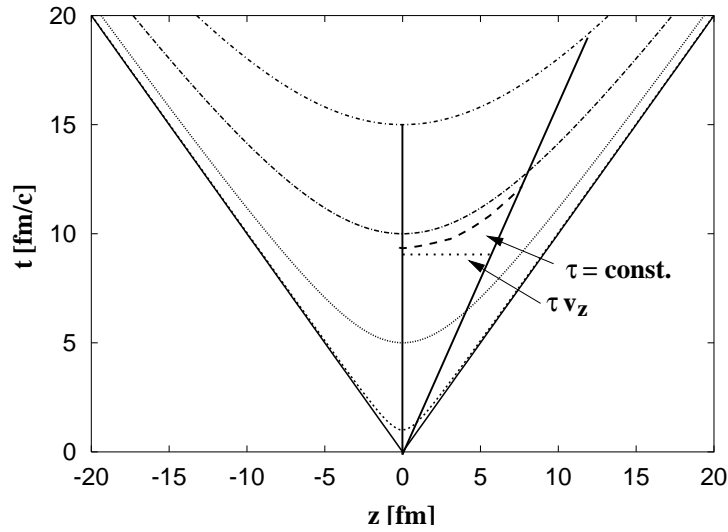

FIGURE 5.11: The mismatch between the naive (dotted) and the exact expression (dashed) for the expansion of a proper time volume

For an expansion with constant speed, the longitudinal extent $z_{c.m.}$ of the fireball in the c.m. frame after a time τ is given as $z_{c.m.} = v_z\tau$, whereas the correct expression of the longitudinal size z of the volume with $\tau = const.$ and expansion speed v_z reads

$$z(\tau) = \int_0^{z_0} \sqrt{1 + \frac{z}{\sqrt{\tau^2 + z^2}}}dz \quad \text{with} \quad z_0 = \frac{\tau v_z}{\sqrt{1-v_z^2}}. \tag{5.15}$$

As $v_z \to c$ (=1), z_0 gets very large and the mismatch between exact expression and approximation grows as large as a factor three for $v_z = 0.9\,c$. Therefore, for the values of

longitudinal flow found in section 5.2.6, it is absolutely mandatory to use the exact expression. For an accelerated motion, no analytic solution can be obtained, the problem however can still be solved numerically (and yields an unique solution for every τ) if the motion of the fireball front in lab time t is known.

As an amusing side remark, we note that accelerated expansion can display interesting effects if the fireball front is already close to the lightcone. In this case, z_0 grows very steeply with v_z and the apparent growth of the $\tau = const.$ volume into z direction can exceed the speed of light. This is not prohibited by special relativity, as the collection of volume elements $V(\tau)$ is defined across infinitely many frames.

The transverse expansion is now superimposed onto the longitudinal scenario. As typically $v_\perp \ll v_z$ (see Section 5.2.6), we neglect the additional time delay in the following and assume that the volume can be calculated as

$$V(\tau) = 2\pi z(t(\tau)) \cdot R^2(\tau) \tag{5.16}$$

if the longitudinal expansion $z(t)$ is known in the c.m. frame and the transverse dynamics $R(\tau)$ is known at midrapidity. Here, the factor 2 comes from the fact that the fireball expands both in the positive and negative z-direction. Note that there is no single Lorentz frame in which thermodynamics could be discussed, as there is no frame of reference, in which all volume elements are at rest.

5.3.2 Rapidity distributions

So far, the discussion of the freeze-out state has covered the transverse dynamics only, so we still need to prove that a homogeneous fireball with the dynamics indicated in the previous section is able to describe the particle rapidity distributions. The momentum distribution emitted by a thermal source in its rest frame is given by

$$\frac{d^3N}{d^3p} = \frac{dV}{(2\pi)^3} \frac{1}{\exp[p_0/T] \pm 1}. \tag{5.17}$$

Here, the $+$ sign holds for fermions and the $-$ sign for bosons. If the source is boosted, the distribution gets

$$\frac{d^3N}{d^3p} = \frac{dV}{(2\pi)^3} \frac{1}{\exp[p_\mu u^\mu/T] \pm 1}, \tag{5.18}$$

where u^μ denotes the four velocity of the source. Switching to the more useful description in terms of rapidity y and transverse mass m_t and taking Y_z and $Y_\perp$ as longitudinal and transverse rapidity of the emission source, we find

$$\frac{1}{\exp[p_\mu u^\mu/T] \pm 1} = \frac{1}{\exp[m_t \cosh Y_\perp \cosh(Y_z - y) - p_t \sinh Y_\perp \cos(\Phi - \phi)/T] \pm 1}. \tag{5.19}$$

Here, azimuthal orientation of particle emission and source movement are denoted by ϕ and Φ respectively. In order to discuss momentum spectra, we now have to consider a superposition of boosted sources,

$$\frac{d^3N}{dy dp_t^2 d\phi} = \frac{V_f m_t}{2(2\pi)^3} \int_{-Y_z^f}^{Y_z^f} dY_z \int dY_\perp \int d\Phi f(Y_z, Y_\perp) \cosh(Y_z - y) \frac{1}{\exp[p_\mu u^\mu/T \pm 1]}. \tag{5.20}$$

The information on the fireball geometry is contained in V_f, which represents the volume at the time of particle emission and $f(Y_z, Y_f)$, a normalized function which specifies the amount of V_f moving at a given longitudinal and transverse rapidity. Here, azimuthal

symmetry of the fireball has been assumed. The integral over Φ can be carried out, resulting in

$$\frac{d^2N}{dydp_t^2} = \frac{V_f m_t}{2(2\pi)^3} \int dY_\perp I_0 \left((p_t/T)\sinh Y_\perp\right)$$

$$\times \int_{-Y_z^f}^{Y_z^f} dY_z f(Y_z, Y_\perp) \cosh(Y_z - y) \frac{1}{\exp[(m_t/T)\cosh(Y_z - y)\cosh(Y_\perp)] \pm 1}.$$

$$(5.21)$$

Integrating this expression over p_t^2 yields the rapidity distribution of particles inside the fireball, integrating over y the transverse momentum spectra. For the homogeneous fireball, we assume a linear growth of the rapidity with position relative to the fireball center

$$Y_z(z) = \frac{z}{z_f} Y_z^f \quad \text{and} \quad Y_\perp(r) = \frac{r}{r_{box}} Y_\perp^f. \tag{5.22}$$

Here, Y_z^f and $Y_\perp^f$ denote the maximal expansion rapidities in longitudinal and transverse direction, which are reached at the fireball edges. During the fireball evolution, these quantities depend on proper time, but Eq. (5.22) is assumed to hold at all times. This leads to a boost-invariant scenario at freeze-out: $f(Y_z, Y_\perp)$ becomes a function of $Y_\perp$ only, with the form $f(Y_\perp) = 2Y_\perp/(Y_\perp^f)^2$.

If we now insert the parameters of the freeze-out analysis and compare the p_t^2 integrated Eq. (5.22) to the measured data, we have completely fixed the freeze-out state of the fireball. Good agreement is achieved with all of the hadronic observables discussed so far by construction, as we have used the best fit result (see section 5.2.6) to determine the relevant parameters of the model.

5.3.3 Evolution dynamics

We continue the discussion of the fireball model by making an ansatz for its evolution. We choose

$$z(t) = z_0 + v_z^0 t + \int dt' dt'' c_z \frac{p(t)}{\epsilon(t)} \tag{5.23}$$

and

$$R(\tau) = R_0 + \int d\tau' d\tau'' c_\perp \frac{p(\tau)}{\epsilon(\tau)} \tag{5.24}$$

as an input into Eq. (5.16). The motion of volume elements inside the fireball is assumed to be described by Eq. (5.22) at all times. In this ansatz, z_0 describes the longitudinal extent of the earliest thermalized volume (and is related to τ_f, the thermalization time), R_0 corresponds to the initial nuclear overlap radius and v_z^0 denotes the initial expansion velocity of the fireball. In the Bjorken expansion scenario, v_z^0 would be equal to $v_z(t_f)$, the longitudinal expansion speed at freeze-out, and in the Landau scenario it would be zero. For the time being, we leave v_z^0 as a free parameter. This ansatz allows for free streaming of matter ($\sim v_z^0 t$) in longitudinal direction as well as pressure-driven acceleration in both longitudinal and transverse direction. Note the absence of a term $v_\perp^0 \tau$ — the initial high-energy scattering processes favour forward scattering, therefore no significant initial free-streaming in radial direction is expected.

There is the possibility of accelerated motion in the ansatz, where the acceleration is given by a constant times the ratio of pressure over energy density. This can be motivated as follows: In a consistent hydrodynamical approach, $a = \frac{\nabla p}{\epsilon}$ would give the acceleration of a volume element. In our simplified framework, however, this expression makes no

sense, as we average out all pressure gradients inside the fireball. So one must think of a suitable averaging procedure in the presence of a pressure gradient. Consider the edge region ΔR of a fireball characterized by hydrodynamic evolution. The pressure gradient will be steeper than the gradient of the energy density, since the pressure is the driving force for the flow of energy density. So, ϵ can be assumed constant over the region ΔR where ∇p is large. Furthermore, both quantities can be written as $N(T) \cdot S(r)$, where N denotes the normalization and S describes the shape of the distribution in space (const. over ΔR for ϵ). The gradient acts on $S(r)$ only and results in some average acceleration of the edge region. As the fireball expands, the temperature drops, thus modifying $N(T)$ for both pressure and energy density. Assuming that the shape of the fireball edge does not change drastically, $a \sim p/\epsilon$ follows. This ansatz allows that the presence of a soft point in the EoS actually influences the evolution dynamics by reducing the acceleration near the phase transition.

Besides v_z^0, three more free parameters of the model remain: The freeze-out (proper) time t_f (τ_f) and the two constants giving the magnitude of the acceleration. On the other hand, from overlap calculations we know R_0 and from the analysis of the freeze-out state in section 5.2.6, we can derive

$$R(\tau_f) = R_f \,, \ \overline{v}_\perp(\tau_f) = \overline{v}_\perp^f \quad \text{and} \quad T(\tau_f) = T_f. \tag{5.25}$$

Once we specify an EoS and calculate thermodynamical properties, the three constraints uniquely determine the three remaining free parameters.

5.3.4 Thermodynamics

Specifying the volume expansion by inserting any trial ansatz for the ratio p/ϵ and the free parameters, we proceed by calculating the thermodynamic response of the temperature T to the changing volume $V(\tau)$. Key quantity here is the total entropy S_0 of the system, which is more commonly given in terms of the entropy per participant baryon s/ρ_B times the number of participants N_{part}.

The total entropy can be obtained by measuring charged particle multiplicities N^+ and N^- in suitable rapidity bins and calculating

$$D_Q = \frac{N^+ - N^-}{N^+ + N^-}. \tag{5.26}$$

The quantity D_Q stands for the inverse of the specific entropy s/ρ_B per net baryon, and the product $D_Q(s/\rho_B)$ roughly measures the entropy per pion [72]. For SPS collisions at 160 AGeV, we find $s/\rho_B = 26$ for central collisions.

Once S_0 is known, the entropy density inside the fireball can be obtained as

$$s(\tau) = S_0/V(\tau). \tag{5.27}$$

By inverting the EoS discussed in section 3.5 (Eq. (3.24)), which determines $s(T)$ (in general, this has to be done numerically), the temperature $T(\tau)$ at a given proper time can be calculated. Again, using the EoS (Eqs. (3.22) and (3.23)), $p(\tau)$ and $\epsilon(\tau)$ follow. Baryon density follows as $\rho_B = N_{part}/V(\tau)$ and the baryochemical potential $\mu_B(\tau)$ can be calculated using the relation:

$$\frac{V(\tau)}{(2\pi)^3} \int d^3p \frac{1}{\exp[(p_0 - \mu_B(\tau))/T] + 1} = N_{part}. \tag{5.28}$$

Having obtained all these quantities, we iterate the trial ansatz in order to obtain a self-consistent solution. It turns out that transverse dynamics can be determined from purely

kinematic constraints whereas v_0 mainly connects to the freeze-out temperature. The solution in terms of the temperature evolution in proper time can be found in Fig. 5.12. Key parameters are summarized in Tab. 5.2.
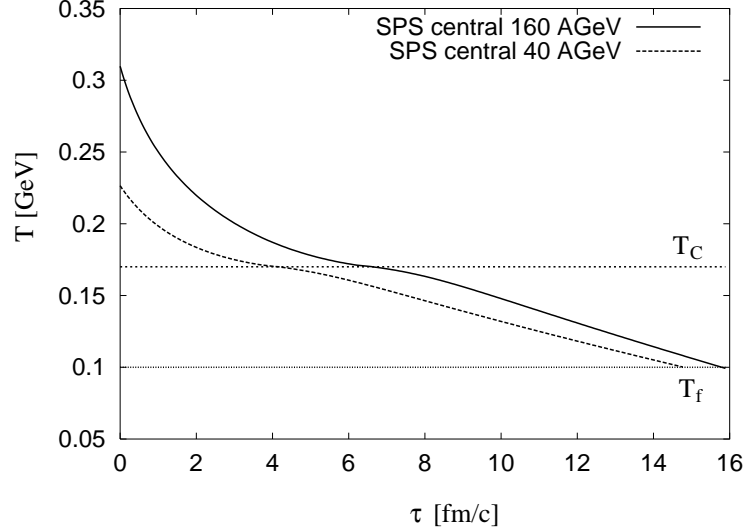

FIGURE 5.12: Temperature profile for the SPS 158 and 40 AGeV 5% most central Pb-Pb collision scenario.

One finds that the fireball starts out with a large initial temperature slightly above 300 MeV, expands in the QGP phase for about 7 fm/c and remains another 10 fm/c in the hadronic phase until kinetic freeze-out occurs at a temperature of 100 MeV. At first sight, both the large initial temperature and the long lifetime of the partonic phase appear surprising. Naive estimates of the initial temperature and the QGP lifetime based on the Bjorken scenario [73] give much smaller values. This discrepancy, however, has two main reasons. First, in this model we use a more realistic EoS of the QGP phase than that of an ideal gas, resulting in an enhancement of the initial temperature of $\sim 30\%$. Near the phase transition, s/T^3 in the realistic EoS is characterized by a massive reduction of active degrees of freedom as compared to an ideal gas. If the total entropy S_0 is kept constant, this implies that the cooling is delayed. In the scenario for SPS discussed here, this amounts to a partonic phase which lasts about a factor two longer than in the ideal gas case.

The second important difference is the presence of longitudinal acceleration. From the fit to the final state analysis, we find $v_0 = 0.45\,c$, apparently different from the flow velocity $v_z^f = 0.9\,c$ found in the analysis of the rapidity distribution of produced particles (see section 5.2.6), so necessarily longitudinal acceleration had to take place. In the Bjorken scenario, no longitudinal acceleration is present, therefore the mapping of final state rapidity distributions to initial state spatial distributions results in a larger initial volume than the one in our scenario. If we assume no or only small longitudinal acceleration in order to compare the two approaches, we find initial temperatures between 220 and 240 MeV, consistent with the Bjorken estimate. This initially smaller expansion speed also prohibits a fast cooling of the fireball and prolongs the partonic phase.

In the following, we will refer to the scenario discussed in this section as "standard scenario". It describes 5% most central Pb-Pb collisions at SPS for 158 AGeV beam energy and is based on the freeze-out analysis carried out in [60].

5.3.5 Longitudinal acceleration

The presence of longitudinal acceleration is not a big surprise if one considers the fireball evolution from an approach based on thermodynamics; if one thinks in terms of conventional multiparticle production mechanisms (like the Lund string model [49], the dual parton model [48] etc.), the mismatch between initial and final expansion velocity indeed contradicts the expectation. This raises the question whether longitudinal acceleration can be avoided in the thermal description in order to reconcile the two approaches.
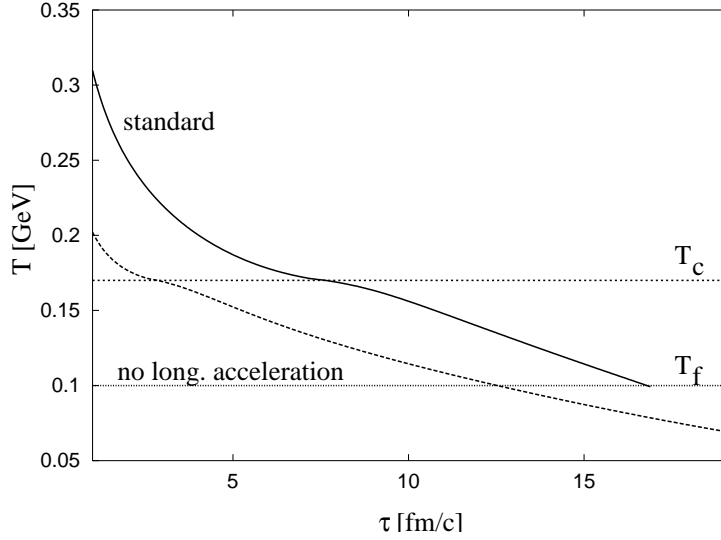
FIGURE 5.13: The difference between the standard scenario (solid) and one assuming no longitudinal acceleration (dashed).

Let us artificially remove the longitudinal acceleration term from the fit procedure while allowing for a different freeze-out temperature. This result is shown in Fig. 5.13. The emerging scenario is characterized by a faster volume expansion, resulting in a lower temperature at all times. Since this scenario starts out very close to the phase transition, the transverse acceleration is small for the initial times due to the soft point in the EoS and it takes comparatively long to built up the observed transverse flow and radius, resulting in a prolonged overall lifetime. The freeze-out temperature however is completely off — it is hard to have a thermal ensemble of even pions at such low temperature that describes the observed number, even if one introduces a pion chemical potential, as $\mu_\pi < m_\pi$ in order to avoid Bose-Einstein condensation which is certainly not observed (for a more detailed discussion of the pion number in the model, see chapter 6).

One might think of stopping the evolution as soon as the temperature drops below 100 MeV, but this is no way out — transverse flow and radius will be off, as they determine the endpoint in Fig. 5.13. In order to compensate, transverse acceleration must be increased, in turn resulting in an even faster drop of the temperature and a dramatically reduced lifetime. Additionally, the system of equations relating transverse acceleration $c_\perp$ and freeze-out proper time τ_f to radius and flow has a unique solution, so one cannot go away from the standard scenario without missing either the radius or the amount of flow. Only if a flow profile $v(r)$ is constructed in such a way as to meet the data on average flow and the radius, such an ansatz remains in agreement with the data.

Assuming such an alternative description could be found, the main differences between the standard scenario and the one without longitudinal acceleration were two: First, the partonic phase would be almost completely gone and secondly, the lifetime of the system

would be dramatically reduced. The latter one is a generic feature independent of thermalization: As the extension in z direction grows, the density of energy and particles drops accordingly, increasing the mean free path of particles inside the system. Thus, kinetic freeze-out will occur earlier.

Is there any way of distinguishing these two possibilities? Certainly, as already discussed in section 5.2.6, a small lifetime seems barely adequate to allow for the observed expansion of the source, but it cannot be ruled out. There are, however, observables different from the ones discussed so far, such as electromagnetic probes, which allow to study the entire expansion process of the system instead of only the freeze-out state. Their information on the question of longitudinal acceleration will be discussed later.

5.4 EXTENDING THE SCENARIO

So far, we have discussed the conditions of the 5% most central Pb-Pb collisions at SPS, 158 AGeV in our framework. The reason is that these are the only conditions under which we have a reliable analysis of the freeze-out state. A wealth of data has been taken, however, at different centralities and beam energies. In order to discuss these results as well, the standard scenario of fireball evolution must somehow be adapted to different beam energies, collision systems and centralities. This has to be done in such a way as to fit existing hadronic observables and to employ the relevant physics for the extrapolation of the model.

5.4.1 Variations in centrality

As for the modifications of the evolution dynamics induced by nonzero impact parameters, we benefit from the fact that the relevant physics is at least qualitatively known. Let us start discussing the most obvious changes with respect to central collisions.

First of all, the number of participant baryons will be reduced as the impact parameter increases. This can be taken into account within the framework of eikonal calculations as discussed in section 4.3.1. Along with this change, we find a reduction of the initial overlap area. Also the shape of the overlap region changes: The circular area transforms into an almond shaped one.

In principle, the expansion geometry is different if one starts from an almond shaped overlap area, leading to the phenomenon of elliptic flow. This difference, however, washes out after an evolution time of a few fm/c. Furthermore, global thermodynamics is only sensitive to the transverse area, not to its shape. This suggests that, in order to keep the model framework simple, one can ignore the complications of initial geometry and just parametrize the fireball as an expanding cylinder for any impact parameter. The alternative way, modifying the parametrization, would introduce more free parameters without actually increasing the predictive power of the model, therefore we will not pursue this approach further, keeping in mind that we expect the model to fail increasingly as we approach more and more peripheral collisions where these effects become important. Note that we expect this failure anyway at some impact parameter, as the limit for very peripheral collisions is p-p, which we hardly expect to be described by a thermal approach.

Assuming that the entropy per baryon is independent of the collision centrality, one is able to find the total entropy for the process from the number of participants.

For the final state, we assume that the freeze-out condition is still given by $T = T_f$, thus all radius and flow parameters have to be reduced accordingly. This makes sense, as it is

mainly the pion density which determines the mean free path inside the fireball and the geometrical dimensions of the system at freeze-out do not change drastically. We choose

$$v_\perp \to cv_\perp^c, \quad \Delta V = c\Delta v^c \quad \text{and} \quad R_f = c^2 R_f^c, \tag{5.29}$$

appropriate for an accelerated motion. Here the superscript c denotes the quantities in the central case, Δv represents the amount of velocity picked up by longitudinal acceleration and c is a free parameter.

In order to fix the new free parameter c, we have to impose one more condition on the system. We choose to fix v_z^0, the initial longitudinal velocity. This can be done, because we know both the limits of this quantity at central and most peripheral collisions. For $b = 0$, we have found $v_z^0 = 0.45$, whereas in p-p collisions, the rapidity loss of the bulk matter amounts to one unit, translating into $v_z^0 \approx 0.89$, thus the longitudinal acceleration vanishes completely as it should. We interpolate linearly between these two limits.

In principle, the thermalization time τ_0 should also be dependent on centrality, since p-p collisions never thermalize, indicating that the dropping energy density is insufficient to support a collision rate large enough to reach equilibrium. Unfortunately, there is no clean way to constrain this effect. Therefore, we will not try to determine the exact conditions under which equilibrium is reached but rather keep the value of τ_0 for all centralities, keeping in mind that additional errors (to the ones created by neglecting elliptic flow) are introduced in this way.

5.4.2 Results for different centrality

In Fig. 5.14, the resulting temperature evolution for different impact parameter b are shown for the SPS 158 AGeV scenario.
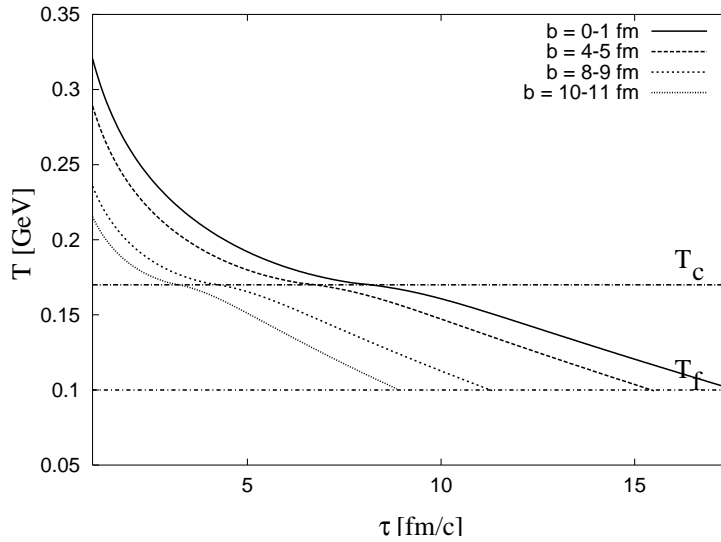

FIGURE 5.14: Temperature evolution for different impact parameters at 158 AGeV Pb-Pb collisions (model calculation).

As expected, the lifetime of the fireball and the initial temperature decrease with increasing b. For b between 10 and 11 fm, there is hardly any QGP phase left, however, it never seems to vanish completely. This is most likely a result of the simplified assumption $\tau_0 = 1$ fm/c for all impact parameters; if one would increase τ with b, the lifetime of the QGP phase would drop even further.

Both the lowering of the initial temperatures and the increased slope of the curves in the hadronic phase is mainly driven by the transition from significant rapidity loss of the produced matter in central collisions to small rapidity loss in peripheral collisions. The drop in total entropy is hardly sufficient to account for these effects, because the fireball volume drops also and the net effect is small.

No direct sign for a breakdown of the thermal model at any b is apparent from the curves. Obviously, comparison to observables is needed to obtain new information.

5.4.3 Variations in beam energy

The extension of the model to different beam energies poses a more difficult task. The reason is that the behaviour of the system changes not only quantitatively but qualitatively. At SPS conditions, the participant baryons are important, as their density is high, and the decay of their higher lying resonance states increases the number of pions populating the hadronic phase. When the participant baryons are distributed over larger and larger rapidity intervals, their role becomes less and less important. Thus one expects less overpopulation of the pion phase space in baryon-free regions and correspondingly a different EoS and different freeze-out conditions. This will be explored in more detail in chapter 6. For now, only the prescription needed to construct the model is given here. As we vary the beam energy from 40 (fixed target) to 200 AGeV (collider), we interpolate the EoS between the one taking into account pion overpopulation as observed at SPS and the one assuming no net baryon density. The freeze-out temperature is assumed to rise from 100 MeV (SPS) to 130 MeV (RHIC) accordingly in order to compensate for the reduced pion density. For the time being, these values can only be qualitative estimates, only a detailed freeze-out analysis for RHIC is sufficiently powerful to yield enough constraints for a quantitative description. Details of the modifications can be found in Tab. 5.1.

Apart from these qualitative changes, there are some quantitative issues as well. First data on hadronic observables for Au-Au collisions at RHIC at $\sqrt{s} = 130$ MeV have been analyzed.

Figure 5.15 shows the pseudorapidity η distribution of negatively charged hadrons h^- for a variety of collision centralities, as measured by the PHOBOS collaboration at RHIC for 130 AGeV Au-Au collisions [74]. Comparing with Fig. 5.2, we find again the same broad plateau in the distribution around midrapidity, although it is even more pronounced for at RHIC. The rapidity region in which the distribution is large has grown considerably ($\sim$ -4 to 4 at RHIC as compared to $\sim$ -1.5 to 1.5 at SPS, as well as the rapidity density of particles. This indicates that the overall entropy production is greatly enhanced and the fireball matter is indeed distributed across a larger volume, thus the density of net baryons is reduced correspondingly.

Figure 5.16 shows HBT correlation radii R_{out}, R_{side} and R_{long} as measured by the STAR collaboration [75] for 130 AGeV Au-Au collisions at RHIC using π^+ and π^- correlations. Comparing with Figs. 5.5, 5.6 and 5.7, no dramatic difference can be observed. In particular R_{side}, which measures the transverse geometry of the source remains in the order of 5 fm. This indicates that the transverse freeze-out geometry is hardly changed even for dramatically increased collision energies. About the same holds true for the behaviour of R_{out} which is sensitive to the radial expansion also, even if one considers the m_t dependence. Therefore one can conclude that the radial expansion $\overline{v}_\perp$ is also very similar to the SPS case.

For these reasons we keep the freeze-out radius R_f and the transverse expansion velocity $v_\perp^f$ approximately constant. The exact values of these parameters for different energies are shown in Tab. 5.1. As for the longitudinal dynamics, it turns out that for all measured
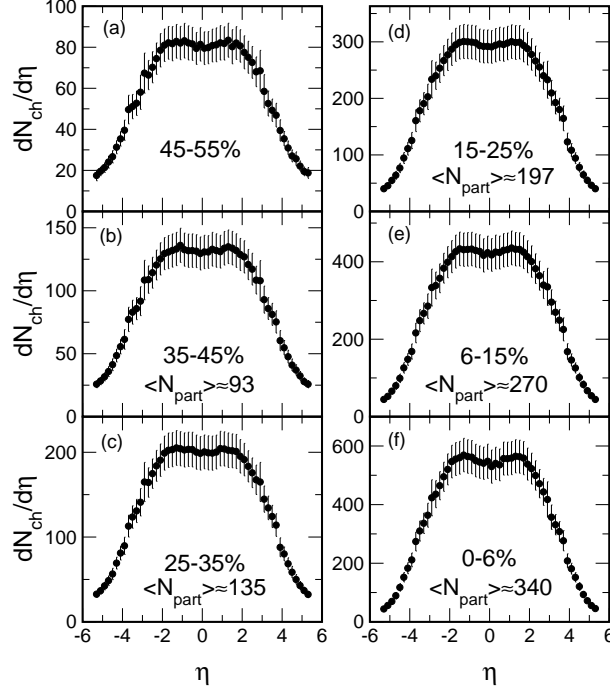
FIGURE 5.15: Pseudorapidity distributions of negatively charged particles h^- for different collision centralities as obtained by the PHOBOS collaboration at RHIC in 130 AGeV Au-Au collisions [74].

energies (SPS 40 AGeV and 158 AGeV, RHIC 130 AGeV and 200 AGeV) the edge of the h^- rapidity distribution is always about one unit of rapidity away from the kinematic limit. We make use of this in order to model the longitudinal freeze-out conditions. Following the same procedure as in the standard scenario, the initial longitudinal motion is then fit to the freeze-out temperature T_f.

The remaining task is to fix the entropy per participant baryon in order to provide the initial conditions for the thermodynamics. Assuming that the produced entropy scales with the number of produced particles, we use the result for SPS 158 AGeV as a baseline and scale everything else with the measured multiplicity of negatively charged hadrons. In the energy region between SPS and RHIC, we use a fit to the data of the form $N_{h^-} = a \cdot \ln(s) - b$ which gives a good description of the data to interpolate (see Fig. 5.17).

E_{beam}	E_{cm}	s/ρ_B	y_z^f	T_f	τ_f	$v_\perp^f$	R_f
40	8.76	10	2.86	100	1.5	0.33	7.1
158	17.38	26	3.55	100	1.0	0.53	8.55
500	30.67	39.15	4.12	110	0.9	0.54	8.87
1400	51.29	51	4.63	115	0.8	0.55	9.21
5500	101.29	67	5.31	120	0.7	0.55	9.21
	200	94	5.5	130	0.6	0.56	9.4

TABLE 5.1: Parameters of the extension of the fireball model towards different beam energies. Times are given in fm/c, length scales in fm and energies in AGeV.
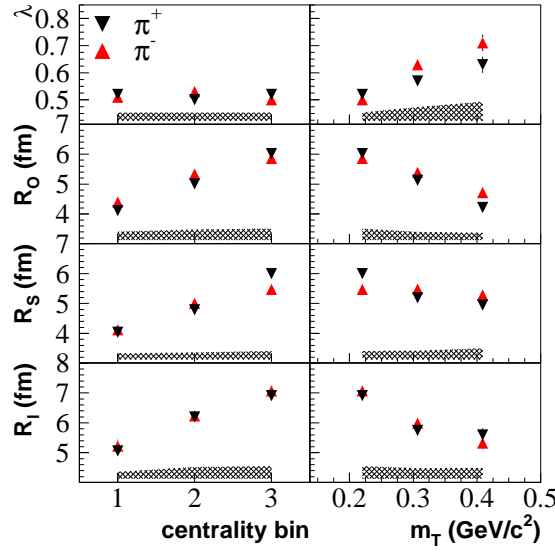
FIGURE 5.16: HBT correlation radii R_{long}, R_{out} and R_{side} (denoted here as R_l, R_o and R_s) for different centrality (left panel) and different transverse mass m_t (right panel) as obtained by the STAR collaboration at RHIC in 130 AGeV Au-Au collisions [75].

5.4.4 Results for different beam energy

The resulting fireball evolution temperatures for increasing beam energies are shown in Fig. 5.18.

Surprisingly, there is not much change for the whole range of beam energies under consideration, apart from the fact that the initial temperature seems to rise quite substantially towards ~ 400 MeV. The lifetime of the partonic medium and its relative contribution to the total lifetime change only moderately.

The reason for this lies in the experimental observation that transverse dynamics seems unchanged. This implies similar freeze-out proper times. Consequently, the growth of en-
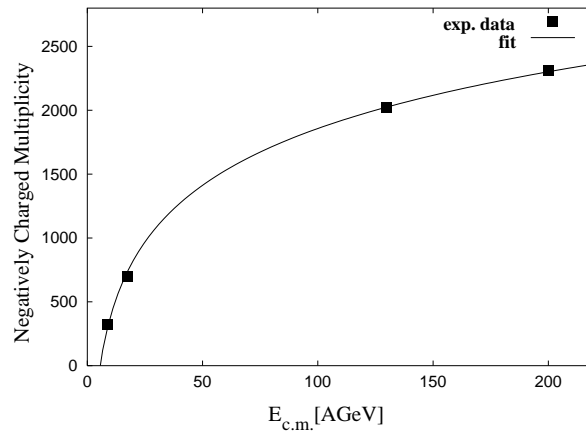
FIGURE 5.17: Logarithmic fit to measured total multiplicities.
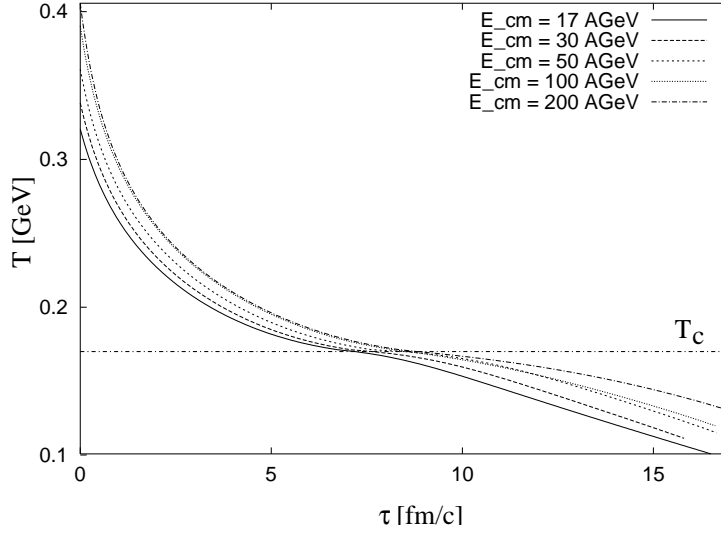
FIGURE 5.18: Temperature evolution for different $E_{c.m.}$ in Pb-Pb collisions (model calculation).

tropy with beam energy must be dominantly absorbed into longitudinal dynamics. Looking at the parameters (see Tab. 5.2), one indeed observes that the initial longitudinal motion grows, thus one finds less rapidity loss of the produced matter and the evolution dynamics approaches the Bjorken scenario, as appropriate for increasing energies. The entropy is distributed across a larger region in longitudinal direction and therefore the transverse dynamics is only weakly influenced.

Some important properties of the different fireball scenarios discussed in this chapter are summarized in Tab. 5.2.

$E_{c.m.}$	τ_0	τ_c	τ_f	R_f	$v_\perp^f$	v_0	v_z^f	s/ρ_B
9 AGeV	1.5	4.0	15.0	7.1	0.36	0.45	0.75	13
17 AGeV	1.0	6.5	16.0	8.55	0.53	0.45	0.9	26
30 AGeV	0.9	7.0	15.5	8.87	0.54	0.57	0.975	39
100 AGeV	0.7	8.0	16.0	9.21	0.55	0.65	0.997	67
200 AGeV	0.6	9.0	18.0	9.4	0.56	0.9	0.9985	95

TABLE 5.2: Key properties of the fireball evolution (for 5% most central collisions). Times are given in fm/c and length scales in fm.

Chapter 6

HADROCHEMISTRY AND CHEMICAL EQUILIBRIUM

In chapter 5, we outlined the construction of a model for the description of the thermalized fireball created in a heavy-ion collision. This model is based on a fit to a set of hadronic observables, specifically rapidity and transverse mass spectra and HBT correlations, and on information about thermodynamic properties of the QGP phase coming from lattice QCD calculations. We have used the total multiplicity of produced particles as an input for the total entropy, but no attempt was made to distinguish between different species of particles. In the present chapter, we will apply the commonly used statistical hadronization model to predict the relative abundancies of particles and compare to the experimentally observed ratios.

6.1 CHEMICAL EQUILIBRIUM AND STATISTICAL HADRONIZATION

6.1.1 Introduction

If a system of interacting particles is given enough time without a change in its boundary conditions, it will eventually reach equilibrium, i.e. particle populations n_i will be distributed according to the grand canonical ensemble

$$n_i = \frac{d_i}{2\pi^2} \int_0^\infty \frac{p^2 dp}{\exp\{[E_i(p) - \mu_i]/T\} \pm 1}. \tag{6.1}$$

Here, d_i denotes the degeneracy factor of particle species i (spin, isospin, particle / antiparticle) and the +(-) sign is used for fermions (bosons) and $E_i(p) = \sqrt{m_i^2 + p^2}$. In

the presence of conserved charges (e.g. baryon number), chemical potentials μ_i have to be introduced if the conservation on average is required (charges are allowed to propagate through the system), or the canonical ensemble has to be used if strictly local charge conservation is imposed.

The abundance of particles i is determined by its degeneracy factor d_i and by its mass entering E_i. This, however, holds only if the system was actually able to reach equilibrium. An expanding fireball, on the other hand, is a rapidly expanding system, governed by timescales of ~ 10 fm/c in the hadronic phase, so if the relaxation time of the system is comparable to this external scale, equilibrium cannot be maintained.

The elastic collision rate is responsible for the momentum distributions of each particle species (thermal equilibrium), but only inelastic collisions are able to change abundancies between different particle species (chemical equilibrium). It turns out that for most hadrons the thermally averaged elastic cross section is much larger than the inelastic one for temperatures characteristic for the hadronic phase, thus even if momentum spectra are thermalized (see section 5.2.2), this does not automatically imply equilibrium in particle abundancies [76–79].

The thermal relaxation time τ_i for particle species i is given by

$$\tau_i^{-1} = \sum_h \langle \sigma_{ih} v_{rel} \rangle \rho_h. \tag{6.2}$$

Here, the sum extends over all hadrons in the system, σ_{ih} denotes the cross section for a collision between species i and h, v_{rel} gives the velocity of the collision and ρ_h is the density of the hadronic medium. Standard resonance dominated processes (e.g. $\pi\pi \to \rho \to \pi\pi, \pi N \to \Delta \to \pi N \ldots$) lead to thermally averaged cross sections of $\langle \sigma \rangle \sim 50$ mb, which, for a (rather dilute) gas of normal nuclear matter density implies thermal equilibration times ~ 2 fm/c. On the other hand, for inelastic processes (like $\pi\pi \leftrightarrow K\overline{K}\ldots$) one finds typical thermally averaged cross sections of $\langle \sigma \rangle \sim 1$ mb, leading to equilibration times of ~ 100 fm/c, well above even the most optimistic estimates of fireball lifetimes (see [85] and references therein for numerical values of cross sections).

This fact has given rise to the picture of subsequent chemical and thermal freeze-out. It implies that, due to the large chemical relaxation time, the abundancies of particles are fixed for all but the most dense hadronic systems at or very near the hadronization temperature T_C. Thus, as the system cools off, only resonance decays are able to change the number of observed particles. Eventually, only particles with lifetimes larger than the fireball lifetime τ_f will be observed, their phase space density however will be significantly above the thermal expectation value.

Therefore, if one calculates the abundancies of particles at T_C and follows all the resonance decays until T_f, one should in principle find the measured particle abundancies.

6.1.2 Successes and caveats

The correct distribution of particle species at hadronization time is not known, given the limited knowledge of the de(confinement) / chiral transition. On the other hand, the number of hadrons in the system is large, and so one can expect to describe hadronization as a statistical process, which in turn leads to thermal distributions. Furthermore, if the quasiparticle description of the QGP (see chapter 3) is correct, there is more time for the equilibration of pre-hadronic clusters which then might be 'born' into equilibrium already.

Under the assumption that the distribution of hadrons at T_C can indeed be described by the grand canonical ensemble, final particle yields have been investigated using the temperature

T and μ_b as free parameters for a fit to experimentally observed particle ratios. This has been done successfully for a variety of collision energies from AGS up to RHIC [80–82]. The results can be seen in Figs. 6.1 and 6.2.
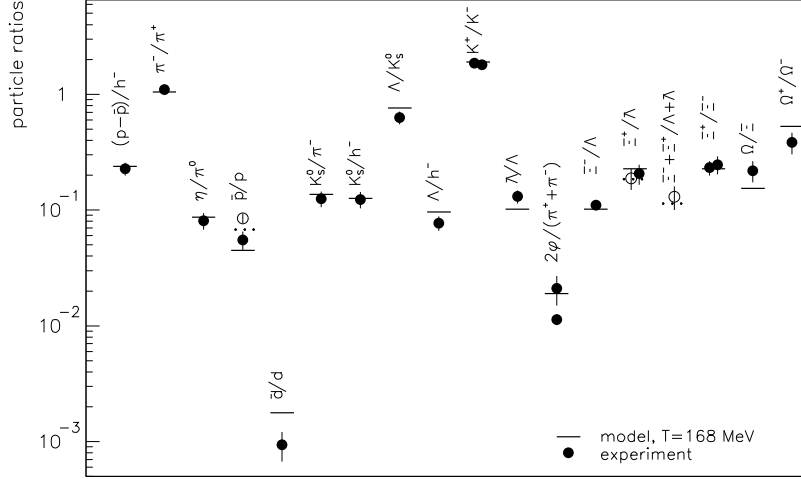

FIGURE 6.1: Statistical model fit to particle ratios as compared to experiment (see [81]) Here, T denotes the temperature at which the chemical freeze-out occurs.

From Fig. 6.2, it appears that for very dense hadronic systems (as created at SIS or AGS) there is still some degree of inelastic equilibration even deep in the hadronic phase whereas for the higher collision energies the parameters of the chemical freeze-out basically coincide with the phase boundary.

The apparent success of the statistical description of particle abundancies however hides one important fact: there is some evidence that particle properties, especially masses and widths, are substantially modified by the interaction with the medium whereas in statistical model calculations vacuum properties of particles are commonly used. Unfortunately, there is no way of assessing these properties reliably near the phase boundary due to the breakdown of perturbation theory. We will examine the sensitivity of the description to in-medium particle properties in more detail in section 6.3.3.

There are yet other questions concerning the statistical hadronization description: While for most hadronic scattering processes the inelastic cross section is small, this is clearly not so for some of them, especially the $p\overline{p}$ annihilation process which exhibits a thermally averaged cross section of ~ 50 mb (see [85] and [83]), enough of preventing the reaction from being 'frozen' from the beginning of the hadronic phase. On the other hand, the measured $p/\overline{p}$ ratio is nicely described by the statistical model fit for all energies, which is puzzling, as the fit reflects the distribution at a temperature different from T_f. An evaluation of the $p/\overline{p}$ ratio using the thermal freeze-out temperature T_f, however, leads to 50% disagreement to data.

This problem has been examined in greater detail in [83] within the framework of rate equations. The essential findings were that multi-pion fusion ($n\pi \rightarrow p\overline{p}$) is able to regenerate the $p/\overline{p}$ ratio, provided that there is a significant overpopulation of pion phase space, which enhances the fusion process. This overpopulation however is experimentally well
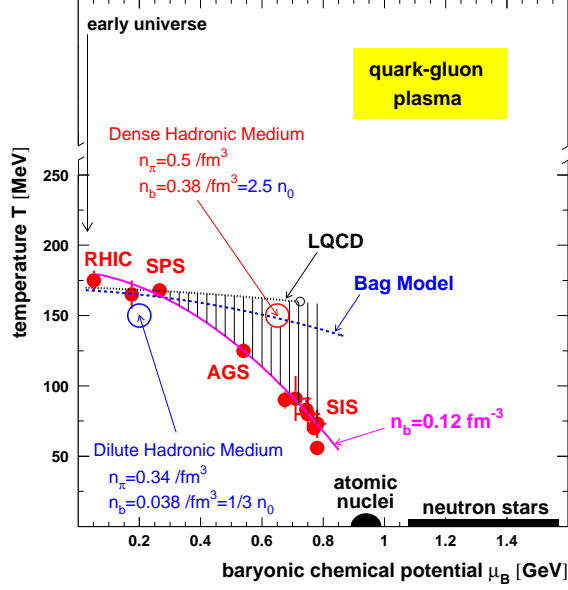
FIGURE 6.2: QCD phase diagram with chemical freeze-out line as extracted from statistical model fits (see [80–82]).

established and can be explained within the framework of statistical hadronization by the decay of resonances created at the phase transition.

6.2 THE MODEL

6.2.1 Basic equations

In order to predict hadronic multiplicities within our model of fireball evolution, we use the grand canonical ensemble

$$n_i = \frac{d_i}{2\pi^2} \int_0^\infty \frac{p^2 dp}{\exp\{[E_i(p) - \mu_i]/T_C\} \pm 1} \tag{6.3}$$

to calculate particle densities at the phase transition temperature T_C. The chemical potential for particle species i is linked to the particle's baryon number B_i and strangeness content S_i as

$$\mu_i = \mu_B B_i - \mu_S S_i. \tag{6.4}$$

We neglect isospin asymmetry (implying an additional chemical potential μ_I which has been found to be small in the fit procedures). Two important constraints link the volume with the chemical potentials: The net baryon number has to be equal to the number of participant baryons in the collision and the overall strangeness must be zero,

$$V \sum_i n_i B_i = Z + N, \qquad V \sum_i n_i S_i = 0. \tag{6.5}$$

In [80–82], the temperature T and baryochemical potential μ_B have been used as fit parameters, but since we possess a model of fireball evolution already, we are able to proceed without further free parameters and determine T and μ_B as follows: Assuming that

hadronization happens at T_C and that further inelastic interactions are negligible, we insert the volume $V(T_C)$ into Eq. (6.5) and calculate the baryochemical potential μ_B. Using μ_B, we can now calculate particle densities and iteratively adjust μ_S in order to fulfill Eq. (6.5). Analogous to previous calculations, we correct the result for the amount of volume which is excluded by the nonzero eigenvolume of the particles themselves, using a hard core radius of 0.3 fm for all mesons and baryons. This number is suggested by the hard core volume observed in nucleon-nucleon scattering experiments [84] and has been used in [81] also. Specifically, we calculate the absolute number N_i of particles i as

$$N_i = V_{eff} n_i \quad \text{with} \quad V_{eff} = V_0 - \sum_i N_i V_{ex}. \tag{6.6}$$

Here, V_0 is the volume of the fireball at chemical freeze-out and V_{ex} denotes the excluded volume of a single particle with radius R_{hc}. Again, this correction has to be applied iteratively in order to find a self-consistent result. This procedure enables us to predict absolute numbers of particles and resonances at the phase transition within our framework.

6.2.2 Resonance decays

We include all mesons and mesonic resonances up to masses of 1.5 GeV and all baryons and baryonic resonances up to masses of 2 GeV into the treatment. This amounts to 30 (strange and nonstrange) mesonic states and 36 (nonstrange to multistrange) baryonic states. In order to compare their experimental results, we calculate their decay into particles which are long-lived as compared to the fireball, such as $\pi, K, \eta, N, \Lambda, \Sigma$ and Ω.

All data on particles is taken from [85]. For many higher-lying states, the properties as well as the decay channels are poorly known. In these cases, we proceed as follows: If some quantity (e.g. mass, width...) is known only within a certain range, the arithmetic mean of this range is used in the model. Decay channels which are reported to be 'seen' are assumed to receive equal contributions from the branching ratio which is left after all known channels have been accounted for. Branching ratios less than 1% have been neglected. Decay chains (such as $a_2 \to \rho\pi \to \pi\pi\pi$) have been followed through. For resonances with large width, we integrate Eq. (6.3) over the mass range of the resonance using a Breit-Wigner distribution.

At first sight, one would expect that directly produced thermal pions contribute most to the observed particles, but quite the opposite is true. The density of resonances increases almost exponentially with mass, and so there are a lot of resonances contributing at masses above 1.5 GeV. Furthermore, these high-lying states are typically characterized by large spin and isospin degeneracy factors d_i, enhancing their contribution further. And as for their contribution to the finally observed particles, due to their large mass, they decay typically into four or more pions. These effects are only partially counterbalanced by the exponential suppression in the Fermi(Bose) weight. For example, the $\Delta(1232)$ comes with a degeneracy factor $d_{\Delta(1232)}$ of 32 (4 spin, 4 isospin, particle/antiparticle), whereas d_π is only 3 (isospin).

6.3 RESULTS

6.3.1 Standard scenario

The number of particles at thermal freeze-out has been calculated using the fireball scenario for central collisions at SPS with 158 AGeV beam energy. The resulting ratios are shown

in Fig. 6.3 along with the experimentally determined values of selected particle ratios [69, 70, 86–94].
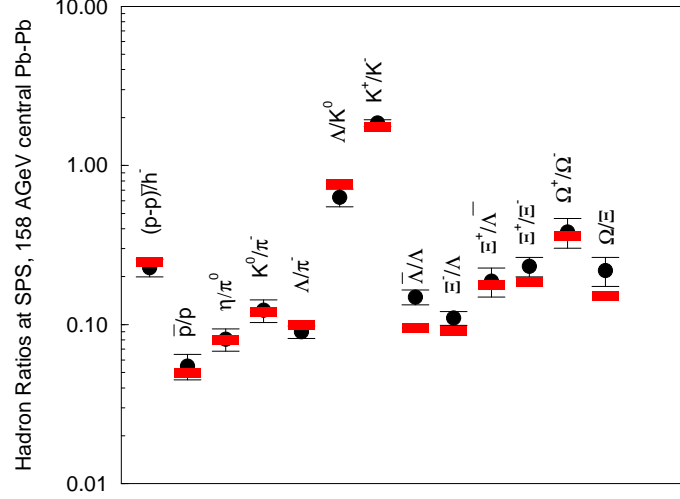

FIGURE 6.3: Results of the statistical hadronization model in the standard SPS fireball evolution for 158 AGeV collisions (dashes) as compared to data (filled circles) for a chemical freeze-out temperature $T_{ch} = 170$ MeV.

One observes that the description of the data is not perfect, but the overall trend is well reproduced. The most significant deviations concern the Λ hyperon. Note that the agreement to data is necessarily worse than in [81], as T and μ_B are not free parameters in the present calculation, but rather determined from Eq. (6.5) assuming the fireball evolution is known. Given the fact that there is still the possibility of (huge) in-medium modifications of particles, the agreement has to be considered as satisfactory. The detailed values are listed in Tab. 6.1, along with the experimental result.

The link between the fireball evolution and the statistical hadronization model is obviously given by the EoS and the total entropy content S_0 of the system, as those uniquely define $V(T_C)$. Therefore, the particle ratios are not suited to test dynamical properties of the fireball, such as τ_C or longitudinal vs. transverse expansion. The hadrochemistry is, however, a valid test for the endpoint at T_C of the EoS as determined in the quasiparticle model coming from the high temperature regime. It is also a test for the extraction of s/B from the multiplicity data, and for the hypothesis that entropy is conserved during the expansion in at least the hadronic phase.

It has been argued that the statistical distribution of particles is no indication for a thermalized system at all, as it is also able to describe the particle yield from e^+e^- annihilation [95] or p-p (p-$\overline{p}$)-collisions [96], which are by no means thermalized systems. There is, however, one important difference. In the description of e^+e^- reactions, the canonical ensemble has to be used, whereas for the description of heavy-ion data the grand canonical ensemble is appropriate, indicating that strangeness can propagate freely over large distances inside the fireball [97].

6.3.2 Late chemical freeze-out

Looking at Fig. 6.2, one could argue that the chemical freeze-out might occur slightly after the phase transition. In order to test this conjecture, we have calculated particle ratios

with the same formalism as introduced above, but selected a different chemical freeze-out temperature T_{ch} and a correspondingly different volume $V(T_{ch})$. The result is summarized in Fig. 6.4.
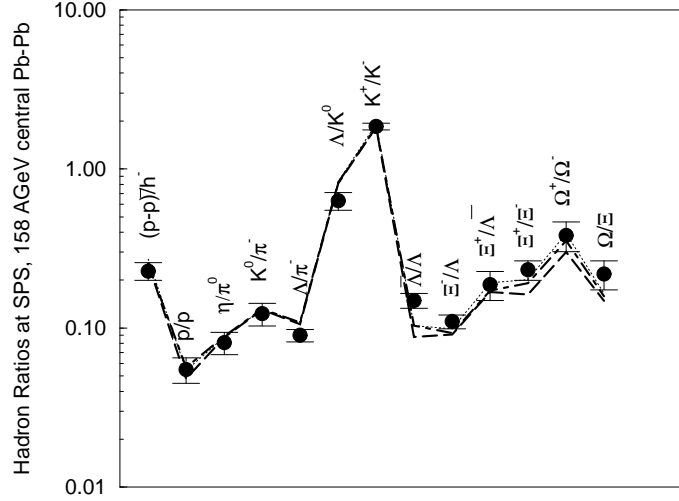

FIGURE 6.4: Hadron ratios for different chemical freeze-out temperatures $T_{ch} = 170$ MeV (thin dotted) 165 MeV (dash-dotted) and 160 MeV (solid) for SPS, 158 AGeV Pb-Pb collisions.

One observes that the overall impact of the variation of T_{ch} is small. The $(p - \overline{p})/h^-$ ratio improves slightly if the temperature is lowered. This is caused by the larger volume corresponding to $T = 165$ MeV in the fireball evolution model, which in turn enhances the direct production of light mesons, as these are not suppressed by a Bose factor. On the other hand, once the temperature drops to 160 MeV and below, the description of multi-strange particle ratios gets increasingly worse, as these are heavy states and suffer considerably from the suppression in their Fermi distribution functions.

In conclusion, it appears that a chemical freeze-out temperature T_{ch} between 170 and 160 MeV is favoured, but this is only a qualitative statement. Once T_{ch} differs from T_C there would be different chemical freeze-out temperatures for all particle species, as determined by their participation in inelastic reactions. One can therefore not assign a strong quantitative significance to a universal chemical freeze-out temperature T_{ch}.

6.3.3 In-medium modifications

Large uncertainties are attached to possible in-medium modifications of particle properties. In an approach where free parameters are fitted to the data, part (or all) of the induced changes may be absorbed in a refit of the parameters, but given the tight constraints of the present approach, the direct impact of such modifications on the particle abundancies can be observed.

In order to roughly quantify these effects, we allow for both mass shifts and broadening of the particles due to in-medium effects at T_C (from either finite temperature or due to finite density effects).

In many model calculations, hadron masses decrease as the chiral transition is approached. We have tested the consequences of reducing particle masses by 10 and 20% (note that this

is only a qualitative estimate, since a mass reduction without broadening is unrealistic). The mass of the pion has been left unchanged because of its Goldstone boson nature. The resulting particle abundancies are shown in Fig. 6.5.
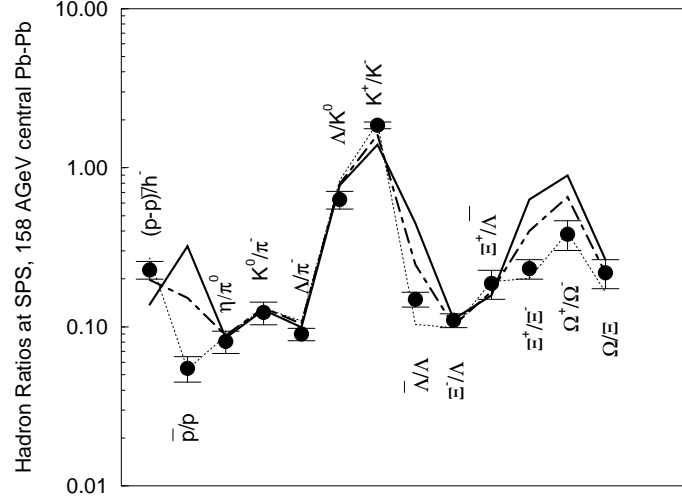

FIGURE 6.5: Hadron ratios for different in-medium mass reductions at SPS, 158 AGeV Pb-Pb collisions, shown are vacuum mass (thin dotted) reduction by 10 (dash-dotted) and 20% (solid).

The induced changes show up most prominently in the $\overline{p}/p$ ratio. This, however, is a weak constraint, as this ratio is likely to be adjusted dynamically by multi-pion fusion processes during the hadronic evolution phase. There are, however, strong deviations from the measured ratios in the multi-strange sector also which are not so easily disregarded. Obviously, a strong reduction of particle masses in medium alone is incompatible with the presented fireball evolution scenario and the data.

In the next run, we increased the width of all particles by 20 and 50%. The results are shown in Fig. 6.6. The results are similar as in the case of mass shifts, though not as pronounced, and all ratios except $\overline{p}/p$ still agree with the data. This is not surprising, as an increase of the particle width cannot get as much strength into the lower mass region favoured by the Fermi (Bose) distribution as a direct mass shift. Nevertheless, the result is reassuring as increases in width are almost certain to show up in the medium due to the opening of new interaction channels, not present in the vacuum.

There is one more possibility that needs to be explored. The failure of the mass-shifted scenarios to account for the data can be understood as follows: A decrease of masses enhances overall particle production, therefore less baryochemical potential μ_B is needed to account for the number of net nucleons. This has a direct impact on the $\overline{p}/p$ ratio and indirectly influences also the strange chemical potential μ_s via single strange particles. In the medium, however, particles are likely to be more loosely bound, and so their radius may increase, reflecting in a larger excluded volume correction. This, in turn, reduces particle production again and implies a larger value of μ_B which in turn influences μ_s. Therefore, the effects of decreasing particle masses and/or increasing widths might be partially compensated by an increase of particle radii. We investigate the sensitivity of all results to different hard core radii ranging from 0.225 fm/c to 0.375 fm/c in Fig. 6.7. Note that this corresponds to a variation in the excluded volume correction of a factor ~ 4.6. The resulting effects are rather weak.
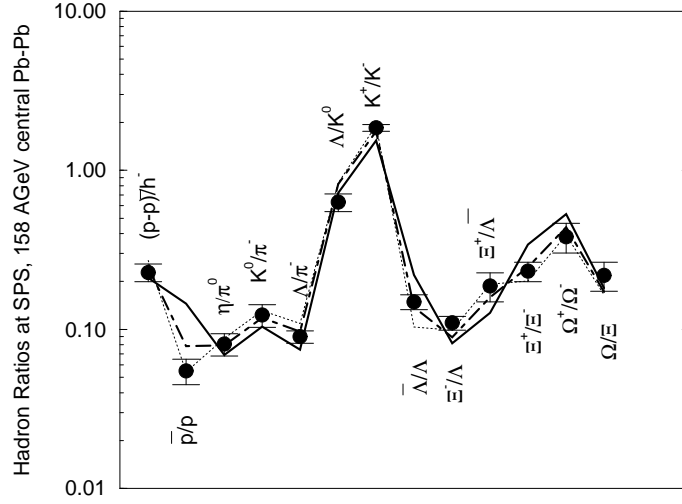
FIGURE 6.6: Hadron ratios for different in-medium width increase at SPS, 158 AGeV Pb-Pb collisions, shown are vacuum width (thin dotted) increase by 20 (dash-dotted) and 50% (solid) and measured ratios (filled circles).
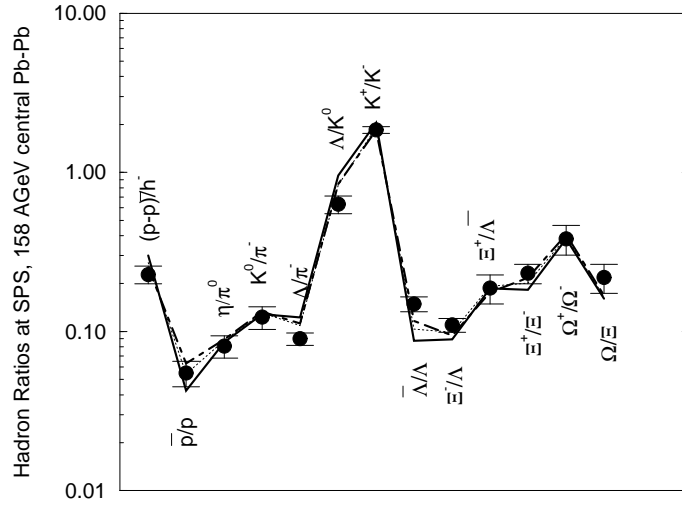

FIGURE 6.7: Hadron ratios with hard core radius 0.3 fm (thin dotted), decreased to 0.225 fm (dash-dotted) and increased to 0.375 fm (solid) compared to measured ratios at SPS for 158 AGeV Pb-Pb collisions (filled circles).

The partial compensation of modifications is demonstrated in Fig. 6.8, where we present the result for a simultaneous increase of particle width and radius by 50%. One indeed observes the expected behaviour — the key ratio $\bar{p}/p$ improves significantly and so do, to a lesser degree, the multistrange ratios. An in-medium modification which, at last qualitatively, counterbalances the effect of broadening or mass shifts is obviously interesting. It allows the statistical hadronization model to persist even in the presence of nontrivial physics inside hadronic matter. To make these statements more precise at a quantitative level is a major challenge.
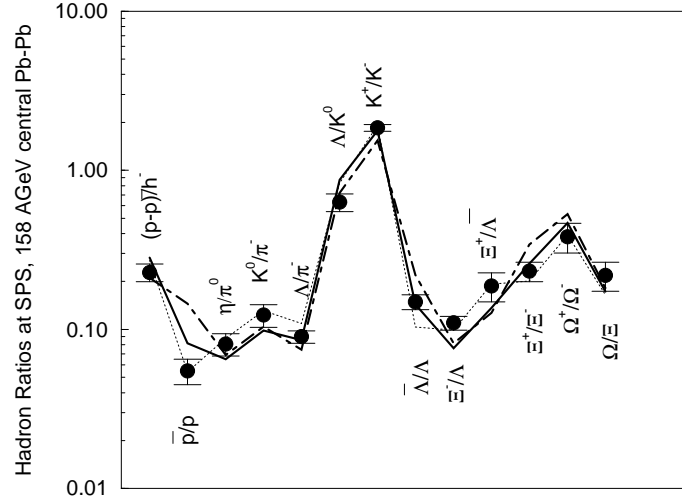
FIGURE 6.8: Hadron ratios for in medium width increase by 50%, with hard core radius increased from 0.3 fm (dash-dotted) to 0.45 fm (solid) compared to measured ratios at SPS for 158 AGeV Pb-Pb collisions (filled circles).

What, then, can be learned from the hadrochemistry? One finds agreement with the data, at least qualitatively, if moderate changes are introduced in either the fireball evolution (in terms of the EoS and s/ρ_B) or the in-medium properties of particles. But the model cannot accommodate drastic changes of e.g. the fireball volume or the total entropy by a factor ~ 2, or mass shifts of 50%. One can conclude that the standard fireball scenario for SPS Pb-Pb collisions at 158 AGeV constructed in chapter 5 is certainly within the correct range of parameters.

Particles	prediction	experiment
$(p - \overline{p})/h^-$	0.27	0.228(29)
$\overline{p}/p$	0.054	0.055(10)
η/π^0	0.088	0.081(13)
K_s^0/π^-	0.131	0.125(19)
Λ/h^-	0.108	0.077(11)
Λ/K_s^0	0.98	0.63(8)
K^+/K^-	1.91	1.85(9)
$\overline{\Lambda}/\Lambda$	0.103	0.131
Ξ^-/Λ	0.092	0.110(10)
$\Xi^+/\overline{\Lambda}$	0.180	0.188(39)
Ξ^+/Ξ^-	0.201	0.232(33)
Ω^+/Ω^-	0.392	0.383(81)
Ω/Ξ	0.165	0.219(45)

TABLE 6.1: Statistical model predictions for SPS 158 AGeV Pb-Pb collisions using the standard fireball evolution scenario vs. experimental data on particle ratios.

6.4 HADRON RATIOS AT RHIC

Particle ratios have also been measured at RHIC for 130 AGeV collisions at midrapidity. This presents the first challenge for the evolution scenarios which have been extrapolated towards higher collision energies. Using the $V(T_C)$ for the 130 AGeV scenario at RHIC, one can predict the total particle yields. The result is shown in Fig. 6.9 (stars).
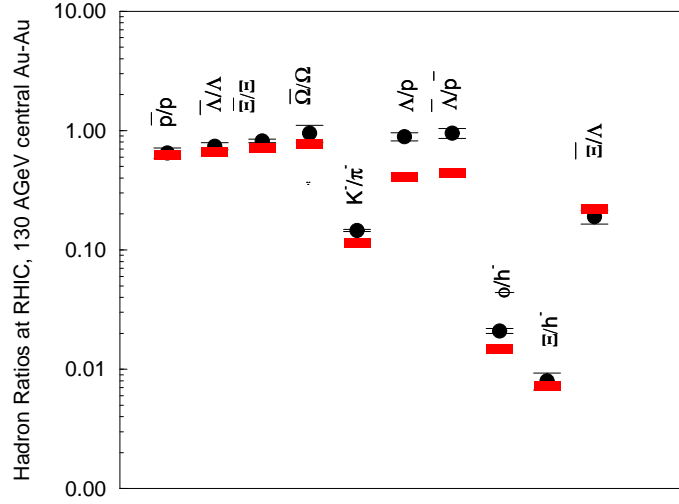

FIGURE 6.9: Hadron ratio predictions from the statistical hadronization model for midrapidity yield (dashes) as compared to experimental data. (filled circles).

If applied naively the same way as at SPS, the model fails badly for some of the ratios (taken at midrapidity) (including $\overline{p}/p$ and multistrange, which appear to be the most sensitive ones). The reason for this failure becomes only apparent if one takes a closer look at the rapidity distributions of net baryons [98] and produced particles (entropy) (see Fig. 5.15). Here one finds that the rapidity distribution of entropy follows a broad plateau shape, whereas there is a significant depletion of net baryons at midrapidity. If one wants to compare to experimental data (taken at midrapidity) [99–104], one should therefore not use the average entropy per baryon of 75, which can be calculated for the whole fireball, but rather the larger value of 220 which reflects the conditions at midrapidity. If this is done, the agreement with experiment is achieved as apparent from Fig. 6.9. This is the first indication that a suitable fireball model for RHIC has to reflect the qualitatively different conditions at different rapidity regions caused by the non-uniform distribution of net baryon number.

Chapter 7

DILEPTONS -
A VIEW INTO THE FIREBALL CORE

So far, we have only discussed observables which reflect only a certain moment of the fireball evolution; i.e. momentum spectra for the kinetic freeze-out and particle abundancies for the chemical freeze-out. A considerably harder challenge to the model is posed by observables which probe the whole time evolution. This is due to two reasons: First, they are sensitive to the magnitude of the four-volume in spacetime that is occupied by the evolution, i.e. a faster expansion implies less occupation of four-volume and therefore less overall magnitude of the signal. Second, these observables may display qualitative differences between early and late evolution stages.

Dileptons (e^+e^- and $\mu^+\mu^-$ pairs) are interesting probes in this context since they do not interact strongly and escape unthermalized from the hot region at all stages of the collision. Therefore, in contrast to hadronic probes, dileptons carry information also on the early moments of the collision where the QGP phase is expected to exist. In the QGP phase, dileptons originate mainly from $q\bar{q}$ annihilation processes, whereas in the hadronic phase the main sources are pion and kaon annihilation processes which are enhanced due to the formation of the light vector mesons ρ, ω and ϕ. In order to interpret signals from the QGP, one must obviously first understand the hadronic phase.

7.1   DILEPTONS FROM A FIREBALL

The lepton pair emission rate from a hot domain populated by particles in thermal equilibrium at temperature T is proportional to the imaginary part of the spin-averaged, photon self-energy, with these particles as intermediate states. This can be understood cutting relevant Feynman diagram Fig. 7.1.
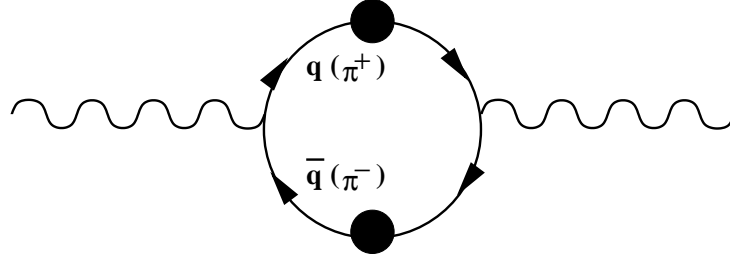
FIGURE 7.1: The Feynman diagram corresponding to the self-energy of a virtual photon in a strongly interacting thermal medium. The filled circles indicate full in-medium propagators of the particles coupling to the photon.

The cut diagram corresponds to a process where two particles from the heat bath annihilate to create a virtual photon (which can then decay into a lepton pair). If the intermediate particles are quarks, the process is to lowest order just $q\bar{q}$- annihilation where the thermal distribution functions of the quarks have to be added to the quark lines. Cutting the full in-medium propagator ensures that the complete dynamics of the medium is taken into account. It contains all possible processes (e.g. $q\bar{q}$- annihilation with bremsstrahlung, thermal self-energy insertions etc.).

The differential pair production rate is then given by

$$\frac{dN}{d^4x d^4q} = \frac{\alpha^2}{\pi^3 q^2} \frac{1}{e^{\beta q^0}-1} \operatorname{Im}\bar{\Pi}(q,T) = \frac{\alpha^2}{12\pi^4} \frac{R(q,T)}{e^{\beta q^0}-1}, \tag{7.1}$$

where $\alpha = e^2/4\pi$, $\beta = 1/T$, and we have neglected the lepton masses. We have defined $\bar{\Pi}(q) = -\Pi^\mu_\mu/3$ and introduce the averaged photon spectral function $R(q,T) = (12\pi/q^2) \operatorname{Im}\bar{\Pi}(q,T)$. Here Π^μ_μ denotes the trace over the thermal photon self-energy which is equivalent to the thermal current-current correlation function

$$\Pi_{\mu\nu}(q,T) = i \int d^4x \, e^{iqx} \langle \mathcal{T} j_\mu(x) j_\nu(0) \rangle_\beta, \tag{7.2}$$

where j_μ is the electromagnetic current. Eq.(7.1) is valid to order α in the electromagnetic interaction and to all orders in the strong interaction. (For a derivation of these relations see appendix C.)

The differential rate of Eq.(7.1) can be integrated over the space-time history of the collision using the fireball evolution model introduced in chapter 5 to compare the calculated dilepton rates with the CERES/NA45 data [105] taken in Pb-Au collisions at 158 AGeV (corresponding to a c.m. energy of $\sqrt{s} \sim 17$ AGeV) and 40 AGeV ($\sqrt{s} \sim 8$ AGeV). The CERES experiment is a fixed-target experiment. In the lab frame, the CERES detector covers the limited rapidity interval $\eta = 2.1 - 2.65$, *i.e.* $\Delta\eta = 0.55$. We integrate the calculated rates over the transverse momentum p_T and average over η, given that $d^4p = M p_T \, dM \, d\eta \, dp_T \, d\theta$. The formula for the space-time- and p-integrated dilepton rates hence becomes

$$\frac{d^2N}{dM d\eta} = \frac{2\pi M}{\Delta\eta} \int_0^{\tau_f} d\tau \int d\eta \, V(\eta, T(\tau)) \int_0^\infty dp_T \, p_T \, \frac{dN(T(\tau), M, \eta, p_T)}{d^4x d^4p} \, Acc(M, \eta, p_T), \tag{7.3}$$

where τ_f is the freeze-out proper time of the collision, $V(\eta, T(\tau))$ describes the proper time evolution of the fireball and its rapidity distribution and the function $Acc(M, \eta, p_T)$ accounts for the experimental acceptance cuts specific to the detector. At the CERES experiment, each electron/positron track is required to have a transverse momentum $p_T > 0.2$

GeV, to fall into the rapidity interval $2.1 < \eta < 2.65$ in the lab frame and to have a pair opening angle $\Theta_{ee} > 35$ mrad. Eq.(7.3) is then convoluted with the finite energy resolution of the detector. Finally, for comparison with the CERES data, the resulting rate is divided by $dN_{ch}/d\eta$, the rapidity density of charged particles.

RHIC operates as a collider experiment, so in this case the fireball is centered around $\eta = 0$. Here, the PHENIX detector acceptance can be schematically modelled by requiring that each electron/positron track falls in the rapidity interval $-0.35 < \eta < 0.35$, has transverse momentum $p_T > 0.2$ GeV and a pair opening angle of $\Theta_{e\bar{e}} > 35$ mrad.

7.2 CALCULATION OF THE PHOTON SPECTRAL FUNCTION

There are three main ingredients for Eq. (7.3): The spacetime evolution of the fireball (which has been discussed in chapter 5, the detector acceptance which has been addressed in the previous section and the photon spectral function $R(q,T)$. In this section, we will proceed by calculating $R(q,T)$ using methods of thermal field theory for finite temperature T and baryochemical potential μ_B, using the appropriate degrees of freedom above and below the phase transition temperature T_C.

7.2.1 The quark-gluon phase

As long as the thermodynamically active degrees of freedom are quarks and gluons, the timelike photon dominantly couples to the continuum of thermally excited $q\bar{q}$ states and subsequently converts into a charged lepton pair. The calculation of the photon spectral function at the one-loop level is performed using standard thermal field theory methods. The well-known leading-order result for bare quarks and gluons as degrees of freedom is:

$$\mathrm{Im}\overline{\overline{\Pi}}(q^0, \mathbf{q}, T) = -\frac{q^2}{12\pi} \cdot 3 \sum_{f=u,d,s} \theta(q^2 - 4m_f^2) e_f^2 \left(1 + \frac{2m_f^2}{q^2}\right) \sqrt{1 - \frac{4m_f^2}{q^2}}$$

$$\times \left(1 + 2\left[\frac{T}{|\mathbf{q}|} \frac{1}{\sqrt{1 - \frac{4m_f^2}{q^2}}} \ln\left(\frac{f_D\left(\frac{q_0}{2} - \frac{|\mathbf{q}|}{2}\sqrt{1 - \frac{4m_f^2}{q^2}}\right)}{f_D\left(\frac{q_0}{2} + \frac{|\mathbf{q}|}{2}\sqrt{1 - \frac{4m_f^2}{q^2}}\right)}\right) - 1\right]\right),$$

(7.4)

where $q = (q^0, \mathbf{q})$ is the four-momentum of the virtual photon, e_f the quark electric charge and m_f the quark mass of flavour f. This result, however, holds only up to perturbative higher order corrections in g_s that take into account collective plasma effects. Here, contributions from soft gluons lead to strong modifications. The corresponding two- and three-loop contributions show no clear convergence [106, 107]. Close to the phase transition, we also expect non-perturbative confinement physics to enter. Consequently, we follow a different approach.

Recalling the results of chapter 3, the thermodynamic properties of the QGP as given by lattice QCD are well reproduced by a gas of quasiparticles. Let us now assume that a quark quasiparticle couples to a photon in the same way as a bare quark (a form factor representing the 'cloud' of the quasiparticle could in principle also be included, but in absence of information about the detailed quasiparticle structure we ignore this point). For a gas of non-interacting quasiparticles, the one-loop result for $\mathrm{Im}\overline{\overline{\Pi}}$ is adequate, with

input properly adjusted. All higher order QCD effects manifest in the thermal quasiparticle masses $m(T)$, the function $B(T)$ and the confinement factor $C(T)$. Incorporation of the first two features in the calculation is straightforward. The bare quark masses in Eq. (7.4) simply have to be replaced by the T-dependent quasiparticle masses for each flavour. The thermal vacuum energy $B(T)$ does not contribute to the dilepton rate.

The naive replacement $f_D \to C(T)f_D$ is, however, not permitted in Eq. (7.4). Since any modification of the free particle distribution functions leads to non-equilibrium field theory, products of delta functions (pinch singularities) may arise in loop calculations. Therefore, the quasiparticle model as it stands cannot be used in expressions derived from simple perturbative thermal field theory. Recalling the physical interpretation of the confinement factor $C(T)$, we can use the expression for the dilepton rate, Eq. (7.1), instead. The mechanism for dilepton production at tree-level is the annihilation of a $q\overline{q}$ pair into a virtual photon where the quark lines are multiplied by the distributions $f_D(T)$, giving the probability of finding a quark or an antiquark in the hot medium. This also becomes clear when we look at the limit $\mathbf{q} \to 0$ of Eq. (7.4). Then,

$$\mathrm{Im}\overline{\overline{\Pi}}(q^0, T) \sim \mathrm{Im}\overline{\overline{\Pi}}(q^0, T = 0) \cdot (1 - 2f_D(q^0/2)), \tag{7.5}$$

and the temperature enters only in the Pauli-blocking of the quarks propagating in the loop. Now, from Eq. (7.1)

$$\frac{dN}{d^4x d^4q} \sim f_B(q^0)\mathrm{Im}\overline{\Pi}(q, T). \tag{7.6}$$

Combining the different thermal occupation factors, we end up with the well-known result

$$\frac{dN}{d^4x d^4q} \sim \left[f_D(q^0/2)\right]^2, \tag{7.7}$$

so the differential dilepton rate is proportional to the probability of finding a quark q times the probability of finding an antiquark $\bar{q}$ with the correct momentum, as anticipated [1]. The incorporation of the confinement factor is now obvious: since it reduces the number of thermally active degrees of freedom, it also reduces the dilepton rate by a factor of $C(T)^2$.

In summary, Eq. (7.1) can be used to calculate the dilepton rate originating from a hot QGP phase in the framework of the quasiparticle model, provided an overall factor $C(T)^2$ is applied to account for the reduced probabilities, and the bare masses m_f in the one-loop expression (7.4) are replaced by the T-dependent thermal masses. The rôle of the factor $C(T)$ is illustrated in Fig. 7.2, where the differential dilepton rate originating from a hot QGP in the quasiparticle approach is shown for different temperatures. Note that the plotted quantity is independent of the fireball volume, so the resulting differences are only due to the dropping quasiparticle masses and the squared confinement factor $C(T)$, which is responsible for a decrease by more than an order of magnitude at $T \sim T_C$ as compared to the highest temperature shown. One also observes that, as expected, the (negative) slope of the production rate in the region of high invariant mass gets steeper as the temperature decreases. It is important to note that this setup neglects contributions from hadronic degrees of freedom above T_C. As mentioned, quarks and gluons become clustered into hadrons (glueballs, mesons) as the temperature approaches T_C from above. These hadronic excitations are comparatively heavy and thus do not contribute much to the thermodynamics. Since we do not know in detail how the statistical re-arrangement of degrees of freedom occurs, we refrain from including these hadronic sources of dilepton yield above T_C. Our calculation is therefore expected to give a *lower limit* on the leptonic radiation from the QGP phase.

---

[1] We neglect a possible chemical potential μ_B for the quarks. For a finite μ_B, the corresponding expression would be $\frac{dN}{d^4x d^4q} \sim f_D((q^0 - \mu_B)/2)f_D((q^0 + \mu_B)/2)$.
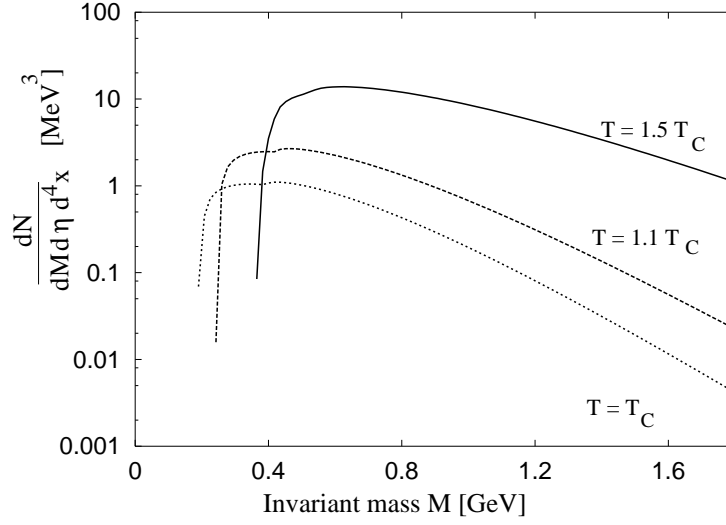
FIGURE 7.2: Dilepton rates originating from the QGP phase in the quasiparticle model for different temperatures.

The quasiparticle model does not take into account collective plasma modes, such as the (longitudinal) gluonic plasmons and the (helicity-flipped) quark plasminos [108]. Since their residues are exponentially suppressed in the HTL approximation for thermal momenta $k \sim T$, their contributions to the thermodynamical quantities are negligible. However, in the case of soft dilepton production it is well known that these modes lead to sharp, distinct structures in the spectrum, referred to as Van Hove singularities [109]. The plasmino branch has a minimum in its dispersion relation at $k \neq 0$ (which follows on very general grounds [110], independent of the HTL approximation). This leads to a diverging density of states which, in turn, shows up in the dilepton spectrum as a pronounced peak. Our model cannot exhibit, by construction, such plasmino effects. However, since the peaks are roughly located at $\simeq 2m_q(T)$, where $m_q(T)$ is the thermal mass of the quasiparticles, these Van Hove singularities would be smeared out by the fireball evolution. The thermal mass drops as the temperature goes down, dragging along the peak position with it. Furthermore, since $m_q(T)$ is of the order of the temperature T or smaller in our model, the singularities appear at low invariant mass (< 500 MeV) where they are overwhelmed by the hadronic part of the dilepton production. Therefore the presence of these collective modes would presumably not influence our results for the dilepton rate in the QGP phase.

We compare out model of the QGP phase also with a recent lattice calculation [111] of thermal vector meson correlation functions above T_C in quenched QCD with Clover improved Wilson fermions. Using the maximum entropy method, the vector spectral function was extracted from the corresponding current correlator. Although the statistical uncertainties are still considerable, it is interesting to note that the resulting spectrum resembles the free spectral function, as in our case, and has a gap at low energies given by a thermal mass threshold of $(2 - 3)T$, which is indeed close to $2m_q(T)$, the natural cut-off of the spectrum and, correspondingly, of the thermal dilepton radiation in the confinement model (see Figs. 7.2 and Fig. 7.3). Furthermore, this result seems to rule out heavy quark quasiparticles in the deconfined phase, as predicted by other phenomenological models [34, 112]. Of course, higher statistics and improved actions are mandatory to confirm these observations.
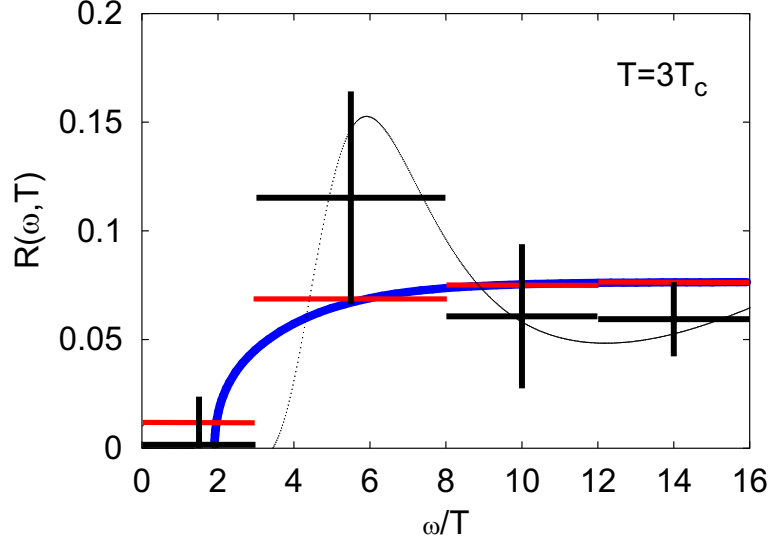
FIGURE 7.3: Photon spectral function as obtained in lattice calculations (crosses) [111] as compared to the one obtained within the quasiparticle picture (solid line) and binned as the lattice data (dashes).

7.2.2 The hadronic phase

Below T_C, confinement sets in and the effective degrees of freedom change to colour singlet, bound $q\bar{q}$ or qqq ($\bar{q}\bar{q}\bar{q}$) states. The photon couples now to the lowest-lying 'dipole' excitations of the vacuum, the hadronic $J^P = 1^-$ states: the ρ, ω and ϕ mesons and multi-pion states carrying the same quantum numbers. The electromagnetic current-current correlation function can be connected to the currents generated by these mesons using an effective Lagrangian which approximates the $SU(3)$ flavour sector of QCD at low energies. The appropriate model for our purposes is the *improved Vector Meson Dominance* model combined with chiral dynamics of pions and kaons as described in [113]. Within this model, the following relation between the imaginary part of the irreducible photon self-energy $\mathrm{Im}\bar{\Pi}$ and the vector meson self-energies $\Pi_V(q)$ in vacuum is derived:

$$\mathrm{Im}\bar{\Pi}(q) = \sum_V \frac{\mathrm{Im}\Pi_V(q)}{g_V^2} |F_V(q)|^2, \quad F_V(q) = \frac{\left(1 - \frac{g}{g_V^0}\right)q^2 - m_V^2}{q^2 - m_V^2 + i\mathrm{Im}\Pi_V(q)}, \qquad (7.8)$$

where m_V are the (renormalized) vector meson masses, g_V^0 is the γV coupling and g is the vector meson coupling to the pseudoscalar Goldstone bosons $\pi^\pm, \pi^0$ and $K^\pm, K^0$. Eq.(7.8) is valid for a virtual photon with vanishing three-momentum $\mathbf{q}$. For finite three-momenta there exist two scalar functions $\bar{\Pi}_L$ and $\bar{\Pi}_T$, because the existence of a preferred frame of reference (the heat bath) breaks Lorentz invariance, and one has to properly average over them. However, taking the limit $|\mathbf{q}| \to 0$ should be reasonable for our purposes in view of the fact that the c.m. rapidity interval accessible at CERES and RHIC restricts $|\mathbf{q}|$ on average to only a fraction of the vector meson mass m_V.

Finite temperature modifications of the vector meson self-energies appearing in Eq.(7.8) are calculated using thermal Feynman rules. The explicit expressions for the ρ- and ϕ-meson are taken from ref. [39]. At the one-loop level, the ρ and ϕ are only marginally affected by temperature even close to T_C because of the comparably large pion and kaon masses: $m_\pi \simeq T_C$, $m_K \simeq 3\,T_C$. The thermal spectral function of the ω-meson has been discussed in detail in [40]. Here, the reaction $\omega\pi \to \pi\pi$ was found to cause a considerable

broadening of the ω spectral function, leading to $\Gamma_\omega(T_C) \simeq 7\,\Gamma_\omega(0)$. The corresponding photon spectral function is displayed in Fig. 7.4 (left panel).

At higher invariant masses $1\,\text{GeV} < M < 2\,\text{GeV}$, πa_1 annihilation is the dominant source of dileptons [114, 115]. The vacuum vector and axialvector spectral functions become mixed to order T^2 with a strength $T^2/(6f_\pi^2)$ ($f_\pi \simeq 93$ MeV is the pion decay constant) due to their coupling to the pionic heat bath [116] and should be degenerate at the point of chiral symmetry restoration. The effect of the a_1 and higher resonances on the photon spectral function can then be approximately subsumed in a structureless continuum above 1 GeV [117], reminiscent of the perturbative plateau of $q\bar{q}$ annihilation.
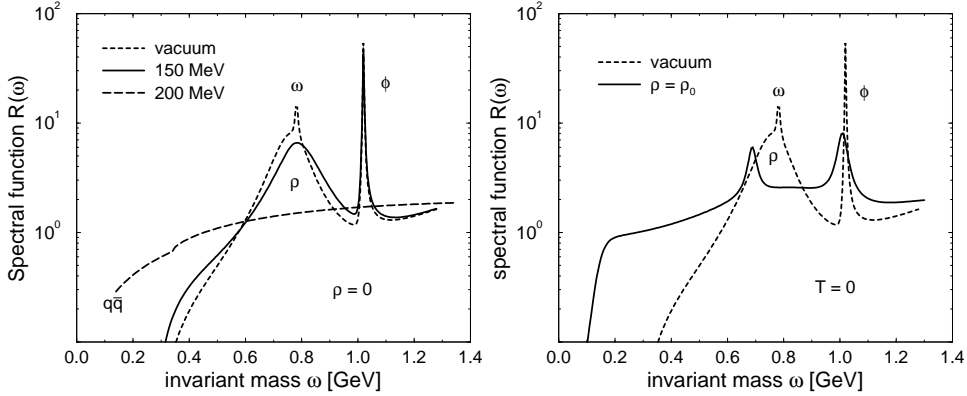
FIGURE 7.4: The photon spectral function $R(\omega) = (12\pi/\omega^2)\,\text{Im}\bar{\Pi}(\omega)$ at finite temperature and $\rho_B = 0$ (left panel) [39, 40] and at $T = 0$ and baryon density of normal nuclear matter, $\rho_B = \rho_0 = 0.17\,\text{fm}^{-3}$ (right panel) [38]. For orientation, the $q\bar{q}$ line in the left panel shows the spectral function in the QGP phase with massless u- and d-quarks and $m_s = 150$ MeV for s-quarks, neglecting α_s-corrections.

There is still considerable stopping of the interpenetrating nuclei at SPS energies, resulting in a net baryon density ρ_B in the central rapidity region, as already discussed in chapter 6. At RHIC, measurements [118, 119] indicate that the proton over antiproton excess is small, implying that the baryons are distributed over a larger rapidity interval. Therefore, finite baryon density effects should not play such an important role at RHIC kinematics. This has also been addressed in chapter 6 in greater detail.

For the evaluation of density effects which are relevant at SPS conditions, we use the results discussed in [38]. There it was shown that in the linear density approximation, Π_V is related to the vector meson - nucleon scattering amplitude T_{VN}:

$$\Pi_V(q^0, \vec{q} = 0; \rho) = \Pi_V^{vac} - \rho_B T_{VN}(q)$$
$$T_{VN}(q) = -\frac{i}{3} \int d^4x\, e^{iqx} \langle N | \mathcal{T} j_\mu(x) j^\mu(0) | N \rangle, \tag{7.9}$$

with $|N\rangle$ being zero-momentum free nucleon states. In the following, we assume that the temperature- and density dependences of Π_V factorize, *i.e.* we replace Π_V^{vac} in Eq. (7.9) by the temperature-dependent $\Pi_V(T)$ and leave T_{VN} unaffected. This amounts to neglecting contributions from matrix elements such as $\langle \pi N | \mathcal{T} j_\mu(x) j^\mu(0) | \pi N \rangle$ (nucleon-pion scatterings where the pion comes from the heat bath). Furthermore, this approximation does not take into consideration a possible T-dependent pion or nucleon mass. Some effective models suggest that, near the phase transition, the nucleon mass follows the behaviour of the chiral condensate $\langle \bar{\psi}\psi \rangle$ and drops abruptly as the quarks lose their constituent masses [41]. Such modifications of particle properties may have a considerable impact on the spectral functions. However, since the temperature range over which the dropping takes place is

narrow, we expect such effects not to leave distinct signals in the dilepton spectra which are only sensitive to the integrated time (and hence temperature) evolution of the system.

The photon spectral function at finite density and zero temperature is depicted in Fig. 7.4 (right panel). The interaction with nucleons causes a strong broadening of the ρ meson down to the one pion threshold, leading to a complete dissolution of its quasiparticle peak structure. The modifications of the ω and ϕ meson spectral distributions are more moderate: The mass of the ω drops by about 100 MeV at normal nuclear matter density, and its width increases by a factor of about 5, whereas the ϕ mass stays close to its vacuum value, accompanied by a ninefold increased width.

To summarize, the most prominent changes of the photon spectral function, when compared to the vacuum case, arise from the broadening of the ρ due to finite baryon density effects and the broadening of the ω due to scattering off thermal pions. The ϕ meson retains its distinct peak structure even under extreme conditions of density and temperature. Very close to T_C, however, these results based on perturbative calculations, are not expected to be reliable.

7.2.3 After freeze-out contributions

At the freeze-out stage, there are still vector mesons present. These will decay with their vacuum properties on their way to the detector and add to the dilepton yield from the previous thermalized phase. The invariant mass region below approximately 400 MeV is mainly filled by the Dalitz decays of the vector mesons. We take these contributions from the experimental analysis of the CERES collaboration for SPS conditions. Since the PHENIX acceptance starts only above 1 GeV, the Dalitz decays do not play a significant rôle at RHIC.

For the calculation of the direct decay of a vector meson V into a lepton pair we start with the following formula:

$$\frac{dN_V}{dMd\eta} = \frac{1}{\Delta\eta} \frac{\alpha^2}{12\pi^4} R_V(M, T = 0) \int_{\tau_f}^{\infty} d\tau \, V_f \int d^3q \, \frac{M}{q^0} \, f_B(q^0, T_f) \exp\left(-\frac{\tau - \tau_f}{\gamma(q)\tau_0^V}\right).$$

Here, T_f and V_f are the fireball temperature and volume, respectively, at freeze-out. After τ_f, the freeze-out time, all medium effects are switched off, so the vacuum photon spectral function $R_V(M, T = 0)$ determines the rate. The corresponding momentum distribution is given by the thermal Bose function, evaluated at the freeze-out temperature T_f. However, the *absolute number* N of vector mesons as a function of time is not a constant: since the mesons decay and there is no thermal recombination, N decreases exponentially like $\exp\left(-(\tau - \tau_f)/(\gamma(q)\tau_0^V)\right)$. The vacuum life time of the vector meson V under consideration is denoted by τ_0^V, and $\gamma(q)$ accounts for time dilatation effects on particles with finite three-momentum:

$$\gamma(q) = \frac{1}{\sqrt{1 - v^2}} = \frac{q^0}{M}.$$

After the time integration we end up with:

$$\frac{dN}{dMd\eta} = \frac{1}{\Delta\eta} \frac{\alpha^2}{12\pi^4} \tau_0 R(M, T = 0) V_f \int d^3q \, f_B(q^0, T_f).$$

The averaged space-time four-volume that is available after freeze-out is therefore $V_f\tau_0^V$, as anticipated. The integral over d^3q now yields the freeze-out particle density $n(M) = N(M)/V$ of the virtual photons as a function of invariant mass. Note that the information on the vector mesons remains *entirely* in the photon spectral function. With the factor V_f

we obtain the total number of photons at freeze-out. When weighted with $R_V(M)$, this gives the dN/dM distribution for the process meson $\to \gamma^* \to e^+ e^-$.

We have also checked that a commonly used Breit-Wigner *ansatz* of the form

$$\frac{dN_{e^+e^-}}{dM} = [V_f n(T_f, M)] \, \xi \, B_V \frac{M^2 \, \Gamma_V(M)}{(M^2 - m_V^2)^2 + M^2 \Gamma_V(M)^2} \qquad (7.10)$$

yields almost identical results. Here, $\Gamma_V(M)$ stands for the M-dependent decay width, ξ is the normalization factor and B_V the branching ratio for the leptonic decay of the corresponding vector meson.

7.2.4 Drell-Yan and charm contributions

At invariant masses $M > 1$ GeV the Drell-Yan mechanism, i.e., hard quark-antiquark annihilation $q\bar{q} \to \ell^+ \ell^-$ at leading order (LO), constitutes another source of (non-thermal) dileptons. Its differential LO cross section in a nucleus(A_1)-nucleus(A_2) collision reads

$$\frac{d\sigma(A_1 A_2)}{dy \, dM} = \frac{8\pi\alpha^2}{9 \, M \, s} \sum_q e_q^2 \times \qquad (7.11)$$

$$\left[\left(Z_1 \, f_q^p(x_1) + (A_1 - Z_1) \, f_q^n(x_1) \right) \left(Z_2 \, f_{\bar{q}}^p(x_2) + (A_2 - Z_2) \, f_{\bar{q}}^n(x_2) \right) + (q \leftrightarrow \bar{q}) \right]$$

where $\sqrt{s}$ denotes the c.m. energy of the nucleon-nucleon collision and the momentum fractions of the beam (and target) parton are denoted by $x_{1,2} = M/\sqrt{s} \, \exp(\pm y)$ respectively.

The Drell-Yan cross section (7.11) is computed using the LO MRST parametrization [120] for the parton distributions $f_i^p(x, \mu^2)$ evaluated at the hard scale $\mu^2 = M^2$. However, it has been checked that using different LO sets (e.g., CTEQ5L [121] or GRV98LO [122]) affects the results by only 10 % at SPS and 20% at RHIC energies. To account for higher order corrections, we multiply the LO expression (7.11) by a K factor $K = 2$ fitted from p–p data [123]. Finally, nuclear effects like shadowing or quark energy loss are expected to suppress the Drell-Yan yield by about 30-50% [124, 125]. Since these effects are still poorly known quantitatively, we neglect them and consider our Drell-Yan rate as an *upper limit* on the actual rate.

Using the Glauber model of multiple independent collisions, the average dilepton multiplicity in a A_1-A_2 collision at impact parameter b is given by

$$\frac{dN(A_1 A_2)}{dy \, dM}(b) = T_{A_1 A_2}(b) \times K \frac{d\sigma(A_1 A_2)}{dy \, dM}, \qquad (7.12)$$

where the normalized thickness function $T_{A_1 A_2}(b)$ is computed assuming the standard Woods-Saxon nuclear density profile. The Drell-Yan pair multiplicity (7.12) is then averaged for the 30% and 6% most central collisions to be compared with CERES and PHENIX data, respectively[2].

Another source of dileptons in the high invariant mass region consists of semileptonic decays of charmed mesons. Whereas earlier calculations found a considerable yield from

---

[2]In addition to these centrality cuts, we need to rely on further assumptions to take properly into account the acceptance of these experiments. Therefore, we shall assume the generic form $d\sigma/dp_\perp \propto p_\perp/(1 + (p_\perp/p_0)^2)^6$ ($p_0 = 3$ GeV) for the $p_\perp$ dependence of the DY process [123]. Furthermore, neglecting corrections due to the intrinsic $k_\perp$ of the incoming partons, the angular distribution is taken to be $dN/d\Omega \propto 1 + \cos^2\theta$ where θ is the angle between the lepton and the beam axis.

open charm exceeding the thermal radiation [126], the subsequent inclusion of medium effects like energy loss led to a suppression of the dielectron rate and made it comparable to or even lower than the Drell-Yan yield [127, 128]. Since the Drell-Yan contribution plays only a subdominant rôle in the following, we will not explicitly include the open charm contributions.

7.3 DILEPTON INVARIANT MASS SPECTRA

Once the time evolution of the fireball is given in terms of the temperature $T(\tau)$, the baryon density $\rho(\tau)$ and the volume $V(\tau)$, and with the knowledge of the photon spectral function, we have all the necessary ingredients to calculate dilepton rates using Eq. (7.3). We fold the result with the acceptance of the CERES and the PHENIX detectors, respectively, and average over the rapidity region covered by these two experiments. The so-called 'hadronic cocktail', dileptons produced after freeze-out through various decay processes, with the exception of vector-meson decays, is then added. This contribution fills the region of very low invariant masses ($M < 150$ MeV). The dilepton yields resulting from direct vector meson decays after freeze-out, as described in subsection 7.2.3, and the Drell-Yan yield from subsection 7.2.4 are added to the hadronic cocktail, taking into account the limited kinematic acceptance and resolution of the detector.

7.3.1 SPS data at 40 and 158 AGeV

We start with a discussion of the SPS CERES/NA45 experiment, treating 40 AGeV and 158 AGeV data in parallel. The final results for the dilepton invariant mass spectra are shown in Figs. 7.5 and 7.6.

Our calculation reproduces the overall spectrum of the 158 AGeV CERES data quite well. It overestimates the rates somewhat around invariant masses of 200 to 400 MeV and achieves a good description in the region above 400 MeV up to 1.8 GeV. Recall that our QGP model rate constitutes only a lower limit on the actual rate because it neglects the radiation from non-partonic (cluster) degrees of freedom above the critical temperature. Bearing in mind that the region above 1 GeV is mainly populated by dileptons originating from the QGP phase, as evident from the left panel of Fig. 7.5, there might still be additional radiation close above T_C arising from hadronic clusters embedded in a QGP environment. The Drell-Yan contribution is non-negligible, but still outshined by the QGP by a factor of 3.

Changes in the spectra of the vector mesons indicate tendencies towards chiral symmetry restoration, so the right panel of figure 7.5 shows the contributions of ρ, ω and ϕ mesons separately, not including the after freeze-out yield. The ρ meson loses its quasiparticle structure entirely due to strong collision broadening at finite density, and fills the whole low mass region between the two pion threshold and ~ 800 MeV. The ω meson, a sharp peak in the vacuum, broadens at finite temperature due to the thermal scattering process $\omega\pi \to \pi\pi$. Furthermore, the mass shift at finite baryon density smears the remaining peak structure considerably. Effectively, the remaining signal arises from the direct decays of ω mesons after freeze-out. The ϕ has become a spread-out but still visible resonance structure, showing only moderate broadening at finite temperature and baryon density. It might therefore be a suitable candidate for gauging the strength of vector meson modification.

To test the modelling of the vector meson spectra, we calculate the total number of ω and

ϕ meson, suitably averaged over their medium-induced spread in invariant mass, as

$$\langle N_\omega \rangle = \frac{1}{N_{ch}} \int\limits_{0.65 \text{ GeV}}^{0.9 \text{ GeV}} dM \, \frac{d^2 N_{\omega \to ee}}{d\eta dM} = 9 \cdot 10^{-7}$$

and

$$\langle N_\phi \rangle = \frac{1}{N_{ch}} \int\limits_{0.95 \text{ GeV}}^{1.1 \text{ GeV}} dM \, \frac{d^2 N_{\phi \to ee}}{d\eta dM} = 1.8 \cdot 10^{-7}.$$

Comparing with numbers from a statistical model calculation, $\langle N_\omega \rangle = 4 \cdot 10^{-7}$ and $\langle N_\phi \rangle = 2.2 \cdot 10^{-7}$ [131], we indeed find reasonable agreement. Note that the relatively large ω meson yield is primarily caused by the pion fugacity factor $[\exp(\mu_\pi/T_f)]^3$ at freeze-out, which reflects the enhanced feeding through the $3\pi \to \omega$ process. This is clearly an oversimplified treatment, as it assumes that the ω remains in chemical equilibrium with the surrounding matter until kinetic freeze-out, somewhat in contradiction to the results of chapter 6. The lifetime of the vacuum ω, however, is not much larger than the fireball lifetime, and by imposing detailed balance one can conclude that the back-reaction $3\pi \to \omega$ is not very strong. On the other hand, it is strong enough to make the pure chemical freeze-out scenario questionable, especially in the presence of medium modification. A detailed treatment of the magnitude of the ω and ϕ signal clearly requires a more dynamical approach like solving rate equations.

Going from 158 AGeV to 40 AGeV beam energy, analyses of HBT radii and transverse radial flow [129] indicate that the reaction dynamics do not change dramatically, therefore we do not expect drastic differences in the rate. Indeed, the data at 40 AGeV look similar to the 158 AGeV case, and the calculated rate, shown in Fig. 7.6, also bears this similarity and achieves a good fit without tuning the setup of the model. Since the initial temperature is lower and the QGP phase shorter in the 40 AGeV case, the partonic dilepton contribution is obviously much smaller, but nevertheless still present. Owing to the greater initial baryonic density, the in-medium modifications of the vector mesons become more pronounced, most prominently visible in the ω meson channel. Its downward mass shift drags the peak structure along the time evolution of the fireball, creating a small bump on top of the completely dissolved ρ meson that fills up the low-mass region again. Its yield after freeze-out constitutes a visible signal that may be experimentally observable with suitable energy resolution. The ϕ meson contribution clearly sticks out above the smooth ρ meson 'continuum'. To conclude, we find no distinct differences in our calculation for the two beam energies probing dilepton production at SPS so far, in accord with experimental findings. This indicates that the general setup of our model is fairly robust. Future data at 20 and 80 AGeV will aid to test this statement.

The fact that we moderately overestimate the data in the region between 200 and 300 MeV invariant mass requires a comment. Since this range is dominated by the low-mass behaviour of the ρ meson spectral function at finite density, this behaviour may indicate that very region or that the influence of finite three-momentum on the spectra is non-negligible. Consider the 158 AGeV data taken for different transverse momenta $\mathbf{p}_t < 500$ MeV and $\mathbf{p}_t > 500$ MeV, shown in figure 7.7. We observe that the general shape of the data pattern is well described by the calculation for both $\mathbf{p}_t$ regions. However, for the high $\mathbf{p}_t$ case, the calculation again overshoots the data in the low mass region whereas this is not so in the low $\mathbf{p}_t$ case. This feature is also present in the 40 AGeV case. This can be traced to the use of the spectral functions for three-momentum equal to zero in order to describe the photon spectral function in the hadronic phase. This approximation is of limited validity at high $\mathbf{p}_t$ where the spectral function ought to become smaller than in our approximation. Therefore we expect improved agreement with the data for the low invariant mass region both at 40 and 158 AGeV once this effect is taken into account properly.
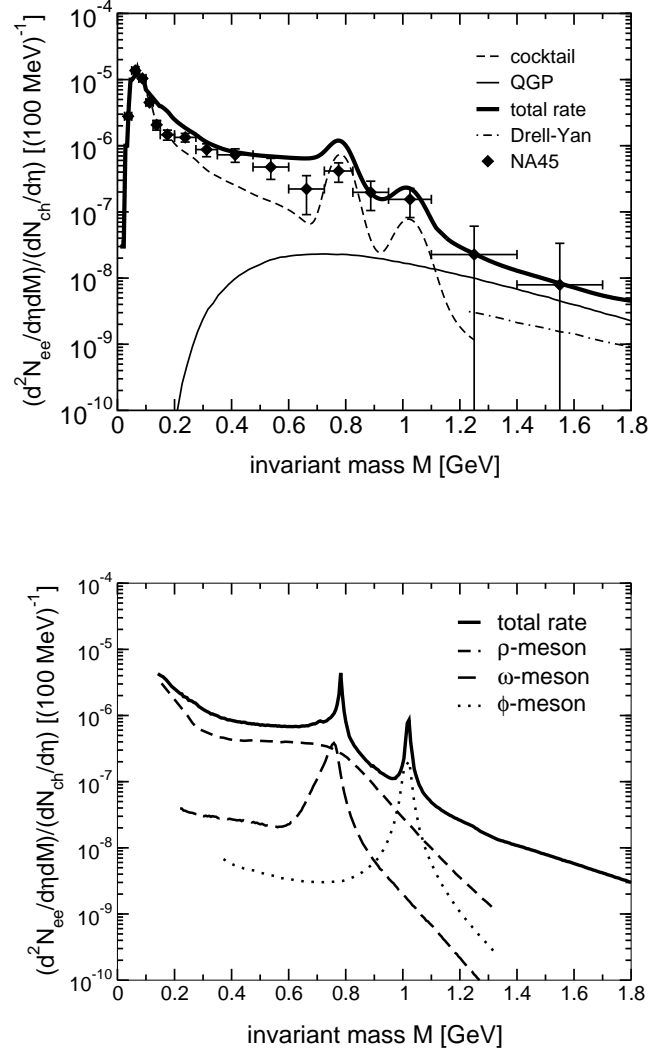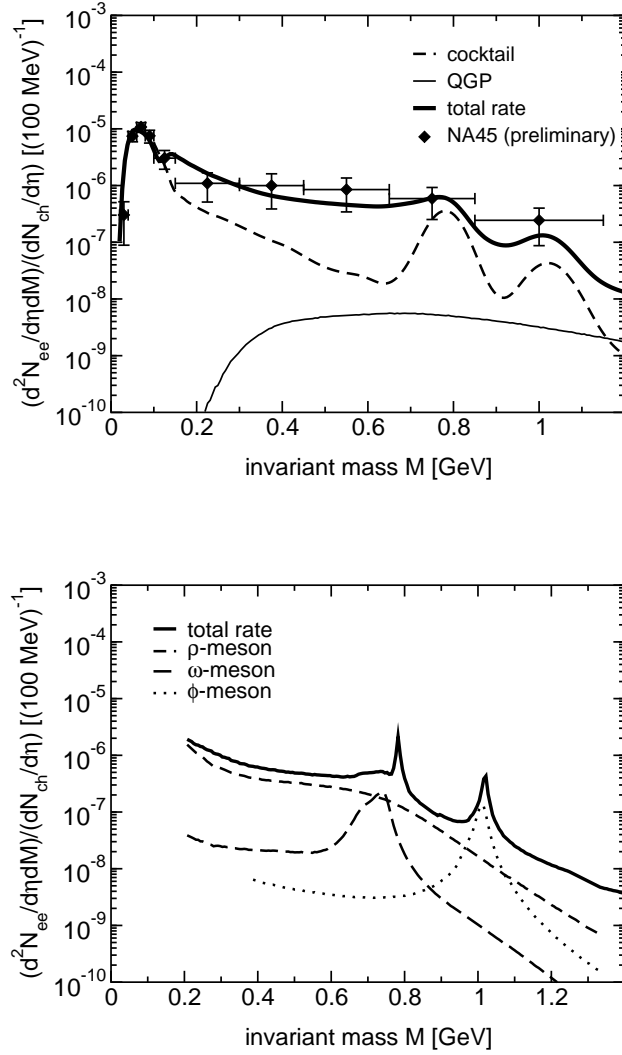
FIGURE 7.5: Left: Dilepton invariant mass spectra (see Eq. (7.3)), normalized to $dN_{ch}/d\eta = 250$, in units of $(100 \text{ MeV})^{-1}$, for the SPS CERES/NA45 Pb(158 AGeV)+Au experiment [132]. Shown are the data, the total rate, the cocktail contribution including the after freeze-out decays of vector mesons, the QGP contribution and the Drell-Yan yield. Right: Contributions from ρ-, ω- and ϕ-mesons (excluding after freeze-out yield) shown separately, assuming perfect detector resolution.

Our setup of the fireball model enables us to gain additional detailed insight into the time evolution of the dilepton yield. This is demonstrated in Fig. 7.8. Here the different stages of the fireball evolution leave distinct marks in the time-resolved dilepton yield. For early times, dileptons come entirely from the $q\bar{q}$ quasiparticle annihilation processes. The movement of the invariant mass threshold reflects the temperature dependence of the quasiparticle mass which decreases near the phase transition at $\tau \sim 7$ fm/c. One observes that, in spite of the growing fireball volume, the contributions from later timeslices to the total yield become progressively less important until the hadronic phase takes over at $\tau > 7$ fm/c. This surprising behaviour is enforced by the confinement factor $C(T)$ which reduces the thermodynamically active degrees of freedom significantly near the phase boundary.

FIGURE 7.6: Left: Dilepton invariant mass spectra (see Eq. (7.3)), normalized to $dN_{ch}/d\eta = 210$, in units of $(100 \text{ MeV})^{-1}$, for the SPS CERES/NA45 Pb(40 AGeV)+Au experiment [133]. Shown are the preliminary data, the total rate, the cocktail contribution including the after freeze-out decays of vector mesons and the QGP contribution. Right: Contributions from ρ-, ω- and ϕ-mesons (excluding after freeze-out yield) shown separately, assuming perfect detector resolution.

The system then enters the hadronic evolution phase without going through a mixed phase. The most prominent feature is the rapid filling of the low invariant mass region through the density-broadened ρ meson spectrum which ends up as an enhanced pion continuum. The ϕ meson starts contributing its characteristic peak and, as the system cools down further, the ω meson begins to emerge, albeit as a broad structure. Note that while the hadronic contributions fill primarily the low invariant mass region, their yield above 1 GeV is negligible in this late evolution phase.
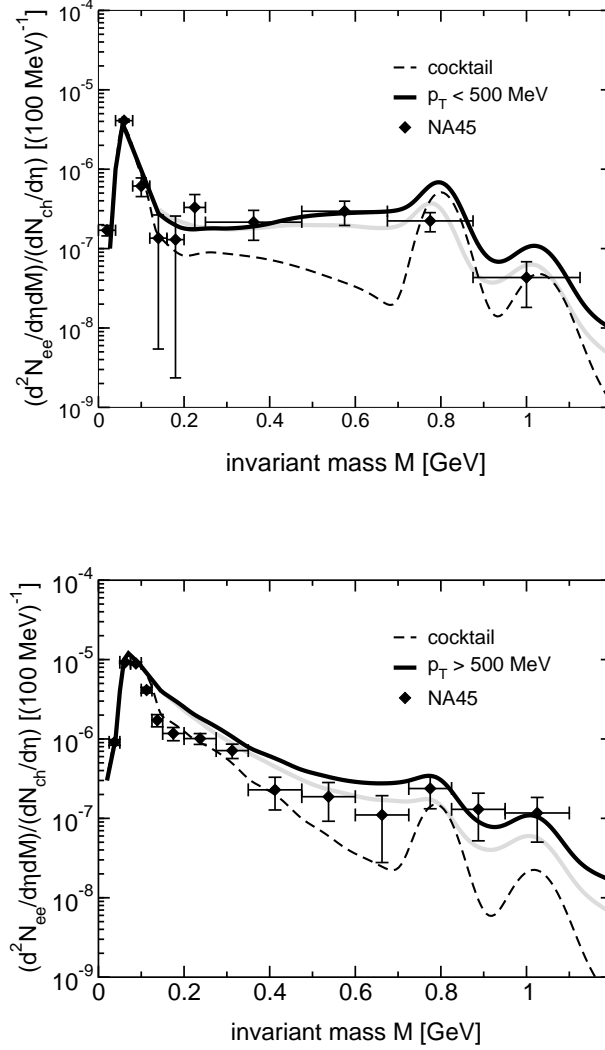
FIGURE 7.7: Left: Dilepton invariant mass spectra for transverse momenta of the e^+e^- pair $\mathbf{p}_t < 500$ MeV for the SPS CERES/NA45 Pb(158 AGeV)+Au experiment [132]. Shown are the data, the total rate and the cocktail contribution. The grey line displays the same calculation for 40 AGeV. Right: Same for $\mathbf{p}_t > 500$ MeV.

7.3.2   RHIC at $\sqrt{s} = 200$ AGeV

For the RHIC scenario, thermally generated dileptons are dominant. Measurements of proton ratios at $\sqrt{s} = 130$ AGeV indicate that the central collision region remains almost net-baryon free, compared to SPS energies. Within a statistical thermal model, the particle ratios are accounted for by a small baryon chemical potential of about 50 MeV at chemical freeze-out [82]. At 200 AGeV, this value is predicted to be even smaller. Effects of finite baryon density are therefore almost absent and consequently both the ρ and the ϕ are expected to show up in the spectrum as pronounced structures, whereas there should be no clear trace of the in-medium ω due to its strong thermal broadening. Contributions from Drell-Yan processes, which dominate in the very high invariant mass region, are an order of magnitude smaller.
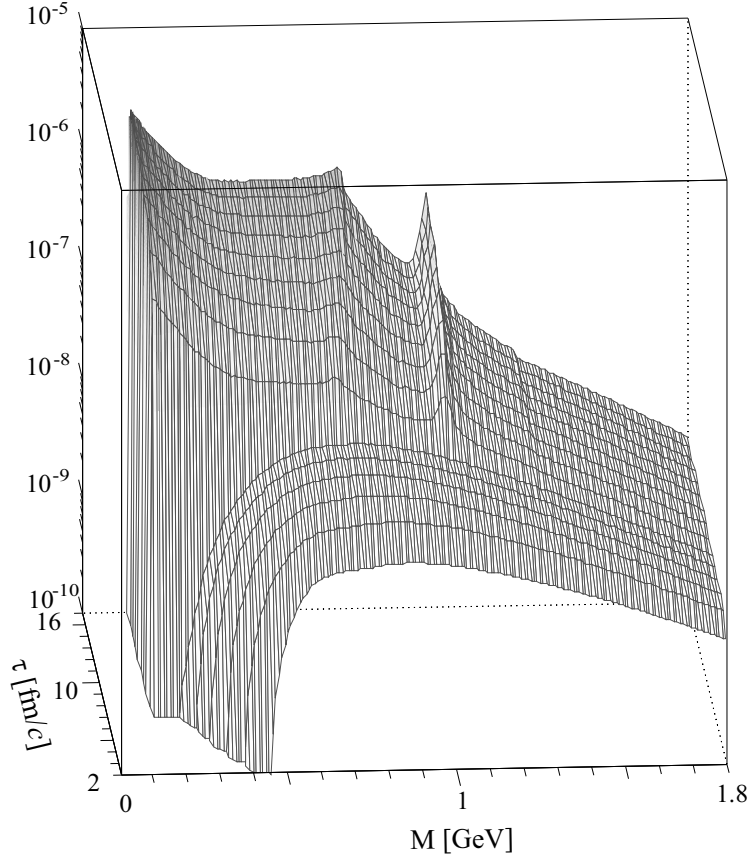
FIGURE 7.8: Time evolution of the (integrated) dilepton yield for the SPS scenario. The vertical scale is the same as in fig. 7.5. The cocktail contribution has not been included in this picture, and perfect resolution was assumed.

As the distribution of net-baryon content in rapidity space exhibits a pronounced structure, which in turn leads to different physical conditions at different rapidities regarding the EoS, pion densities and freeze-out conditions (see section 6.4), one has to specify at what rapidity the dilepton yield is measured. We give all prediction for the di-electron rapidity range of PHENIX covering $-0.35 < y < 0.35$ with the appropriate entropy per participant baryon $s/\rho_B = 250$.

The prediction for the dilepton yield at 200 AGeV, including the schematic acceptance for the PHENIX detector, is shown in Fig. 7.9. The ω and ϕ meson resonances clearly stick out over the smooth ρ meson and QGP contributions. Although PHENIX will only start to measure at $M \geq 1$ GeV, it may be possible to resolve the ϕ meson peak. However, a significant part of the peak strength is built up by the after freeze-out contributions, making it difficult to disentangle the in-medium modifications on the hadrons. For $M \geq 1.3$ GeV, the dilepton spectrum is dominated by thermal QGP radiation, outshining the hard Drell-Yan dilepton yield.

Comparing our prediction for PHENIX with the one shown in ref. [31], we find rough agreement of the rate for the low mass region below ~ 1 GeV. Although the dilepton yield from the QGP phase is suppressed in our case by the factor $C(T)^2$ (cf. section 7.2.1), we still find an enhancement of a factor of about 4 in the range $1.3 - 2.5$ GeV over the rate in [31] that employs a (perturbative) chemical undersaturation model in the QGP phase. Owing to the non-perturbative nature of the QGP close to T_C, this model may not be
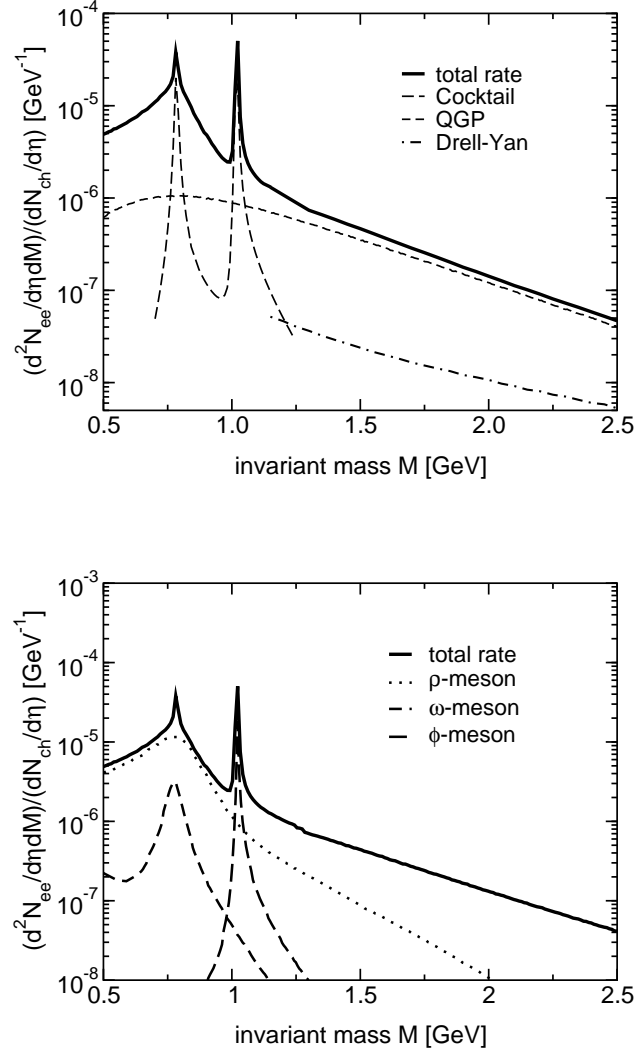
FIGURE 7.9: Left: Dilepton invariant mass spectra, normalized to $dN_{ch}/d\eta = 650$ [130], in units of GeV^{-1}, for the RHIC experiment PHENIX at $\sqrt{s} = 200$ AGeV. Shown are the total rate, the cocktail consisting of the after freeze-out decays of ω and ϕ vector mesons, the QGP contribution and the Drell-Yan yield. Right: Contributions from ρ-, ω- and ϕ-mesons (excluding after freeze-out yield) shown separately.

applicable in that very region. Note that our rate also constitutes only a lower limit there, so that the actual rate may even be larger. High precision data will allow to pin down one or the other model.

7.3.3 Sensitivity to model parameters

We would like to stress that the gross features of our model are set, once the parametrization of the fireball evolution has been matched to the hadronic observables and the EoS of both phases has been constructed in accordance with lattice QCD and empirical constraints. The remaining uncertainties, mainly about the initial state of the fireball, the thermal masses of

the quasiparticles and the detailed shape of the EoS, do not alter the results substantially; they lead to only moderate or even weak dependence on those parameters. Fine-tuning is still possible, but only within the limits that retain consistency with the overall framework.

We have investigated the sensitivity of the model to parameter changes in some detail for the SPS scenario at 158 AGeV. In order to get a theoretical 'error band', we investigated the extremes of our parameter ranges, a combination of parameters that yields the largest and the smallest possible QGP contribution. The resulting range is shown in Fig. 7.10 as a grey band, together with the data points and the curve from the previous section.
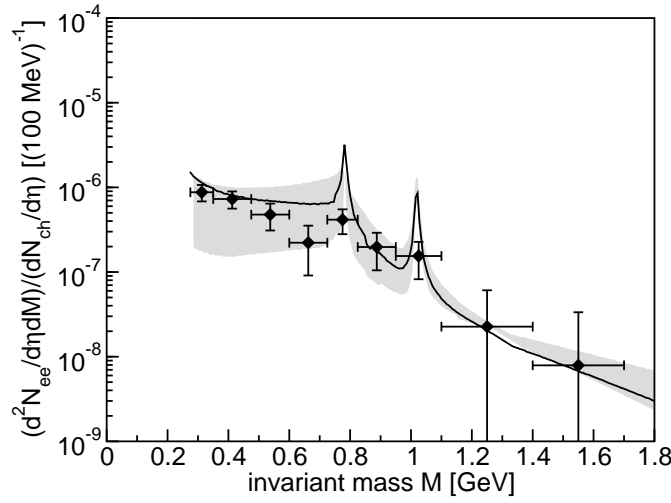
FIGURE 7.10: Dilepton invariant mass spectra for the SPS CERES/NA45 experiment at 158 AGeV. Shown are data (symbols), the total rate introduced in section 7.3.1 (solid line) and a band (shaded) that represents the range in the dilepton yield when varying the parameters τ_0, v_z^i and T_c. See text for details.

Regarding the initial conditions, the largest uncertainty comes from the initial fireball formation length z_0 or, equivalently, the time τ_0. We let it vary from 0.5 fm/c to 2 fm/c, i.e. from fast to slow equilibration. Consider next the initial longitudinal flow velocity v_z^i. A variation of this quantity from 0.3 c to 0.8 c implies a modification of the pressure-driven accelerated motion in order to arrive at the same final velocity of 0.9 c, as determined by the rapidity distributions of the observed hadrons. Strong deviations from $v_z^i \simeq 0.5$ c, however, lead to inconsistent values for the thermal freeze-out temperature T_f. Finally, modifications of the critical temperature T_C influence mainly the relative weight of the contributions from the QGP phase and the hadronic gas phase to the dilepton yield and hence change the shape of the dilepton spectra. Lattice data on T_C suggest a range from 140 MeV for three massless, thermally active flavours to about 185 MeV for two massless flavours and a realistic pion mass. Due to the self-consistent modelling of the temperature and volume evolution, there is no simple one-to-one correspondence of these parameters to the dilepton yield.

The upper limit of the grey band in figure 7.10 now corresponds to the scenario with a *small* QGP contribution, *i.e.* large τ_0, large v_z^i and high T_C. On the other hand, the lower limit includes a *large* QGP contribution with small τ_0, small v_z^i and low T_c. It is instructive to note that the shape of the spectrum changes only moderately above 1 GeV invariant mass within these extreme parameter variations. The first scenario, however, tends to overestimate the data in the region of the ρ peak, whereas the second scenario does not leave enough time

for the hadronic phase to build up the e^+e^- excess in the low-mass region between 200 and 800 MeV, effectively ruling out a large QGP contribution.

The fact that the grey errorband covers the data points indicates that is indeed possible to improve the agreement of the calculation to the data in the low mass region without being constrained by the high mass region by a suitable fine-tuning procedure of the fireball evolution. This, however, is not a sensible thing to do as the fireball evolution was tied to the hadronic observables in order to get rid of the ambiguity between evolution dynamics and dilepton emission dynamics.

7.4 Conclusions

What can we, finally, learn about the QGP by measuring dileptons? Looking at Figs. 7.5 and 7.6, we find that the signal of the QGP is almost completely outshined by the one of the hadronic gas in the invariant mass range below 1 GeV. This is unfortunate, as the data statistics gets dramatically worse in the mass region above 1 GeV where the QGP signal is dominant, thus inhibiting any decisive conclusions. The situation might improve at RHIC, where there is a possible window for the observation of the QGP between the ϕ peak and the region which is filled by semileptonic decays of charm mesons, provided that the data statistics can be significantly improved and the hadronic contributions can be assessed reliably. The originally proposed signal for the onset of the QGP, the enhancement of dilepton yield below the ρ mass as compared to p-p and p-A collisions can be entirely explained by in-medium modifications of the ρ, either, as within the present framework, by a dramatically increased width or by a drop of its mass as the chiral transition is approached.

On the other hand, the presented framework assuming early thermalization and a long-lasting QGP phase is clearly in line with all of the measured data on dileptons. This is not trivial, as thermalization is quite a restrictive assumption as far as the fireball evolution is concerned (note that parameter changes regarding initial longitudinal expansion of the fireball immediately lead to disagreement to hadronic data). It appears that the simple framework of the model is also able to account also for the essential dynamics of the fireball evolution.

Obviously, a continuous emission process like dilepton emission probes the four-volume of the fireball if the medium is thermalized. In contrast to a decaying (and emitting) ensemble of particles, in a thermalized system the reservoir of emitting particles (e.g. the ρ) is continuously refilled by back-reactions (e.g. $\pi\pi \to \rho$) which do not take place in a system with negligible interactions. In that sense, dileptons may not reveal the QGP directly, but they provide additional constraints on the spacetime evolution of the fireball via their normalization. As apparent form Fig. 7.10, there is no room for a prolonged hadronic phase, thus it is important in the present framework that the radiation during the early evolution time is of a qualitatively different nature and does not strongly populate the low invariant mass region.

The strong evidence for in-medium modification also renders the naive application of the statistical hadronization model questionable (see section 6.3.3). Clearly, a better resolution of the ω and the ϕ peak is needed in order to disentangle contributions from thermal yield and decays after kinetic freeze-out. On the theoretical side, the behaviour of these two mesons must be explored in more detail, as their typical timescales are not cleanly separated from the one of the fireball.

Chapter 8

THERMAL PHOTON EMISSION — KEY TO THE INITIAL TEMPERATURE

8.1 INTRODUCTION

The emission of photons out of hot hadronic matter is closely related to the emission of dileptons — for vanishing invariant mass M of the lepton pair in Eq. (7.1), one formally recovers the expression for real photons. Therefore, the potential information about the fireball evolution carried by thermal photons is in principle already contained in the dilepton emission rate. In practice, however, the momentum regimes in which data have been taken are quite different for real photons and dileptons, therefore a detailed study of the photon emission rate constitutes a nontrivial test for the fireball evolution model and leads to qualitatively new information.

Although the physics of photon emission and dilepton emission is so closely related, it is unfortunately impossible to treat both processes within the same calculational framework of the quasiparticle description we have used successfully so far. The reason is that the process $q\overline{q} \to \gamma$ is kinematically impossible for a real photon γ as long as the quark and antiquark are considered as free quasiparticles which, by definition, do not experience strong interactions. As already indicated in section 4.5.1, one needs to improve the naive quasiparticle picture to allow for a substructure which can be resolved if the momentum scales are large enough.

In the absence of such an improved quasiparticle picture, we will adopt the following point of view: We will discuss data for the emission of photons with transverse momenta k_t in the range 1 GeV $< k_t <$ 4 GeV, i.e. at scales well above the thermal scale given by the

temperature T. Therefore, at least one of the plasma particles participating in the photon production process will also have a large momentum which allows to neglect the effect of the thermal mass in the propagator and the confinement factor (a single high-momentum quark/gluon will only hadronize outside the fireball). The calculation of the interaction of such a particle with another low momentum plasma quasiparticle can be treated correctly in HTL resummed perturbation theory as far as the quasiparticle mass is concerned. The incorporation of the (phenomenological) confinement factor $C(T)$ into such a perturbative framework is impossible, but we will verify a posteriori that the photon emission rate is dominated by the very early evolution phase where $C(T)$ is expected to be close to unity.

8.2 THE PHOTON EMISSION RATE

8.2.1 The QGP phase

As already mentioned, the leading order contribution to the diagram shown in Fig. 7.1 is absent in the case of real photons. The leading order polarization tensor for real photons is therefore given by the diagram shown in Fig.8.1.
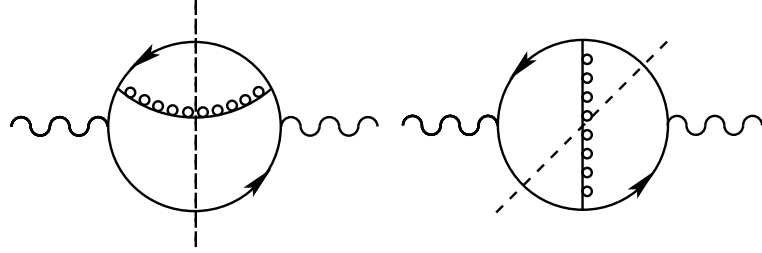
FIGURE 8.1: Leading order contributions to the imaginary part of the self energy of real photons, shown are the two possible cuts of the diagram.

The two possible cuts of the diagram correspond to the processes shown in Fig. 8.2, the QCD Compton process and $q\overline{q}$-annihilation.
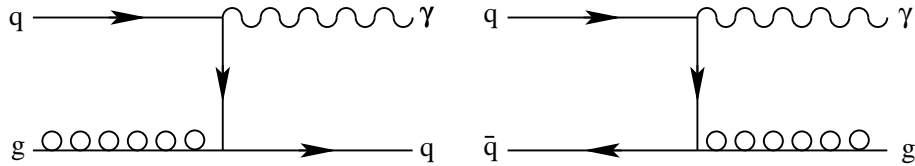
FIGURE 8.2: Leading order processes for photon production in the QGP: QCD Compton scattering (left) and $q\overline{q}$ annihilation (right).

These diagrams have been calculated in [134, 135], where it was found that the singularities caused by the exchange of massless states in the t-channel could be cured by HTL resummation leading to the appearance of a thermal mass. We will refer to these formally leading order processes as $2 \leftrightarrow 2$ processes in the following.

However, it was shown in [136–138] that the diagrams shown in Fig. 8.3 corresponding to bremsstrahlung and annihilation with scattering (aws) also contribute to leading order in α_s, as they contain collinear enhancements. Numerically, their contribution to the rate exceeds the one of $2 \leftrightarrow 2$ processes.

It was also pointed out in [137, 138] that there is a suppression of these diagrams due to the Landau-Pomeranchuk-Migdal (LPM) effect [139–141], the appearance of destructive interference between different multiple scattering processes during the photon emission. This was consistently taken into account in [142, 143], where the complete rate to $O(\alpha_s)$ is given and it is argued that no other diagrams contribute to leading order. The suppression of the LPM effect results in a $\sim 30\%$ correction to the processes shown in Fig. 8.3.
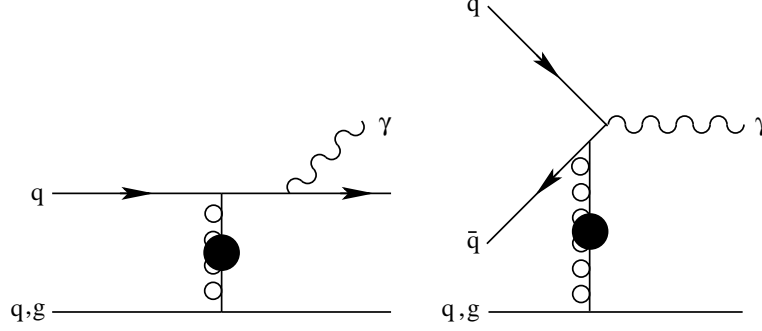
FIGURE 8.3: Processes which, because of near-collinear singularities, contribute to leading order photon production in the QGP: Bremsstrahlung (left) and annihilation with scattering (aws) (right). The filled circles represent HTL resummed propagators.

The final result can be written as

$$\frac{dN}{d^4x d^3k} = \frac{1}{(2\pi)^3}\mathcal{A}(k)\left(\ln(T/m_q(T)) + \frac{1}{2}\ln(2E/T) + C_{tot}(E/T)\right),\qquad(8.1)$$

with $E = k$ and $m_q^2(T) = 4\pi\alpha_s T^2/3$ the leading order large momentum limit of the thermal quark mass. The leading log coefficient $\mathcal{A}(k)$ reads

$$\mathcal{A}(k) = 2\alpha(N_C\sum_s q_s^2)\frac{m_q^2(T)}{E}f_D(E).\qquad(8.2)$$

Here, the sum runs over the involved quark flavours and q_s denotes the fractional quark charges in units of elementary charge. The Fermi-Dirac distribution $f_D(E)$ dominates the momentum dependence of the rate: To a good approximation, it is an exponential decrease with E. The dependence on the specific photon production process is contained in the term $C_{tot}(E/T)$:

$$C_{tot}(E/T) = C_{2\leftrightarrow2}(E/T) + C_{brems}(E/T) + C_{aws}(E/T).\qquad(8.3)$$

All these functions $C(E/T)$ involve non-trivial multidimensional integrals which can only be solved numerically. In [143], parametrizations for the results are given as

$$C_{2\leftrightarrow2}(E/T) \simeq 0.041(E/T)^{-1} - 0.3615 + 1.01\exp[-1.35E/T]\qquad(8.4)$$

and

$$C_{brems}(E/T) + C_{aws}(E/T) \simeq \sqrt{1 + \frac{1}{6}N_f}$$
$$\times\left(\frac{0.548\ln(12.28 + 1/(E/T))}{(E/T)^{3/2}} + \frac{0.133E/T}{\sqrt{1 + (E/T)/16.27}}\right).$$
$$(8.5)$$

We use these expressions for the photon emission rate from the QGP phase in our further investigations.

8.2.2 The hadronic phase

Due to vector meson dominance (VMD), the vector mesons (ρ, a_1) play a very important role for the emission of photons from a hot hadronic gas. The first calculation of such processes has been performed in [144] in the framework of an effective Lagrangian. It has been found that the dominant processes are pion annihilation, $\pi^+\pi^- \rightarrow \rho\gamma$, 'Compton scattering', $\pi^\pm\rho \rightarrow \pi^\pm\gamma$ and ρ decay, $\rho \rightarrow \pi^+\pi^-\gamma$.

Several more refined approaches have been made since then (for an overview, see [145]). In the following, we will use a simple parametrization of the rate from a hot hadronic gas taken from [146] which is given as

$$E\frac{dN}{d^4xd^3k}[\text{fm}^{-4}\,\text{GeV}^{-2}] \simeq 4.8T^{2.15}\exp[-1/(1.35ET)^{0.77}]\exp[-E/T]. \qquad (8.6)$$

We will demonstrate a posteriori that the detailed choice of the hadronic emission rate is of no importance, as it is a small correction to the contribution coming from the QGP phase.

8.2.3 The integrated rate

The spectrum of emitted photons has been measured for 158 AGeV Pb-Pb collisions by the WA98 collaboration at the CERN SPS [147]. In order to compare to the experimentally measured spectrum, we have to integrate Eq. (8.1) over the space-time evolution of the fireball,

$$\frac{dN}{d^2k_tdy}\bigg|_{y=0} = \frac{\pi}{\Delta y}\int d\tau R^2(\tau)\int_{z_{min}(\tau)}^{z_{max}(\tau)}dz\int_{k_{min}(y(z))}^{k_{max}(y(z))}dk_z\frac{dN}{d^4xd^3k}. \qquad (8.7)$$

In this expression, $R(\tau)$ stands for the radial expansion of the fireball, Δy denotes the rapidity interval over which the detector measures, $y(z)$ is the rapidity of a volume element at position z and the limits of the k_z integration come from the fact that a photon emitted at the (boosted) edge of the fireball has to have a longitudinal momentum in a certain range in order to be detected in the rapidity window of the experiment.

8.2.4 Prompt photons

In addition to the thermal emission of photons due to secondary interactions, there is also a contribution coming from the primary hard scattering processes in the pre-equilibrium phase of the fireball evolution. These so-called prompt photons cannot be separated from the thermal photons experimentally and hence have to be taken into account if one wants to compare to data.

Theoretically, the production of prompt photons from hard parton scatterings can be computed similarly to the thermal rate: The relevant diagrams are shown in Figs. 8.2 and 8.3. However, in contrast to the calculation of the thermal emission rate, the external legs of the diagrams are not multiplied by the thermal distributions of partons but by the parton distributions characteristic of the colliding nuclei. As usual, the calculation should first be compared to p-p collision data.

However, in order to explain the experimental data in p-p collisions [148], it proved necessary to include an intrinsic transverse momentum (p_t) distribution of partons as a phenomenologically motivated non-perturbative effect into the calculation [149–151]. Using the uncertainty principle with the radius of the nucleon R_N, one finds $\sqrt{\langle p_t^2\rangle} \approx \pi/2R_N \approx$ 0.37 GeV. This value, however, is too small to explain the data which require $\langle p_t^2\rangle \approx 1-1.5$ GeV [152].

This discrepancy can be explained by a number of mechanisms (for an overview, see [145]). New effects and further uncertainties arise in the extrapolation of these results to p-A and A-A collisions where qualitatively new effects, such as shadowing [153] and initial state momentum broadening (the Cronin effect) [154] enter.

In view of these uncertainties, we will not make an attempt to quantify the contribution of prompt photons at this point, but rather present the result obtained in [152] to illustrate the possible range of predictions dependent on the average value of p_t. This is done in Fig. 8.4.
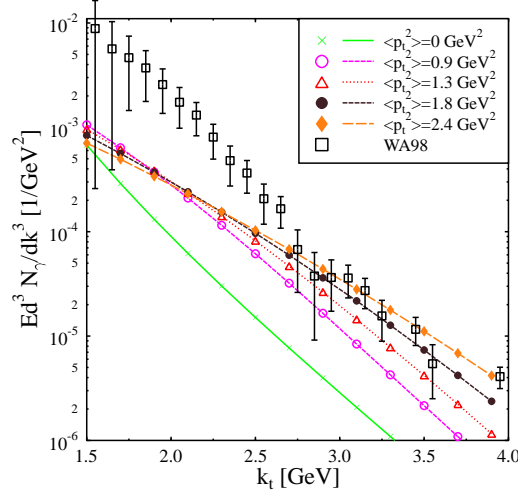
FIGURE 8.4: Prompt photon production in Pb-Pb collisions as a function of the photon transverse momentum k_t for different values of average parton intrinsic transverse momentum $\langle p_t^2 \rangle$ [152] as compared to experimental data [147].

Regardless of the value of $\langle p_t^2 \rangle$, the prompt photon contribution fails to explain the data in the region $k_t < 2.7$ GeV. This can be taken as evidence that there is indeed a contribution to the photon spectrum resulting from secondary interactions.

8.3 RESULTS

The result of the evaluation of Eq.(8.7) with the fireball evolution model described in chapter 5 is shown in Fig. 8.5.

The overall agreement with the data is remarkably good. Above 2 GeV, the calculation systematically underestimates the data somewhat, leaving room for a contribution of prompt photons of about the same magnitude as the thermal yield. Note that the spectrum is almost completely saturated by the QGP contribution — for $k_t > 3$ GeV, the hadronic contribution is almost two orders of magnitude down. This can in essence be traced back to the strong temperature dependence of the emission rate normalization and justifies our approximate treatment of the hadronic contribution a posteriori.

In order to study the importance of the initial, high temperature phase in more detail, we present the time evolution of the spectrum in Fig. 8.6.

One observes that the large k_t region is almost exclusively dominated by the first fm/c of evolution proper time, whereas the yield in the low k_t region is not yet saturated after 2 fm/c. Therefore, the high k_t yield is potentially capable of providing information about the initial temperature reached immediately after equilibration. Unfortunately, this capability is seriously flawed in practice by the need to assess an unknown contribution of prompt
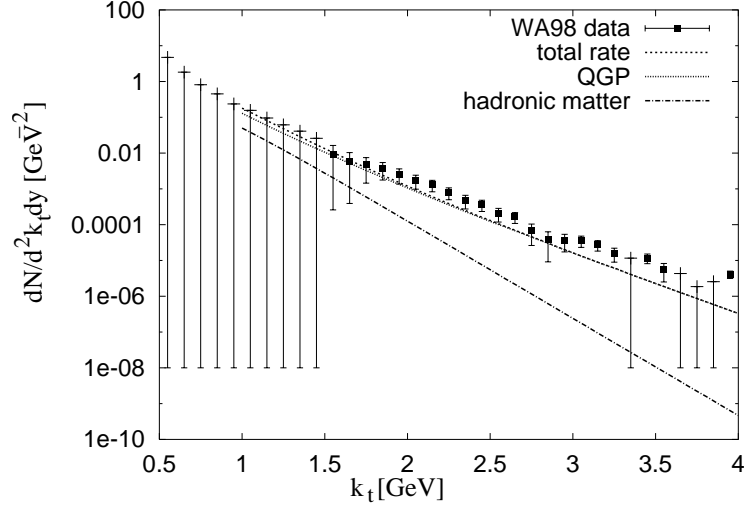
FIGURE 8.5: Thermal photon spectrum for 10% most central Pb-Pb collisions at SPS, 158 AGeV Pb-Pb collisions, shown are calculated rate (total, contribution from QGP and hadronic gas) and experimental data [147].
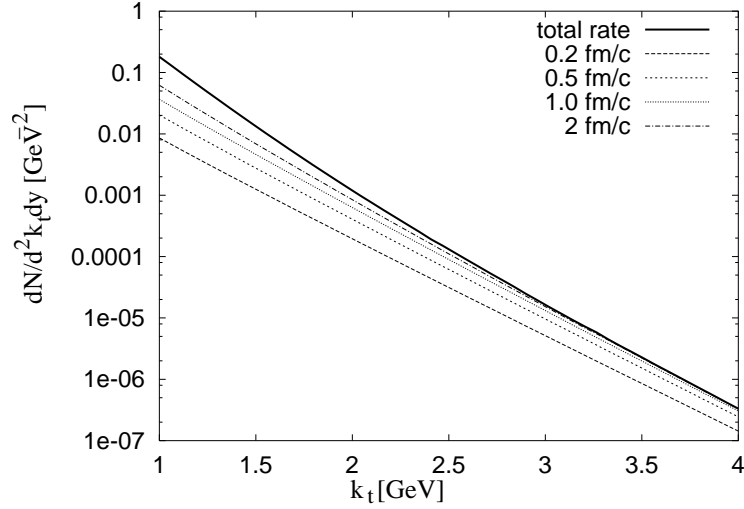

FIGURE 8.6: The total photon emission spectrum and the integrated rate at proper times $\tau = 0.2, 0.5, 1.0$ and 2 fm/c of the fireball evolution.

photons, which may be large in this region. Nevertheless, bearing this uncertainty in mind, we pursue this idea further in Fig. 8.7 where we investigate the sensitivity of the result to the equilibration time τ_0 of the fireball. As this is one of the most uncertain parameters in the model, any opportunity to determine its experimental limits is extremely valuable.

We find that the low k_t region of the spectrum is hardly affected by different choices for the equilibration time, in accordance to our expectation that only the high k_t part probes the initial temperature. A short equilibration time of 0.5 fm/c, corresponding to an initial temperature of 370 MeV leads to a good description of the data without the inclusion of prompt photons. On the other hand, a slow equilibration corresponding to $\tau_0 = 2$ fm/c and an initial temperature of 260 MeV requires a sizeable contribution of prompt photons, which in turn implies intrinsic parton momenta of $\langle p_t^2 \rangle \approx 1.5$ GeV. Note that the description
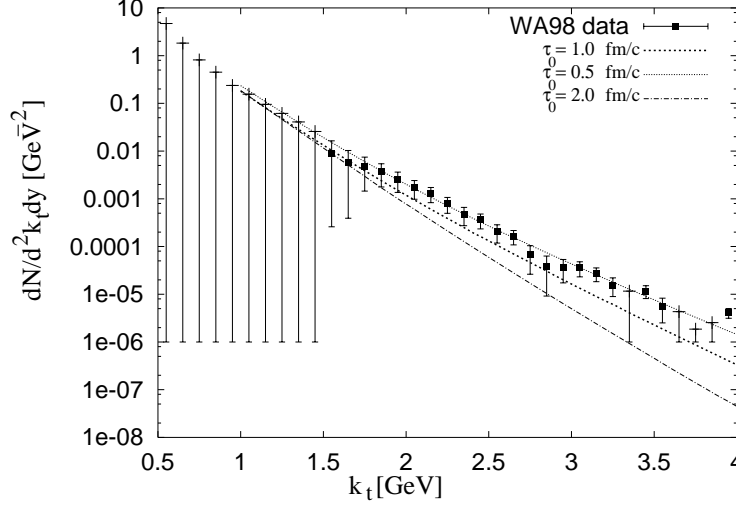
FIGURE 8.7: The thermal photon emission spectrum for different choices of the equilibration time τ_0 as compared to experimental data [147].

of the data between 2 and 2.5 GeV is already bad for the choice $\tau = 2.0$ fm/c. As we have seen, this cannot be cured for any value of intrinsic transverse parton momentum, so equilibration cannot happen much later than after a proper time $\tau_0 \approx 1$ fm/c.

In [155], it was found that a description of the data within a hydrodynamical framework was possible, provided one assumes an equilibration time as short as 0.2 fm/c. This is clearly out of range of the present analysis. The main reason for this discrepancy lies in the use of the EoS of an ideal gas of quarks and gluons in [155]. In the framework presented here, the quasiparticle properties of the QGP near the phase transition naturally lead to an initial temperature which is increased by $\sim 30\%$ as compared to one calculated for the ideal QGP which in turn implies an enhanced photon yield due to the strong temperature dependence of the rate. In [156], it was shown, although still with an ideal gas EoS, that such a small value of τ_0 is unnecessary if one considers a scenario with longitudinal acceleration, since this leads naturally to increased initial temperatures as compared to longitudinal free flow.

8.4 CONCLUSIONS

Despite the strong connection between the physics of photon emission and dilepton emission, the available data sets probe a very different kinematical regime in both cases which allows to investigate distinct phases of the fireball evolution. The fact that the thermal photon emission spectrum for high transverse momenta k_t is strongly dependent on the initial temperature and the total yield is almost exclusively created within the first 1-2 fm/c of evolution time provide the unique opportunity to study the equilibration time τ_0, which is poorly constrained by other measurements.

Before we turn to more quantitative statements, let us briefly review the uncertainties of the calculation. The main flaw of the present approach is certainly the fact that the quasiparticle description has not been incorporated consistently. Specifically, the role of the confinement factor $C(T)$ in the reduction of the rate is unclear. Let us estimate the effect of neglecting $C(T)$ as follows: A typical diagram, say $q\bar{q}$ annihilation, has the structure $R_0 \sim f_D(E/T)^2 |\mathcal{M}|^2 (1 + f_B(E/T))$, with the thermal quark distributions f_D in front of the squared matrix element $\mathcal{M}$ corresponding to the process in vac-

uum and a Bose enhancement factor for the gluon emitted into the final state. The modification of the rate R with respect to the rate R_0 in the presence of $C(T)$ will read $R \sim C(T)^2 f_D(E/T)^2 |\mathcal{M}|^2 (1 + C(T) f_B(E/T))$ which is always larger than $C(T)^3 R_0$. In the case of quarks in the final state, $C(T)$ leads even to a reduced Pauli blocking (the final state modification becomes $(1 - f_D(E/T)C(T))$ which is larger in the presence of confinement).

Therefore, regardless of whether we describe a high momentum plasma particle in the quasiparticle framework or not, $C(T)^3$ can be taken as a conservative estimate of the effect introduced by the confinement factor. The rate is dominated by the evolution phase $\tau < 2$ fm/c. In this phase, the fireball temperature is always above 250 MeV, leading to $C(T) > 0.9$ and $C(T)^3 \approx 0.7$, therefore we find an uncertainty of at most 30 % by neglecting detailed quasiparticle properties. This is acceptable, given the fact that the choice of α_s in the rates suffers from similar uncertainties. What is a possibly larger source of error which cannot be estimated so readily is the fact that we have used the rate to leading order α_s, while this α_s is not a small quantity.

Given those uncertainties, the fireball evolution model is able to describe the data remarkably well for a reasonable choice of the equilibration time τ_0. As only the very first evolution phase is probed, this constitutes a nontrivial test for the parametrization of the initial longitudinal expansion velocity and the EoS. Note that in the absence of longitudinal acceleration, the fireball cools off faster and the agreement with the data disappears.

There is still considerable uncertainty regarding the role of prompt photons. However, in the region 2 GeV $< k_t <$ 2.5 GeV, the data allow to probe the thermal contribution without significant contamination by prompt photons. Focusing on this region, we found for the equilibration time 0.5 fm/c$< \tau_0 <$ 2 fm/c. In view of the above uncertainty, one comes to the conservative conclusion that the fireball has to be thermalized at time scales exceeding 3 fm/c. This agrees with the constraints given by elliptic flow and is an important piece of information in the search for the QGP. Based on the photon rate only, however, one cannot determine whether the additional thermal contribution is of hadronic or partonic origin.

Chapter 9

CHARMONIUM DISSOCIATION — A PROBE OF THE EARLY FIREBALL EVOLUTION

9.1 INTRODUCTION

The suppression of charmonium ($J/\Psi, \Psi', \chi_C\ldots$) production was first suggested as a probe for a deconfined medium in [157]. The basic idea is as follows: The charmonium states are bound by the force responsible for confinement. If such a bound $c\bar{c}$ state is immersed into a hot medium, the interquark potential is screened as deconfinement sets in (see section 3.2), leading to a break-up of the state. The freed charm quarks then end up at hadronization in pairs of D mesons. The experimental signal for this process is the observed suppression of the production of J/Ψ in A-A collisions, where the produced states are embedded into a medium after the production process, as compared to (scaled) p-p collisions, where there is no such medium present.

There are several arguments in favour of the J/Ψ as a probe for the hot medium. All of them rely on the charm mass being large. First, this fact allows to neglect thermal production of $c\bar{c}$ pairs in the heat bath, which are exponentially suppressed by a Fermi factor. The large scale set by the charmonium mass also allows for a perturbative treatment of the initial production of a $c\bar{c}$ pair, although the formation of the charmed mesons out of this pair is a generically nonperturbative process. Finally, the rareness of charm in in the medium created by the collision allows for a clean separation between medium evolution and charm evolution: charm does not contribute significantly to the evolution (thermo)-dynamics.

Unfortunately, the observation of suppression of charmed states is not an unambiguous sig-

nal for deconfinement. First observed signs of suppression in A-A collisions [158] were later explained by more conventional mechanisms already present in p-A collisions [159]. The reason is that a $c\bar{c}$ pair can be produced at any nucleon in the nucleus, which implies that a large fraction of produced pairs has to traverse a substantial part of (cold) nuclear matter before emerging in the (hot) matter produced in the course of the collision. Furthermore, in principle charmonia can also be dissociated by collision processes in hot nuclear matter, therefore experiments probe processes in all stages of the evolution from the early hard collisions until kinetic freeze-out.

There is also the possibility of charm recombination in A-A collisions. If the density of charmed quarks in the medium is sufficiently high, there is a sizable probability that a a charm and anticharm quark, which were produced at different nucleons initially, coalesce and form a new bound state. Such processes do not have an equivalent in p-p collisions and therefore lead to an enhancement of the measured charmonium production rate in A-A experiments which competes against the suppression due to the deconfined medium.

Data on the suppression of J/Ψ has been taken at the CERN SPS, where the predicted 'anomalous' suppression beyond the one observed in p-A collisions has been observed [160]. The interpretation of this data as the effect of a deconfined medium is however difficult: Other nuclear effects are known which can potentially account for the observed effect, as they scale non-linearly with the number of collision participants, which may lead to significant contributions only when one goes beyond p-A collisions. Among these effects are initial state gluon radiation [161], color excitation [162], initial state parton energy loss [163] and coherence effects [164].

In view of these uncertainties, we will in the following consider all processes leading to suppression or enhancement which can be assessed reliably within the given framework of the fireball evolution model described in chapter 5. In doing so, we will study if the data allow room for other, different mechanisms.

9.2 CHARMONIUM SUPPRESSION IN DIFFERENT PICTURES

The potential between two static coloured sources can be studied in lattice simulations (see chapter 2). In [165], such studies were carried out for the case of 3 flavour QCD. The resulting temperature dependence of the potential is shown in Fig. 9.1.

The potential displays two regions: For $\sqrt{\sigma} > 2 - 3$, the potential is essentially flat, indicating that the colour string responsible for the linear growth of the potential in pure SU(3) can be broken by $q\bar{q}$ pairs (see section 3.3). In the region $\sqrt{\sigma} < 2 - 3$, a Coulomb-like behaviour persists, which shows a strong temperature dependence due to screening effects. Specifically, the potential gets much shallower for $T > T_C$, thus reducing the binding energy.

One can parametrize these results, solve the Schroedinger equation for a bound state of charm quarks and determine the break-up temperatures of the different charmonium states in this way. This has been done in [166]. In doing so, one utilizes a rather idealized picture of the conditions realized in heavy-ion collisions. First of all, lattice calculations assume static sources. This should be in principle a good approximation due to the large charm mass, but a possible movement of the produced charmonium relative to the surrounding fireball matter is not taken into account. Furthermore, the application of lattice results require that charmonia are thermalized along with all the fireball matter, but this is a non-trivial assumption as charmonia are rather tightly bound and require the interaction with an
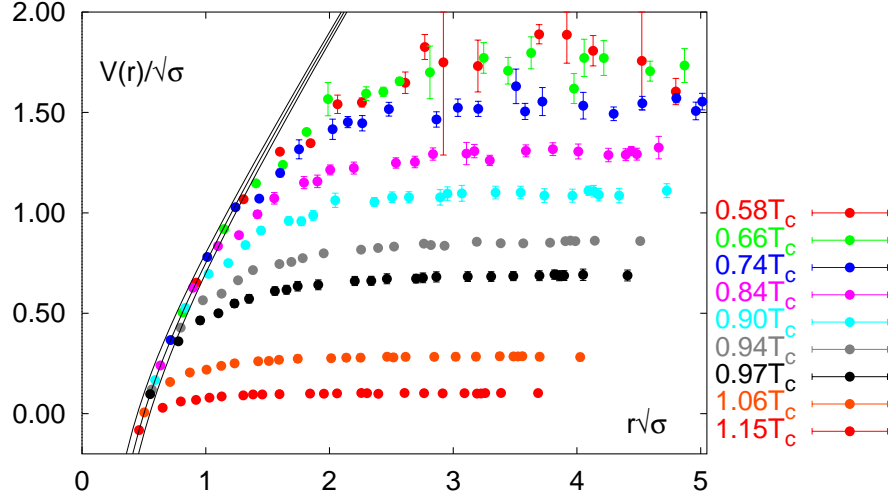
FIGURE 9.1: Temperature dependence of the heavy quark potential in 3 flavour QCD measured on the lattice [165]. Here, σ denotes the string tension.

energetic gluon from the heat bath for breakup. Specifically, there is a relation between the observed screening and the collision of gluons from the heat bath with the bound object: The interquark potential can be written as

$$V(\mathbf{r}) \sim \int d^3k \frac{e^{i\mathbf{kr}}}{k^2 - (m^2 + \Pi(k,T))} \qquad (9.1)$$

The medium modifications of the potential thus enter via the polarizability in the static limit $k_0 = 0$, or, in other words, the self-energy insertion of the field quanta Π, which depends on momentum k and temperature T. As already discussed in chapter 7, self-energies of particles stem from a diagrammatic expansion like Fig. 7.1. In Eqs. (2.6), (2.7) and (2.17) to (2.20) we saw that the propagation of particles in a thermal medium can be explicitly separated into a $T = 0$ part and a temperature dependent part. Indicating this schematically into the diagrammatic approach, we find the situation depicted in Fig. 9.2.
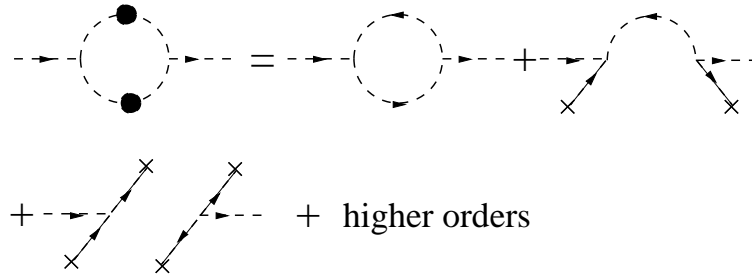
FIGURE 9.2: The lowest orders in the diagrammatic expansion of $\Pi(k,T)$. Here, we have separated vacuum propagation from thermal propagation: In the last two diagrams, particles from the heat bath (marked by x) scatter with the propagating particle and enter the heat bath again.

Thus we see that a substantial part of the modification of the heavy-quark potential can be described in terms of particles from the heat bath scattering off the colour string.

This immediately leads to an alternative (and more dynamical) description of J/Ψ dissociation by scattering with particles from the heat bath. This description can be cast into

the framework of rate equations, which allows for a time-resolved study of the dissociation process, in doing so avoiding question of charm equilibration.

Thus, we end up with two possibilities: Charmonium dissociation can be described in terms of the temperature dependent screening as observed in lattice calculations. Here, the full QCD dynamics enters, but the results can only be obtained in a situation which is very far from the physics realized in a heavy-ion collision. On the other hand, the dissociation process can be described in terms of scattering processes. In doing so, part of the dynamics is necessarily neglected, however, the treatment is more adapted to the rapidly changing conditions inside a fireball. One has to take care, however, that both views are not mixed: Introducing both approaches in a single model framework is corresponds certainly to some degree of double-counting. In the following, we will pursue the second approach and describe charmonium dissociation in terms of scattering processes.

9.3 THE FATE OF CHARMONIA

In order to discuss the evolution of charmonia inside the fireball, we must first establish the initial distribution of charmonia created in the hard collision processes preceeding the creation of thermalized matter. In the following, we will make the (simplifying) assumption that all charmonium states are indistinguishable and only discuss the evolution of a generic state Ψ.

Directly after their production, the states Ψ are subject to dissociation due their subsequent propagation through the nucleus ('normal nuclear absorption'). After we have accounted for that effect, the charmonia are placed in the medium. We use the evolution model introduced in chapter 5 to model the conditions inside the fireball. The energy dependence of the charm dissociation cross section by gluons is specified and the time dependence of the charmonium density within rate equations is then calculated. We do not take into account dissociation processes in the hadronic phase after the phase transition, instead, we consider the suppression obtained in our model a lower bound.

9.3.1 Charm production

The first step of the calculation is to assess the distribution of $c\bar{c}$ pairs in the initial hard collisions. The production of charmed quarks is commonly described within perturbative QCD. The perturbative approach is strictly valid only for processes involving large virtualities, usually provided by large momentum exchange or large masses. In the present case the smallest scale is that of the charm quark mass $m_c \simeq 1.5$ GeV, implying that perturbation theory at lowest order is inadequate. Moreover, computations are accurate only large enough transverse momenta p_T, whereas small values of p_T contribute significantly to total yields.

In the following discussion we will consider a minimal approach, neglecting features which are sub-dominant and do not influence the quality of the results. We therefore restrict ourselves to the leading order treatment presented in [167, 168], with suitable adjustments in order to meet phenomenology. We consider the leading processes $q\bar{q} \to c\bar{c}$ and $gg \to c\bar{c}$. In terms of their elementary differential cross sections $d\hat{\sigma}_i/d\hat{t}$, the spectrum of c quarks produced in pp collisions at rapidity y_c and transverse momentum p_T is

$$\frac{d\sigma_{pp}^c}{dy_c\,dp_T^2} = K \int dy_{\bar{c}} \sum_{i=u,d,s,g} x_1 f_{i/p}(x_1, \mu_c^2)\, x_2 f_{i/p}(x_2, \mu_c^2)\, \frac{d\hat{\sigma}_i}{d\hat{t}}\,, \qquad (9.2)$$

where $x_{1,2}$ are the momentum fractions of the partons in the colliding protons. The factorization scale is taken at $\mu_c = 1.4$ GeV, which is of the order of the c quark mass, and an empirical scaling factor $K = 2$ is used. We employ the GRV94LO parton distributions $f_{i/p}$ and neglect the effect of intrinsic transverse momentum of partons. In this way it is possible to effectively reproduce to good accuracy the next-to-leading order computations for total (y_c- and p_T-integrated) charm production as computed in [168] and conveniently parametrized in [169].

To estimate the spectrum of c quarks in AB collisions, the simplest approach is to scale the pp result with the overlap function

$$T_{AB}(b) = \int d^2s \, T_A(s) \, T_B(\tilde{s}) \tag{9.3}$$

being $T_{A,B}(b) = \int dz \, \rho_{A,B}(z, b)$ the usual overlap functions as longitudinal integral of the nuclear densities $\rho_{A,B}$ and $\tilde{s} = |\mathbf{b} - \mathbf{s}|$.

On the other hand, as the collision energy increases, shadowing effects are expected to become important, reducing the total yield [170]. Another correction to be introduced is the Cronin effect on the transverse momenta of partons. This results in a broader p_T spectrum of charmed quarks. For simplicity we neglect these effects. The charmed quark spectrum in AB collisions is then computed as

$$\frac{dN_{AB}^c}{dy_c \, dp_T^2}(b) = \frac{d\sigma_{AB}^c}{dy_c \, dp_T^2} \, T_{AB}(b) \,. \tag{9.4}$$

A comparison of the total number of charm quarks $N_c = \sigma_c/\sigma_i n$ produced, for example, in a Au-Au collision can be obtained by integrating the spectrum given in the latter equation.

9.3.2 Charmonium production

The description of charmonium production in nuclear collisions is a more complicated task as compared to $c\bar{c}$ production. At the root of the problem lies the fact that exclusive production of composite particles in hadronic collisions is basically a non-perturbative process. Only at large transverse momenta it is possible to make robust predictions for the spectra. Nevertheless, at least at the phenomenological level, much work has been done in order to understand the physics underlying the results of several experiments. Let us first consider p-p collisions

For later use we need the p_T spectrum of Ψ at mid-rapidity. In the following we assume a Gaussian form for the p_T-dependent part, with width parameter $\Lambda = 1$ GeV. The rapidity modulation can be inferred from the relation $d\sigma/dy \sim x_1 g(x_1) \, x_2 g(x_2)$ where $xg(x) \sim (1-x)^5$ is the gluon distribution in the proton and $x_{1,2} = (m_\Psi/\sqrt{s}) \exp(\pm y)$. For the overall normalization we use the parametrization for the total charmonium production cross section [171]

$$\sigma_{pp}^\Psi(s) = 2 \, \sigma_0 \, (1 - m^\Psi/\sqrt{s})^n \,, \tag{9.5}$$

where $\sigma_0 = 1.28 \, \mu$b and $n = 12$.

We can write the invariant Ψ spectrum in p-p collisions as

$$\frac{d\sigma_{pp}^\Psi}{dy \, d^2p_T} = \sigma_{pp}^\Psi(s) \, F(s, y) \, (\pi\Lambda^2)^{-1} \exp(-p_T^2/\Lambda^2) \,, \tag{9.6}$$

where the y-dependent part is

$$F(s, y) = C(s) \left[1 - 2(m_\Psi/\sqrt{s}) \cosh y + m_\Psi^2/s \right]^5 \tag{9.7}$$

while $C(s)$ is chosen to satisfy the constraint $\int dy \, F(s, y) = 1$.

9.3.3 Nuclear absorption

We now consider nuclear effects, starting with the simpler case of p-A collisions. It has been shown that the experimental results on charmonium production can be explained using

$$\sigma_{pA}^{\psi} = \sigma_{pp}^{\psi} \int d^2b \, T_A(b) \, S_A^{abs}(b) \tag{9.8}$$

for the total production cross section. The factor

$$S_A^{abs}(b) = \frac{1 - \exp\left[-\sigma_{\psi N}^{abs} T_A(b)\right]}{\sigma_{\psi N}^{abs} T_A(b)} \tag{9.9}$$

is the survival probability for Ψ to escape the nucleus without being dissociated. It includes the effective absorption cross section $\sigma_{\psi N}^{abs}$, a quantity of the order of 3 mb for mid-rapidity Ψs as measured at $E_{lab} = 800$ GeV at Fermilab, while it amounts to $5 - 7$ mb for mid-rapidity Ψs as measured at $E_{lab} = 158 - 200$ GeV at the SPS. The absorption cross section parametrizes various poorly known effects, with varying importance depending on the collision energy. Among these effects are the presence of color degrees of freedom in the dynamics of colliding nucleons, initial state parton energy loss and coherence length and shadowing effects. A common property of all of the above is the linear dependence on the path length, at least to leading order. Using Eq. (9.9) can therefore be justified, provided a suitable re-scaling and re-interpretation of $\sigma_{\psi N}^{abs}, \to \sigma_{\psi N}$ and $S_{A,B}^{abs} \to S_{A,B}^{NUC}$ is done.

When looking at Ψ production in nucleus-nucleus (AB) collisions, one can estimate the cross section for a given impact parameter by generalizing Eq. (9.8). The effects of the produced medium are the central topic of this paper and will be thoroughly discussed in the following sections. neglecting them for the moment, one obtains

$$\frac{dN_{AB}^{\Psi}}{dy\, d^2p_T}(b) = \frac{d\sigma_{pp}^{\Psi}}{dy\, d^2p_T} \, T_{AB}(b) \, S_{AB}^{NUC}(b) \,, \tag{9.10}$$

where nuclear effects are included in the suppression function

$$S_{AB}^{NUC}(b) = T_{AB}^{-1}(b) \int d^2\vec{s} \, T_A(s) \, S_A^{NUC}(s) \, T_B(\tilde{s}) \, S_B^{NUC}(\tilde{s}) \tag{9.11}$$

which has the obvious property $S_{AB}^{NUC} < 1$ and $S_{AB}^{NUC} \to 1$ if $\sigma_{\psi N} \to 0$.

Since nuclear effects depend on energy, we have chosen $\sigma_{\psi N}^0 = 5$ mb at the SPS energy $\sqrt{s_0} = 17.3$ GeV in order to be in agreement with the p-A measurement, and assumed the relation

$$\sigma_{\psi N}(s) = \sigma_{\psi N}^0 \, (s/s_0)^{\lambda} \tag{9.12}$$

with $\lambda = 0.2$ in order to simulate nuclear effects as predicted in [172].

9.3.4 The charmonium dissociation cross section

We will now discuss how charmonium states will interact with the quarks and gluons from the produced medium. To lowest order one might expect that the two processes illustrated in Fig. (9.3) are contributing to Ψ dissociation. On the other hand, a quark can interact only via gluon exchange. Within the spirit of the quasiparticle model, the process labelled (b) in the figure is effectively already included in the definition of the temperature dependent gluon mass. Computing both contributions would cause an erroneous double counting. In other words, Ψs only see quasiparticle gluons in the plasma.
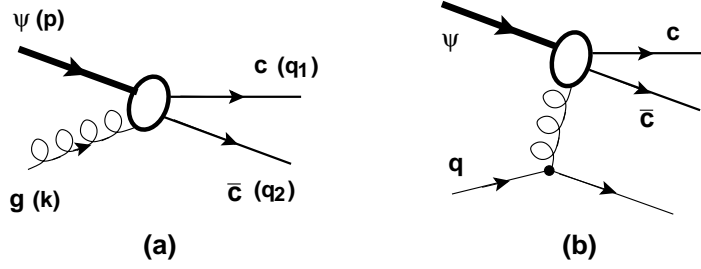
FIGURE 9.3: Diagrams contributing to lowest order to Ψ dissociation. The process involving a gluon quasiparticle (a) exhausts the amplitude since it already takes into account the one involving a quark quasiparticle (b).

Concentrating now on the process labelled (a) in Fig. (9.3) we come to the problem of computing a cross sections involving a relativistic bound state. In the present case one can argue that the $c\bar{c}$ system is, to first approximation, non-relativistic, greatly simplifying the treatment.

Moreover, as was done originally by Bhanot and Peskin [173, 174] one can argue, justified to some extent by the magnitude of the heavy quark mass, that the lowest lying levels of a quarkonium can be described by the Coulomb part of the potential. Then, use operator product expansion techniques or more recent non-relativistic factorization techniques [175], it is possible to obtain the analytic expression

$$\sigma_D(\omega) = \frac{2\,\pi}{3}\left(\frac{32}{N_c}\right)^2 \frac{1}{\mu^{3/2}\epsilon^{1/2}} \frac{(\omega/\epsilon - 1)^{3/2}}{(\omega/\epsilon)^5} \tag{9.13}$$

for the gluon dissociation process of a heavy quarkonium. It is a function of the gluon energy ω in the rest frame of the quarkonium and contains the threshold energy ϵ and the mass scale μ, related to the heavy quark mass. The threshold energy is related to the binding energy ϵ_0 by the condition that $s = (p + k)^2 > 4m_c^2$ which implies that $\epsilon = \epsilon_0 + \epsilon_0^2/(2m_\Psi)$. While the above formula appears to be applicable for bottomonium, in the case of charmonium it is certainly a more serious approximation. Inclusion of higher states is in principle necessary in order to have a reliable description of the dissociation process, together with formation as will be discussed next. All this can be done within a potential model for the $c\bar{c}$ system, but such a study falls beyond the scope of the present treatment.

In what follows the binding energy is taken to be $\epsilon_0 = 780$ MeV and the mass parameter is $\mu_c = 1.95$ GeV, as chosen in [174] to fit the mass values of the first two levels (J/ψ and ψ') of the charmonium system.

9.3.5 Kinetic description of charmonium evolution

Having specified the cross section for the process $\Psi + g \rightarrow c\bar{c}$, one might ask about the inverse process. Indeed, there is a possibility for charmonium recombination due to $c\bar{c}$ fusion, and the cross section can be inferred from Eq, 9.13 by detailed balance arguments. However, the average charmonium production rate at SPS is less than one in a central collision, i.e. the charm density is small and recombination processes are not very important. On the other hand, such processes might play a role at RHIC or LHC energies, therefore we present a complete treatment including a charm formation term here but neglect the latter in practical calculations for SPS.

The natural framework in which to study the time evolution of Ψ is that of kinetic theory. We make use of a semi-classical treatment, setting up a relativistic Boltzmann equation for the Ψ phase-space distribution. The collision term, which contains interaction cross sections, provides the interface between charm and the medium. More in detail we have

$$p^\mu \partial_\mu f_\Psi(p) = \int \frac{d^3k}{E_k} \frac{d^3q_1}{E_1} \frac{d^3q_2}{E_2} \, \delta^4(p{+}k{-}q_1{-}q_2) \, W_{c\bar{c}\leftrightarrow\Psi g} \left[f_c(q_1) f_{\bar{c}}(q_2) - f_\Psi(p) f_g(k) \right] ,$$
(9.14)

which is the Boltzmann equation for f_Ψ, characterized by a collision term containing the interaction probability $W_{c\bar{c}\leftrightarrow\Psi g} = W_{\Psi g\leftrightarrow c\bar{c}}$. Kinematics is such that p is the Ψ momentum, k the gluon one and q_1 and q_2 the c and $\bar{c}$ momenta. We have suppressed the normalization factors 2πs of phase space for clarity. Due to the δ-function, some of the phase space integrals can be carried through, leading to the intuitive result

$$(\partial_t + \mathbf{v}\cdot\partial_r) \, f_\Psi(\mathbf{r}, \mathbf{p}, t) = -\lambda_D(\mathbf{r}, \mathbf{p}, t) \, f_\Psi(\mathbf{r}, \mathbf{p}, t) + \lambda_F(\mathbf{r}, \mathbf{p}, t) .$$
(9.15)

The dissociation (loss) term

$$\lambda_D(\mathbf{r}, \mathbf{p}, t) = \sum_n \int d^3k \, \sigma_D^n(s) \, v_{rel}(\mathbf{k}, \mathbf{p}) \, f_n(\mathbf{r}, \mathbf{k}, t)$$
(9.16)

consists of a sum over the various constituents of the medium, each interacting with Ψ with a different dissociation cross section σ_D^n. v_{rel} is the relative velocity between Ψ and constituent n. The center of mass energy is $s = (p + k)^2$ while the relative velocity $v_{rel}(\mathbf{k}, \mathbf{p}) = F_{\Psi g}(s)/E_p E_k$, with $F_{\Psi g}(s) = \sqrt{[s - (m_\psi{+}m_g)^2][s - (m_\Psi{-}m_g)^2]}/2$. In principle n labels different degrees of freedom depending on the elapsed time. At early times the medium constituents are quasiparticles quarks and gluons, later on hadrons. The formation (gain) term

$$\lambda_F(\mathbf{r}, \mathbf{p}, t) = \int d^3q_1 \, \sigma_F(s) \, v_{rel}(\mathbf{q_1}, \mathbf{q_2}) \, f_{\bar{c}}(\mathbf{r}, \mathbf{q_1}, t) \, f_c(\mathbf{r}, \mathbf{q_2}, t)$$
(9.17)

describe the coalescence process of Ψ formation by c and $\bar{c}$ quarks. Here the center of mass energy is $s = (q_1 + q_2)^2$ while the relative velocity $v_{rel}(\mathbf{q_1}, \mathbf{q_2}) = F_{c\bar{c}}(s)/E_1 E_2$, with $F_{c\bar{c}}(s) = \sqrt{s(s - 4m_c^2)}/2$. Implicit in the last equation there is the approximation that the position of the quarks c and $\bar{c}$ are the same at coalescence. This is reasonable, since the relative position has to be compared with the typical size of the whole system, which is more than an order of magnitude larger.

Consistently with the model for the medium described in chapter 5, we assume to have a system which expands as function of proper time in a cylindrical volume where densities are uniform. Changing variables such as $t = \tau \cosh(\eta)$ and $z = \tau \sinh(\eta)$ greatly simplifies the description.

Integrating over Ψ transverse momenta we can reduce Eq. (9.15) to the much simpler first order differential equation

$$\frac{d}{d\tau} N_\Psi^y = -\sum_n \langle\langle \sigma_D^n v_{rel} \rangle\rangle \rho_n N_\Psi^y + \langle\langle \sigma_F v_{rel} \rangle\rangle \rho_{\bar{c}} N_c^y ,$$
(9.18)

which now depends on the proper time τ. The double brackets indicate average over the momenta of the initial particles, except for the last rapidity integral which is left undone. In other words

$$\langle\langle \sigma v_{rel} \rangle\rangle = \frac{\int d^2p_a^T \, f_a(p_a) \int d^3p_b \, \sigma v_{rel}(p_a, p_b) f_b(p_b)}{\int d^2p_a^T \, f_a(p_a) \int d^3p_b \, f_b(p)} ,$$
(9.19)

where p_a and p_b indicate Ψ and g momenta for dissociation, while c and $\bar{c}$ momenta for formation. We insist that leaving the y-integration is important since we intend to compute the value of the final Ψ rapidity distribution at mid-rapidity, and not the whole yield. Notice that also N_c^y is a rapidity density, while the charm density is $\rho_{\bar{c}} = \rho_c = N_c/V$. The medium constituent's density is denoted by ρ_n.

It is clear that an equation analogous to (9.18) but with opposite sign on the r.h.s. is necessary for charm in order to ensure its conservation as function of time. This means that the initial (constant) total amount of charmed quark pairs is $N_c^0 = N_\Psi + N_c$, implying that, strictly speaking, Eq. (9.18) can be re-written as a Riccati equation, whose solution can be obtained only numerically. On the other hand, at each rapidity it is a good approximation to assume that the total charm distribution equals the distribution of unbound quarks $N_c^y = N_{\bar{c}}^y \gg N_\Psi^y$, allowing to simplify the rate equation to

$$\frac{d}{d\tau} N_\Psi^y(\tau) = -\lambda_D(\tau)\, N_\Psi^y(\tau) + \lambda_F(\tau)\,, \tag{9.20}$$

with the rates now assuming the form

$$\lambda_D(\tau) = \sum_n \langle\langle \sigma_D^n\, v_{rel} \rangle\rangle(\tau)\, \rho_n(\tau) \quad \text{and} \quad \lambda_F(\tau) = \langle\langle \sigma_F\, v_{rel} \rangle\rangle\, N_c^0\, N_c^y / V(\tau)\,, \tag{9.21}$$

where we have explicitly indicated where time dependence appears. In particular the dissociation term is time dependent also because of the implicit temperature dependence in the phase space density of the medium, used to average the dissociation cross section. On the other hand, since charmed quark distributions are time independent, the formation cross section is also.

Having reduced the Boltzmann equation to a much simple one, consistently with the description of the medium as being spatially uniform, it is possible to integrate directly Eq. (9.20), obtaining a simple solution which can be written in closed form as

$$N_\Psi^y(t) = \left\{ N_\Psi^y(0) + \int_{t_0}^t dt'\, \lambda_F(t')\, \exp\left[\int_{t_0}^{t'} dt''\lambda_D(t'') \right] \right\} \exp\left[-\int_{t_0}^t dt'\lambda_D(t') \right]\,. \tag{9.22}$$

The structure of the solution is quite self-evident. Neglecting formation we obtain the usual exponential suppression, while the formation term becomes important as soon as the number of charmed quarks becomes large enough. This is expected to be the case as the collision energy increases, eventually overwhelming suppression.

9.4 RESULTS

Using the elements of the calculation as discussed in the previous sections, we are now in the position of computing observables. We start from the case of Pb-Pb collision at $\sqrt{s} = 17.4$ GeV ($E_{lab} = 158$ GeV) and use the solution of the kinetic equation given in Eq. (9.22). This is done as function of the impact parameter b. The result is divided by the number of collisions, which provides the centrality dependence of the Drell-Yan cross section. The normalization is fixed at 50 and the ratio Ψ/DY as function of b is converted into a function of the measured transverse energy with a simplified version of the standard procedure [176]. In fact, here we do not perform the usual convolution with the $E_T - b$ correlation function, but scale the mean transverse energy with the b dependence coming from the number of participants as

$$E_T(b) = \epsilon_T\, N_p(b)\,. \tag{9.23}$$

The quantity $\epsilon_T = 0.297$, which represents the amount of produced transverse energy per participant, is used in order to describe correctly the total inelastic (minimum-bias) cross section as function of centrality. In this way we arrive at the results plotted in Fig. (9.4). The agreement with data is quite remarkable and the whole result deserves some detailed comments. First of all it is immediately obvious that the curves end at $E_T \simeq 110$ GeV, which corresponds to $b = 0$. To go beyond this point it is necessary to include effects of fluctuations, which are quite straightforward to address [177].
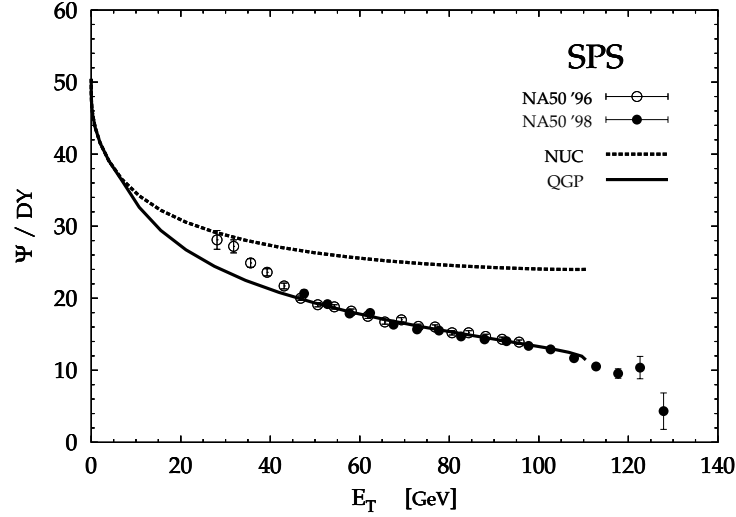
FIGURE 9.4: Result at SPS energy for the ratio Ψ/DY as function of the transverse energy. The dashed curve includes only nuclear effects, while the full line is the complete result including gluon dissociation

An important finding is that hadronic dissociation of Ψ is ruled out, not because cross sections are small, rather because the hadronic number density is more than an order of magnitude lower than the partonic one, and only a fraction of fm^{-3} already at hadronization. This is also apparent from Fig. 9.5 where we show particle densities for the relevant degrees of freedom as a function of the temperature. Clearly, the density of particles in the early evolution phase is orders of magnitude larger than in the hadronic phase.

For $E_T < 40$ GeV, a systematic deviation of the model calculation from the data is visible. This should not be a surprise: A thermalized fireball model as the one used in the present approach is ill suited to describe very peripheral collisions, so one should expect at some transverse energy. As the impact parameter of the collision increases, the number of participants gets less and less. Therefore, thermalization gets more and more difficult, which should be manifest in an increase of the thermalization time τ_0. Increasing τ_0, however, directly reflects in an increased initial volume, which in turn translates into a lower entropy density corresponding to a lower initial temperature. Effectively, the duration of the partonic phase is reduced, resulting in a decrease of the associated suppression factor. Therefore, for very peripheral, unthermalized events one should recover the normal nuclear absorption only, which is also displayed by the data.

9.5 CONCLUSIONS

Of all the data presented so far, the results on charmonium suppression are the ones most closely linked to the properties of a partonic medium. Apart from theoretical expectations
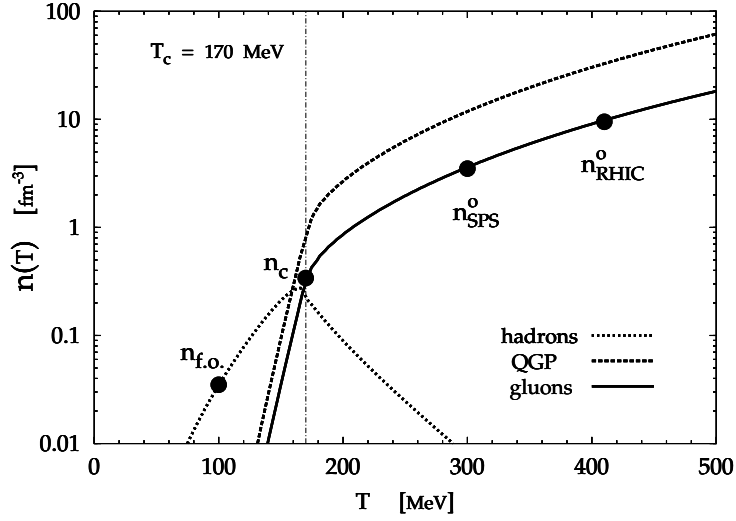
FIGURE 9.5: Particle densities as a function of the temperature T in the hadronic and partonic phases. Here, $n_{f.o.}$ denotes the freeze-out density of the fireball, n_c the critical density, n^i_{SPS} the initial quasiparticle gluon density at SPS and n^i_{RHIC} the corresponding value at RHIC. The vertical line indicates the value of the critical temperature $T_c = 170$ MeV.

concerning screening of the binding potential, however, there is little *direct* evidence for the creation of a QGP. On the other hand, charmonium suppression yield a valuable bit of information to be combined with other observables.

The data show a strong absorption due to effects of the produced medium. If one does not assume that cross sections for charmonium in A-A collisions are an order of magnitude different from those in p-A collisions, then this medium has to be a very dense one. A priori, however, it is unclear if this dense medium is of hadronic or partonic origin.

But if we make use of the information from other measurements, we may reason as follows: The existence of elliptic flow (see section 5.2.4) indicates early thermalization. If we now use the EoS as found in lattice calculations (as appropriate for a thermalized medium) we can calculate the temperature of a medium with given number- and entropy density. In doing so, we find that only a partonic medium can provide the necessary particle densities for the observed charmonium suppression. In that sense, charmonium suppression gives indirect evidence for the production of a QGP.

It is clearly reassuring that the charmonium suppression scenario described here agrees well with the fireball evolution which is constrained by independent observables, thus supporting the approach. However, one has to keep in mind that there are still several unresolved issues: The precise value of the charmonium dissociation cross section is not well known. This translates into an overall uncertainty regarding the normalization of the suppression. Furthermore, the problem of screening versus dissociation by scattering indicated in section 9.2 is not solved completely. Clearly, for a spatially averaged fireball evolution model as presented here, it is preferable to consider at least the time evolution of the suppression, but this is at the expense of incorporating only part of the QCD dynamics. However, the fact that the data are so well described by the rate equations may hint that the relevant processes are already incorporated. This subject certainly requires further investigation.

In contrast to the dilepton data, charmonium suppression is more sensitive to the early stages of the fireball evolution. This is fortunate, as it allows to probe both hadronic and partonic phase in complementary measurements. The suppression of charmonia is sensitive

to the four-volume of the early evolution: The longer the system remains in a given temperature region the more dissociation will happen and the 3-volume of the fireball enters via the density of scattering partners.

Once one tries to model the evolution of the charmonium density at RHIC or LHC, it is mandatory to include not only the 'loss' terms due to collisional dissociation, but also 'gain' terms, $c\bar{c}$ coalescence where charm and anticharm were created in different processes. As the density of charmed quarks grows, coalescence processes will eventually dominate and lead to an enhancement of the measured charmonia as compared to p-A collisions. At the moment, however, determining the degree of thermalization of the produced quarks (which is necessary to model their momentum distribution) is still a difficult task.

Chapter 10

SUMMARY AND CONCLUSIONS

10.1 SUMMARY

In the present work, an overview over the physics of ultra-relativistic heavy-ion collisions has been given with the aim of discussing the quest for the quark-gluon plasma. This is a vast subject, as physics from many different areas has to be combined to gain an understanding of the processes occurring in the course of such a collision.

In the initial stages of the collision, one deals with hard processes like Drell-Yan and jet events, which prepare the distribution of particles for the later phases of the evolution. These processes are in principle calculable in perturbative QCD. However, secondary particle production quickly lowers the relevant energy scales and limits the validity of pQCD predictions. Ultimately, the hard physics seems to culminate in particle distributions in equilibrium or very close to equilibrium. This appears to happen after a short period of time of only a few fm/c. Evidence from both theory (section 4.4) and experiment (section 5.2.4) has been brought forward to support this scenario.

After all initial hard scattering processes have taken place and a large fraction of the incident energy has been converted into the production of secondary particles (entropy), the properties of the system change qualitatively. In a strongly interacting system of many hundreds of particles, individual particle trajectories become unimportant. Instead, collective behaviour dominates and the properties of the system are determined by a few macroscopic parameters; a description in terms of thermo/hydrodynamics is more likely to be appropriate.

This regime of particles in equilibrium can be treated within the framework of finite temperature field theory as introduced in chapter 2. Unfortunately, a perturbative approach does not seem to be feasible in the temperature region accessible in current experiments, as the QCD coupling constant is not yet small for typical momentum transfers inside such

a system. Furthermore, we have summarized some results of such thermal pQCD calculations and shown evidence for a breakdown of the perturbative series caused by collective phenomena inside the QGP.

Instead, lattice QCD calculations seem to be the adequate tool to study the properties of thermal QCD. In chapter 3, we have summarized the expected properties of hot QCD, namely the existence of a partonic phase, the QGP, and introduced several of its key attributes: Significant changes in the EoS, the chiral transition and deconfinement. All of those features leave characteristic traces in the evolution history of a heavy ion collision. We have analyzed the relevant degrees of freedom inside the QGP phase and found that the thermodynamic properties find a natural explanation in terms of a system of weakly interacting massive plasma quasiparticles.

Returning to the experimental situation, we have summarized the space-time geometry and the different evolution phases of the fireball created in an ultra-relativistic heavy-ion collision in chapter 4. Using estimates for the initially created entropy, we argued, by using the EoS taken from the lattice simulations, that there is a natural sequence of evolution phases following the initial hard collisions: QGP $\rightarrow$ phase transition $\rightarrow$ hadronic phase $\rightarrow$ freeze-out. We have discussed in a qualitative way how this sequence of phases leaves distinct traces in experimentally accessible quantities.

In chapter 5, we reviewed extensively the wealth of experimental information gathered so far. We focused on the situation at the CERN SPS and discussed how quantitative statements on the space-time evolution of a fireball can be extracted from observables like the rapidity distribution of produced particles (section 5.2.1), transverse momentum spectra (section 5.2.2) and HBT interferometry measurements (section 5.2.3). All these observables show strong evidence for collective phenomena like radial flow.

Experimental information from hadronic momentum spectra can only determine the evolution endpoint, the kinetic freeze-out. On the other hand, overlap calculations help to constrain the initial fireball geometry. Assuming local thermal equilibrium at all times, we have used the lattice EoS as represented in the quasiparticle picture as a link to connect initial and final state by an dynamical evolution model in the remainder of the chapter. This model has been constructed in such a way as to be in agreement with all hadronic observables discussed so far. No additional information is put in by hand. Therefore, the evolution model is completely constrained by the available data. Furthermore, we have discussed the possible extension of the scenario to situations where no detailed knowledge of the freeze-out geometry is available. In the last part, we reviewed the data situation at RHIC and suggested a plausible fireball evolution scenario for the collider kinematics.

In the next series of chapters, we turned to several special processes happening in the course of the fireball evolution and examined their potential to yield signals for the creation of a partonic phase.

First, in chapter 6, we discussed hadrochemistry, the relative abundance of hadronic species measured after freeze-out. It turns out that the experimentally measured abundancies can be naturally explained by the picture of subsequent chemical and thermal freeze-out. Assuming the hadron ratios to be fixed at the phase transition, we have shown that good agreement of the fireball evolution model suggested in chapter 5 with the data is achieved. Contrary to previous works, we have not used a fit procedure to find the relevant thermodynamical parameters, temperature T and baryochemical potential μ_B, but rather fixed them beforehand by the evolution model.

There is, however, a caveat in this statistical hadronization model: There are both experimental and theoretical indications that particles embedded into a hot medium undergo modifications of mass and width. Therefore, we have tested the possibility of mass shifts, increased widths and increases of particle radii in a schematic way. We found that there

is little room for both mass shifts and width increases alone, however, the effects of an increase in the core radius of particles can to some degree counterbalance the effects of the other modifications, therefore there is a possibility to consistently introduce in-medium modifications of particles into an analysis of the hadrochemistry. Due to the limited knowledge of hadron properties near the phase boundary, all these statements are on a very qualitative level though.

In chapter 7, we discussed the emission of lepton pairs from the fireball. Electromagnetic probes, such as photons and dileptons, are interesting since they are capable of leaving the interaction region without rescattering. Therefore they carry direct information on all evolution phases. As a new key ingredient to the emission rate, we have presented the spectral function of a virtual photon in both the hadronic and the partonic phase calculated using methods of perturbative thermal field theory. Here, in-medium modifications as discussed qualitatively in chapter 6 show up explicitly in the vector meson channels at finite temperature and/or baryon density.

The model calculation is able to describe the data well for both 40 and 158 AGeV collisions. We found that the invariant mass spectrum of dileptons below 1.2 GeV where data from CERES exists is mainly dominated by contributions from the hadronic phase. This is caused by the significantly larger radiating four-volume as compared to the partonic phase. The observed enhancement of dilepton yield in the region below the ρ mass can be explained by a strong broadening of the ρ peak due to finite baryon density effects. However, the most crucial result is that the fireball evolution also describes the late part of the evolution (as probed by the emission of the hadronic phase) rather well. This is not trivial, as hadronic observables only reflect the conditions at kinetic freeze-out, not the dynamical evolution. We concluded the chapter by giving predictions for the invariant mass spectrum of emitted dileptons at RHIC. Here we have found qualitative differences due to the fact that the baryon density is significantly lowered, as a similar number of participant nucleons is distributed across a larger rapidity interval. Most prominently, the vector meson peaks are expected to appear more pronounced.

Chapter 8 has presented an investigation of thermal photon emission from the fireball. We have argued that, in spite of the fact that the physics of photon and dilepton emission is closely related, data have been taken in very different kinematic regimes, thus allowing to study two different aspects of the fireball evolution. Due to the breakdown of the simple quasiparticle picture in the case of real photon production, we have used the perturbative emission rates to order α_s and have argued a posteriori that the errors introduced this way are small.

We find good agreement to the data obtained by the WA98 collaboration for 10% most central Pb-Pb collisions at SPS using our standard model for the spacetime evolution of the fireball. The rate turns out to be almost exclusively dominated by the first moments of the evolution, especially for large photon transverse momenta. We have made use of this sensitivity to get an estimate for the equilibration time τ_0 which is poorly constrained by other measurements and have argued that the fireball has to be thermalized at latest after 3 fm/c, but not earlier than 0.5 fm/c. Again, the fact that initial temperature and spacetime evolution of the fireball are able to describe the data rather well is a non-trivial test for the model. Specifically, the presence of longitudinal acceleration which is crucial to account for the photon data is enforced by a careful analysis of the freeze-out state already.

In chapter 9, we continued the discussion of signals for the production of a QGP with charmonium suppression. There are different ways to look at the mechanism for charmonium dissociation in a plasma: We have argued in section 9.2 that there is no fundamental difference between screening the interquark potential and employing rate equations for scattering processes which destroy the charmonium state — both are related and appear to be just different levels of approximation. As it turned out to be more suitable for the purpose of

our fireball evolution model, we have used rate equations to discuss the fate of charmonia immersed into a thermal partonic medium. Using a parametrization for the charmonium dissociation cross section by quasiparticle gluons, we were able to use the fireball evolution scenario from chapter 5 to characterize the distribution of gluons for all times and solve the rate equations.

We found a good description of the data obtained by the NA50 collaboration by this scenario alone, indicating that there is little dissociation of charmonia in the hadronic evolution phase. In some sense, this finding complements the results of chapter 7, as charmonium suppression is sensitive to the *early* phase of the medium evolution. The fact that both dilepton data and charmonium data are described by the same evolution model makes certainly a strong case for the scenario described in the present work.

Naturally, not all interesting aspects and details of the field could be covered in this thesis. In many cases, only the most relevant ideas for the purpose of the specific section could be sketched whereas for further subtleties the reader is referred to the literature.

10.2   CONCLUSIONS

In search for the QGP, we started out with very general considerations, then turned towards the experimental situation and constructed a model for the evolution of the produced medium. We demonstrated that this simple model, based on an isentropic expansion of matter in thermal equilibrium, is able to describe a wealth of data. Within the framework of this model, the QGP phase is a necessary ingredient.

In the construction of the model, we have tried to minimize uncertain theoretical input by using a subset of the measured data as a guideline and constraint for the construction of our model. The framework is chosen as simple as possible within the information given by the data. The resulting parametrization of the fireball evolution can then be taken as a basis, containing essential features of the fireball evolution, on top of which additional ideas can be implemented.

There is no justification for using a simplistic model such as ideal Bjorken hydrodynamics without transverse expansion and longitudinal acceleration: Such a model has distinct differences in its space-time evolution as compared to the evolution scenario in chapter 5 and consequently fails in the description of both HBT data and transverse mass spectra, where the transverse dynamics leaves characteristic imprints. Therefore, there is also no reason to assume that the very same model should reproduce e.g. dilepton data; and even if it does — what should then be the interpretation? Clearly, the setup has to be consistent with *all* existing data. One cannot ignore a particular data set at liberty.

On the other hand, for many purposes it is unnecessary to choose a more complex model, as observable quantities are unable to resolve details of the evolution. Take for example the case of dilepton emission in the framework presented here and in a hydrodynamical evolution model: In local thermal equilibrium, the dilepton emission rate coming from a volume element dV depends only on temperature and baryon density inside dV. In a hydrodynamical evolution, the spatial distribution of temperature and density is not homogeneous, i.e. the collection of volume elements at a given proper time τ is in general different in both approaches. However, if one divides the hydrodynamical fireball into a collection of n volume elements dV_n containing each the entropy $S_n = S_0/n$, one can imagine grouping these volume elements not along sheets of constant proper time, but along sheets of constant entropy density s_0. The total volume $\sum_n dV_n(s = s_0)$ obtained in this way will exactly correspond to the volume in the simple fireball evolution characterized by the same entropy

density (which in this case also corresponds to a given proper time τ). Thus, reparametrizing the hydrodynamical fireball in terms of an evolution in the entropy density s provides a mapping into the simple approach. But *global* properties such as the freeze-out proper time and volume and the initial volume have to be very similar in both hydrodynamics and simple evolution model, as they are tightly constrained by experiment. This ensures that although the emission rate at a given proper time may be different, the space-time integral over the fireball evolution leads to very similar results.

For these reasons, we conclude that the simple fireball evolution model is indeed a valid description for gross quantities such as integrated rates, but the detailed time dependence of observables is in general not described adequately.

Keeping this in mind, let us now turn towards the results for the fireball evolution. Although we have fitted the evolution model to hadronic data only, other observables are sensitive to different phases of the evolution and therefore provide independently nontrivial cross-checks for the model. This is indicated in Fig. 10.1.
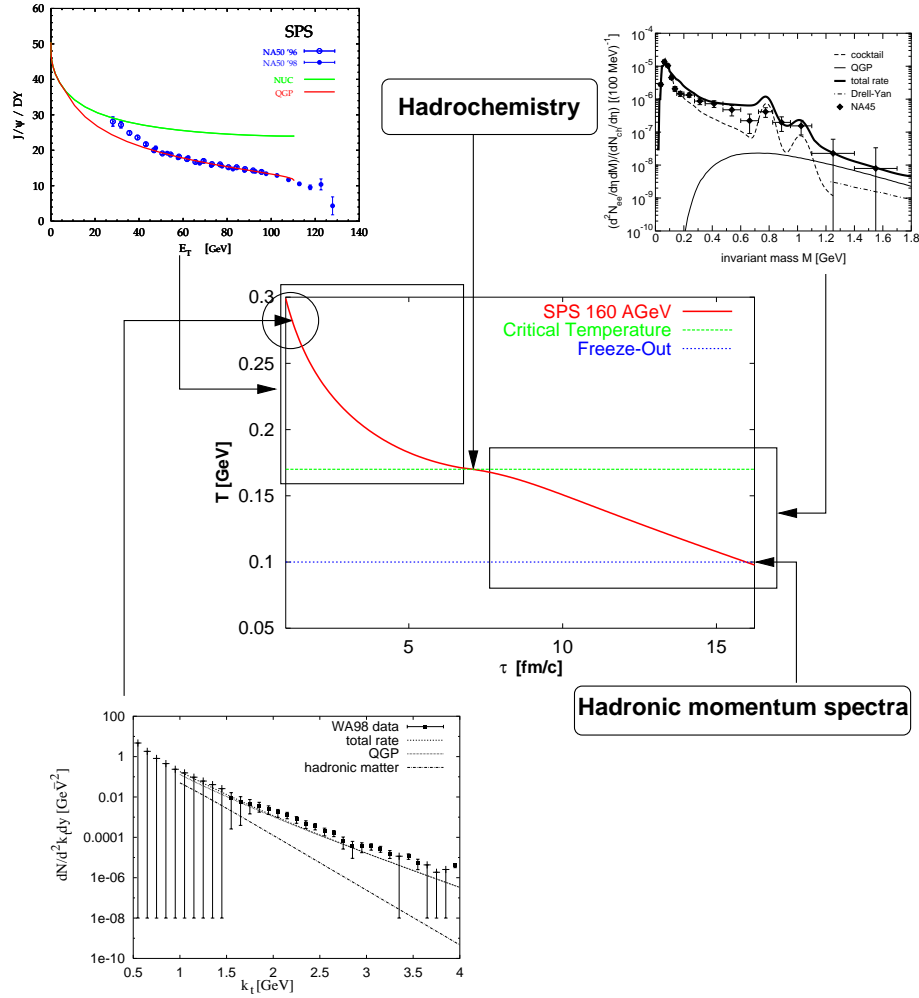
FIGURE 10.1: Temperature evolution of the fireball shown with the regions of interest for selected observables.

As described in chapter 5, hadronic momentum spectra and HBT data carry primarily information about the freeze-out state. This information can be used to determine the fireball volume and expansion velocity at freeze-out along with the corresponding temperature.

The extrapolation of these parameters backwards in time through the hadronic phase is probed by the dilepton emission rate. This quantity is sensitive to the space-time volume of the fireball and the temperature evolution in this region.

Assuming statistical hadronization and subsequent chemical freeze-out, the phase transition point is probed by the ratios of observed hadrons which depend on the fireball volume at the critical temperature T_C via the baryochemical potential μ_B. This volume in turn is determined by the EoS of the QGP as given in the quasiparticle picture (see chapter 6).

For the study of the partonic evolution phase, the suppression of charmonia is an adequate observable. This is because the number density of scattering partners for inelastic charmonium dissociation is orders of magnitude larger in the QGP phase. Here, the total suppression is sensitive to the space-time volume of the fireball and the associated temperature evolution (see chapter 9).

Finally, as argued in chapter 8, the emission of real photons at large transverse momentum k_t is sensitive to the very early partonic phase and especially to the initial temperature, the initial expansion and the equilibration time.

Thus, we find the whole evolution pattern from the early equilibration until kinetic freeze-out confirmed by a number of different observables. In the light of this information, let us now investigate the two main assumptions of the evolution model — thermalization and isentropic expansion.

In section 4.4, we have seen that early thermalization can be achieved by perturbative processes within timescales of a few fm/c. On the other hand, experimental data on elliptic flow (section 5.2.4) indicates the presence of strong secondary interactions at timescales of 2–3 fm/c. Similarly, the data on direct photon emission require the presence of strong inelastic processes in the produced medium at timescales 0.5 fm/c $< \tau < 2$ fm/c. This is certainly no proof that the system is completely equilibrated at these early timescales already, but compelling evidence that the system is at least close to equilibrium. Note that the assumption of early thermalization is well in line with the data on charmonium suppression, which is also sensitive to the early evolution.

Regarding the conservation of total entropy, the most relevant observables are given by the hadron ratios and the charmonium suppression. From the abundancies of hadronic spectra, we find that the ensemble of particles observed in the final state can be well described by resonance decays in an ensemble of hadrons in equilibrium at T_C with the same entropy. Therefore, there is no reason to assume strong entropy production in the hadronic phase.

Entropy production in the partonic phase would imply that the density of quarks and gluons is lower than in the model discussed here. Such a scenario is clearly not in line with the charmonium suppression data which require a sizeable density of scattering partners in order to achieve the observed reduction in the yield. Therefore, we have good reason to assume that entropy conservation is a useful concept for the description of the whole evolution.

In summary, the analysis presented here finds that a pronounced QGP phase is already present at SPS conditions. This phase leaves no unambiguous trace in any single observable, however, the synopsis of all observables combined with information from lattice QCD thermodynamics allows no other conclusion given the current experimental knowledge.

10.3 OUTLOOK

Naturally, there are many open questions left in the understanding of ultra-relativistic heavy-ion collisions. Even in the model framework presented here, several issues require

additional attention.

For collisions as realized at SPS energies, the model framework is most advanced due to the tight constraints on the freeze-out state. This allows to use the evolution model as a 'lab' to study interesting questions, notably the changes of vector meson properties in medium as manifest in the dilepton emission. Different shapes of the photon spectral function have been predicted by various approaches (see e.g. [39, 40, 71, 178]). The use of a 'standardized' evolution model which is well supported by other observables allows to study the differences in these approaches in comparison to data and hopefully allows to identify the relevant physics of in-medium effects.

There are yet other observables which have not been discussed quantitatively in the present work: Event by event fluctuations [36] of charge ratios (see section 4.5.2) can be calculated dynamically using the evolution model. As the beam energy increases (at RHIC and even more pronounced at LHC), new diagnostic tools become available: High momentum partons are produced in initial hard scattering processes ('jet events'). These particles experience energy loss as they traverse the produced medium, which manifests itself in a reduction of experimentally observed jets as compared to pQCD expectations ('jet quenching'). Since the energy loss is dependent on the density of the medium, this effect is capable of providing information on the early phases of the collision [179–185].

With more and more data coming from the ongoing measurements at RHIC, it will eventually become mandatory to improve the level of sophistication of the fireball evolution model in order to stay consistent with experimental results. There are indications that for RHIC conditions a longitudinal averaging procedure is not justified [98]; one should rather introduce a more detailed dependence of the thermodynamic parameters on rapidity. Similarly, in order to describe peripheral collisions, the transverse geometry has to be assessed more carefully.

We have made considerable advances in understanding qualitative aspects of the relevant physics and know the orders of magnitude involved in the physics of ultra-relativistic heavy-ion collisions. However, as far as quantitative predictions are concerned, there is still striking disagreement between different approaches of modelling a fireball. The wealth of data currently produced at RHIC will certainly lead to new insights into QCD matter under extreme conditions.

$\Pi\alpha\nu\theta\alpha\ \rho\epsilon\iota.$
'Everything is in flow.' (Heraklit)

Appendix A

PROPERTIES OF QCD

In this appendix, we summarize the properties of Quantum Chromodynamics (QCD). QCD is a non-Abelian gauge theory with the colour gauge group SU(N_C) and $N_C = 3$. There are two types of degrees of freedom in the theory: Massless spin-1 gauge bosons, the gluons A_μ^a, characterized by a Lorentz vector index μ and a colour index a ($a = 1..N_C^2 - 1$) which transform unter the adjoint representation of the group; and massive spin-$\frac{1}{2}$ fermions, the quarks Ψ, which transform under the fundamental representation and hence carry N_C different colour charges.

A.1 THE LAGRANGIAN

The dynamics of these degrees of freedom is governed by the Lagrangian

$$\mathcal{L}_{QCD} = \mathcal{L}_q + \mathcal{L}_\mathcal{G} = \overline{\Psi}(i\gamma_\mu D^\mu - \mathbf{m})\Psi - \frac{1}{4}\mathcal{G}_{\mu\nu}\mathcal{G}^{\mu\nu}. \tag{A.1}$$

This expression involves the (gauge invariant) gluon field strength tensor

$$\mathcal{G}_{\mu\nu} = (\partial_\mu A_\nu^a - \partial_\nu A_\mu^a + gf^{abc}A_{\mu,b}A_{\nu,c})t_a \tag{A.2}$$

and the quark part

$$\overline{\Psi}(i\gamma_\mu D^\mu - \mathbf{m})\Psi, \tag{A.3}$$

which is coupled to the gluon field by the gauge covariant derivative

$$D_\mu = \partial_\mu - igt_a A_\mu^a. \tag{A.4}$$

In all these expressions, a runs from 1 to $N_C^2 - 1$. t^a denotes the generators of the SU(3) gauge group which are related to the structure constant by $[t^a, t^b] = if^{abc}t^c$. They can be

written in terms of the Gell-Mann matrixes as $t^a = \lambda^a/2$. The parameter g denotes the strong coupling constant. Commonly, $\alpha_s \equiv g^2/(4\pi)$ is defined.

Eq. (A.1) is invariant under local gauge transformations $G(x)$ described by SU(3) rotation matrices in colour space, $G(x) = \exp[i\omega_a(x)t^a]$. Explicitly, the gauge transformations act as

$$\Psi(x) \to \Psi'(x) = G(x)\Psi(x), \qquad \overline{\Psi}(x) \to \overline{\Psi}'(x) = \overline{\Psi}(x)G^\dagger(x) \qquad (A.5)$$

and

$$A_\mu(x) \to A'_\mu(x) = G(x)A_\mu(x)G^\dagger(x) - \frac{i}{g}G(x)\partial_\mu G^\dagger(x). \qquad (A.6)$$

There are $N_f = 6$ known flavours of quarks: up (u), down (d), strange (s), charm (c), bottom (b) and top (t). Among them, there is a natural distinction between 'light' and 'heavy' quarks: One finds $m_u, m_d, m_s = 4,7,150$ MeV and $m_c, m_b, m_t = 1.5, 4.5, 170$ GeV. Thus, as far as thermodynamic properties of hot QCD are concerned, it is justified to neglect the influence of the heavy flavours for temperatures reached in current experiments of the order of a few hundred MeV. Thus, thermal QCD is effectively an $N_f = 3$ theory, where there still remains a distinction between the almost massless u and d quarks and the s quark with a mass comparable to the temperature. In this limit, we find

$$\Psi(x) = \begin{pmatrix} u_\alpha(x) \\ d_\alpha(x) \\ s_\alpha(x) \end{pmatrix} \qquad (A.7)$$

with $\alpha = 1...3$ the colour index and the mass matrix $\mathbf{m}$ becomes

$$\mathbf{m} = \begin{pmatrix} m_u & & \\ & m_d & \\ & & m_s \end{pmatrix}. \qquad (A.8)$$

QCD is a renormalizable quantum field theory, hence its bare parameters, the coupling g and the masses m_q depend on the energy scale. at which the theory is probed. Observable quantities however can not depend on the choice of a renormalization scale μ. This requirement leads to the renormalization group equations. For the coupling $\alpha_s(\mu)$, this equation reads (in NNLO):

$$\mu\frac{d}{d\mu}\alpha_s(\mu) = \beta(\alpha_s) = -\frac{\beta_0}{6\pi}\alpha_s^2 - \frac{\beta_1}{24\pi^2}\alpha_s^3 - O(\alpha_s^4), \qquad (A.9)$$

where

$$\beta_0 = 11N_C - 2N_f \qquad \text{and} \qquad \beta_1 = 34N_C^2 - \left(10N_C + \frac{3}{N_C}(N_C^2 - 1)\right)N_f. \quad (A.10)$$

Its solution, the running of α_s with the scale μ displays *asymptotic freedom*, i.e. the coupling constant gets arbitrary small for very high energy scales and the degrees of freedom become quasifree. One finds

$$\alpha_s(\mu) = \frac{12\pi}{\beta_0 \log(\mu^2/\Lambda_{QCD}^2)} - \frac{36\pi\beta_1 \log(\log(\mu^2/\Lambda_{QCD}^2))}{\beta_0^3 \log^2(\mu^2/\Lambda_{QCD}^2)} + O\left(\frac{\log^2(\log\mu)}{\log^3\mu}\right). \quad (A.11)$$

Since $N_f < 16$, this expression leads indeed to a decreasing coupling for large scales μ. We have introduced the fundamental scale of QCD, $\Lambda_{QCD} \simeq 0.2 - 0.3$ GeV. Experimentally, one finds e.g. $\alpha_s(m_\tau = 1.77 \quad \text{GeV}) = 0.35$, which makes a perturbative expansion of the QCD dynamics in terms of diagrams meaningful.

On the other hand, Eq. (A.11) has a Landau pole in the infrared. Therefore, the coupling becomes large and a perturbative expansion in terms of quarks and gluons as degrees of freedom is no longer feasible. In nature, colourless bound states of quarks and gluons are observed at low energies. These are called hadrons. They appear in two species, corresponding to two different ways of forming colour singlet objects: $q\bar{q}$ states (mesons) and qqq ($\overline{qqq}$) states (baryons).

The requirement that quarks at low energies have to be part of a bound colourless state has been called 'colour confinement'. This property has significant impact on the ground state of the theory: The empty Fock space cannot be the ground state, as otherwise it would be possible to excite a single quark as asymptotic state. This hints to the presence of condensates in the QCD vacuum.

A.2 SYMMETRIES AND CONDENSATES

The behaviour of the theory at low energies is mostly governed by the symmetries of the QCD Lagrangian and its symmetry breaking pattern with the associated condensates.

In the chiral limit, $m_q \to 0$, the symmetries of the classical QCD Lagrangian, apart from Poincaré invariance, are given by

$$\mathcal{S}[\mathcal{L}_{QCD}]_{cl} = \mathrm{SU}(3)_c \otimes \mathrm{SU}(N_f)_L \otimes \mathrm{SU}(N_f)_R \otimes \mathrm{U}(1)_V \otimes \mathrm{U}(1)_A \otimes \mathcal{C}. \qquad \text{(A.12)}$$

The local gauge symmetry $\mathrm{SU}(3)_c$ determines the dynamics of the gluon and quark fields. The global $\mathrm{U}(1)_V$ symmetry is responsible for baryon number conservation, whereas the global $\mathrm{U}(1)_A$ symmetry is broken in the quantized theory due to the presence of the axial anomaly.

In the chiral limit, QCD is characterized by a single dimensionless coupling parameter g. Therefore, the QCD action $S_{cl} = \int d^4x \mathcal{L}_{QCD}$ is invariant under global scale transformations:

$$x_\mu \to \lambda^{-1} x_\mu, \qquad A_\mu^a \to A_\mu^a(\lambda x), \qquad \Psi \to \lambda^{\frac{3}{2}} \Psi(\lambda x). \qquad \text{(A.13)}$$

Following the Noether theorem, there is a conserved quantity associated with the scale transformation invariance, the dilatation current

$$j_D^\mu = x_\nu T^{\mu\nu}, \quad \partial_\mu j_D^\mu = T^\mu_\mu = 0, \qquad \text{(A.14)}$$

with $T^{\mu\nu}$ the energy-momentum tensor. At the quantum level, however, this symmetry is broken due to the appearance of the scale Λ_{QCD}. Hence the divergence of the dilatation current does not vanish any more but becomes

$$\partial_\mu j_D^\mu = \frac{\beta(\alpha_s)}{4\alpha_s} \mathcal{G}^a_{\mu\nu} \mathcal{G}^{\mu\nu}_a \simeq -\frac{\beta_0}{24} \mathcal{G}^2. \qquad \text{(A.15)}$$

The last expression follows from the leading order β-function. There is a scalar vacuum expectation value associated with the broken scale invariance, the *gluon condensate*

$$\langle \mathcal{G}^2 \rangle \equiv \langle 0|\mathcal{G}^2|0 \rangle \simeq (1.5 \pm 0.5) \, \text{GeV/fm}^3. \qquad \text{(A.16)}$$

In the limit of vanishing quark masses, the different flavours become indistinguishable and $\mathcal{L}_{QCD}$ is invariant under global vector and axialvector rotations in SU(3) flavour space,

$$\Psi' \to \exp[ia_i \lambda^i/2]\Psi \quad \text{and} \quad \Psi' \to \exp[i\gamma_5 a_i \lambda^i/2]\Psi. \qquad \text{(A.17)}$$

Decomposing the quark field into left- and right-handed chirality components $\Psi_{R,L} = \frac{1}{2}(1 \pm \gamma_5)\Psi$, we find the SU(3)$_l \otimes$ SU(3)$_R$ chiral symmetry. The conserved vector and axial vector currents are

$$j_{V,i}^\mu = \overline{\Psi}\gamma^\mu \frac{\lambda_i}{2}\Psi \quad \text{and} \quad j_{A,i}^\mu = \overline{\Psi}\gamma^\mu \gamma_5 \frac{\lambda_i}{2}\Psi. \tag{A.18}$$

In nature, however, only the vector current appears to be conserved, This is evident from the fact that the masses in the pseudoscalar meson octet differ considerably from those of the scalar meson octet, the same is true for the vector and axialvector octet. One finds e.g. the ρ mass as 770 MeV, whereas the mass of its axial partner, the a_1, is 1260 MeV.

Thus, SU(3)$_L \otimes$ SU(3)$_R$ is spontaneously broken down to SU(3)$_V$ in nature. Therefore, axial symmetry generators do not annihilate the ground state, $\exp[i\gamma_5 a_i \lambda^i/2]|0\rangle \neq |0\rangle$; the symmetry is present in the Nambu-Goldstone realization.

As each spontaneously broken global symmetry implies the existence of a Goldstone boson, we expect to find those in the particle multiplets with masses lower than the typical hadronic scale of 1 GeV. Indeed, the π and η acquire their masses of 140-500 MeV only due to the explicit symmetry breaking by the finite quark masses. Another consequence of the Goldstone theorem is that there is a non-vanishing axial current matrix element between the vacuum and a Goldstone boson,

$$\langle 0|j_{A,i}^\mu|\pi_j(p)\rangle = ip^\mu \delta_{ij} f_\pi e^{-ipx}. \tag{A.19}$$

Here, the index i runs through the SU(2) subgroup, π_i denotes the pion field and f_π is the pion decay constant with $f_\pi = 92.4$ MeV.

For chiral symmetry and its spontaneous breaking, the scalar quark condensate $\langle \overline{q}q \rangle$ acts as an order parameter — it can be interpreted as quark-antiquark pair condensation in the ground state of QCD. It is defined by the short distance limit of the full quark propagator,

$$\langle \overline{q}q \rangle = -\lim_{y \to x_+} \text{Tr}\langle 0|\mathcal{T}[q(x)\overline{q}(y)|0\rangle. \tag{A.20}$$

Here, $\mathcal{T}[\dots]$ indicates time ordering. Using the Wick theorem, one can write

$$\mathcal{T}[q(x)\bar{q}(y)] =: q(x)\bar{q}(y): + q(\widehat{x)\bar{q}}(y), \tag{A.21}$$

where $: \cdots :$ is the normal-ordering and $\widehat{\cdots}$ the contraction of two field operators. As $y \to x$, the perturbative propagator encodes the ultra-violet physics and the normal ordered terms in Eq. (A.21) vanish in perturbation theory. Hence, a non-vanishing $\langle \overline{q}q \rangle$ stems from long-range, non-perturbative physics.

The condensate can be related to the observable quantity f_π via the Gell-Mann, Oakes, Renner (GOR) relation [186]

$$m_\pi^2 f_\pi^2 = -\frac{1}{2}(m_u + m_d)\langle \overline{u}u + \overline{d}d \rangle + O(m_{u,d}^2). \tag{A.22}$$

Inserting the quark masses, $m_u = 5$ MeV and $m_d = 7$ MeV yields values of $\langle \overline{u}u \rangle = \langle \overline{d}d \rangle \simeq -(250\text{MeV})^3$.

Appendix B

BOTTOM-UP THERMALIZATION

As the 'Bottom-up' thermalization scenario provides an interesting link between the soft, thermal scales of fireball physics and the hard initial collision scales, this appendix serves to explore it in somewhat greater detail than in the main text.

B.1 PARTON SATURATION

It is known for a long time that the gluon distribution in the nucleon grows, if smaller and smaller fractions of the nucleon light cone momentum x are probed. This can be intuitively understood as follows: If one probes the nucleon with larger momentum, one also increases the resolution on its substructure. At low resolution, a gluon emitting another gluon and recombining again is seen as just one gluon, but as resolution increases, the same process appears as two gluons carrying both a fraction of the original gluons momentum. As gluons transform under the color adjoint representation, the splitting processes carry large color factors and are enhanced as compared to processes involving quarks. Therefore, a low x the dynamics of the system is almost exclusively dominated by gluons, as apparent from the growth of the gluon structure function [187].

However, this behaviour cannot persist to arbitrarily small x. If the gluon density is large enough, recombination processes must come into play, which stop the growth of the distribution function [188]. The gluons condense into a classical field with large occupation numbers $O(1/\alpha)$ for each state, the 'color-glass condensate' [23–28]. Cross sections provide an alternative view onto the problem: As cross sections scale with the parton distribution functions, an ever-increasing gluon distribution would violate the bounds enforced by unitarity [23, 189].

In p-p collisions, this saturation domain lies at very low x and may just be accessible in present experiments. The situation is, however, different in heavy-ion experiments. Here, the gluon distribution of several hundred nucleons overlap, which practically leads to the

possibility of reaching the saturation density much earlier. This has been explored in detail in the saturation model of McLerran and Venugopalan [25].

In this model, the initial state is described as follows: In the center of mass frames, both incoming ions appear as Lorentz contracted discs of size $\Delta z = 2 \cdot R_0 \cdot \frac{m}{p}$, where R_0 is the uncontracted radius, m the nucleon mass and p the momentum per nucleon. For very high beam energies, $\Delta z = 0$ becomes a good approximation and the nucleus can effectively be seen as a flat disc with a two dimensional density of valence quarks $n_q(b)$.

This valence quark density is the source of soft gluons. The color charge at a given impact parameter therefore follows from a random addition of the color charges of the individual quarks, as long as saturation has not yet set in. A single quark yields $\frac{\alpha C_F}{\pi} \ln Q^2/\mu^2$ at scale Q^2 and per unit rapidity, so the gluon distribution outside the saturation region in the nucleus is

$$\frac{dxG_A(x, l^2)}{d^2bd^2l_\perp} = n_q(b)\frac{\alpha C_F}{\pi^2 l_\perp^2}. \tag{B.1}$$

Inside the saturation region, the expression becomes

$$\frac{dxG_A(x, l^2)}{d^2bd^2l_\perp} = \frac{N_C^2 - 1}{4\pi^3\alpha N_C} \ln Q_S^2/l_\perp^2, \tag{B.2}$$

which is valid for $l_\perp^2 \ll Q_S^2$ and where Q_S^2 is given by

$$Q_S^2 = \frac{8\pi^2\alpha N_C}{N_C^2 - 1}\sqrt{R^2 - b^2}\rho_0 xG(x) \tag{B.3}$$

In order for the whole approach to give a meaningful perturbative description of the initial state of a heavy-ion collision, Q_S must be a perturbative scale. For RHIC, Eq. (B.3) yields 1 GeV, whereas for LHC one finds $\sim 2 - 3$ GeV. Therefore, for RHIC conditions, the approach may lead only to a rough estimate, whereas at LHC a more appropriate description is given.

B.2   Shattering the Color-Glass Condensate

At the time of the collision, gluons in the nucleus wavefunction are distributed according to Eqs. (B.1) and (B.2). For $l_\perp^2 \ll Q_S^2$, the expression is constant (up to a logarithm) and so the gluon density is given by phase space, so only very few gluons in the wave function fulfill $l_\perp^2 \ll Q_S^2$ and so they are unimportant for the collision dynamics.

Thus the two gluon (jet) production cross section can be written as

$$\frac{d\sigma}{dy_1 dy_2 d^2l_\perp d^2b} = \int d^2b_1 d^2b_2 \delta(\mathbf{b_1} - \mathbf{b_2} - \mathbf{b})\frac{d\sigma}{dt}\frac{dx_1 G_A(x_1, l^2)}{d^2b_1}\frac{dx_2 G_A(x_2, l^2)}{d^2b_2} \tag{B.4}$$

where xG_A is given by Eq. (B.1). As the cross section $\frac{d\sigma}{dt}$ scales like $l_\perp^{-4}$, contributions to particle production are drastically enhanced by lowering $l_\perp$. However, lowering $l_\perp$ in Eq. (B.1) is bounded by Q_S where its validity breaks down and the above arguments about the saturated region take over. Therefore, the dominant region for particle production is where gluons have transverse momentum of order Q_S. At a time of order $1/Q_S$, these gluons are freed from the nuclear wave function.

B.3 Creation of soft gluons

As shown in the previous section, the gluons freed from the nuclear wave function have typical momenta of order Q_S and occupation number $1/\alpha$. These gluons will be called 'hard' in the following. Initially, the system expands linearly in τ along the z-axis at high energies, which implies that the density of hard gluons drops in time,

$$n_H \sim \frac{Q_S^3}{\alpha(Q_S\tau)} \tag{B.5}$$

In absence of any interaction, the occupation number would remain, however, small angle elastic scattering is always present and lowers the occupation number $f_H = n_H/(Q_S^2 p_z)$. The lowest possible momentum exchange is given by the Debye mass

$$m_D^2 \sim \alpha \int d^3p \frac{f_h(p)}{p} \sim \frac{\alpha n_h}{Q_S} \sim \frac{Q_S^2}{Q_S\tau}, \tag{B.6}$$

all lower momenta probe large distances and are screened. If $m_D \ll p_z$, most collisions do not take particles away from the region where the occupation number is large. The frequency of collisions encountered by a particle is then enhanced by a Bose factor $(1+f_H)$, namely

$$\frac{dN_{col}}{d\tau} \sim \sigma n_H(1+f_H) \sim \frac{\alpha n_H}{m_D^2 p_z \tau} \tag{B.7}$$

for large occupation numbers. The increase in the longitudinal momentum is then

$$p_z^2 \sim N_{col}m_D^2 \sim \frac{\alpha n_H}{p_z} \quad \text{implying} \quad p_z \sim (\alpha n_H)^{1/3} \sim \frac{Q_S}{(Q_S\tau)^{1/3}}. \tag{B.8}$$

Inserting this for p_z, the typical occupation number $f_H = n_H/(Q_S^2 p_z)$ is large until $Q_S\tau \sim \alpha^{-3/2}$. Additionally, inelastic scatterings produce additional soft gluons within a momentum range down to m_D. However, as these soft gluons continue to interact with the hard ones, their momentum is raised and the smallest momentum for soft gluons is of order $k_s \sim p_z$. Their number can be estimated using the Bethe-Heitler formula as

$$n_s \sim \tau\frac{\partial n_s}{\partial \tau} \sim \tau \int d^3p f(p)\frac{dI^{BH}}{dt}(1+f_H)^2 \sim \tau\frac{\alpha^3}{m_D^2}n_H^2(1+f_H)^2 \sim \frac{Q_S^3}{\alpha(Q_S\tau)^{4/3}} \tag{B.9}$$

B.4 Soft gluons take over

Once $Q_S\tau > \alpha^{-3/2}$, the occupation number ceases to be large and the collision rate Eq. (B.7) ceases to be dominated by the Bose factor. The typical momentum of soft gluons becomes now

$$k_S^2 \sim N_{col}m_D^2 \sim \tau\sigma n_H m_D^2 \sim \alpha Q_S^2 \tag{B.10}$$

which now is a constant. The number of soft gluons becomes

$$n_S \sim \tau\frac{\alpha^3}{m_D^2}n_H^2 \sim \frac{\alpha Q_S^4}{m_D^2 \tau} \tag{B.11}$$

The contribution to the debye mass (Eq. (B.6)) from hard and soft gluons is determined by $m_D^2 \sim \frac{\alpha n_H}{Q_S} + \frac{\alpha n_S}{k_S}$. Assuming that the Debye mass is now dominated by contributions of soft gluons, which will be verified a posteriori, we can calculate n_S and find

$$n_S \sim \frac{\alpha^{1/4}Q_S^3}{(Q_S\tau)^{1/4}} \quad \text{and} \quad m_D \sim \frac{\alpha^{3/8}Q_S}{(Q_S\tau)^{1/4}}. \tag{B.12}$$

One indeed finds $n_S/k_S \gg n_H/Q_S$ for $Q_S\tau \gg \alpha^{-3/2}$. The density of soft gluons, n_S is, however, still smaller than the density of hard gluons until $Q_S\tau \gg \alpha^{-5/2}$.

B.5 THERMALIZED SOFT SECTOR

After timescales $Q_S\tau \gg \alpha^{-5/2}$, most of the gluons in the system are soft. As the coupling between soft gluons is not governed by the hard scale any more, they quickly achieve thermalization among themselves. The whole system is still not in equilibrium, as most of the energy is still carried by a small fraction of hard gluons with momentum Q_S.

These hard gluons can, however, transfer their energy to the heat bath of the soft gluons. This can happen the following way: A hard gluon emits one with a softer momentum k_b during the timescale τ, which successively splits into two gluons with comparable momentum. The emitted softer gluons then quickly cascade further down in momentum and feed energy into the heat bath.

What is a likely value for k_b? The time for its emission is of order τ, and this time can be related to the thermalization time of the same gluon, which is a soft process and therefore one power down in α; $\alpha\tau \sim \tau_{th}$, where τ_{th} is the time needed for the gluon to be absorbed into the heat bath. This time is approximately given by $\tau_{th} \sim k_b/k_t^2$, where k_t denotes the transverse momentum of the gluon after the time τ_{th} and can be estimated as $k_t \sim m_D^2\tau_{th}n_S\sigma$. Using $\sigma \sim \alpha^2/m_D^2$, one finds

$$\frac{1}{\tau} \sim \frac{\alpha^2 n_s^{1/2}}{k_b^{1/2}}. \tag{B.13}$$

The soft gluons in the heat baths are presumably thermalized, so a temperature for the soft part can be defined and one can use $n_S \sim T^3$ with the temperature T. Therefore $k_b \sim \alpha^4 T^3\tau^2$, with an unknown time dependence of T. The rate, at which gluons with momentum k_b are emitted is

$$\frac{dN(k_b)}{d\tau} \sim \frac{n_H}{\tau_b} \sim \frac{\alpha^2 n_S^{1/2} n_H}{k_b^{1/2}} \sim \frac{Q_S^2}{\alpha\tau^2}, \tag{B.14}$$

so the energy flow from the hard gluons to the soft thermal bath is

$$k_b \frac{dN(k_b)}{d\tau} \sim \alpha^3 Q_S^2 T^3. \tag{B.15}$$

As this energy flow increases the energy of the heat bath, which goes like T^4, one finds

$$T \sim \alpha^3 Q_S^2\tau. \tag{B.16}$$

Surprisingly, the temperature of the soft sector increases linearly as the system expands, so hard gluons continuously transfer energy into the soft sector, counterbalancing the temperature decrease due to the volume expansion. This phase terminates as soon as the hard gluons have lost all their energy, which happens when $k_B \sim Q_S$ or $Q_S\tau \sim \alpha^{-13/5}$. The temperature achieves a maximal value of order $\alpha^{2/5}Q_S$. After this, the system is in complete thermal equilibrium and the temperature decreases, as the volume expands further.

Some of the rough estimates of the previous section have been worked out in greater detail within the framework of Boltzmann equations in [22], where it is found that the parametrical estimates remain in principle valid.

Appendix C

THE DILEPTON RATE FROM A HOT SOURCE

In this appendix, we give a derivation of Eq. (7.1) which is the master formula for the calculation of dilepton emission out of the fireball.

Consider a system of strongly interacting matter at a given temperature T. For typical fireballs created in heavy-ion collisions, the mean free path of particles with only electromagnetic interactions exceeds the dimensions of the system by far (see chapter 5). This is due to the smallness of the electromagnetic coupling α_{em} as compared to the strong coupling α. Thus it is justified to neglect any final state interaction of photons and leptons being radiated from the medium and consider free propagation of those particles only. Furthermore, given the overall uncertainties regarding the properties of the producing medium, a calculation of the electromagnetic part of the emission process to order α_{em} appears sufficient. This corresponds to a process where a virtual photon is emitted from the medium and subsequently decays into a lepton pair.

The transition rate for the emission rate R of a lepton pair per unit volume of spacetime is calculated using Fermi's golden rule. We integrate the possible transition probabilities over the momenta p_1 and p_2 of the produced leptons,

$$\frac{dR}{d^4x} = \int \frac{d^3p_1}{(2\pi)^3 2E_1} \frac{d^3p_2}{(2\pi)^3 2E_2} \frac{d^4q}{(2\pi)^4} \delta^4(q - p_1 - p_2) \sum_{f,i,spin} |S_{fi}(p_1, p_2, q)|^2, \quad \text{(C.1)}$$

and differentiate the result with respect to the virtual photon four momentum q.

We have

$$S_{fi} = \overline{u}^s(p_1)(-ie\gamma_\nu)v^r(p_2)\frac{-ig^{\mu\nu}}{q^2 + i\epsilon} \cdot e \int d^4x e^{iqx}\langle f|j_\mu(x)|i\rangle. \quad \text{(C.2)}$$

Here, j_μ denotes the electromagnetic current carried by the strongly interacting particles of

the medium,

$$j_\mu(x) = q_f \overline{\psi}(x)\gamma_\mu\psi(x), \tag{C.3}$$

and eq_f being the charge of particles associated with the current j_μ. The squared matrix element reads

$$\begin{aligned}|S_{fi}(p_1,p_2,q)|^2 =&\frac{e^4}{q^4} \left(\overline{u}^s(p_1)\gamma^\mu v^r(p_2)\right)\left(\overline{v}^r(p_2)\gamma^\nu u^s(p_1)\right)\\ &\times \int d^4x e^{iqx}\langle f|j_\mu(x)i|\rangle \int d^4x' e^{-iqx'}\langle i|j_\nu(x')|f\rangle\end{aligned} \tag{C.4}$$

In a homogeneous medium, we can exploit translation invariance to write

$$\langle i|j_\nu(x')|f\rangle = \exp[i(p_f - p_i)x']\langle i|j_\nu(0)f\rangle. \tag{C.5}$$

Here, p_f and p_i denote the momenta of final and initial state. The x' integration can be carried out to yield a momentum-conserving delta function for the process where a photon with momentum q is emitted in the transition from $|i\rangle$ to $|f\rangle$. Thus we are left with

$$\begin{aligned}|S_{fi}(p_1,p_2,q)|^2 =&\frac{e^4}{q^4} \left(\overline{u}^s(p_1)\gamma^\mu v^r(p_2)\right)\left(\overline{v}^r(p_2)\gamma^\nu u^s(p_1)\right)\\ &\times (2\pi)^4\delta^4(p_i - p_f - q) \int d^4x e^{iqx}\langle i|j_\nu(0)|f\rangle\langle f|j_\mu(x)|i\rangle.\end{aligned} \tag{C.6}$$

In order to find the total thermal emission rate, we have to sum over the lepton spins s and r and average over the initial states and momenta with a Boltzmann weight factor $\mathcal{Z}(T)^{-1}\exp(-\beta E_n)$. In this expression, $\mathcal{Z}(T)$ stands for the partition function of the system, $\beta = 1/T$ and E_n is the energy of the state n. Additionally, we sum over the final states and momenta using $\sum_f |f\rangle\langle f| = 1$. The delta function ensures energy and momentum conservation for the emission process. We find

$$|S_{tot}|^2 = \sum_{s,r,f,i} \frac{1}{\mathcal{Z}} e^{-\beta E_i} |S_{fi}(p_1,p_2,q)|^2. \tag{C.7}$$

The summation over the lepton spins yields the usual leptonic tensor

$$l^{\mu\nu}(p_1,p_2) = 4(p_1^\mu p_2^\nu + p_2^\mu p_1^\nu - g^{\mu\nu}[p_1\cdot p_2 + m_l^2]), \tag{C.8}$$

where m_l is the lepton mass. We identify the remaining hadronic part with the retarded current-current correlation function $\Pi_{\mu\nu}^<(q)$,

$$\int d^4x e^{iqx}\frac{1}{\mathcal{Z}}\sum_i \langle i|e^{-\beta E_i} j_\nu(0)j_\mu(x)|i\rangle = -i\Pi_{\mu\nu}^<(q). \tag{C.9}$$

The correlation function $\Pi_{\mu\nu}(q)$ can be related to the one-particle irreducible photon self-energy $\Pi_{\mu\nu}^s(q)$. To order α_{em}, $\Pi_{\mu\nu}^s = \Pi_{\mu\nu}$, therefore we can make use of relations for thermal self-energies in the following.

In the vacuum, Lorentz invariance and the Ward identity lead to a transverse structure of the self-energy: $\Pi_{\mu\nu}^s(q) = (g_{\mu\nu} - q_\mu q_\nu/q^2)\overline{\Pi}^s(q)$. This is no longer true at finite temperature, as the presence of the heat bath explicitly breaks Lorentz invariance by introducing a preferred frame of reference characterized by u_μ, is four-velocity. For calculations in the rest frame of the heat bath, $u_\mu = (1, \mathbf{0})$. Thus, in general the self energy acquires an additional longitudinal component and its tensor structure can be decomposed as

$$\Pi_{\mu\nu}^s(q) = -P_{\mu\nu}^T(q,u)\overline{\Pi}_T^s(q,u) - P_{\mu\nu}^L(q,u)\overline{\Pi}_L^s(q,u) \tag{C.10}$$

Factors q_0 in the distribution functions generalize to $\omega = q_\mu u^\mu$ and the magnitude of the three-momentum (which is $|\mathbf{q}|$ in the rest frame of the heat bath) becomes $\overline{q} = \sqrt{\omega^2 - q^2}$.

The transverse and longitudinal projection tensors read

$$P_{\mu\nu}^T = g_{\mu\nu} - \frac{q_\mu q_\nu}{q^2} + \frac{q^2}{\overline{q}^2}(u_\mu - \omega q_\mu/q^2)(u_\nu - \omega q_\nu/q^2) \qquad \text{(C.11)}$$

and

$$P_{\mu\nu}^L = -\frac{q^2}{\overline{q}^2}(u_\mu - \omega q_\mu/q^2)(u_\nu - \omega q_\nu/q^2). \qquad \text{(C.12)}$$

The scalar invariant $\overline{\Pi}^s(q^2)$, which in the vacuum was $\overline{\Pi}^s(q^2) = 1/3\Pi_\mu^\mu(q)$ similarly breaks into a transverse and longitudinal part, which are given by

$$\overline{\Pi}_T^s(q, u) = \frac{1}{2}\left(\Pi_\mu^\mu + \frac{q^2}{\overline{q}^2}u^\mu u^\nu \Pi_{\mu\nu}^s\right) \qquad \text{(C.13)}$$

and

$$\overline{\Pi}_L^s(q, u) = -\frac{q^2}{\overline{q}^2}u^\mu u^\nu \Pi_{\mu\nu}^s. \qquad \text{(C.14)}$$

In the real time formalism of thermal field theory, the self energy acquires a 2×2 matrix structure [2] (see also chapter 2. This ensures that unphysical singularities from products of delta functions cancel. In the Keldysh-Schwinger prescription, the retarded self-energy $\Pi_s^<(q)$ is given by an off-diagonal element of the self-energy matrix,

$$\Pi_s^< = \Pi_s^{(12)} \qquad \text{(C.15)}$$

This expression can be related to the physical self-energy $\overline{\Pi}$ which modifies the bare propagators by

$$\Pi_s^{(12)}(q) = \Pi_s^<(q) = -2i\epsilon(q_0)f_B(q_0)\text{Im}\overline{\Pi}(q). \qquad \text{(C.16)}$$

Here, $\epsilon(x) = \text{sgn}(x)$. Keeping in mind that the thermal self-energy has a transverse and a longitudinal part, we replace

$$\Pi_s^<(q) = -2i\epsilon(q_0)f_B(q_0)(P_{\mu\nu}^T\text{Im}\overline{\Pi}_T(q) + P_{\mu\nu}^L\text{Im}\overline{\Pi}_L(q)) \qquad \text{(C.17)}$$

The basic structure of Eq. (C.1) reads

$$\frac{dR}{d^4x d^4q} = \frac{e^4}{(2\pi)^4 q^4} \cdot L^{\mu\nu}(q)(-i\Pi_{\mu\nu}^<(q)), \qquad \text{(C.18)}$$

with

$$\begin{aligned}
L^{\mu\nu}(q) &= (2\pi)^4 \int \frac{d^3p_1}{(2\pi^3 2E_1)} \frac{d^3p_2}{(2\pi^3 2E_2)} \delta^4(p_1 + p_2 - q) \cdot l^{\mu\nu}(p_1, p_2, q) \\
&= \frac{1}{6\pi}(q^\mu q^\nu - q^2 g^{\mu\nu})\left(1 + \frac{2m_l^2}{q^2}\right)\left(1 - \frac{4m_l^2}{q^2}\right)^{1/2}.
\end{aligned} \qquad \text{(C.19)}$$

If one is interested in electron emission, the mass terms in the last expression can be safely neglected as $m_e \ll T$. Inserting Eq. (C.17) into Eq. (C.18) and gathering constants we find

$$\frac{dR}{d^4x d^4q} = -\frac{\alpha^2}{3\pi^3 q^2} \cdot \frac{1}{e^{\beta q_0} - 1}\left(\frac{q^\mu q^\nu}{q^2} - g^{\mu\nu}\right)\left(P_{\mu\nu}^T\text{Im}\overline{\Pi}_T(q) + P_{\mu\nu}^L\text{Im}\overline{\Pi}_L(q)\right) \qquad \text{(C.20)}$$

Contracting the Lorentz indices, this becomes

$$
\begin{aligned}
\frac{dR}{d^4x d^4q} &= -\frac{\alpha^2}{3\pi^3 q^2} \cdot \frac{1}{e^{\beta q_0} - 1} \frac{2\mathrm{Im}\overline{\overline{\Pi}}_T(q) + \mathrm{Im}\overline{\overline{\Pi}}_L(q)}{3} \\
&= -\frac{\alpha^2}{3\pi^3 q^2} \cdot \frac{1}{e^{\beta q_0} - 1} \mathrm{Im}\overline{\overline{\Pi}}^{\mu}_{\mu}(q^0, \mathbf{q}),
\end{aligned}
\tag{C.21}
$$

which exactly corresponds to Eq. (7.1) used in chapter 7 to calculate dilepton yields from a fireball.

BIBLIOGRAPHY

[1] J. I. Kapusta, *Finite-temperature field theory* (Cambridge University Press, Cambridge, England, 1989).

[2] M. Le Bellac, *Thermal Field Theory* (Cambridge University Press, Cambridge, England, 1996).

[3] M. E. Peskin and D. V. Schroeder, *An Introduction To Quantum Field Theory*, (Addison-Wesley, Reading, USA 1995).

[4] R. D. Pisarski, Phys. Rev. Lett. **63** (1989) 1129; E. Braaten and R. D. Pisarski, Phys. Rev. **D 45** (1992) 1827.

[5] T. Muta, World Sci. Lect. Notes Phys. **57** (1998) 1.

[6] A. W. Thomas and W. Weise, *The Structure Of The Nucleon* (Wiley-VCH, Berlin, Germany, 2001).

[7] R. A. Schneider, PhD thesis.

[8] R.A. Schneider and W. Weise, Phys. Rev. **C 64** (2001) 055201.

[9] H. Satz, Rept. Prog. Phys. **63** (2000) 1511.

[10] J. P. Blaizot and E. Iancu, Phys. Rept. **359** (2002) 355.

[11] C. Zhai and B. Kastening, Phys. Rev. **D 52** (1995) 7232.

[12] P.-P. Blaizot, E. Iancu and A. K. Rebhan, Phys. Rev. Lett. **83** (1999) 2906; Phys. Lett. **B 470** (1999) 181; Phys. Rev. **D 63** (2001) 065003.

[13] G. Boyd et al., Phys. Rev. Lett. **75** (1995) 4169.

[14] G. Boyd et al., Nucl. Phys. **B 469** (1996) 419.

[15] M. Okamoto et al. (CP-PACS), Phys. Rev. **D 60** (1999) 094510.

[16] B. Beinlich et al., Eur. Phys. J. **C 6** (1999) 133.

[17] F. Karsch, E. Laermann and A. Peikert, Phys. Lett. **B 478** (2000) 447.

[18] F. Karsch, E. Laermann and A. Peikert, Nucl. Phys. **B 605** (2001) 579.

[19] F. Karsch and E. Laermann, Phys. Rev. **D 50** (1994) 6954.

[20] T. D. Cohen, R. J. Furnstahl and D. K. Griegel, Phys. Rev. **C 45** (1992) 1881; P. Gerber and H. Leutwyler, Nucl. Phys. **B 321** (1989) 387.

[21] R. V. Gavai, A. Goksch and M. Ogilvie, Phys. Rev. Lett. **56** (1986) 815.

[22] R. Baier, A. H. Mueller, D. Schiff and D. T. Son, Phys. Lett. **B 502** (2001) 51.

[23] L. V. Gribov, E. M. Levin and M. G. Ryskin, Phys. Rep. **100** (1983) 1.

[24] J.-P. Blaizot and A. H. Mueller, Nucl. Phys. **B 289** (1987) 847.

[25] L. McLerran and R. Venugopalan, Phys. Rev. **D 49** (1994) 2233; Phys. Rev. **D 49** (1994) 3352; Phys. Rev. **D 50** (1994) 2225.

[26] J. Jalilian-Marian, A. Kovner, L. Mclerran and H. Weigert, Phys. Rev. **D 55** (1997) 5414.

[27] K. J. Eskola, K. Kajantie, P. V. Ruuskanen, K. Tuominen, Nucl. Phys. **B 570** (2000) 379.

[28] A. H. Mueller, Nucl. Phys. **B 572** (2000) 227.

[29] J. Y. Ollitrault, Phys. Rev. **D 46** (1992) 229.

[30] E. V. Shuryak, Phys. Rev. Lett **68** (1992) 3270, E. V. Shuryak and L. Xiong, Phys. Rev. Lett **70** (1993) 2241.

[31] R. Rapp, Phys. Rev. **C 63** (2001) 054907.

[32] D. M. Elliott and D. H. Rischke, Nucl. Phys. **A 671** (2000) 583.

[33] A. Peshier, B. Kampfer, O. P. Pavlenko and G. Soff, Phys. Rev. **D 54** (1996) 2399.

[34] P. Levai and U. W. Heinz, Phys. Rev. **C 57** (1998) 1879.

[35] A. Peshier, Phys. Rev. **D 63** (2001) 105004.

[36] S. Jeon and V. Koch, Phys. Rev. Lett. **85** (2000) 2076.

[37] J. Gasser and H. Leutwyler, Phys. Lett. **B 188** (1987) 477.

[38] F. Klingl, N. Kaiser and W. Weise, Nucl. Phys. **A 624** (1997) 527.

[39] R. A. Schneider and W. Weise, Eur. Phys. J. **A 9** (2000) 357.

[40] R. A. Schneider and W. Weise, Phys. Lett. **B 515** (2001) 89.

[41] T. Schwarz, private communication.

[42] B. Tomasik and U. A. Wiedemann, nucl-th/0207074.

[43] C. M. Hung and E. Shuryak, Phys. Rev. **C 57** (1998) 1891.

[44] H. Sorge, H. Stöcker and W. Greiner, Ann. Phys. **192** (1989) 266; H. Sorge, M. Berenguer, H. Stöcker and W. Greiner, Phys.Lett. **B 289** (1992) 6; H. Sorge, Phys. Rev. **C 52** (1995) 3291.

[45] S. Soff, S. A. Bass, M. Bleicher, L. Bravina, E. Zabrodin, H. Stöcker and W. Greiner, Phys. Lett. **B 471** (1999) 89; M. Bleicher, M. Belkacem, S. A. Bass, S. Soff and H. Stöcker, Phys. Lett. **B 485** (2000) 213; M. Bleicher, W. Greiner, H. Stöcker and N. Xu, Phys. Rev. **C 62** (2000) 061901.

[46] X.-N. Wang and M. Gyulassy, Comput. Phys. Commun. **83** (1994) 307.

[47] D. E. Kahana and S. H. Kahana, Phys. Rev. **C 58** (1998) 3574.

[48] A. Capella, U. P. Sukhame, C. I. Tan and J. Tran Thanh Van, Phys. Lett. **B 81** (1979) 69; Phys. Rept. **236** (1994) 225.

[49] B. Andersson, G. Gustafson and B. Söderberg, Z. Phys. **C 20** (1983) 317.

[50] J. Sollfrank, P. Huovinen, M. Kataja, P. V. Ruuskanen, M. Prakash and R. Venugopalan, Phys. Rev. **C 55** (1997) 392.

[51] T. Hirano, K. Tsuda and K. Kajimoto, nucl-th/0011087.

[52] H. Sorge, Phys. Lett. **B 373** (1996) 16.

[53] T. Renk, R. A. Schneider and W. Weise, Phys. Rev. **C 66** (2002) 014902.

[54] R. Hanbury-Brown and R. Q. Twiss, Phil. Mag. **45** (1954) 663.

[55] U. A. Wiedemann and U. W. Heinz, Phys. Rept. **319** (1999) 145.

[56] H. Appelshauser *et al.* (NA49 Collaboration), Phys. Rev. Lett. **82** (1999) 2471.

[57] I. G. Bearden *et al.* (NA44 Collaboration), Phys. Rev. Lett. **78** (1997) 2080.

[58] E. Schnedermann, J. Sollfrank and U. W. Heinz, Phys. Rev. C **48** (1993) 2462.

[59] N. S. Amelin, N. Armesto, C. Pajares and D. Sousa, Eur. Phys. J. **C 22** (2001) 149.

[60] B. Tomasik, U. A. Wiedemann and U. W. Heinz, nucl-th/9907096.

[61] G. Bertsch, Nucl. Phys. **A 498** (1989) 173c, S. Pratt, Phys. Rev. **D 33** (1986) 1314.

[62] H. Appelshauser, hep-ph/0204159.

[63] R. J. Snellings, H. Sorge, S. A. Voloshin, F. Q. Wang and N. Xu, Phys. Rev. Lett. **84** (2000) 2803.

[64] P. F. Kolb, P. Huovinen, U. W. Heinz and H. Heiselberg, Phys. Lett. **B 500** (2001) 232.

[65] H. Appelshauser *et al.* [NA49 Collaboration], Phys. Rev. Lett. **80** (1998) 4136.

[66] M. Gyulassy, I. Vitev and X. N. Wang, Phys. Rev. Lett. **86** (2001) 2537.

[67] K. H. Ackermann *et al.* [STAR Collaboration], Phys. Rev. Lett. **86** (2001) 402.

[68] U. W. Heinz and S. M. Wong, Phys. Rev. **C 66** (2002) 014907.

[69] P. G. Jones (NA49 Collaboration), Nucl. Phys. **A 610** (1996) 188c.

[70] H. Appelshäuser et al. (NA49 Collaboration), Eur. Phys. J. **C 2** (1998) 611.

[71] R. Rapp and J. Wambach, Eur. Phys. J. **A 6** (1999) 415.

[72] J. Letessier, A. Tounsi, U. Heinz, J. Sollfrank and J. Rafelski, Phys. Rev. **D 51** (1995) 3408.

[73] J. D. Bjorken, Phys. Rev. **D 27** (1983) 140.

[74] B. B. Back *et al.* (PHOBOS Collaboration), Phys. Rev. Lett. **87** (2001) 102303.

[75] C. Adler *et al.* (STAR Collaboration), Phys. Rev. Lett. **87** (2001) 082301.

[76] E. Shuryak, Phys. Lett. **B 207**, 345 (1988); Phys. Rev. **D 42**, 1764 (1990);
P. Gerber, H. Leutwyler and J. L. Goity, Phys. Lett. **B 246**, 513 (1990);
H. Bebie, P. Gerber, J.L. Goity and H. Leutwyler, Nucl. Phys. **B 378**, 95 (1992).

[77] C.M. Hung and E. Shuryak, Phys. Rev. **C 57**, 1891 (1998).

[78] R. Stock, Nucl. Phys. **A 661**, 282c (1999).

[79] H. Sorge, Phys. Rev. **C 52**, 3291 (1995).

[80] P. Braun-Munzinger, J. Stachel, J. P. Wessels and N. Xu, Phys. Lett. **B 344** (1995) 43.

[81] P. Braun-Munzinger, I. Heppe and J. Stachel, Phys. Lett. **B 465** (1999) 15.

[82] P. Braun-Munzinger, D. Magestro, K. Redlich and J. Stachel, Phys. Lett. **B 518** (2001) 41.

[83] R. Rapp and E. V. Shuryak, Phys. Rev. Lett. **86** (2001) 2980.

[84] see, e.g., A. Bohr and B. Mottelson, *Nucl. Structure* (Benjamin, New York 1969), Vol.1, 266.

[85] D. E. Groom et al. (Particle Data Group), Eur. Phys. **C 15** (2000) 1.

[86] G. Roland (NA49 Collaboration), Nucl. Phys. **A 638** (1998) 91c.

[87] M. Kaneta, (NA44 Collaboration), Nucl. Phys. **A 639** (1998) 419c.

[88] E. Andersen et al. (WA97 Collaboration), J. Phys. **G 25** (1999) 171, Phys. Lett. **B 449** (1999) 401.

[89] H. Appelshäuser et al. (NA49 Collaboration), Phys. Lett. **B 444** (1998) 523.

[90] F. Gabler (NA49 Collaboration), J. Phys. **G 25** (1999) 199.

[91] S. Margetis (NA49 Collaboration), J. Phys. **G 25** (1999) 189.

[92] D. Jouan (NA50 Collaboration), Nucl. Phys. **A 638** (1998) 483c, A. de Falco (NA50 Collaboration), Nucl. Phys. **A 638** (1998) 487c.

[93] F. Pühlhofer (NA49 Collaboration), Nucl. Phys. **A 638** (1998) 431c.

[94] A. Mischke, nucl-ex/0209002.

[95] F. Beccatini, Z. Phys. **C 69** (1996) 485.

[96] F. Becattini and U. W. Heinz, Z. Phys. **C 76** (1997) 269.

[97] K. Redlich, hep-ph/0111383.

[98] N. S. Amelin, N. Armesto, C. Pajares and D. Sousa, hep-ph/0012276.

[99] C. Adler *et al.* (STAR Collaboration), Phys. Rev. Lett. **89** (2002) 092301.

[100] K. Adcox *et al.* (PHENIX Collaboration), Phys. Rev. Lett. **89** (2002) 092302.

[101] C. Adler *et al.*, Phys. Rev. C **65** (2002) 041901.

[102] C. Adler *et al.* (STAR Collaboration), Phys. Rev. Lett. **86** (2001) 4778.

[103] C. Suire (STAR Collaboration), talk given at Quark Matter 2002, Nantes.

[104] J. Castillo (STAR Collaboration), talk given at Quark Matter 2002, Nantes.

[105] G. Agakichiev et al., CERES collaboration, Phys. Rev. Lett. **75** (1995) 1272; G. Agakichiev et al., CERES collaboration, Phys. Lett. **B 422** (1998) 405.

[106] P. Aurenche, F. Gelis, R. Kobes and H. Zaraket, Phys. Rev. **D 58** (1998) 085003.

[107] P. Aurenche, F. Gelis and H. Zaraket, Phys. Rev. **D 61** (2000) 116001.

[108] A. Peshier and M. H. Thoma, Phys. Rev. Lett. **84** (2000) 841.

[109] E. Braaten, R. D. Pisarski and T.C. Yuan, Phys. Rev. Lett. **64** (1990) 224.

[110] A. Peshier and M. H. Thoma, Phys. Rev. Lett. **84** (2000) 841.

[111] F. Karsch, E. Laermann, P. Petreczky, S. Stickan and I. Wetzorke, Phys. Lett. **B 530** (2002) 147.

[112] A. Peshier, B. Kämpfer and G. Soff, Phys. Rev. **C 61** (2000) 045203.

[113] F. Klingl, N. Kaiser and W. Weise, Z. Phys. **A 356** (1996) 193.

[114] C. Song, C. M. Ko and C. Gale, Phys. Rev. **D 50** (1994) R1827.

[115] G. Q. Li and C. Gale, Nucl. Phys. **A 638** (1998) 491.

[116] V. L. Eletsky and B. L. Ioffe, Phys. Rev. **D 47** (1993) 3083; V. L. Eletsky and B. L. Ioffe, Phys. Rev. **D 51** (1995) 2371.

[117] M. Urban, M. Buballa and J. Wambach, Phys. Rev. Lett. **88** (2002) 042002; E. Marco, R. Hofmann and W. Weise, Phys. Lett. **B 530** (2002) 88.

[118] W. A. Zajc et al. (PHENIX Collaboration), Nucl. Phys. **A 698** (2002) 39.

[119] PHOBOS Collaboration, Phys. Rev. Lett. **87** (2001) 102301.

[120] A. D. Martin, R. G. Roberts, W. J. Stirling and R. S. Thorne, Phys. Lett. **B 531** (2002) 216.

[121] H. L. Lai et al. (CTEQ), Eur. Phys. J. **C 12** (2000) 375.

[122] M. Glück, E. Reya, and A. Vogt, Eur. Phys. J. **C 5** (1998) 461.

[123] P. L. McGaughey et al. (E772), Phys. Rev. D**50** (1994) 3038.

[124] K. J. Eskola, V. J. Kolhinen and C. A. Salgado, Eur. Phys. J. **C 9** (1999) 61.

[125] F. Arleo, Phys. Lett. **B 532** (2002) 231.

[126] S. Gavin, P. L. McGaughey, P. V. Ruuskanen and R. Vogt, Phys. Rev. **C 54** (1996) 2606.

[127] E. Shuryak, Phys. Rev. **C 55** (1997) 961.

[128] Z. Lin, R. Vogt and X.-N. Wang, Phys. Rev. **C 57** (1998) 899.

[129] S. Y. Panitkin, Nucl. Phys. **A 698** (2002) 323.

[130] PHOBOS Collaboration, Phys. Rev. Lett. **88** (2002) 022302.

[131] H. J. Specht, private communication.

[132] CERES Collaboration, Nucl. Phys. **A 661** (1999) 23.

[133] S. Damjanovic for the CERES collaboration, Proceedings of the Fourth International Conference on Physics and Astrophysics of Quark Gluon Plasma (ICPAQGP),Jaipur, 2001, to appear in Pramana, India; see also nucl-ex/0111009.

[134] J. Kapusta, P. Lichard and D. Seibert, Phys. Rev. **D 44** (1991) 2774.

[135] R. Baier, H. Nakkagawa, A. Niegawa and K. Redlich, Z. Phys. **C 53** (1992) 433.

[136] P. Aurenche, F. Gelis, R. Kobes and H. Zaraket, Phys. Rev. **D 58** (1998) 085003.

[137] P. Aurenche, F. Gelis and H. Zaraket, Phys. Rev. D **61** (2000) 116001.

[138] P. Aurenche, F. Gelis and H. Zaraket, Phys. Rev. D **62** (2000) 096012.

[139] L. D. Landau and I. Pomeranchuk, Dokl. Akad. Nauk. Ser. Fiz. **92** (1953) 535; Dokl. Akad. Nauk. Ser. Fiz. **92** (1953) 735.

[140] A. B. Migdal, Dokl. Akad. Nauk. S.S.S.R. **105** (1955) 77.

[141] A. B. Migdal, Phys. Rev. **103** (1956) 1811.

[142] P. Arnold, G. D. Moore and L. G. Yaffe, JHEP **0111** (2001) 057.

[143] P. Arnold, G. D. Moore and L. G. Yaffe, JHEP **0112** (2001) 009.

[144] J. I. Kapusta, P. Lichard and D. Seibert, Phys. Rev. **D 44** (1991) 2774.

[145] T. Peitzmann and M. H. Thoma, Phys. Rept. **364** (2002) 175.

[146] F. D. Steffen and M. Thoma, Phys. Lett. **B 510** 2001 98.

[147] M. M. Aggarwal *et al.* (WA98 Collaboration), nucl-ex/0006007.

[148] W. Vogelsang and M. R. Whalley, J. Phys. **G 23** (1997) A1.

[149] R. P. Feynman, R. D. Field and G. C. Fox, Phys. Rev. **D 18** (1978) 3320.

[150] M. Fontannaz and D. Schiff, Nucl. Phys. **B 132** (1978) 457.

[151] J. Hutson *et al.*, Phys. Rev. **D 51** (1995) 6139.

[152] A. Dumitru, L. Frankfurt, L. Gerland, H. Stocker and M. Strikman, Phys. Rev. **C 64** (2001) 054909.

[153] G. Piller and W. Weise, Phys. Rept. **330** (2000) 1.

[154] G. Papp, P. Levai and G. Fai, Phys. Rev. **C 61** (2000) 021902.

[155] D. K. Srivastava and B. Sinha, Phys. Rev. **C 64** (2001) 034902.

[156] P. Huovinen, P. V. Ruuskanen and S. S. Rasanen, Phys. Lett. B **535** (2002) 109.

[157] T. Matsui and H. Satz, Phys. Lett. **B 178** (1986) 416.

[158] C. Baglin *et al.* (NA38 Collaboration), Phys. Lett. **B 220** (1989) 471; Phys. Lett. **B 255** (1991) 459.

[159] C. Gerschel and J. Hufner, Phys. Lett. **B 207** (1988) 253; Z. Phys. **C 56** (1992) 171.

[160] M. C. Abreu *et al.* (NA50 Collaboration), Phys. Lett. **B 410** (1997) 327.

[161] J. Hufner and B. Z. Kopeliovich, Phys. Lett. **B 445** (1998) 223.

[162] J. Hufner, B. Z. Kopeliovich and A. Polleri, Eur. Phys. J. **A 11** (2001) 457.

[163] B. Z. Kopeliovich and F. Niedermayer, *Nuclear Screening In J / Psi And Lepton Pair Production*, JINR-E2-84-834, available as scanned preprint on the KEK dadabase, unpublished.

[164] B. Kopeliovich, A. Tarasov and J. Hufner, Nucl. Phys. **A 696** (2001) 669.

[165] F. Karsch, E. Laermann and A. Peikert, Nucl. Phys. **B 605** (2001) 579.

[166] S. Digal, P. Petreczky and H. Satz, Phys. Rev. **D 64** (2001) 094015.

[167] R. K. Ellis, FERMILAB-CONF-89-168-T *Lectures given at 17th SLAC Summer Inst., Stanford, CA, Jul 10-21, 1989.*

[168] R. V. Gavai *et al.*, Int. J. Mod. Phys. **A 10** (1995) 2999.

[169] M. I. Gorenstein *et al.*, Phys. Lett. **B 524** (2002) 265.

[170] B. Z. Kopeliovich and A. V. Tarasov, hep-ph/0205151.

[171] R. Vogt, Phys. Rept. **310** (1999) 197.

[172] B. Kopeliovich, A. Tarasov and J. Hufner, Nucl. Phys. **A 696** (2001) 669.

[173] M. E. Peskin, Nucl. Phys. **B 156** (1979) 365.

[174] G. Bhanot and M. E. Peskin, Nucl. Phys. **B 156** (1979) 391.

[175] Y. Oh, S. Kim and S. H. Lee, Phys. Rev. **C 65** (2002) 067901.

[176] D. Kharzeev, C. Lourenco, M. Nardi and H. Satz, Z. Phys. **C 74** (1997) 307.

[177] A. Capella, E. G. Ferreiro and A. B. Kaidalov, Phys. Rev. Lett. **85** (2000) 2080; J. P. Blaizot, M. Dinh and J. Y. Ollitrault, Phys. Rev. Lett. **85** (2000) 4012; J. Hufner, B. Z. Kopeliovich and A. Polleri, nucl-th/0012003.

[178] A. Mishra, J. Reinhardt, H. Stocker and W. Greiner, nucl-th/0201042.

[179] M. Gyulassy and M. Plumer, Phys. Lett. **B 243**, (1990) 432; X. Wang and M. Gyulassy, Phys. Rev. Lett. **68**, (1992) 1480.

[180] M. Gyulassy and X. Wang, Nucl. Phys. **B 420**, (1994) 583.

[181] R. Baier, Y. L. Dokshitzer, A. H. Mueller, S. Peigne and D. Schiff, Nucl. Phys. **B 483**, (1997) 291; Nucl. Phys. **B 484**, (1997) 265; R. Baier, Y. L. Dokshitzer, A. H. Mueller and D. Schiff, Phys. Rev. **C 60**, (1999) 064902; R. Baier, Y. L. Dokshitzer, A. H. Mueller and D. Schiff, Phys. Rev. **C 64** (2001) 057902.

[182] B. G. Zakharov, JETP Lett. **65**, (1997) 615.

[183] U. A. Wiedemann, Nucl. Phys. **B 588**, (2000) 303.

[184] M. Gyulassy, P. Levai and I. Vitev, Phys. Rev. Lett. **85**, (2000) 5535; Nucl. Phys. **B 594**, (2001) 371.

[185] E. Wang and X. N. Wang, Phys. Rev. Lett. **87** (2001) 142301.

[186] M. Gell-Mann, R. Oaks and B. Renner, Phys, Rev. **175** (1968) 2195.

[187] J. Breitweg et al., Eur. Phsy. J. **67** (1999) 609.

[188] A. H. Mueller and J. w. Qiu, Nucl. Phys. **B 268** (1986) 427.

[189] M. Froissart, Phys. Rev. **123** (1961) 1053; A. Martin, Nuovo Cim. **42** (1966) 930.

LIST OF FIGURES

151

THANKS

A work of this length would not have been possible without the support of many people around me. This section is dedicated to them. I would like to thank all of them, especially...

- Prof. Dr. Wolfram Weise, for constant support and interest, the many opportunities to attend conferences and schools, and, last but not least, the occasional reminder that I could still do better.

- Roland Schneider, my collaborator who stood his ground next to me in the darkest hours of this project, for countless hot debates, Blackadder and other movie nights and good company all along.

- Alberto Polleri, my other collaborator, for many lively discussions and new insights into charm and other physics.

- J. Stachel, P. Braun-Munzinger, H. Satz and U. Heinz, from whom I was able to learn quite a lot about heavy-ion physics.

- Stefan W., Stefan F., Thomas and Michael, roommates and partners in the lively after-work program of T39, for a pleasant atmosphere during worktime.

- Kerstin, Sanja, Daniela, Katja, Andre, Lars, Jörg, Rainer and Hendrik — without you, conferences would just have been interesting; with you, they were really good!

- Rachel Weatherhead, who performed the miracle of making a six month stay in Italy seem as easy as visiting a friend in downtown Munich.

- the other members of ECT* for their hospitality.

- my girlfriend Doris, who always managed to cheer me up if the work wasn't going well.

- my parents, for arousing my early interest in science and for finally giving up the dream of me studying medicine.

Last but not least, I thank the patient reader who has come this far.